Title

Multi-wavelength population studies of Active Galactic Nuclei and Galaxies using PRIMUS and AEGIS /

Author

Mendez, Alexander John

Publication Date

2014

UNIVERSITY OF CALIFORNIA, SAN DIEGO

Multi-wavelength population studies of Active Galactic Nuclei and Galaxies using PRIMUS and AEGIS.

A dissertation submitted in partial satisfaction of the
requirements for the degree
Doctor of Philosophy

in

Physics

by

Alexander John Mendez

Committee in charge:

Professor Alison Coil, Chair
Professor William Coles
Professor Kim Griest
Professor Dušan Kereš
Professor Barnaby Rickett

2014

The dissertation of Alexander John Mendez is approved, and it is acceptable in quality and form for publication on microfilm and electronically:

Chair

University of California, San Diego

2014

DEDICATION

To my parents
For their love and inspiration,
in both life and science.

EPIGRAPH

Count what is countable,
measure what is measurable,
and what is not measurable, make measurable.
— Galileo Galilei

TABLE OF CONTENTS

LIST OF FIGURES

LIST OF TABLES

ACKNOWLEDGEMENTS

First, I thank Alison Coil for her support and guidance though the minefield of graduate school. Alison has been an outstanding role model, and has inspired me to be be a better observer, researcher, and scientist. I am grateful for the the unending knowledge, advice, and guidance of the individuals within the research group that she has cultivated at UCSD: John Moustakas, James Aird, Aleks Diamond-Stanic, Ramin Skibba, and Mojegan Azadi. I would also like to thank my thesis committee, Kim Griest, William Coles, Dušan Kereš, Barney Rickett and the late Arthur Wolfe for their feedback on my research projects and reading of this work.

I thank my family who have supported me in all of the small things, big and little. My parents, May and David, and my sister Meily have given me an amazing childhood and encouragement throughout my life.

I would like to thank the my fiends who have helped to make the graduate experience a truly enjoyable one. Thank you to Michael Erikstad for being a great friend, roommate, and robot construction aficionado. I thank Agneiszka Cieplak for her guidance and perspective, in short, she is awesome. I thank Darcy Barron for all of the hiking, biking, “baconing”, and “Kentucky-ing”. Many thanks to the Jonathan Whitmore and Marc Rafelski comedy-team in welcoming me to CASS, and helping me get started in research. I would like to thank Chad Kishimoto for being a great office-mate. Thank you Nathan Johnson, Matthew Affolter, Dave Boettger, the rest of my cohort, and all of CASS for the interesting conversations at Thursday lunch, BASH, and tea time.

OFFICIAL ACKNOWLEDGEMENTS

Chapter 2, in full (with minor exceptions to conform to this thesis), is a reprint of material previously published as “AEGIS: The Morphologies of Green Galaxies at $0.4 < z < 1.2$”, by Alexander J. Mendez, Alison L. Coil, Jennifer Lotz, Samir Salim, John Moustakas, & Luc Simard, published in the The Astrophysical Journal, 2011, Vol. 736, p. 736. I was the primary investigator and author of this paper.

Chapter 3, in full (with minor exceptions to conform to this thesis), is a reprint of material previously published as “PRIMUS: Infrared and X-ray AGN Selection Techniques at $0.2 < z < 1.2$”, by Alexander J. Mendez, Alison L. Coil, James Aird, Aleksandar M. Diamond-Stanic, John Moustakas, Michael R. Blanton, Richard J. Cool, Daniel J. Eisenstein, Kenneth C. Wong, & Guangtun Zhu, published in the The Astrophysical Journal, 2013, Vol. 770, p. 40. I was the primary investigator and author of this paper.

Chapter 4 is a draft of material that will be submitted as “AEGIS + PRIMUS: Clustering of X-ray-, Radio- and IR-AGN at $z \sim 0.7$” by Alexander J. Mendez, Alison L. Coil, James Aird, Ramin A. Skibba, Aleksandar M. Diamond-Stanic, John Moustakas, Michael R. Blanton, Richard J. Cool, Daniel J. Eisenstein, Kenneth C. Wong, & Guangtun Zhu, to the The Astrophysical Journal. I am the primary investigator and author of this paper.

VITA

2008	B. S. in Physics and Astronomy with College Honors, University of Washington
2008	B. S. in Mathematics, University of Washington
2010	M. S. in Physics, University of California, San Diego
2014	Ph. D. in Physics, University of California, San Diego

PUBLICATIONS

Mendez, A. J., Coil, A. L., Aird, J., Diamond-Stanic, A. M., Skibba, R. A., Moustakas, J., Blanton, M. R., Cool, R. J., Eisenstein, D. J., Wong, K. C., and Zhu, G., "AEGIS+PRIMUS: X-ray, Radio and IR-AGN Clustering At $z \sim 0.7$", 2014 in prep.

Mendez, A. J., Coil, A. L., Skibba, R. A., Aird, J., Diamond-Stanic, A. M., Moustakas, J., Blanton, M. R., Cool, R. J., Eisenstein, D. J., Wong, K. C., and Zhu, G., "AEGIS+PRIMUS: Stellar Mass and Star Formation Rate Dependent Galaxy Clustering at $z \sim 0.7$", 2014 in prep.

Mendez, A. J., Coil, A. L., Aird, J., Diamond-Stanic, A. M., Moustakas, J., Blanton, M. R., Cool, R. J., Eisenstein, D. J., Wong, K. C., and Zhu, G., "PRIMUS: Infrared and X-Ray AGN Selection Techniques at $0.2 < z < 1.2$", 2013, ApJ, 770, 40

Cool, R. J., Moustakas, J., Blanton, M. R., Burles, S. M., Coil, A. L., Eisenstein, D. J., Wong, K. C., Zhu, G., Aird, J., Bernstein, R. A., Bolton, A. S., Hogg, D. W., and **Mendez, A. J.**, "The PRIsm MUlti-object Survey (PRIMUS). II. Data Reduction and Redshift Fitting", 2013, ApJ, 767, 118

Moustakas, J., Coil, A. L., Aird, J., Blanton, M. R., Cool, R. J., Eisenstein, D. J., **Mendez, A. J.**, Wong, K. C., Zhu, G., and Arnouts, S., "PRIMUS: Constraints on Star Formation Quenching and Galaxy Merging, and the Evolution of the Stellar Mass Function from $z = 0 - 1$", 2013, ApJ, 767, 50

Rafelski, M., Wolfe, A. M., Prochaska, J. X., Neeleman, M., and **Mendez, A. J.**, "Metallicity Evolution of Damped Ly Systems Out to $z \sim 5$", 2012, ApJ, 755, 89

Mendez, A. J., Coil, A. L., Lotz, J., Salim, S., Moustakas, J., and Simard, L., "AEGIS: The Morphologies of Green Galaxies at $0.4 < z < 1.2$", 2011, ApJ, 736, 110

Chornock, R., Bloom, J. S., Cenko, S. B., Filippenko, A. V., Silverman, J. M., Hicks, M. D., Lawrence, K. J., **Mendez, A. J.**, Rafelski, M., and Wolfe, A. M. "The Quasar SDSS J1536+0441: An Unusual Double-peaked Emitter", 2010, ApJL, 709

ABSTRACT OF THE DISSERTATION

Multi-wavelength population studies of Active Galactic Nuclei and Galaxies using PRIMUS and AEGIS.

by

Alexander John Mendez

Doctor of Philosophy in Physics

University of California, San Diego, 2014

Professor Alison Coil, Chair

This dissertation uses large galaxy redshift surveys and multi-wavelength imaging to place observational constraints on the evolution of galaxies and the supermassive black holes that they host since the Universe was roughly half its current age.

In the first chapter, we use data from the AEGIS survey to present quantitative morphological measurements of green valley galaxies, to constrain the mechanism(s) responsible for quenching star formation in this transition population and creating elliptical galaxies. We show that green galaxies are generally massive ($\langle \mathcal{M}_* \rangle \sim 10^{10.5}\, \mathcal{M}_\odot$) disk galaxies with high concentrations of light. We find that major mergers are not the dominant mechanism responsible for quenching star formation, and we find that either more mild external processes or internal secular processes play a crucial role in halting star formation.

In the second chapter, we use data from the PRIMUS survey to investigate *Spitzer*/IRAC and X-ray AGN selection techniques in order to quantify the overlap, uniqueness, contamination, and completeness of each AGN selection. For roughly similar depth IR and X-ray data, we find that $\sim$75% of IR-selected AGN are also identified as X-ray AGN. For the deepest X-ray data, this fraction increases to $\sim$90%, indicating that at most $\sim$10% of IR-selected AGN may be heavily obscured. While similar overall, the IR-AGN samples preferentially contain more luminous AGN, while the X-ray AGN samples identify AGN with a wider range of accretion rates, where the host galaxy light dominates at IR wavelengths. A more complete AGN sample is created by combining both IR and X-ray selected AGN.

Finally, we present a clustering study of X-ray AGN, Radio AGN and IR-AGN selected AGN using spectroscopic redshifts from the PRIMUS and DEEP2 redshift surveys. Using the cross-correlation of AGN with dense galaxy samples, we find differences in the clustering properties of AGN selected at different wavelengths. However, we find no significant differences in the clustering of each AGN sample with matched galaxy samples that have the same distribution of redshift, stellar mass, and star formation rate. The observed differences in the clustering of AGN selected at different wavelengths can therefore be explained by the clustering differences of their host populations.

Chapter 1

Introduction

The universe is as complicated as it is vast in size and scale. In the past century great strides have been made in understanding the universe within the so-called Λ-Cold Dark Matter (λCDM) framework. Briefly, in this model there are quantum fluctuations in the mass-energy density of the universe that were created during the Big Bang. From these initially minuscule perturbations, over cosmic time overdensities in dark matter density field gravitationally collapsed into halos where the first stars and eventually the galaxies formed that we observe today (Mo, van den Bosch, & White 2010). Current precision observations of the universe span many decades of size, energy and time, and suggest that the universe is currently composed of $\sim$68.3% dark energy (Λ), $\sim$26.8% cold dark matter (CDM), and a minor $\sim$4.9% of baryonic matter (Planck Collaboration et al. 2013). Dark energy is the proposed energy content in the universe that accelerates the expansion of the universe. Dark matter is the proposed dominant matter content in the universe that does not interact electromagnetically and is inferred though gravitational effects on baryonic matter. λCDM has become the accepted framework in which to study galaxy formation from the combination of precision measurements of the cosmic microwave background, large-scale structure, light-element abundances and the acceleration of the universe. Alone, however, this framework is not enough to understand the underlying physical processes driving the variety of observed morphological, spectral, and evolutionary properties of galaxies. For example, λCDM overpredicts the number density of dwarf galaxies compared to what is observed and has a different prediction for the inner dark matter density profiles found on galactic scales where baryonic processes (e.g., interactions with the stellar and gaseous component of galaxies) are expected to dominate.

Similar to looking at the night side of Earth from space, where cities trace out both the geographical contours and the political history of the land, galaxies are visible tracers of both the underlying dark matter distribution and the history of baryonic interactions. Galaxies are gravitationally bound systems composed of stars, gas, dust, and dark matter, and they often have a central supermassive black hole (SMBH) with a mass $M_{BH} \sim 10^6 - 10^8 \mathcal{M}_\odot$. The goal of this dissertation is to provide key observational details within the structure of λCDM to help address the following questions related to galaxies and SMBHs: What different physical mechanisms change the stellar and gaseous component of galaxies? How can we use galaxy morphological information to constrain these physical mechanisms? How do galaxies and SMBH co-evolve? How complete or biased are our current SMBH samples? What can we learn about the triggering and fueling of the SMBH with our current observed samples?

1.1 Galaxy Historical Background

Until the early part of the twentieth century, the general picture of the entire universe was thought to be contained within our own galaxy, the Milky Way. Observations of so-called "island universes" (spiral-structured diffuse light; Rosse 1850) suggested that there were many other galaxies similar to our own. Measurements by Edwin Hubble of their velocities and distances dramatically extended the size and composition of our known universe by proving that these sources were outside of our own galaxy. From this, the study of extragalactic astronomy and galaxy formation and evolution was born.

Historically, there were two competing models which attempted to explain the formation of these gravitationally bound collections of stars and gas: monolithic collapse of matter (Eggen, Lynden-Bell, & Sandage 1962) and hierarchical formation (Searle & Zinn 1978). Monolithic collapse suggests that a single cloud of gas and dust gravitationally collapses to form a rapidly rotating disk. Today, the more commonly accepted theory explains that galaxies generally grow from the bottom up, hierarchically combining lower-mass galaxies to form the larger ones (Rees & Ostriker 1977; Silk 1977). Interactions between lower-mass galaxies can result in many different physical mechanisms which not only change the morphology of a galaxy, but can also drive changes in the rate at which stars form within each galaxy.

To understand the differences in the observed galaxy populations, early galactic studies focused on galaxy morphology. The famous Hubble "tuning-fork" diagram (Hubble 1926) categorized galaxies into "early" and "late" types, where early-type galaxies have smooth, elliptical morphologies, while late-type galaxies are dominated by spiral arm structure. The finer classification of spiral galaxies was defined by how tight the spiral arms were and whether there was an observed stellar bar structure at the center of the galaxy. In this classification scheme, Hubble suggested that galaxies started as early-type and evolved with time into late-type (i.e., from ellipticals into spirals). Measurements of the larger rotational velocities of late-type spiral galaxies disproved this hypothesis. Today this temporally backwards nomenclature for galaxies still exists as it correlates well with many other properties of galaxies (e.g., stellar masses, star formation rates, luminosities, and colors).

Following the tuning fork classification scheme, many different parametric and nonparametric analysis techniques have been developed to measure galaxy morphology. Parametric methods fit free-parameter models of the surface brightness to provide estimates of the galaxy size, axis ratios and profile shapes. Non-parametric methods identify key metrics (e.g., concentration, asymmetry, and smoothness) to estimate quantities from imaging data without an imposed model of the galaxy. Many of these models are extended to include irregular or disturbed galaxies and barred spiral-galaxies. While different in their technique, methodology, and reliability, all of these classification schemes generally identify the bulk of galaxies as either early- or late-type, forming a bimodality of galaxy morphologies in the local universe (e.g., Blanton & Moustakas 2009; Mignoli et al. 2009).

Large photometric surveys of galaxies can efficiently measure the differences in the stellar populations in these two galaxy types (e.g., Strateva et al. 2001). A “color-magnitude diagram” (CMD) shows the distribution of galaxies in terms of their optical colors and magnitudes (luminosity). The color, or difference in luminosity in two broadband photometric filters, reflects the dominant stellar population and is related to the recent star formation history of a galaxy. The optical color is well matched to the specific star formation rate (sSFR, star formation rate per unit galaxy stellar mass; Mostek et al. 2013), which reflects how efficiently star formation contributes to the growth of galaxies of different stellar masses. Essentially, sSFR is the reciprocal of the required time to form the current stellar population with the current star formation efficiency and removes the nearly linear stellar mass dependance found in the star formation rate (SFR).

The two main features visible in an optical CMD are the “red-sequence”, a relatively tight region of galaxies with red colors, dominated by ellipticals, and the “blue cloud”, a more diffuse group of blue galaxies, dominated by spirals. As the color reflect the amount of high energy photons emitted by young stars from regions of active star formation, these CMD features also reflect differences in the stellar populations of these two galaxy types: elliptical galaxies are comprised of older stellar populations with redder colors, while spiral galaxies have ongoing star formation with bluer colors. These two populations, referenced as quiescent galaxies and star forming galaxies, form a bimodality in optical color or sSFR. The minimum between the two galaxy popluations is generally referred to as the “green valley” (e.g., Baldry et al. 2004; Martin et al. 2007; Wyder et al. 2007; Salim et al. 2009).

In order to understand how galaxies have changed with time, local galaxy samples ($z \sim 0$) are compared to higher redshift samples ($z \gtrsim 0.5$) that include galaxies at an earlier cosmic epoch. Galaxy samples at $z \sim 1$ probe the galaxy population at roughly half the current age of the universe and show dramatic differences compared to local samples in terms of galaxy’s morphologies, SFRs, number densities, and sizes. Wide area surveys have found more red sequence galaxies at $z \sim 0$ compared to $z \sim 1$ (Bell et al. 2004; Faber et al. 2007). The growth of red sequence galaxies is strongly stellar mass dependent with the number density of $\sim 10^{10}\,\mathcal{M}_{\odot}$ quiescent galaxies increasing by a factor of 2-3 since $z \sim 1$ while the number density of more massive galaxies remains approximately constant (Moustakas et al. 2013). The increase in the number density of red sequence galaxies indicates that blue cloud galaxies shut down their star formation and become red sequence galaxies. The star formation must be quenched (quickly shut down in $<$ 1 Gyr) or the observed color bimodality would be smeared out. Understanding these star formation and morphological changes observed over the last half of cosmic time are driving much of the work in the field of galaxy evolution today.

1.2 Active Galaxy Historical Background

In the past century, the study of so-called active galaxies started alongside the study of extragalactic astronomy. Today, it is well established that most galaxies host a SMBH in their centers (Kormendy & Richstone 1995). Active galaxies are undergoing an intense period of accretion onto the SMBH at the centers of these galaxies and are classified as having an active galactic nucleus (AGN; e.g., Rees 1984; Antonucci & Ulvestad 1985; Urry & Padovani 1995). AGN tend to be extremely bright due to the release of gravitational potential energy from the accreting matter (Shakura & Sunyaev 1973). The resulting luminosity is generally related to the mass accretion rate though the parameterization:

$$L = \epsilon\, c^2 \, \frac{dM}{dt} \tag{1.1}$$

where ϵ is an efficiency parameter and dM/dt is the mass accretion rate. The efficiency parameter depends on the geometric properties of the accretion flow and is typically less than 0.1 (Done 2010).

Understanding the accretion mode and processes that fuel the AGN is related to the rate at which matter is accreted onto the SMBH (Kauffmann & Heckman 2009; Trump et al. 2009). The mass accretion rate can be tracked by the Eddington Ratio: the ratio of the AGN luminosity to the theoretical Eddington limit (L_{Edd}), where the radiation pressure on the infalling matter balances the gravitational force inward for spherically symmetric accretion. This balance is achieved when:

$$F_{\text{gravity}} \sim \frac{G M_{BH} m_p}{r^2} = \frac{L_{Edd}\sigma_T}{4\pi r^2 c} = F_{\text{rad}} \tag{1.2}$$

where G is the gravitational constant, M_{BH} is the black hole mass, m_p is the mass of the proton, L_{Edd} is the Eddington luminosity, and σ_T is the Thompson scattering cross-section. The mass of the electron adds a negligible amount to the gravitational force and is dropped for simplicity. From this equality the Eddington ratio (η) is

$$\eta = \frac{L_{acc}}{L_{edd}} = \frac{\sigma_T\, L_{acc}}{4\pi c m_p\, G M_{BH}}. \tag{1.3}$$

The Eddington ratio is generally estimated to have a wide range of values, between $10^{-4} < \eta < 1$, for typical SMBH masses ($M_{BH} \sim 10^6 - 10^8 \mathcal{M}_{\odot}$) (e.g., Kollmeier et al. 2006; Brusa et al. 2009; Kelly et al. 2010; Aird et al. 2012). While the estimated Eddington ratio assumes spherical accretion, it provides a simple zeroth order approximation that is used widely in the literature (e.g., Marconi et al. 2004; Hopkins et al. 2008).

Our understanding of AGN derives from half a century of multi-wavelength astronomical observations. First identified by Edward Fath in 1908 via their strong nuclear emission-lines, they were not classified until the pioneering work of Seyfert (1943). These sources, now known as Seyfert galaxies, are classified by the emission lines identified in their spectra: type 1 Seyferts show broad emission lines (e.g., H I, He I, He II) and narrow emission lines (e.g., O III), whereas type 2 Seyferts only show narrow emission lines. In the 1950s, Karl Jansky started the science of radio astronomy by identifying radio emission from sources other than the Sun. Radio surveys of the sky identified many bright quasi-stellar objects (QSOs, or quasars) in the sky. These sources were either composed of a single bright radio point source, or two symmetric components structured like an outflowing jet from a central source, and were many times (10-30) brighter than other known radio sources (Hazard 1963). In quick succession, the first rockets with X-ray detectors began identifying X-ray emissions from these and other sources (e.g., Giacconi et al. 1962; Bowyer et al. 1964; Friedman, Byram, & Chubb 1967; Bowyer et al. 1970). Uhuru, the first dedicated X-ray satellite, identified X-ray emission from dozens of Seyfert galaxies (Gursky et al. 1971).

More recently, modern ground-based and satellite telescopes have developed and surveyed the sky across a wide range of wavelengths from the radio to the gamma ray. This wealth of multi-wavelength observations led to the paradigm of AGN unification. This model, proposed by Antonucci & Ulvestad (1985) and elegantly described by Urry & Padovani (1995), suggests that this disparate array of sources, including Seyfert galaxies, radio sources, and bright blue optical point sources, are similar in nature but differ merely in their orientation relative to the observer. They are all assumed to be accreting AGN, where the model proposes that surrounding the SMBH and accretion disk is a highly concentrated gas and dust-filled torus which obscures UV and optical light. X-ray emission may still be visible depending on the column density of the gas and dust along the line of sight through the torus, while radio emission is visible depending on the orientation of the accretion disk relative to the observer and the possible existence of jets extending past the galactic disk.

Despite their significantly different size scales, there are many observed correlations between the evolution, growth and activity of SMBHs and the galaxies that host them. The apparent co-evolution of SMBHs and galaxies stems from two key observations: (1) the cosmic star formation history and AGN mass accretion history are broadly similar, both peaking at $z \sim 2$ (e.g., Soltan 1982; Madau et al. 1996; Franceschini et al. 1999; Zheng et al. 2009; Serjeant et al. 2010); and (2) the relatively tight correlation between the SMBH mass and mass of the galaxy bulge or stellar velocity dispersion (M-σ relationship; e.g., Magorrian et al. 1998; Gebhardt et al. 2000; Tremaine et al. 2002). These correlations hint at the possibility of a combined evolution between the host galaxy and AGN (e.g., Hopkins et al. 2008). While more is known today about these sources, there are key open questions in AGN studies: What triggers AGN activity? What influence does the AGN have on the host galaxy? What influence does the host galaxy have on the AGN? What is the accretion history of the universe?

1.3 Redshift Surveys

A major turning point in the study of galaxies and AGNs was the rise of systematic redshift surveys, which obtained spectroscopic redshifts for large, uniform samples of galaxies. Pioneered by the work of Gregory & Thompson (1978) and Sandage (1978), redshift surveys allow for the measurement of the large-scale structure of the universe and the statistical characterization of galaxies. Completed in 1982, the Center for Astronomy (CfA) Redshift Survey (Davis et al. 1982), was one of the first redshift surveys, targeting $\sim 2,400$ galaxies brighter than 14.5 mag at high galactic latitude. It produced the first quantitative measurement of the three dimensional distribution and clustering of galaxies, identifying dense groups and clusters of galaxies, long filamentary structures, and underdense voids. While expensive in terms of telescope time, due to observing the spectrum for each galaxy individually, this survey quantified the large-scale structure of the universe and paved the way for theoretical models of structure formation.

The reduction in cost and mass production of charged-coupled device (CCD) imaging units led to a boom in redshift surveys. The Two Degree Field Galaxy Survey (2dFGS; Colless et al. 2001) and the Sloan Digital Sky Survey (SDSS; York et al. 2000) revolutionized galaxy and AGN studies, as well as measurements of large-scale structure, by quantifying the nature of relatively nearby galaxies at low redshifts ($z < 0.3$). 2dF and SDSS obtained spectra for $\sim 220,000$ and $\sim 1,000,000$ sources, respectively. The enormous advances made by these survey stem primarily from the rapid technological improvements in multi-object spectrographs and wide-field imaging cameras.

By extending redshift surveys to higher redshifts, one can determine the statistical properties of the galaxy population and their evolution across cosmic time such as merger rates, correlation functions, and luminosity functions. The first surveys to probe higher redshifts ($z \gtrsim 0.2$) were only able to target hundreds to thousands of galaxies in small "pencil beam" surveys, covering a small area on the sky (e.g., Le Fevre et al. 1996; Adelberger et al. 1998; Giavalisco et al. 1998; Small et al. 1999; Hogg et al. 2000). These samples were not large enough to measure statistical properties in multiple bins of redshift or environment, in order to limit bias in their measurements. Further, the uncertainty in the results above $z \sim 0.2$ were dominated by cosmic variance, or the fact that these surveys were not large enough to fully sample the entire matter density distribution in the universe at that epoch. As galaxy properties correlate with the local density of mass, this was the dominant source of error in these surveys. Following these pencil-beam surveys, deeper and wider surveys such as the Deep Extragalactic Evolutionary Probe (DEEP2; Davis et al. 2003) the COMBO-17 Survey (Wolf et al. 2003), the VIMOS VLT

Deep Survey (VVDS; Le Fèvre et al. 2005; Garilli et al. 2008), and the zCOSMOS Survey(Lilly et al. 2007) aimed to measure a large enough volumes to accurately measure large scale structure and galaxy properties to $z \sim 1$. The largest of these surveys was the DEEP2 survey, which measured redshifts for $\sim 60,000$ galaxies at $0.7 < z < 1.4$ using the Deep Imaging Multi-object Spectrograph (DEMIOS) on the Keck telescopes over ~ 90 nights.

While these $z \sim 1$ surveys were a huge step forward, they did not probe a comparable volume to low redshift surveys ($z \sim 0.1$) by necessity, and the volume that they probed at $z < 0.5$ was quite small. The AGN and Galaxy Evolution Survey (AGES; Kochanek et al. 2012) covered this intermediate redshift range but lacked photometric depth to track the evolution of the typical L_* galaxy though $z \sim 0.5$ with small error bars. The PRism MUlti-object Survey (PRIMUS; Coil et al. 2011; Cool et al. 2013) addressed this gap by using low-resolution spectra obtained with a slit-mask and prism to cover a wide area to much deeper photometric depths than the AGES survey. The PRIMUS survey obtained redshifts for a total of $\sim 120,000$ galaxies, by observing $\sim 2,500$ targets at once, using 37 nights on the Magellan Baade telescope. By using a low-dispersion prism, PRIMUS targeted roughly an order of magnitude more galaxies at once than other surveys, thus requiring fewer nights of telescope time to carry out an even wider survey on the sky.

This thesis uses multi-wavelength observations and spectroscopic redshifts from the DEEP2 and PRIMUS redshift surveys. The combination of deep radio, mid-IR, optical, UV, and X-ray data with robust redshifts makes these surveys ideal for measuring the properties of galaxies at $z \sim 0.7$. The GALEX UV data, deep optical data, and *Spitzer* mid-IR data provide accurate estimates of the stellar masses and star formation rates for the galaxies, while the X-ray, mid-IR and radio provide numerous diagnostics for identifying AGN. Together these surveys probe a large volume ($\sim 10\,\mathrm{deg}^2$; $\sim 5 \times 10^7\,h^{-3}\,\mathrm{Mpc}^3$), ensuring robust measurements of galaxy and AGN samples, while limiting cosmic variance.

1.4 Correlation Functions

Redshift surveys that probe large volumes enable accurate measurements of the spatial distribution of galaxies and AGN. Jim Peebles developed the theoretical framework in the 1960s to understand the formation of what is known as large-scale structure, including overdense galaxy clusters and underdense voids. Galaxy clustering is typically measured using correlation functions which estimate the statistical correlation of galaxies relative to an unclustered, random distribution. For galaxies or AGN, the correlation function is estimated using $\xi(r)$, the two-point correlation function, which is defined as the excess probability density, dP/dV, above a Poisson random field of two sources being physically separated by a distance r,

$$\frac{dP}{dV} = n[1 + \xi(r)] \tag{1.4}$$

where n is the mean number density of the full sample (Peebles 1980). In particular, $\xi(r)$ is positive if the sample is more clustered than a random distribution. Rearranging the terms, $\xi(r)$ can be written in terms of the fractional difference of the local density from the average density:

$$\xi(r) = \langle \delta(x)\delta(x-r) \rangle \tag{1.5}$$

where $\delta(x) = (\rho(x) - \bar{\rho})/\bar{\rho}$, $\rho(x)$ is the local density, and $\bar{\rho}$ is the average density. On large enough scales (two-halo term; $\gtrsim 1\,h^{-1}\,\mathrm{Mpc}$), this formulation allows for the direct comparison of the galaxy distribution to the expected dark matter distribution. This allows one to statistically estimate the typical or minimum mass of the dark matter halos that the galaxies trace (Smith et al. 2003; Mo, van den Bosch, & White 2010). On smaller scales (one-halo term; $\lesssim 1\,h^{-1}\,\mathrm{Mpc}$), the two-point correlation function measures the distribution of galaxies within single dark matter halos and is sensitive to the effects of galaxy-galaxy interactions as well the impact that the host halo has on the galaxy.

1.5 Overview

An overview of the chapters contained within this dissertation is as follows. Chapter 2 presents the morphological properties of green valley galaxies, relative to blue cloud and red sequence galaxies, in the Extended Groth Strip to $z \sim 1.2$. We statistically identify the build up of stellar light in the bulges in these transition galaxies and discuss constraints on physical mechanisms that quench star formation at these redshifts. Chapter 3 characterizes the identification of AGN through either the IR or X-ray emission using multi-wavelength data in the PRIMUS survey. We compare the demographics of each population, including differences in the AGN properties and host galaxy properties of AGN identified using either mid-IR color selection techniques or X-ray detection. The reliability, completeness, and contamination of each wavelength selection are presented as a function of depth of a survey, in order to tie together the disparate published values found in the literature. Chapter 4 presents the two-point correlation functions of X-ray AGN, radio AGN, and IR-AGN, as compared both with each other and with matched galaxy control samples, in the PRIMUS and DEEP2 surveys. We investigate how systematic differences seen in the clustering of AGN identified at different wavelengths can be explained by differences in the host galaxy properties, such as stellar mass and redshift, and we compare how the specific accretion rates of the SMBHs found in these galaxies correlate with their clustering properties. Chapter 5 briefly summarizes the major results found in this work and identifies future directions for continued research.

1.6 References

Adelberger, K. L., Steidel, C. C., Giavalisco, M., Dickinson, M., Pettini, M., & Kellogg, M. 1998, ApJ, 505, 18–24

Aird, J., Coil, A. L., Moustakas, J., Blanton, M. R., Burles, S. M., Cool, R. J., Eisenstein, D. J., Smith, M. S. M., Wong, K. C., & Zhu, G. 2012, ApJ, 746, 90

Antonucci, R. R. J., & Ulvestad, J. S. 1985, ApJ, 294, 158–182

Baldry, I. K., Glazebrook, K., Brinkmann, J., Ivezić, Ž., Lupton, R. H., Nichol, R. C., & Szalay, A. S. 2004, ApJ, 600, 681

Bell, E. F., Wolf, C., Meisenheimer, K., Rix, H.-W., Borch, A., Dye, S., Kleinheinrich, M., Wisotzki, L., & McIntosh, D. H. 2004, ApJ, 608, 752–767

Blanton, M. R., & Moustakas, J. 2009, ARA&A, 47, 159

Bowyer, C. S., Lampton, M., Mack, J., & de Mendonca, F. 1970, ApJL, 161, L1

Bowyer, S., Byram, E. T., Chubb, T. A., & Friedman, H. 1964, Nature, 201, 1307–1308

Brusa, M., Fiore, F., Santini, P., Grazian, A., Comastri, A., Zamorani, G., Hasinger, G., Merloni, A., Civano, F., Fontana, A., & Mainieri, V. 2009, A&A, 507, 1277–1289

Coil, A. L., Blanton, M. R., Burles, S. M., Cool, R. J., Eisenstein, D. J., Moustakas, J., Wong, K. C., Zhu, G., Aird, J., Bernstein, R. A., Bolton, A. S., & Hogg, D. W. 2011, ApJ, 741, 8

Colless, M., Dalton, G., Maddox, S., Sutherland, W., Norberg, P., Cole, S., Bland-Hawthorn, J., Bridges, T., Cannon, R., Collins, C., Couch, W., Cross, N., Deeley, K., De Propris, R., Driver, S. P., Efstathiou, G., Ellis, R. S., Frenk, C. S., Glazebrook, K., Jackson, C., Lahav, O., Lewis, I., Lumsden, S., Madgwick, D., Peacock, J. A., Peterson, B. A., Price, I., Seaborne, M., & Taylor, K. 2001, MNRAS, 328, 1039–1063

Cool, R. J., Moustakas, J., Blanton, M. R., Burles, S. M., Coil, A. L., Eisenstein, D. J., Wong, K. C., Zhu, G., Aird, J., Bernstein, R. A., Bolton, A. S., Hogg, D. W., & Mendez, A. J. 2013, ApJ, 767, 118

Davis, M., Huchra, J., Latham, D. W., & Tonry, J. 1982, ApJ, 253, 423–445

Davis, M., Faber, S. M., Newman, J., Phillips, A. C., Ellis, R. S., Steidel, C. C., Conselice, C., Coil, A. L., Finkbeiner, D. P., Koo, D. C., Guhathakurta, P., Weiner, B., Schiavon, R., Willmer, C., Kaiser, N., Luppino, G. A., Wirth, G., Connolly, A., Eisenhardt, P., Cooper, M., & Gerke, B. 2003, In Society of Photo-Optical Instrumentation Engineers (SPIE) Conference Series, P. Guhathakurta, ed., volume 4834 of *Society of Photo-Optical Instrumentation Engineers (SPIE) Conference Series*, pp. 161–172

Done, C. 2010, ArXiv e-prints

Eggen, O. J., Lynden-Bell, D., & Sandage, A. R. 1962, ApJ, 136, 748

Faber, S. M., Willmer, C. N. A., Wolf, C., Koo, D. C., Weiner, B. J., Newman, J. A., Im, M., Coil, A. L., Conroy, C., Cooper, M. C., Davis, M., Finkbeiner, D. P., Gerke, B. F., Gebhardt, K., Groth, E. J., Guhathakurta, P., Harker, J., Kaiser, N., Kassin, S., Kleinheinrich, M., Konidaris, N. P., Kron, R. G., Lin, L., Luppino, G., Madgwick, D. S., Meisenheimer, K., Noeske, K. G., Phillips, A. C., Sarajedini, V. L., Schiavon, R. P., Simard, L., Szalay, A. S., Vogt, N. P., & Yan, R. 2007, ApJ, 665, 265–294

Franceschini, A., Hasinger, G., Miyaji, T., & Malquori, D. 1999, MNRAS, 310, L5–L9

Friedman, H., Byram, E. T., & Chubb, T. A. 1967, Science, 156, 374–378

Garilli, B., Le Fèvre, O., Guzzo, L., Maccagni, D., Le Brun, V., de la Torre, S., Meneux, B., Tresse, L., Franzetti, P., Zamorani, G., Zanichelli, A., Gregorini, L., Vergani, D., Bottini, D., Scaramella, R., Scodeggio, M., Vettolani, G., Adami, C., Arnouts, S., Bardelli, S., Bolzonella, M., Cappi, A., Charlot, S., Ciliegi, P., Contini, T., Foucaud, S., Gavignaud, I., Ilbert, O., Iovino, A., Lamareille, F., McCracken, H. J., Marano, B., Marinoni, C., Mazure, A., Merighi, R., Paltani, S., Pellò, R., Pollo, A., Pozzetti, L., Radovich, M., Zucca, E., Blaizot, J., Bongiorno, A., Cucciati, O., Mellier, Y., Moreau, C., & Paioro, L. 2008, A&A, 486, 683–695

Gebhardt, K., Bender, R., Bower, G., Dressler, A., Faber, S. M., Filippenko, A. V., Green, R., Grillmair, C., Ho, L. C., Kormendy, J., Lauer, T. R., Magorrian, J., Pinkney, J., Richstone, D., & Tremaine, S. 2000, ApJL, 539, L13–L16

Giacconi, R., Gursky, H., Paolini, F. R., & Rossi, B. B. 1962, Physical Review Letters, 9, 439–443

Giavalisco, M., Steidel, C. C., Adelberger, K. L., Dickinson, M. E., Pettini, M., & Kellogg, M. 1998, ApJ, 503, 543–552

Gregory, S. A., & Thompson, L. A. 1978, ApJ, 222, 784–799

Gursky, H., Kellogg, E. M., Leong, C., Tananbaum, H., & Giacconi, R. 1971, ApJL, 165, L43

Hazard, C. 1963, MNRAS, 126, 489

Hogg, D. W., Pahre, M. A., Adelberger, K. L., Blandford, R., Cohen, J. G., Gautier, T. N., Jarrett, T., Neugebauer, G., & Steidel, C. C. 2000, ApJS, 127, 1–9

Hopkins, P. F., Hernquist, L., Cox, T. J., & Kereš, D. 2008, ApJS, 175, 356–389

Hubble, E. P. 1926, ApJ, 64, 321–369

Kauffmann, G., & Heckman, T. M. 2009, MNRAS, 397, 135–147

Kelly, B. C., Vestergaard, M., Fan, X., Hopkins, P., Hernquist, L., & Siemiginowska, A. 2010, ApJ, 719, 1315–1334

Kochanek, C. S., Eisenstein, D. J., Cool, R. J., Caldwell, N., Assef, R. J., Jannuzi, B. T., Jones, C., Murray, S. S., Forman, W. R., Dey, A., Brown, M. J. I., Eisenhardt, P., Gonzalez, A. H., Green, P., & Stern, D. 2012, ApJS, 200, 8

Kollmeier, J. A., Onken, C. A., Kochanek, C. S., Gould, A., Weinberg, D. H., Dietrich, M., Cool, R., Dey, A., Eisenstein, D. J., Jannuzi, B. T., Le Floc'h, E., & Stern, D. 2006, ApJ, 648, 128–139

Kormendy, J., & Richstone, D. 1995, ARA&A, 33, 581

Le Fevre, O., Hudon, D., Lilly, S. J., Crampton, D., Hammer, F., & Tresse, L. 1996, ApJ, 461, 534

Le Fèvre, O., Vettolani, G., Garilli, B., Tresse, L., Bottini, D., Le Brun, V., Maccagni, D., Picat, J. P., Scaramella, R., Scodeggio, M., Zanichelli, A., Adami, C., Arnaboldi, M., Arnouts, S., Bardelli, S., Bolzonella, M., Cappi, A., Charlot, S., Ciliegi, P., Contini, T., Foucaud, S., Franzetti, P., Gavignaud, I., Guzzo, L., Ilbert, O., Iovino, A., McCracken, H. J., Marano, B., Marinoni, C., Mathez, G., Mazure, A., Meneux, B., Merighi, R., Paltani, S., Pellò, R., Pollo, A., Pozzetti, L., Radovich, M., Zamorani, G., Zucca, E., Bondi, M., Bongiorno, A., Busarello, G., Lamareille, F., Mellier, Y., Merluzzi, P., Ripepi, V., & Rizzo, D. 2005, A&A, 439, 845–862

Lilly, S. J., Le Fèvre, O., Renzini, A., Zamorani, G., Scodeggio, M., Contini, T., Carollo, C. M., Hasinger, G., Kneib, J.-P., Iovino, A., Le Brun, V., Maier, C., Mainieri, V., Mignoli, M., Silverman, J., Tasca, L. A. M., Bolzonella, M., Bongiorno, A., Bottini, D., Capak, P., Caputi, K., Cimatti, A., Cucciati, O., Daddi, E., Feldmann, R., Franzetti, P., Garilli, B., Guzzo, L., Ilbert, O., Kampczyk, P., Kovac, K., Lamareille, F., Leauthaud, A., Borgne, J.-F. L., McCracken, H. J., Marinoni, C., Pello, R., Ricciardelli, E., Scarlata, C., Vergani, D., Sanders, D. B., Schinnerer, E., Scoville, N., Taniguchi, Y., Arnouts, S., Aussel, H., Bardelli, S., Brusa, M., Cappi, A., Ciliegi, P., Finoguenov, A., Foucaud, S., Franceschini, R., Halliday, C., Impey, C., Knobel, C., Koekemoer, A., Kurk, J., Maccagni, D., Maddox, S., Marano, B., Marconi, G., Meneux, B., Mobasher, B., Moreau, C., Peacock, J. A., Porciani, C., Pozzetti, L., Scaramella, R., Schiminovich, D., Shopbell, P., Smail, I., Thompson, D., Tresse, L., Vettolani, G., Zanichelli, A., & Zucca, E. 2007, ApJS, 172, 70–85

Madau, P., Ferguson, H. C., Dickinson, M. E., Giavalisco, M., Steidel, C. C., & Fruchter, A. 1996, MNRAS, 283, 1388–1404

Magorrian, J., Tremaine, S., Richstone, D., Bender, R., Bower, G., Dressler, A., Faber, S. M., Gebhardt, K., Green, R., Grillmair, C., Kormendy, J., & Lauer, T. 1998, AJ, 115, 2285–2305

Marconi, A., Risaliti, G., Gilli, R., Hunt, L. K., Maiolino, R., & Salvati, M. 2004, MNRAS, 351, 169–185

Martin, D. C., Wyder, T. K., Schiminovich, D., Barlow, T. A., Forster, K., Friedman, P. G., Morrissey, P., Neff, S. G., Seibert, M., Small, T., Welsh, B. Y., Bianchi, L., Donas, J., Heckman, T. M., Lee, Y.-W., Madore, B. F., Milliard, B., Rich, R. M., Szalay, A. S., & Yi, S. K. 2007, ApJS, 173, 342–356

Mignoli, M., Zamorani, G., Scodeggio, M., Cimatti, A., Halliday, C., Lilly, S. J., Pozzetti, L., Vergani, D., Carollo, C. M., Contini, T., Le Févre, O., Mainieri, V., Renzini, A., Bardelli, S., Bolzonella, M., Bongiorno, A., Caputi, K., Coppa, G., Cucciati, O., de La Torre, S., de Ravel, L., Franzetti, P., Garilli, B., Iovino, A., Kampczyk, P., Kneib, J.-P., Knobel, C., Kovač, K., Lamareille, F., Le Borgne, J.-F., Le Brun, V., Maier, C., Pellò, R., Peng, Y., Perez Montero, E., Ricciardelli, E., Scarlata, C., Silverman, J. D., Tanaka, M., Tasca, L., Tresse, L., Zucca, E., Abbas, U., Bottini, D., Capak, P., Cappi, A., Cassata, P., Fumana, M., Guzzo, L., Leauthaud, A., Maccagni, D., Marinoni, C., McCracken, H. J., Memeo, P., Meneux, B., Oesch, P., Porciani, C., Scaramella, R., & Scoville, N. 2009, A&A, 493, 39–49

Mo, H., van den Bosch, F. C., & White, S. 2010. Galaxy Formation and Evolution

Mostek, N., Coil, A. L., Cooper, M., Davis, M., Newman, J. A., & Weiner, B. J. 2013, ApJ, 767, 89

Moustakas, J., Coil, A. L., Aird, J., Blanton, M. R., Cool, R. J., Eisenstein, D. J., Mendez, A. J., Wong, K. C., Zhu, G., & Arnouts, S. 2013, ApJ, 767, 50

Peebles, P. J. E. 1980. The large-scale structure of the universe

Planck Collaboration, Ade, P. A. R., Aghanim, N., Armitage-Caplan, C., Arnaud, M., Ashdown, M., Atrio-Barandela, F., Aumont, J., Baccigalupi, C., Banday, A. J., & et al. 2013, ArXiv e-prints

Rees, M. J. 1984, ARA&A, 22, 471–506

Rees, M. J., & Ostriker, J. P. 1977, MNRAS, 179, 541–559

Rosse, T. E. O. 1850, Royal Society of London Philosophical Transactions Series I, 140, 499–514

Salim, S., Dickinson, M., Michael Rich, R., Charlot, S., Lee, J. C., Schiminovich, D., Pérez-González, P. G., Ashby, M. L. N., Papovich, C., Faber, S. M., Ivison, R. J., Frayer, D. T., Walton, J. M., Weiner, B. J., Chary, R.-R., Bundy, K., Noeske, K., & Koekemoer, A. M. 2009, ApJ, 700, 161–182

Sandage, A. 1978, AJ, 83, 904–937

Searle, L., & Zinn, R. 1978, ApJ, 225, 357–379

Serjeant, S., Negrello, M., Pearson, C., Mortier, A., Austermann, J., Aretxaga, I., Clements, D., Chapman, S., Dye, S., Dunlop, J., Dunne, L., Farrah, D., Hughes, D., Lee, H.-M., Matsuhara, H., Ibar, E., Im, M., Jeong, W.-S., Kim, S., Oyabu, S., Takagi, T., Wada, T., Wilson, G., Vaccari, M., & Yun, M. 2010, A&A, 514, A10

Seyfert, C. K. 1943, ApJ, 97, 28

Shakura, N. I., & Sunyaev, R. A. 1973, A&A, 24, 337–355

Silk, J. 1977, ApJ, 211, 638–648

Small, T. A., Ma, C.-P., Sargent, W. L. W., & Hamilton, D. 1999, ApJ, 524, 31–48

Smith, R. E., Peacock, J. A., Jenkins, A., White, S. D. M., Frenk, C. S., Pearce, F. R., Thomas, P. A., Efstathiou, G., & Couchman, H. M. P. 2003, MNRAS, 341, 1311–1332

Soltan, A. 1982, MNRAS, 200, 115–122

Strateva, I., Ivezić, Ž., Knapp, G. R., Narayanan, V. K., Strauss, M. A., Gunn, J. E., Lupton, R. H., Schlegel, D., Bahcall, N. A., Brinkmann, J., Brunner, R. J., Budavári, T., Csabai, I., Castander, F. J., Doi, M., Fukugita, M., Győry, Z., Hamabe, M., Hennessy, G., Ichikawa, T., Kunszt, P. Z., Lamb, D. Q., McKay, T. A., Okamura, S., Racusin, J., Sekiguchi, M., Schneider, D. P., Shimasaku, K., & York, D. 2001, AJ, 122, 1861–1874

Tremaine, S., Gebhardt, K., Bender, R., Bower, G., Dressler, A., Faber, S. M., Filippenko, A. V., Green, R., Grillmair, C., Ho, L. C., Kormendy, J., Lauer, T. R., Magorrian, J., Pinkney, J., & Richstone, D. 2002, ApJ, 574, 740–753

Trump, J. R., Impey, C. D., Kelly, B. C., Elvis, M., Merloni, A., Bongiorno, A., Gabor, J., Hao, H., McCarthy, P. J., Huchra, J. P., Brusa, M., Cappelluti, N., Koekemoer, A., Nagao, T., Salvato, M., & Scoville, N. Z. 2009, ApJ, 700, 49–55

Urry, C. M., & Padovani, P. 1995, PASP, 107, 803

Wolf, C., Meisenheimer, K., Rix, H.-W., Borch, A., Dye, S., & Kleinheinrich, M. 2003, A&A, 401, 73–98

Wyder, T. K., Martin, D. C., Schiminovich, D., Seibert, M., Budavári, T., Treyer, M. A., Barlow, T. A., Forster, K., Friedman, P. G., Morrissey, P., Neff, S. G., Small, T., Bianchi, L., Donas, J., Heckman, T. M., Lee, Y.-W., Madore, B. F., Milliard, B., Rich, R. M., Szalay, A. S., Welsh, B. Y., & Yi, S. K. 2007, ApJS, 173, 293–314

York, D. G., Adelman, J., Anderson, Jr., J. E., Anderson, S. F., Annis, J., Bahcall, N. A., Bakken, J. A., Barkhouser, R., Bastian, S., Berman, E., Boroski, W. N., Bracker, S., Briegel, C., Briggs, J. W., Brinkmann, J., Brunner, R., Burles, S., Carey, L., Carr, M. A., Castander, F. J., Chen, B., Colestock, P. L., Connolly, A. J., Crocker, J. H., Csabai, I., Czarapata, P. C., Davis, J. E., Doi, M., Dombeck, T., Eisenstein, D., Ellman, N., Elms, B. R., Evans, M. L., Fan, X., Federwitz, G. R., Fiscelli, L., Friedman, S., Frieman, J. A., Fukugita, M., Gillespie, B., Gunn, J. E., Gurbani, V. K., de Haas, E., Haldeman, M., Harris, F. H., Hayes, J., Heckman, T. M., Hennessy, G. S., Hindsley, R. B., Holm, S., Holmgren, D. J., Huang, C.-h., Hull, C., Husby, D., Ichikawa, S.-I., Ichikawa, T., Ivezić, Ž., Kent, S., Kim, R. S. J., Kinney, E., Klaene, M., Kleinman, A. N., Kleinman, S., Knapp, G. R., Korienek, J., Kron, R. G., Kunszt, P. Z., Lamb, D. Q., Lee, B., Leger, R. F., Limmongkol, S., Lindenmeyer, C., Long, D. C., Loomis, C., Loveday, J., Lucinio, R., Lupton, R. H., MacKinnon, B., Mannery, E. J., Mantsch, P. M., Margon, B., McGehee, P., McKay, T. A., Meiksin, A., Merelli, A., Monet, D. G., Munn, J. A., Narayanan, V. K., Nash, T., Neilsen, E., Neswold, R., Newberg, H. J., Nichol, R. C., Nicinski, T., Nonino, M., Okada, N., Okamura, S., Ostriker, J. P., Owen, R., Pauls, A. G., Peoples, J., Peterson, R. L., Petravick, D., Pier, J. R., Pope, A., Pordes, R., Prosapio, A., Rechenmacher, R., Quinn, T. R., Richards, G. T., Richmond, M. W., Rivetta, C. H., Rockosi, C. M., Ruthmansdorfer, K., Sandford, D., Schlegel, D. J., Schneider, D. P., Sekiguchi, M., Sergey, G., Shimasaku, K., Siegmund, W. A., Smee, S., Smith, J. A., Snedden, S., Stone, R., Stoughton, C., Strauss, M. A., Stubbs, C., SubbaRao, M., Szalay, A. S., Szapudi, I., Szokoly, G. P., Thakar, A. R., Tremonti, C., Tucker, D. L., Uomoto, A., Vanden Berk, D., Vogeley, M. S., Waddell, P., Wang, S.-i., Watanabe, M., Weinberg, D. H., Yanny, B., Yasuda, N., & SDSS Collaboration 2000, AJ, 120, 1579–1587

Zheng, Z., Zehavi, I., Eisenstein, D. J., Weinberg, D. H., & Jing, Y. P. 2009, ApJ, 707, 554–572

Chapter 2

The Morphologies of Green Galaxies

2.1 Abstract

We present quantitative morphologies of ∼300 galaxies in the optically-defined green valley at $0.4 < z < 1.2$, in order to constrain the mechanism(s) responsible for quenching star formation in the bulk of this population. The sample is selected from galaxies in the All-Wavelength Extended Groth Strip International Survey (AEGIS). While the green valley is defined using optical U-B colors, we find that using a green valley sample defined using NUV-R colors does not change the results. Using HST/ACS imaging, we study several quantitative morphological parameters including CAS, B/T from GIM2D, and Gini/M_{20}. We find that the green galaxy population is intermediate between the red and blue galaxy populations in terms of concentration, asymmetry, and morphological type and merger fraction estimated using Gini/M_{20}. We find that most green galaxies are *not* classified as mergers; in fact, the merger fraction in the green valley is *lower* than in the blue cloud. We show that at a given stellar mass, green galaxies have higher concentration values than blue galaxies and lower concentration values than red galaxies. Additionally, we find that 12% of green galaxies have $B/T = 0$ and 21% with $B/T \leq 0.05$. Our results show that green galaxies are generally massive ($M_* \sim 10^{10.5}\ M_\odot$) disk galaxies with high concentrations. We conclude that major mergers are likely not the sole mechanism responsible for quenching star formation in this population and that either other external processes or internal secular processes play an important role both in driving gas towards the center of these galaxies and in quenching star formation.

2.2 Introduction

The wealth of data generated by local large redshift surveys such as the *Sloan Digital Sky Survey* (SDSS, York et al. 2000) and the *Two-Degree Field Galaxy Redshift Survey* (2dFGRS, Colless et al. 2001) have greatly advanced our understanding of galaxy properties at $z \sim 0.1$. These surveys have clearly established that the local galaxy population exhibits a bimodal distribution in terms of optical color (e.g., Strateva et al. 2001; Blanton et al. 2003), UV-optical color (Salim et al. 2007), the 4000Å break $D_n - 4000$ (Kauffmann et al. 2003), and spectral type (Madgwick et al. 2002). In optical color-magnitude diagrams (CMDs) galaxies predominantly lie along either the "red sequence", which is dominated by quiescent, non-star-forming, early-type, bulge-dominated galaxies (e.g., Zhu, Blanton, & Moustakas 2010; Blanton & Moustakas 2009), or in the "blue cloud," characterized by star-forming, late-type, disk-dominated galaxies.

Deeper redshift surveys that probe galaxies at an earlier stage of evolution have shown that this bimodality exists at least to $z \sim 2$ (e.g., Willmer et al. 2006; Faber et al. 2007; Kriek et al. 2008; Williams et al. 2009). The location of the bimodality minimum is bluer at $z \sim 1$ by approximately 0.1 mag, as both blue and red galaxies were bluer in the past (Blanton 2006). Results from the COMBO-17 (Bell et al. 2004) and NOAO Deep Wide-Field Survey (Brown et al. 2007) photometric redshift surveys and the DEEP2 spectroscopic redshift survey (Faber et al. 2007) show that the red sequence has grown in mass by a factor of 2-4 since $z \sim 1$, while the number density of galaxies in the blue cloud has remained roughly constant (Bell et al. 2004; Brown et al. 2007; Faber et al. 2007). The large influx of red sequence galaxies brighter than L_* at $z \leq 0.7$ is dominated by spheroidal systems (Blanton et al. 2003; Bell et al. 2006; Weiner et al. 2005; Scarlata et al. 2007), but red disk-dominated galaxies are more common at fainter magnitudes (Brown et al. 2007).

Recent observational studies investigating galaxies in the minimum of the optical color bimodality, so-called "green valley" galaxies, have begun to probe the nature of this population. Baldry et al. (2004) model the u-r color distribution of SDSS galaxies and find that it can be fit as the sum of separate Gaussian distributions for the red and blue populations, implying that green valley galaxies are not necessarily a distinct population. However, Wyder et al. (2007) use UV-optical colors to more clearly separate the star-forming and quiescent populations and show that there is an excess of galaxies in the green valley galaxy population at $z \sim 0.1$; thus green galaxies may not be a simple mix of blue and red galaxies. Additionally, Salim et al. (2009) show in a comparison of the specific star formation rate (SSFR) versus rest-frame UV-optical color for low redshift galaxies that there is a smooth transition from high to low SSFR as color increases; galaxies at intermediate colors do not have a SSFR distribution that encompasses the values seen for both red and blue galaxies and thus appear to be a transition population.

The observed bimodality of galaxy colors reflects the fact that galaxies are either actively forming stars and are optically blue, are not forming stars and are optically red, or are dusty.

After a galaxy stops forming stars, it should move from the blue cloud to the red sequence; star formation quenching could therefore explain the observed evolutionary trends. From the observed number densities and clustering properties of galaxies as a function of color, the implied timescale for movement to the red sequence after the quenching of star formation must be short, on the order of ~ 1 Gyr, otherwise there would be no observed bimodality (Faber et al. 2007; Martin et al. 2007; Tinker, Wechsler, & Zheng 2010). The short time scale is also a natural consequence of stellar population models; without star formation blue galaxies turn red in ~ 1 Gyr (Bruzual & Charlot 2003).

It is not yet known what physical mechanism or mechanisms cause these galaxies to stop forming stars. A variety of star formation quenching mechanisms have been proposed. It has long been suggested that major mergers are the dominant mechanism responsible for converting blue, star-forming, spiral galaxies into red, quiescent, elliptical galaxies. Simulations show that major mergers randomize the orbits of stars within a galaxy and can change the overall galaxy morphology from a disk into a bulge (e.g. Toomre & Toomre 1972; Toomre 1977; Barnes & Hernquist 1992; Hernquist 1992, 1993; Naab & Burkert 2003; Cox et al. 2006b). During the merger, gas is funneled to the center of the remnant, resulting in a burst of star formation that consumes, expels and/or heats some fraction of the available gas through shocks or feedback from supernovae (e.g. Barnes & Hernquist 1996; Springel, Di Matteo, & Hernquist 2005b; Robertson et al. 2006; Cox et al. 2006a; Steinmetz & Navarro 2002).

Merger-induced starbursts alone are likely insufficient to fully quench star formation or to consume *all* of the available gas, particularly for gas rich mergers at high redshift; additional quenching or gas removal is needed (Dekel & Birnboim 2006; Birnboim, Dekel, & Neistein 2007). Cox et al. (2008) show that in smoothed particle hydrodynamic simulations the starburst efficiency in merger-induced starbursts in recent simulations is lower than what was found previously. Their results suggest that these starbursts will not fully consume or eject all of the gas in the system. Additionally, Lotz et al. (2008a) use similar simulations to show that major merger remnants have enhanced SFR for $\sim$1 Gyr *after* the coalescence of the nuclei, indicating that additional gas removal mechanisms are required. Residual star formation in the remnant can prevent the galaxy from having red colors characteristic of elliptical galaxies (Springel, Di Matteo, & Hernquist 2005a). In order for the green valley to exist, star formation must be quenched on relatively short time scales, of order $\sim$1 Gyr. If instead the residual star formation declines slowly over a Hubble time (Mihos & Hernquist 1994), the remnant would gradually transition to the red sequence, removing the green valley distinction between the red and blue galaxy populations.

Further, simulations show that cold gas accretion from the intergalactic medium can also feed star formation in galaxies, particularly at high redshift (Dekel & Birnboim 2006; Birnboim, Dekel, & Neistein 2007; Kereš et al. 2005, 2009; Brooks et al. 2009). In these simulations, dense filamentary gas collapses to forms cold clouds which are stable against shocks and can penetrate to the centers of dark matter halos and accrete onto galaxies. This cold gas inflow further necessitates additional quenching mechanisms, as red and dead galaxies must remain quenched for the majority of cosmic time. Shock heating of the gas as it falls into a more massive dark matter halo limits the cold gas accretion from the intergalactic medium. For halos with masses above $\sim 10^{12}\ M_{\odot}$, the infalling gas is heated to such a temperature that the cooling time is longer than the Hubble time, so that it cannot radiatively cool, thereby forming a halo of hot gas (Birnboim & Dekel 2003; Kereš et al. 2005; Dekel & Birnboim 2006). Johansson, Naab, & Ostriker (2009) show that gravitational heating may also be an important mechanism in massive halos, through the release of potential energy from infalling stellar clumps.

In addition to shock heating of infalling gas, Croton et al. (2006) has incorporated "radio-mode" Active galactic nucleus(AGN) feedback into simulations, in which an AGN heats gas in massive structures, such as galaxy groups and clusters to limit intergalactic gas from being able fall into the galaxy. This form of AGN feedback is observationally supported by X-ray imaging of evacuated cavities around massive galaxies in the centers of clusters (McNamara et al. 2000, 2001; McNamara & Nulsen 2007). Quasar mode AGN feedback, invoked in many current galaxy evolution models (Hopkins et al. 2006; Davé et al. 2001), could potentially limit the amount of cold gas available for star formation, but there is little direct observational evidence for this picture.

Interestingly, the rate of AGN detection is high in green valley galaxies, whether AGN are selected by deep X-ray surveys (Nandra et al. 2007; Coil et al. 2009; Hickox et al. 2009; Schawinski et al. 2009; Cardamone et al. 2010) or by optical line-ratio diagnostics (Salim et al. 2007). Nandra et al. (2007) find that many X-ray AGN host galaxies are green defined using (U-B) colors, while Pierce et al. (2010) find the same trend using (NUV-R) colors. Coil et al. (2008) show that in coadded spectra of DEEP2 galaxies, the average spectrum of green galaxies at $z \sim 1$ is not a simple mix of the average spectra of blue and red galaxies but instead shows line ratios indicative of enhanced AGN activity. Additionally, Bundy et al. (2008) find that the star formation quenching rate from $z \sim 1$ to today is consistent with the AGN "trigger" rate. It remains unclear, however, whether the presence of an AGN in a green valley galaxy is directly related to the star formation quenching process.

On the observational side, much recent work shows that secular effects may also play a crucial role in establishing the color bimodality. The majority of nearby disk galaxies ($\sim 75\%$) are found to have a stellar bar (Eskridge et al. 2000; Menéndez-Delmestre et al. 2007), and the bar fraction remains high to $z \sim 1$ (Sheth et al. 2003; Elmegreen, Elmegreen, & Hirst 2004; Jogee et al. 2004). The large non-axially-symmetric potential of bar galaxies can induce a large-scale inflow of stars and gas (Sellwood & Wilkinson 1993; Sheth et al. 2005), and studies of gas kinematics in the bar indicate that molecular gas flows inward along the bar dust lanes (Downes et al. 1996; Regan, Sheth, & Vogel 1999; Sheth et al. 2000; Sheth & Tormen 2002). Additionally, López-Sanjuan et al. (2011) find that minor mergers can not fully account for the mass growth of galaxies, suggesting that secular processes are needed to generate a bulge-dominated population.

These bulge-dominated galaxies may be populating early-type spirals such as those observed by Bundy et al. (2010). Interestingly, Masters et al. (2010) and Cameron et al. (2010) find that early-type spirals have higher bar fractions than late-types spirals. At $z \sim 1$ Oesch et al. (2010) and López-Sanjuan et al. (2010) find that major mergers are not common enough to explain the late- to early-type transition and suggest that either minor mergers or secular processes are needed.

Other potential quenching mechanisms need to have enough energy to halt star formation and continue to keep star formation quenched over a Hubble time. Many of the proposed mechanisms either heat the gas such that it cannot collapse to form stars (e.g. AGN feedback, Bower et al. 2006; Croton et al. 2006; Hopkins et al. 2006; Kang, Jing, & Silk 2006; Springel, Di Matteo, & Hernquist 2005a), remove cold gas from the galaxy as it falls into a halo (e.g. ram-pressure stripping Gunn & Gott 1972; Kimm et al. 2009; Quilis, Moore, & Bower 2000; Hester 2006; Farouki & Shapiro 1980; Moore et al. 1996; Abadi, Moore, & Bower 1999), or remove hot, diffuse, gas from a satellite galaxy (e.g. "strangulation" Larson, Tinsley, & Caldwell 1980; Balogh, Navarro, & Morris 2000). Tidal stripping of gas along the orbit of a satellite galaxy both removes gas and causes the galaxy to become more concentrated (van den Bosch et al. 2008), unlike ram-pressure stripping and strangulation, which mainly influence the gas in the galaxy as opposed to the stars. Additionally, gravitational interactions can greatly alter the morphology and gas content of a galaxy from the cumulative effect of many high-speed impulsive encounters, known as "harassment" (Farouki & Shapiro 1981; Moore et al. 1996).

The variety of proposed star formation quenching mechanisms mentioned above should have different morphological consequences. Therefore, in principle, one should be able to study the morphologies of green valley galaxies to constrain the dominant quenching mechanism. For example, parametric measures such as galaxy asymmetry can identify disturbed morphologies caused by major mergers (Conselice, Bershady, & Jangren 2000). In addition, the Gini coefficient (G) and second-order moment of light (M_{20}) parameters can be used to identify both major and minor mergers (Lotz et al. 2010). Gas stripping should lead to galaxies with truncated disks (Moore et al. 1996), while enhanced star formation due to harassment or other environmental interactions should lead to localized luminous areas, increasing the clumpiness (and decreasing the smoothness) of galaxies (Moore, Lake, & Katz 1998).

Previous studies of morphology and color have found that while most red galaxies have early-type, bulge-dominated morphologies, morphologically intermediate type galaxies (type Sa-Sbc) are scattered throughout the CMD, including the red sequence (e.g., Ball et al. 2006; Driver et al. 2006; Bell et al. 2003; Blanton & Moustakas 2009; Pannella et al. 2009). It is not yet clear if the majority of galaxies on the red sequence were already spheroidal when they first joined the red sequence or if they were still disk-dominated and later became spheroidal through mergers with other red galaxies, or if a combination of both processes occurs (Faber et al. 2007). Galaxies could potentially also move from the red sequence to the blue cloud, for example as the result of a merger between a blue and red galaxy. However, the bulk of the movement must be from the blue cloud to the red sequence to explain the observed mass and number density evolution on the red sequence.

In this paper we investigate the morphologies of green valley galaxies at $z \sim 1$ to a) compare their morphological distributions to those of blue and red galaxies at the same redshift, to constrain the dominant star formation quenching mechanism(s) at work, and b) test whether the morphological distribution of green galaxies is consistent with being a simple mix of red and blue galaxies, or whether green galaxies have a distinct morphological makeup. We use a sample of galaxies at $0.4 < z < 1.2$ from the All-Wavelength Extended Groth Strip International Survey (AEGIS) (Davis et al. 2007), combining *HST*/ACS imaging with DEEP2 spectroscopic and CFHTLS photometric redshifts to measure various quantitative morphological parameters.

The outline of the paper is as follows: In §2.3 we present the AEGIS datasets used here. In §2.4 we define the red, green and blue samples used here. In §2.5 we discuss the different morphological parameters measured. In §2.6 we present results on the morphologies of green galaxies compared to the red and blue galaxies at the same redshift. In §2.7 we perform statistical tests with control samples of blue and red galaxies to determine whether the green galaxy population has a distinct morphological distribution. Finally, we discuss and summarize the results in §2.8. Absolute magnitudes given in this paper are in the AB system and are $M_B - 5$ $\log(h)$ with $h = 0.7$, which for the remainder of the paper we denote as M_B. We assume the standard flat ΛCDM model with $\Omega_m = 0.3$ and $\Omega_\Lambda = 0.7$.

2.3 Data

To quantify the morphological distribution of green valley galaxies, we require a large, complete parent sample of galaxies with accurate redshifts, rest-frame colors and magnitudes, and high-resolution imaging. As galaxies in the green valley have a lower space density than either blue or red galaxies, we require a large parent sample to measure the bivariate distribution of morphological parameters with sufficient objects per bin. We use data from the AEGIS survey (Davis et al. 2007), which covers the Extended Groth Strip (EGS) and contains DEEP2 spectroscopic and CFHTLS photometric redshifts. We use *HST*/ACS imaging and CFHTLS photometry to define a complete galaxy sample large enough to allow us to quantify the joint morphological properties of green galaxies. We further use *GALEX* photometry in the field to test the effects of excluding green galaxies that are likely dusty, star-forming blue galaxies, as opposed to true transitionary galaxies. Table 2.1 contains a summary of the datasets and sample sizes.

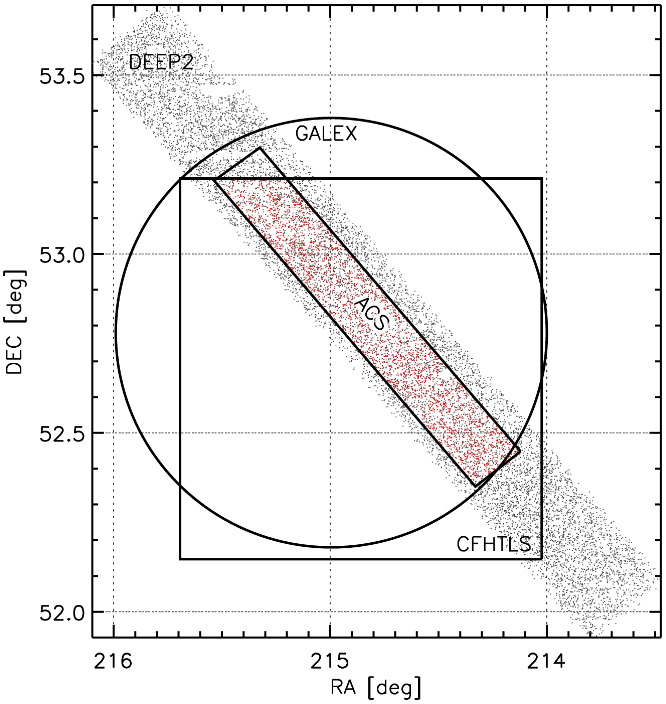

Figure 2.1: **Areal map of AEGIS datasets** — Areal map of the various relevant datasets in the EGS. Individual DEEP2 galaxies are shown in black points to a limit of to $R_{\mathrm{AB}} < 24.1$ and our sample is shown in red. Here we use galaxies that lie within the ACS region of the EGS and have secure DEEP2 spectroscopic redshifts (grey points) or good CFHTLS photometric redshifts (square region), with additional cuts (see Table 2.1 for sample sizes and depths). A single 1 deg deep *GALEX* pointing also overlaps a majority of the region.

2.3.1 *HST*/ACS Imaging

High-resolution images from the Hubble Space Telescope (*HST*) Advanced Camera for Surveys (ACS) were obtained from the AEGIS survey as part of the GO Program, 10134 PI: M. Davis (Davis et al. 2007). The EGS was imaged in both the V (F606 W, 2260 sec) and I (F814W, 2100 sec) bands in a $\sim 10\overset{\prime}{.}1$ by $67\overset{\prime}{.}$ strip along the field. For details about the ACS imaging and reduction see Davis et al. (2007) and Lotz et al. (2008b). The 5σ limiting magnitudes for a point source are $V_{\rm AB} = 28.75$ and $I_{\rm AB} = 28.10$.

2.3.2 CFHTLS *ugriz* Photometry

We use CFHTLS T0004 release *ugriz* photometry (Ilbert et al. 2006) to calculate rest-frame colors and magnitudes for each galaxy. The CFHTLS Deep Field 3 is a $1^\circ \times 1^\circ$ field that covers the majority of the ACS region (see Figure 2.1). We use CFHTLS photometry, flux limited to $i_{\rm AB} < 25$, for objects in the ACS region, to calculate rest frame magnitudes. There are 16,450 objects in the ACS footprint with CFHTLS *ugriz* photometry.

2.3.3 *GALEX* NUV/FUV Photometry

We use near-UV (NUV) and far-UV (FUV) data obtained from the single $1\overset{\circ}{.}2$ diameter pointing of the central region of the EGS, taken with the *Galaxy Evolution Explorer* (*GALEX*; Martin et al. 2005; Morrissey et al. 2007). The 237 ks of NUV imaging and 120 ks of FUV imaging data are part of the third data release (GR3) (Zamojski et al. 2007). We use deblended *GALEX* photometry from Salim et al. (2009), which use an expectation maximization (EM) method to measure fluxes using a Bayesian deblending technique (Guillaume et al. 2006) and optical u-band priors (see Salim et al. 2009, for details). This method overcomes issues of blending and source confusion due to the $4''$-$5''$ spatial resolution (FWHM) of *GALEX* (Morrissey et al. 2007). NUV detections are measured to a flux limit of $NUV < 26.5$, and a FUV flux limit of $FUV < 25$.

2.3.4 Spectroscopic and Photometric Redshifts

The DEEP2 redshift survey provides spectroscopic redshifts to $R_{\rm AB} < 24.1$ in AEGIS; see Davis et al. (2007) for details. Here we use only redshifts between $0.4 < z < 1.2$ with a confidence greater than 95% ($z_{\rm Quality} \geq 3$). With this quality cut, there are 2,885 galaxies with spectroscopic redshifts within the ACS region.

We additionally use photometric redshifts to both increase our sample size and allow us to probe fainter flux limits. We use CFHTLS T0003 release photometric redshifts from Ilbert et al. (2006), derived from *ugriz* imaging covering the central $1^\circ \times 1^\circ$ of the field. We remove from the sample all galaxies that are below our flux limit of $i_{AB} = 25$, that have large photometric errors, or that have a 5% or greater probability of being at a different redshift. We limit the sample to the redshift range $0.4 < z < 1.2$. At lower redshifts the volume probed is small, while the upper limit ensures that the ACS imaging samples rest-frame optical morphologies, thereby minimizing rest-frame wavelength-dependent morphology biases. Combined with DEEP2 redshifts, this results in a sample of galaxies with redshifts in the range $0.4 < z < 1.2$ with a median redshift of 0.75.

Using galaxies that have both DEEP2 spectroscopic and CFHTLS photometric redshifts, we are able to test the redshift precision of the photometric redshifts. Within the redshift range $0.4 < z_{spec} < 1.2$, there are 3,306 galaxies in both catalogs. Among these, 4.2% are catastrophic outliers, defined as having $|\Delta z|/(1 + z_{spec}) > 0.15$. Excluding catastrophic errors, the photometric redshifts have an accuracy of $\sigma_{\Delta z/(1+z_{spec}}) = 0.038$, with a normalized median absolute deviation: $\eta = 1.48$ and a median $[|\Delta z|/(1 + z_{spec})] = 3.1\%$. See Ilbert et al. (2006) for a full discussion of the photometric redshifts.

Table 2.1 contains a summary of the datasets, sample sizes, and depths for the parent sample. The completeness of our parent sample depends on the detection limits of the ACS images and the completeness of the DEEP2 and CFHTLS redshift catalogs, which may depend on color and magnitude. The DEEP2 spectroscopic targeting selection excludes objects with a surface brightness fainter than $\mu_R \sim 26.5$ (Davis et al. 2007), whereas the CFHTLS photometric redshift catalog has no strong selection against low surface brightness objects as compared to the ACS detections (Lotz et al. 2008b). Due to the detection in DEEP2 spectra of emission lines in blue star-forming galaxies and absorption features in older, red galaxies and CFHTLS measurements of spectral breaks in all galaxy populations, the redshift catalogs are not strongly biased against galaxies with either red or blue colors (Lotz et al. 2008b). The dominate selection effect is due to the ACS detection limits of the morphology measurements. The ACS surface brightness detection limit of $\mu \sim 24.7$ results in the lowest surface brightness galaxies, which are likely to be blue, missing from the morphology catalog (Lotz et al. 2008b). For our statistical tests, we ensure to always match the stellar mass distributions of the different comparison samples, which minimized the selection effect of missing the lowest surface-brightness blue galaxies.

2.3.5 K-Corrections and Stellar Masses

We use the CFHTLS *ugriz* photometry and *GALEX* NUV/FUV magnitudes to calculate K-corrections (Blanton & Roweis 2007). We convert the observed fluxes to rest-frame absolute *GALEX* NUV and $UBVR$ magnitudes in the Johnson-Morgan System.

We derive stellar masses for galaxies in our sample following Weiner et al. (2009), who show that reasonably robust stellar masses at these redshifts can be inferred from the rest-frame M_B and (U-B) colors, following color-M/L ratio relations (Bell & de Jong 2001). Comparing these stellar masses to those calculated by Salim et al. (2009), who fit spectral energy distributions (SEDs) for AEGIS galaxies using up to eight bands of photometry from the UV to the near-

Infrared, we find a good agreement, with an offset of 0.13 dex and a scatter of 0.2 dex. The IMF used here and by Weiner et al. (2009) is a "Diet Salpeter" IMF (Bell et al. 2003).

2.4 Galaxy Sample Definitions

We use rest-frame optical (U-B) colors to define our samples. As discussed below, we have tested that our results do not change if we instead use (NUV-R) colors, which more clearly separate star forming and quiescent galaxies. This shows that our results are robust against contamination in the green valley by dusty star forming galaxies. We define the rest-frame red, green, and blue galaxy color samples by first locating the magnitude-dependent minimum of the color bimodality. We use the well-defined magnitude-dependent slope derived using the red sequence and then solve for a color offset to locate the minimum of the green valley. To measure the slope of the red sequence, we fit a double Gaussian to the observed (U-B) color distribution in three magnitude bins (shown in the upper panel of Fig 2.2) and fit a linear color-magnitude relation to the maximum of the Gaussian fit to the red galaxies (shown as red dots in the lower panel of Figure 2.2). We then fit for an offset of this line to match the minimum in the observed color-magnitude diagram. The resulting definition of the center of the green valley is

$$(U-B) = -0.0189(M_B + 19.79) + 0.96 \tag{2.1}$$

where the AB magnitude offset is given at the median of the parent sample.

We define the green valley to have a width of $\delta(U-B) = 0.1$ about the minimum line, with red galaxies having redder colors and blue galaxies having bluer colors. The width of the green valley is relatively arbitrary when using optical colors; our choice follows Coil et al. (2008). See the dot-dashed lines in Figure 2.2 for the color sample definition. From our parent sample of 2,437 galaxies, with this color-magnitude cut there is a total of 571 red, 342 green, and 1,524 blue galaxies. The color-magnitude cut used to separate blue and red galaxies in Willmer et al. (2006) for the DEEP2 sample is very similar to the cut used here. We do not allow the definition of the center of the green valley to evolve with redshift; however if a redshift evolution of ~ 0.1 per unit redshift (Blanton 2006) is included in our color-magnitude cut, none of our results or conclusions change.We do not create strictly volume-limited samples, as we are not attempting to measure evolution in the morphological parameters of green galaxies with redshift. We impose an absolute magnitude limit of $M_B > -18$, to ensure that our colors samples (red, green and blue) are of roughly similar depth. We show in Section 2.6.2 that the distribution of morphological parameters is not a strong function of magnitude near the limit used here.

We test the robustness of our results to the color used to define the green valley. In Figure 2.3 we show in the left panels samples defined using (U-B) colors (in (U-B)-M_B space in the top panel and in (NUV-R)-M_B space in the bottom panel), along with samples defined using

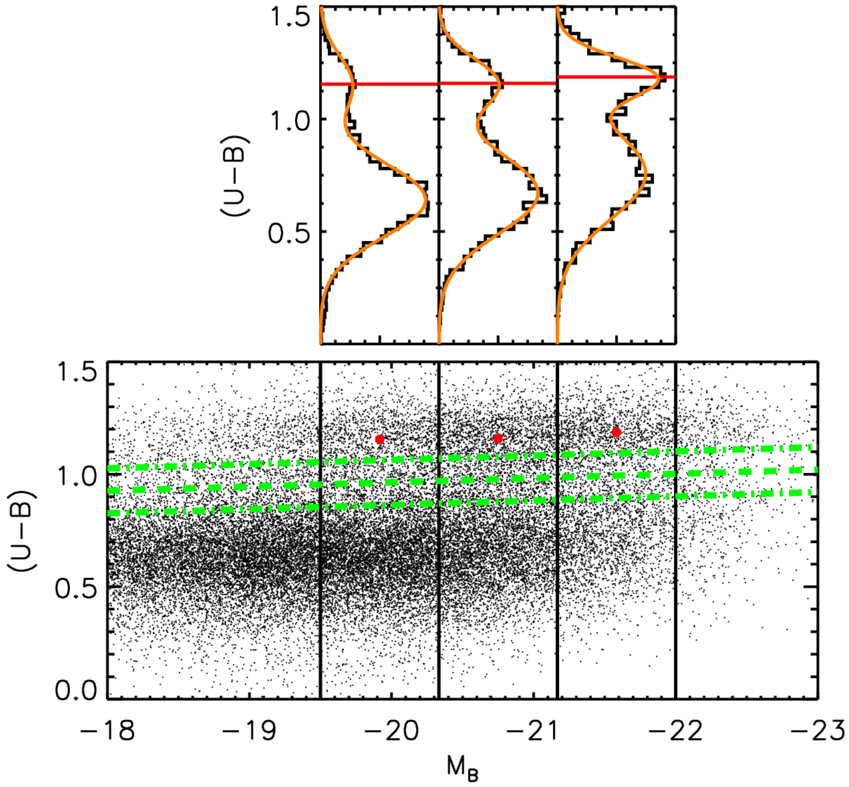

Figure 2.2: **Color-magnitude Diagram** — Color-magnitude diagram for AEGIS galaxies at $0.4 < z < 1.2$ and the definition of red, green, and blue galaxies. The upper panel shows double Gaussian fits (orange) to the (U-B) color distributions (black) for three magnitude bins between M_B =-19.5 and -23.0. We normalize the peak of the distribution in each magnitude bin to unity. We do not fit the magnitude-dependance of the red sequence below M_B=-19.5 or above M_B=-22 due to the lower numbers of red galaxies. The red lines show the peaks of the fit, used to fit a linear magnitude-dependent slope to the red sequence. This same slope is used to define the center of the green valley. The lower panel shows the color-magnitude diagram for galaxies with $0.4 < z < 1.2$. Red points mark the locations of the peak of the red sequence for each magnitude bin, and the green dashed lines show the center and width of the green valley as defined by Equation 2.1.

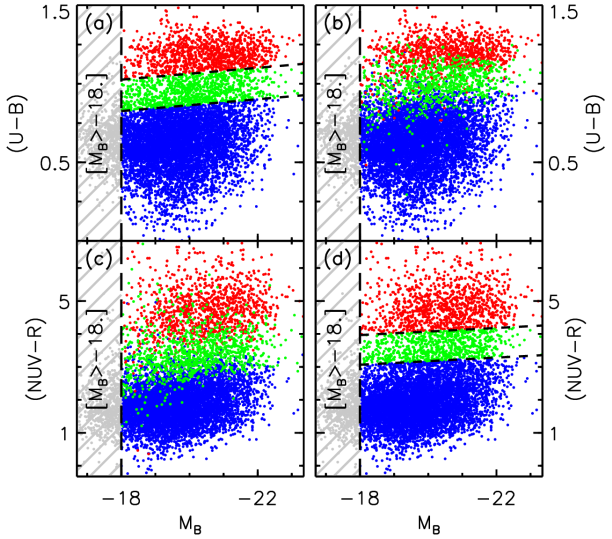

Figure 2.3: **Optical and UV color selection comparison** — Comparison of green valley sample selection in different color-magnitude spaces. (a) Upper left panel: Rest-frame (U-B) color versus M_B magnitude. Green valley galaxies are defined in this space using a tilted color cut (see Equation 2.1). This is the sample definition used throughout the paper. We define the green valley to be within δ(U-B)=0.1 of the minimum of the (U-B) color bimodality. Galaxies are color-coded here by whether they are defined to be red, green, or blue in this space. (c) Lower left panel: Rest-frame (NUV-R) versus M_B for the same galaxies, color-coded by their definition in the panel above. (d) Lower right panel: We present an alternative definition of green valley galaxies using the observed bimodality in rest-frame (NUV-R) versus M_B space. Galaxies here are color-coded by their definition in this space (see text for details). (b) Upper right panel: The same galaxies, color-coded by their definition in the panel below, are shown here in rest-frame (U-B) versus M_B space. This figure shows that the selection of green valley galaxies at $0.4 < z < 1.2$ is very similar using either (U-B) or (NUV-R) colors.

(NUV-R) colors in the right panels (again with (U-B)-M_B in the top panel and (NUV-R)-M_B in the bottom panel). To define the green valley in (NUV-R)-M_B space, we fit for the M_B magnitude slope evolution by fitting a Gaussian to the blue galaxies in four bins in magnitude. The color-magnitude cut is then shifted to the center between the red and blue peaks. The width of the green valley in (NUV-R) color is defined as $\delta(NUV - R) < 0.45$, which is chosen to ensure that a similar fraction of galaxies in the full sample is defined to be green in either (U-B) or (NUV-R) space.

We find that galaxies defined to be in the green valley in (NUV-R) color also lie in or near the green valley as defined in (U-B) color, with some scatter. Galaxies that are defined to be green in one color that are *not* green in the other color still lie very close to the defined green valley. We have verified that performing all of the analyses in this paper with an (NUV-R)-selected sample does not change any of our results.

We note that the definition of the green valley in (NUV-R) color fit for and used here is bluer than the definition in Salim et al. (2009), who defined green galaxies as having $3.5 < (NUV - R) < 4.5$. Here our final green galaxy sample (defined in (U-B)-M_B space) lies within $3.2 < (NUV - R) < 4.1$.

2.5 Measured Morphology Parameters

We derive quantitative morphological parameters for all galaxies in our sample from the *HST*/ACS imaging. To sample rest-frame B-band morphologies across the redshift range $0.4 < z < 1.2$, we use observed V-band morphologies for galaxies with $z < 0.6$ and observed I-band morphologies for galaxies with $z \geq 0.6$. Morphological classifications are flux limited to $I_{AB} < 25$. Following Lotz, Primack, & Madau (2004) and Lotz et al. (2006), we measure morphologies for those objects that have large enough sizes (Petrosian radius $r_p \geq 0.3''$) and high enough signal-to-noise (mean S/N per galaxy pixel > 4 within the segmentation map) to yield robust morphological parameter measurements. The ¡S/N¿ threshold depends on the pixel scale, while the Petrosian radius threshold depends on both the pixel scale and the point spread function; therefore these thresholds are *HST*/ACS specific. The Petrosian radius r_p is defined as the semi-major axis length at which the ratio of the surface brightness at r_p to the mean surface brightness within r_p is equal to 0.2. r_p is computed within an elliptical aperture using the ellipticity computed from the SExtractor galaxy photometry software (Bertin & Arnouts 1996). The flux and radius cuts corresponds to an average surface brightness within the Petrosian radius of $\mu \sim 24.4$ AB magnitudes per square-arcsec (Lotz et al. 2008b). All of the quantitative morphological measurements below use the same segmented maps created by Lotz, Primack, & Madau (2004). With these cuts, our sample contains 2,437 galaxies with measured morphologies and redshifts within $0.4 < z < 1.2$. We derive a variety of morphological parameters; details of each are given below.

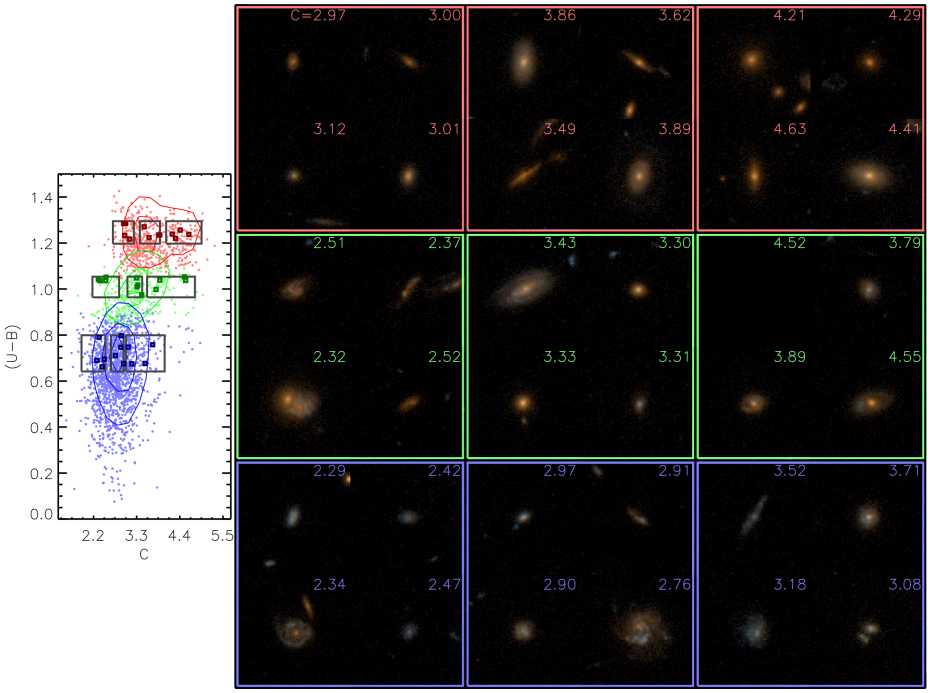

Figure 2.4: **Concentration parameter visualization** — To help visualize the different morphology parameters that we include in this paper, we show here and in Figures 5 and 6 a random selection of *HST*/ACS $V + I$ color image postage stamps spanning the full range of the concentration, asymmetry, and B/T parameter for galaxies in each red, green and blue color space. To select the galaxies, each color space is divided into three areas, comprising the lower 20% extreme of the cumulative relevant morphological distribution, middle 30% centered at the median, and higher 20% extreme. The selection boxes are shown in the bivariate parameter and color plots to the left. Contours contain 30%, 50% and 80% of the individual color-parameter distributions. From within each selection region we randomly draw four galaxies; postage stamps for each are shown on the right, with the value of the measured morphology parameter shown in the top right corner of each postage stamp for that galaxy. Postage stamps are $6''$ across, corresponding to ~ 65 kpc at $z = 0.8$.

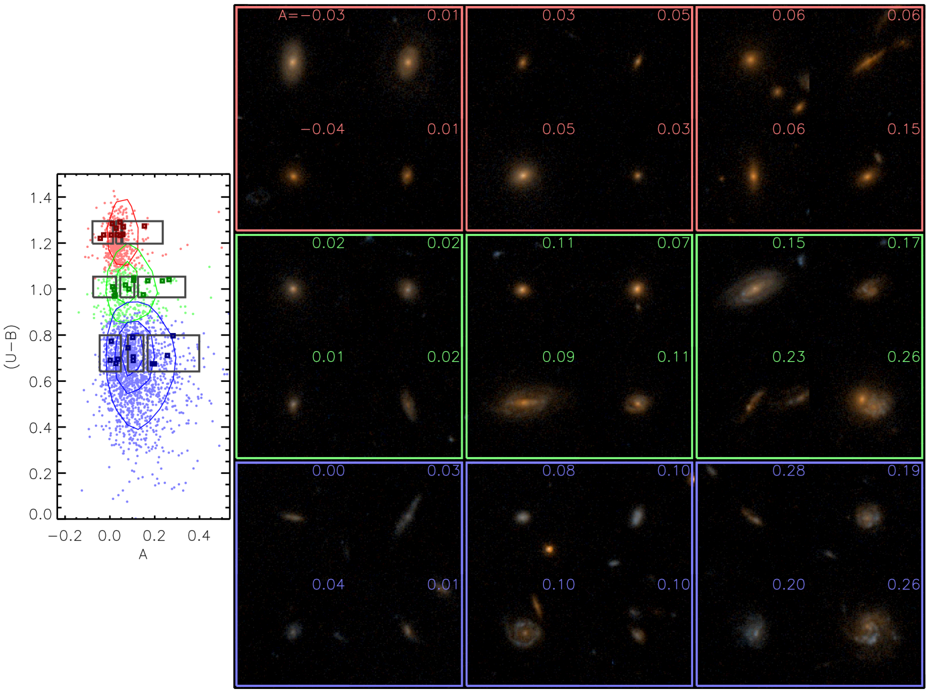

Figure 2.5: **Asymmetry parameter visualization** — A random selection of *HST* postage stamps for galaxies spanning the measured asymmetry parameter (See Figure 2.4 for details).

2.5.1 *CAS* Parameters

We define concentration (C), asymmetry (A), and smoothness (S) following Conselice (2003). The concentration parameter, which measures the central concentration of light in a galaxy (Bershady, Jangren, & Conselice 2000), is defined as

$$C = 5\log\left(\frac{r_{80}}{r_{20}}\right) \tag{2.2}$$

where r_{80} and r_{20} are the radii that contain 80% and 20% of the total light, respectively. Elliptical galaxies are generally the most concentrated with $C \sim 4.5$, and concentration is found to decrease with later Hubble types to $C \sim 2.5$ (Conselice 2003). In Figure 2.4, we show *HST*/ACS postage stamps ($6''$ on a side) of randomly-selected red, green and blue galaxies with relatively low, medium, and high concentration values within each color-selected sample. The left panel shows where the randomly-selected galaxies lie in color-concentration space, relative to the entire sample; the grey boxes show the regions used to select the galaxies with different concentration values. The concentration values for each galaxy shown are given in the upper right corner of each postage stamp.

Asymmetry is defined as the absolute value of the difference between the pixel intensities of a galaxy before ($I(i,j)$) and after a rotated by 180° about its center ($I_{180}(i,j)$), normalized by the integrated intensity:

$$A = \frac{\Sigma_{i,j}\|I(i,j) - I_{180}(i,j)\|}{\Sigma_{i,j}\|I(i,j)\|} - B_{180} \tag{2.3}$$

Here a correction is made to subtract off the averaged asymmetry of the background near the galaxy (B_{180}). (see Conselice, Bershady, & Jangren 2000, for details). Asymmetry can be caused by spiral arms, dust lanes, mergers, or interactions, and is lowest with smooth elliptical light profiles and rises in star-forming and irregular galaxies, as well as on-going mergers (Abraham et al. 1994). Major mergers typically have $A \geq 0.35$, while spirals have $A \sim 0.25$ and elliptical galaxies have $A \sim 0.02$ (Conselice 2003). Similar to Figure 2.4, in Figure 2.5 we show postage stamps for randomly-selected galaxies with different asymmetry values within the red, green, and blue galaxy populations.

Smoothness is defined as the absolute value of the difference between the galaxy intensity pixel values ($I(i,j)$) and boxcar-smoothed intensity pixel values ($I_S(i,j)$) within $1.5 \times r_p$ of the center of the galaxy:

$$S = \frac{\Sigma_{i,j}\|I(i,j) - I_S(i,j)\|}{\Sigma_{i,j}\|I(i,j)\|} - B_S. \tag{2.4}$$

Here again the average smoothness of the background (B_S) is removed. Low S values correspond to smoother light profiles, while high S values correspond to less smooth light profiles. The smoothness parameter is sensitive to higher frequency clumps that are differentiated from the smoother parts of the galaxy. Smoothness correlates with patchiness, which can be due to recent star formation or compact star clusters (Takamiya 1999). An important issue with smoothness is its dependence on the apparent size of a galaxy and the smoothing length ($0.25 \times r_p$), which can cause smaller galaxies to have smoothness values below the average smoothness of the background. This systematic issue with the smoothness parameter can limit its usefulness as a comparison parameter.

2.5.2 B/T: Bulge-to-Total Decomposition

Using two-dimensional bulge plus disk surface brightness profile models, we measure the bulge-to-total light fractions (B/T) using GIM2D (Simard et al. 2002). The B/T parameter provides a rough measure of how disk-dominated or bulge-dominated a galaxy is. The B/T parameter is estimated using a Sérsic profile, with the Sérsic index (n) defined in Sersic (1968), which controls the degree of curvature of the profile: a smaller n reflects a less centrally concentrated profile with a steeper slope at large radii. Often standard B/T fits at low redshift use a classical de Vaucoulers profile with a Sérsic index of $n = 4$ fit to the bulge component. Here we use $n = 2$ to fit our higher redshift, younger galaxies, as many may not yet have formed a classical $n = 4$ bulge component. While using $n = 2$ or $n = 4$ can change the exact value of B/T measured for a given galaxy, it does not change the trends or conclusions we find here. The only significant

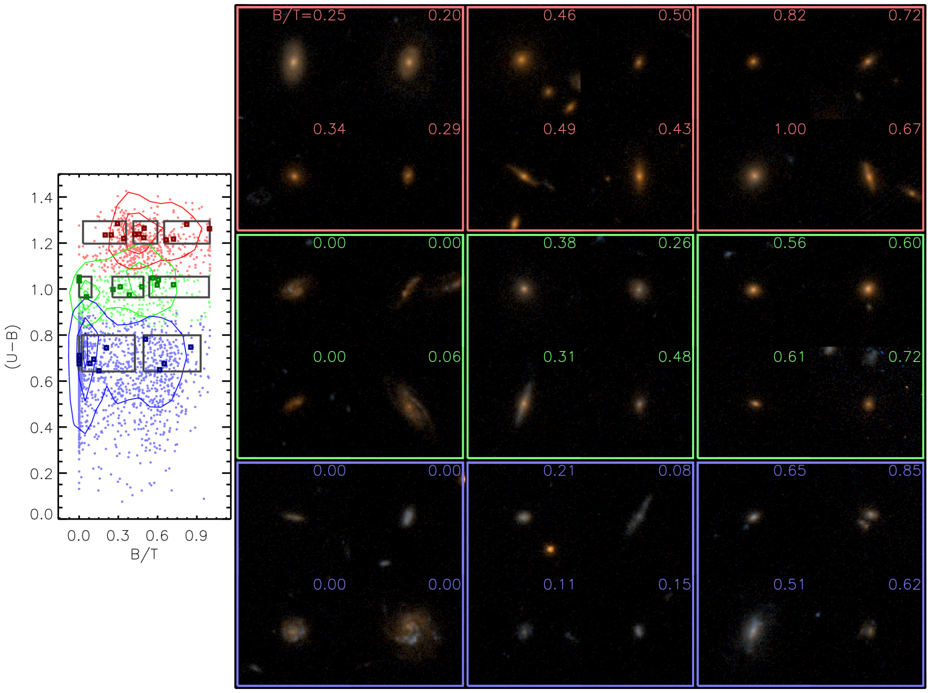

Figure 2.6: B/T **parameter visualization** — A random selection of *HST* postage stamps for galaxies spanning the measured B/T parameter (See Figure 2.4 for details).

difference is that in Table 2.3 we find a statistically different distribution between green and purple galaxies at the 5% level (see Section 2.7.5 for details). To be conservative, we adopt $n = 2$ here.

From the GIM2D V- and I-band best-fit model magnitudes of the entire galaxy (I_{galaxy}, V_{galaxy}) and bulge (I_{bulge}, V_{bulge}), the bulge-to-total fraction is defined as:

$$B/T = \begin{cases} 10.0^{(V_{galaxy} - V_{bulge})/2.5} & \text{for} \quad z < 0.6 \\ 10.0^{(I_{galaxy} - I_{bulge})/2.5} & \text{for} \quad z \geq 0.6 \end{cases}$$

Figure 2.6 shows postage stamps for red, green, and blue galaxies with a range of B/T parameters, similar to Figures 2.4-2.5.

2.5.3 G: Gini Coefficient / M_{20}: Second-Order Moment of the 20% of light.

In addition to the CAS and B/T morphological parameters, we also measure G/M_{20} (Lotz, Primack, & Madau 2004). The Gini coefficient (G) quantifies the distribution of light among the pixels in a galaxy and is defined as the absolute value of the difference between the integrated cumulative distribution of galaxy intensities and a uniform intensity distribution (Abraham, van den Bergh, & Nair 2003):

$$G = \frac{\Sigma_i^n (2i - n - 1)|X_i|}{|\bar{X}|n(n-1)} \tag{2.5}$$

where n is the number of pixels, X_i are the increasing ordered pixel flux values, and $\bar{X}$ is the mean pixel flux over the galaxy. G is close to unity if a single pixel contains all of the intensity and close to zero if the pixel values are uniform across the entire galaxy. G correlates with concentration and surface brightness, but it is not sensitive to the *location* of the brightest pixels. Therefore G is high for galaxies with multiple bright nuclei as well as centrally concentrated spheroids.

M_{20} is the second order moment of the brightest 20% of the galaxy light distribution, defined as the sum of the intensity of each pixel multiplied by the square of the distance from the center of the galaxy for the brightest 20% of the pixels in a galaxy. As such we can define M_{20} as:

$$M_{tot} = \Sigma_i^n f_i[(x_i - x_c)^2 + (y_i - y_c)^2] \tag{2.6}$$

$$M_{20} = \log\left(\frac{\Sigma_i M_i}{M_{tot}}\right), \quad \text{with} \quad \Sigma_i f_i < 0.20\ f_{tot} \tag{2.7}$$

where f_i are pixel fluxes and (x_c, y_c) is the location of the galaxy center that minimizes the total second order galaxy moment, M_{tot}. M_{20} therefore traces the spatial extent of the brightest pixels and is anti-correlated with concentration.M_{20} is typically ~ -1.5 for late-type galaxies and ~ -2 for early-type galaxies (Lotz, Primack, & Madau 2004).

2.6 Green Galaxy Morphologies

We first study various individual and joint distributions of both the general properties of green galaxies and their morphological properties, and compare them to the distributions of red and blue galaxies. The goal of this section is to understand the properties of galaxies in the green valley and how they differ from both red and blue galaxies.

2.6.1 Galaxy Properties

Figure 2.7 shows the general properties of red, green, and blue galaxies in the joint spaces of absolute B-band magnitude M_B, rest-frame (U-B) color, stellar mass, and Petrosian radius (r_p), which we use to estimate the size of the galaxy. Along the diagonal in this figure are individual parameter histograms for each color-selected sample, while off-diagonal panels show bivariate joint distributions.

The green galaxy sample has both an absolute magnitude M_B and stellar mass distribution that is intermediate between the red and blue galaxy samples. This is not surprising given the dependence of stellar mass on both color and magnitude. The median stellar mass of the red, green, and blue galaxy samples are fairly different, at 10.7, 10.3, and 9.6 log $M_*/M_\odot$, respectively. In addition, there is a well-known strong correlation between size, magnitude, and stellar mass, in that brighter and/or more massive galaxies have larger sizes (Blanton & Moustakas 2009). However there is not a strong correlation between (U-B) color and Petrosian radius, except within the blue population. The green galaxy population on the whole has similar size and magnitude distributions to red galaxies. We note that the green galaxy sample has a tail to larger Petrosian radii than either the blue or red galaxy samples. Interestingly, Salim & Rich (2010) find using *HST*/ACS imaging that UV-excess, early-type galaxies that fall mainly in the green valley at low redshift are, on average, larger than either red or blue galaxies. We discuss the statistical significance of this result in Section 2.7.5. In Section 2.7.1, we will address possible stellar mass-dependent morphological differences between these samples by comparing samples with similar stellar mass distributions.

2.6.2 CAS and B/T Parameter Results

We next study the morphological distributions of green galaxies in CAS and B/T space and compare them with samples of red and blue galaxies. Figure 2.8 shows the distribution of red, green, and blue galaxies in terms of CAS, B/T, stellar mass, and (U-B) color with error bars, contours, and histograms similar to Figure 2.7. Error bars on morphological parameters are estimated from Lotz et al. (2006). We begin by investigating the individual parameter space distributions along the diagonal in Figure 2.8.

In terms of the concentration parameter, blue galaxies have $C \sim 2 - 3.5$, while red

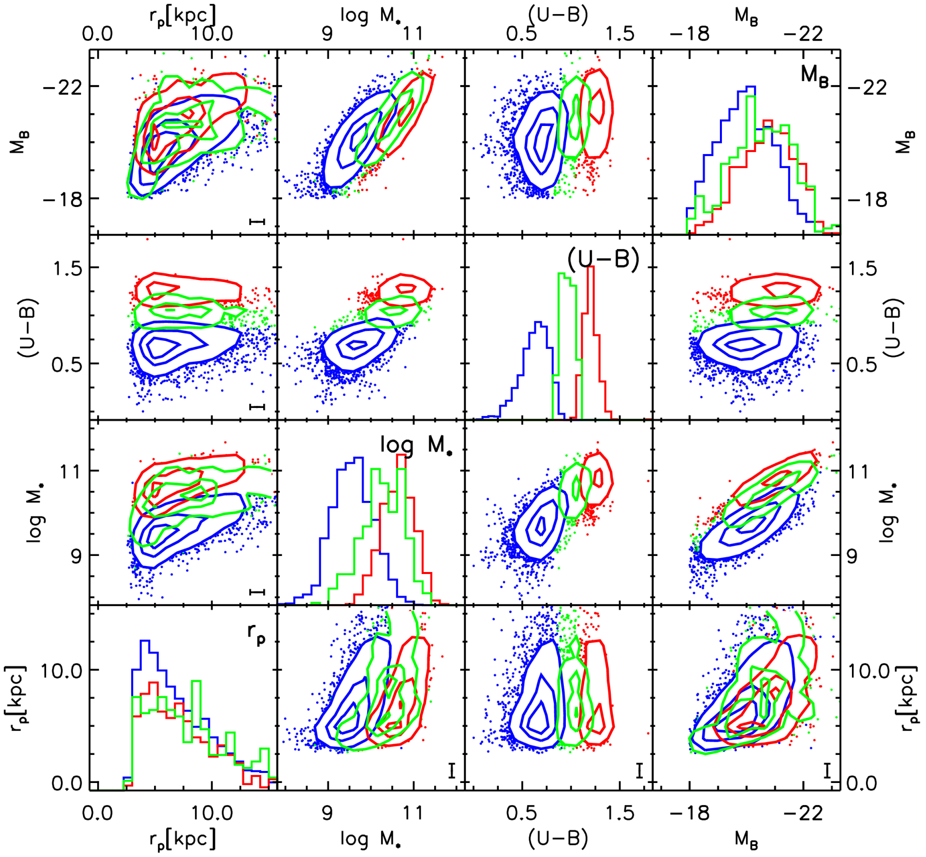

Figure 2.7: **Sample property parameter space diagram** — General properties of the AEGIS galaxy sample used here in the joint space of absolute B-band magnitude M_B, rest-frame (U-B) color, stellar mass, and Petrosian radius (r_p in units of kpc). Along the diagonal are individual parameter histograms for each color-selected sample, where we have weighted the red and blue galaxy histograms by a half and a quarter, respectively, to facilitate comparison with the green galaxies. Off diagonal panels show bivariate joint distributions, with contours containing 30%, 50%, and 80% of the sample; galaxies outside the 80% contour are shown as individual points. Contours have been smoothed using a Gaussian $1/20^{\rm th}$ of the size of the panel. The innermost 30% contour is not plotted if it is smaller than the grid used to calculate the contours. 1σ error bars at the median S/N pixel^{-1} of the sample, estimated from Lotz et al. (2006), are shown in the lower right corner of each space where available.

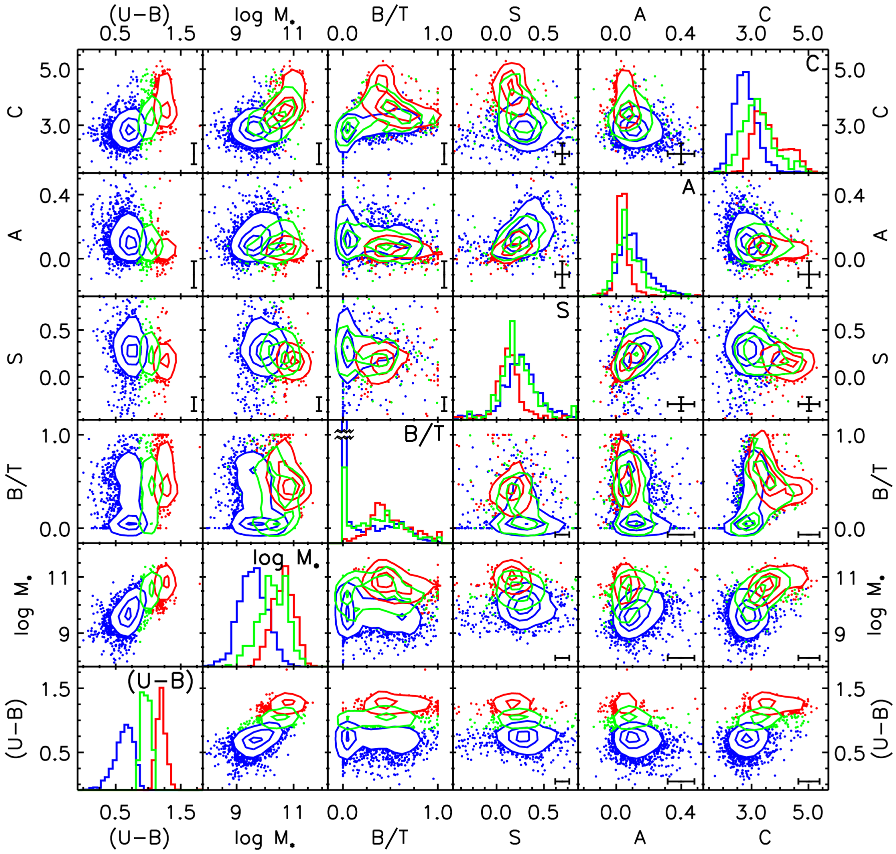

Figure 2.8: **Sample morphological properties** — Morphological properties of red, green, and blue galaxies at $0.4 < z < 1.2$ in AEGIS. Shown are joint distributions of galaxy rest-frame (U-B) color, stellar mass, concentration (C), asymmetry (A), smoothness (S), and bulge-to-total light fraction (B/T). Along the diagonal are distributions for each individual parameter, where the red, and blue distributions have been scaled down by a factor of two, and four, respectively. Due to the large fraction of bulge-less ($B/T = 0$) blue galaxies, we limit the range of B/T to be 50% of the full range. The bivariate parameter distributions have contours plotted at 30%, 50%, and 80% of the total sample. The innermost 30% contour is not plotted if it is smaller than the grid used to calculate the contours. 1σ error bars at the median S/N pixel^{-1} of the sample, estimated from Lotz et al. (2006), are shown in the lower right corner of each space where available.

galaxies have $C \sim 3 - 5$. Green galaxies have an intermediate distribution, with $C \sim 2.5 - 4$. Unlike red galaxies, the green galaxy population does *not* contain a large fraction of galaxies with particularly high concentration values; 10% of green galaxies have $C > 4$ compared to 26% of red galaxies.

The fraction of galaxies with high asymmetry is dependent on color. Blue galaxies have larger asymmetry values than red galaxies on the whole. Using the threshold of $A > 0.35$ that is typically used to define mergers, for example, we find that 3% of blue galaxies and 0.4% of red galaxies have $A > 0.35$. Using a threshold of $A > 0.2$, which clearly separates the tail of the distribution, we find that 17% of blue galaxies and 1.2% of red galaxies have $A > 0.2$. The green galaxy population has a similar asymmetry distribution as the blue galaxy population, though fewer green galaxies have large A values (1.2% have $A > 0.35$ and 8% have $A > 0.2$). Using either high A threshold, we find a lower percentage of highly asymmetric green galaxies compared to blue galaxies. This implies that while green galaxies have similar amounts of asymmetry as blue galaxies due to star formation knots, dust lanes, and/or spiral arms, they do not have as high a fraction of major mergers as the blue galaxy population (see Section 2.6.3 for a discussion of the merger fraction in each population using G-M_{20}).

To determine robustly the smoothness parameter of a galaxy one requires a larger threshold in spatial extent than for measuring concentration or asymmetry. The threshold required for smoothness is $r_p \geq 0.6''$, compared to $r_p \geq 0.3''$ required for concentration and asymmetry. Therefore smoothness can be measured for only roughly half of the galaxies in our sample. We find that red galaxies have lower S values than blue galaxies, on the whole, which reflects the fact that red galaxies generally have smoother light profiles. The green galaxy population has a somewhat similar S distribution as the blue galaxy population, though with more galaxies having lower S values. The median S values of red, green, and blue samples are 0.12, 0.19, and 0.24, respectively.

Continuing down the diagonal of Figure 2.8 to the B/T parameter, we find that while blue galaxies have a range of B/T values from 0 to ~ 0.8, a large fraction (30%) have $B/T = 0$, implying a disk-only galaxy with no bulge component. In Figure 2.8, the smallest B/T bin contains that 44% of blue galaxies with $0 \leq B/T < 0.05$. By-eye inspection of the *HST*/ACS images of these bulge-less galaxies confirms that these are disk-only systems. Due to this enhancement at $B/T = 0$ for the blue population, we limit the y-axis on the histogram plot of B/T to 50% of the peak number of blue galaxies at $B/T = 0$ to clearly show the full distribution of each color sample. Red galaxies have larger B/T fractions than blue galaxies, on the whole, with a distribution centered at $B/T \sim 0.4$, and very few bulge-less galaxies (0.9%, 1.5% with $0 \leq B/T < 0.05$). Green galaxies have a B/T distribution that is similar to blue galaxies, though with a smaller fraction (12%, 21% with $0 \leq B/T < 0.05$) of bulge-less galaxies. Figure 2.6 includes *HST*/ACS postage stamps of four randomly-selected bulge-less green galaxies in the central left sub-panel.

These bulge-less green galaxies are particularly interesting as the creation mechanism for these galaxies is unclear. We have visually inspected the *HST*/ACS images of these sources to check that they indeed have no apparent bulge component and are disk-only systems. We further investigate whether this population is dominated by dusty star-forming galaxies. In the (NUV-R) versus SSFR space shown in Figure 2.13, these bulge-less green galaxies (outlined by black diamonds) span the entire green galaxy population. We find that there is not a statistically significant difference in the dusty fraction of green galaxies with $B/T = 0$ ($27 \pm 5\%$) compared to the entire green galaxy population ($21 \pm 3\%$). Therefore the bulk of this population should be transition objects from the blue cloud to the red sequence. As these galaxies do not have a bulge, it is unlikely that they have central AGNs which could lead to strong feedback. It is also unlikely that they have had many major mergers, which presumably would have led to the creation of a bulge component. The existence of these bulge-less green galaxies therefore places strong constraints on the quenching mechanism(s) at work in this population.

In addition to the individual parameter distributions shown in Figure 2.8, we can study the bivariate distributions between various morphological parameters. In C-A, A-S, and C-S space, in general green galaxies are an intermediate population between red and blue galaxies. The greatest differences between green galaxies compared to red and blue galaxies are seen in concentration and to a lesser extent in asymmetry. In Section 2.7.5 we discuss the statistical significance of these differences since they may provide insight into the underlying physical mechanism(s) that shut off star formation in galaxies.

There are interesting differences between the galaxy populations in the B/T-C parameter space. Within the blue galaxy population there is very little correlation between B/T and C, except that the bulge-less ($B/T = 0$) galaxies have the lowest concentration. However, within the red galaxy population there is an odd correlation in that the galaxies with the highest B/T values have the lowest concentration values. This is likely not real but is due to these red galaxies with low C and high B/T values being very compact, such that C is not well-measured. Comparing C with r_p for each color sample (see Figure 2.9) we find that within the blue and green populations there is no correlation, but within the red population the galaxies with $r_p < 6$ kpc have small measured concentrations, with $C < 4$. These galaxies also have the highest B/T values, with $B/T > 0.7$. Keeping only galaxies with $r_p > 6$ kpc, we find that very few sources have $B/T > 0.6$ and within the red population there is no longer a correlation between B/T and C.

Green galaxies in the B/T-C space have a distribution that is more similar to blue galaxies than red galaxies, though there is a tail with high concentration, as seen in the red galaxy sample. For a given B/T value, green galaxies have higher concentrations than blue galaxies. This trend holds in the sample of galaxies with $r_p > 6$ kpc. We discuss the implications of this in Section 2.8.

Finally, in the M_*-C parameter space, we find that the red and blue galaxy populations lie in distinct regions of this space. The green galaxy population appears to span the red and blue distributions, possibly as a transition population moving from low stellar mass and low

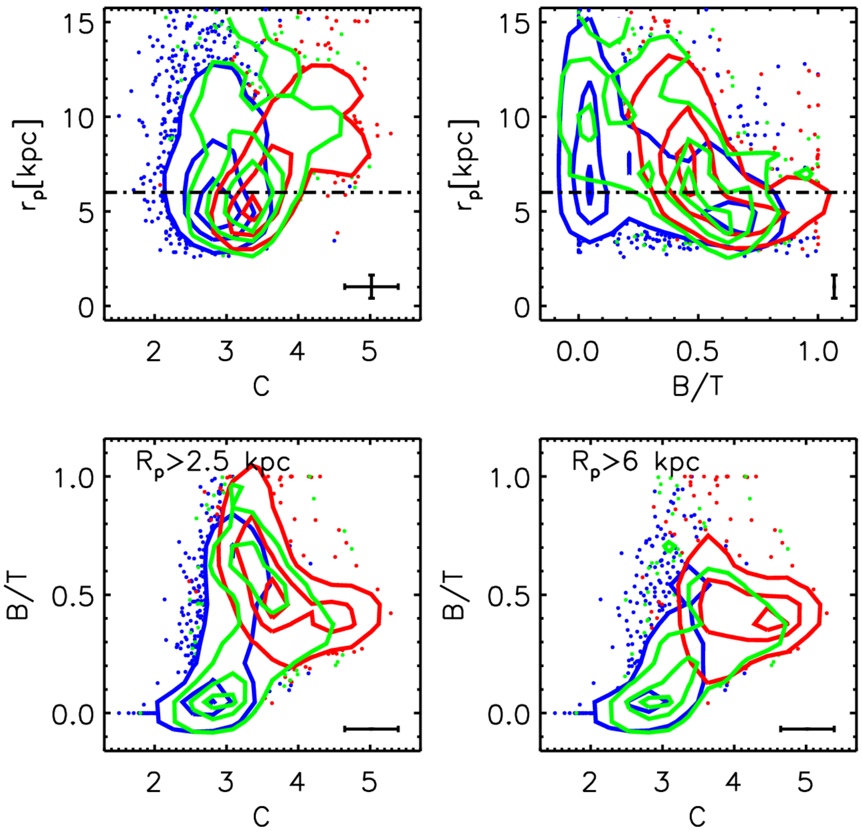

Figure 2.9: **Measured concentration versus Petrosian radius** — An investigation of how the measured C and B/T parameters depend on galaxy size. The upper panels show the measured Petrosian radius (r_p) as a function of C and B/T for our red, green, and blue galaxy samples. The dashed line at $r_p = 6$ kpc shows the threshold used in the lower right panel. Contours and error bars are similar to Figure 2.8. The lower left panel shows B/T versus C for all galaxies with $r_p > 2.5$ kpc. Both green and red galaxies show an odd trend of low C and high B/T. In the lower right panel only galaxies with r_p> 6 kpc are included and this trend disappears.

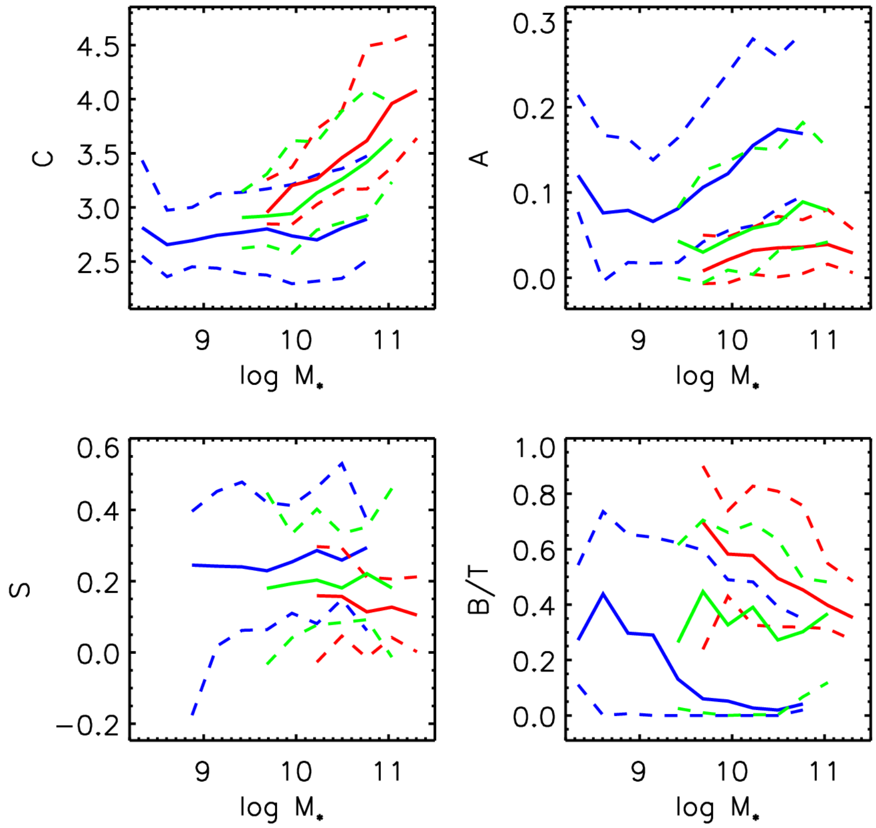

Figure 2.10: **Morphology conditional distribution diagrams** — Conditional distribution plots which show the median and 68% range for the red, green and blue galaxies. The four subplot show concentration, asymmetry, smoothness, and bulge to total fraction values at a given mass. For a fixed stellar mass Green galaxies have higher concentration, and lower asymmetry values as compared to the blue galaxies.

concentration (like the blue galaxies) to higher stellar mass and higher concentration (like the red galaxies).

In Figure 2.10 we highlight these differences by showing the C, A, S, and B/T morphological distributions (mean and 68% range) of each of the red, green, and blue galaxy samples as a function of stellar mass. This figure shows that at a given stellar mass green galaxies have larger C values, lower A values, and lower S values than blue galaxies. The B/T values may be higher than blue galaxies at a given stellar mass, but the noise in the mean and the similar width of the distributions make it difficult to draw a strong conclusion.

2.6.3 Rough Morphological types using G/M_{20}

From the work of Lotz, Primack, & Madau (2004) and Lotz et al. (2008b), galaxies can be classified into rough morphological types: early, late or merger, depending on their location in G-M_{20} space (see Figure 2.11 for the cuts shown in the space). Following Lotz et al. (2008b), we define

$$
\begin{aligned}
\text{Mergers} &: G > -0.14M_{20} + 0.33, \\
\text{Early(E/S0/Sa)} &: G \leq -0.14M_{20} + 0.33, \text{ and} \\
&\quad\; G > 0.14M_{20} + 0.80, \\
\text{Late(Sb} - \text{Ir)} &: G \leq -0.14M_{20} + 0.33, \text{ and} \\
&\quad\; G \leq 0.14M_{20} + 0.80,
\end{aligned}
$$

in the G/M_{20} plane, which are based on visually determined morphologies in the EGS (Lotz et al. 2008b). Note that mergers in this plane include both major and minor mergers, whereas high asymmetry ($A > 0.35$) is only sensitive to major mergers (Lotz, Primack, & Madau 2004).

Table 2.2 contains the fraction of galaxies in the red, green, and blue galaxy populations used here that is classified as early type(E/S0/Sa), late type(Sb-dI), or merger. We derive errors on these fractions by performing Monte Carlo tests using the median errors estimated for G and M_{20} from the median S/N pixel^{-1} (Lotz et al. 2006). We also include in quadrature Poisson errors. Note that these fractions should not be interpreted as the fraction for all galaxies at these redshifts, as our samples are not strictly volume-limited and they cover a wide redshift range. We refer the reader to Table 3 in Lotz et al. (2008b) for the redshift-evolving morphological fraction of volume-limited color-defined galaxy samples at these redshifts. Here we use the derived fractions to compare relative trends between the different color-selected galaxy samples.

From Table 2.2 we find that the green galaxy population is intermediate between the red and blue galaxy populations in terms of each of the three morphological types. Compared to the green galaxy population, the blue population has a statistically higher merger fraction (2σ), more late type galaxies (4σ), and fewer early type galaxies (7σ), while the red population has a lower merger fraction (1σ), fewer late type galaxies (5σ), and more early type galaxies (5σ). Comparing our results with the fractions found by (Lotz et al. 2008b), we find the same general trends, though we have somewhat higher merger fractions for all three galaxy samples.

2.6.4 Rotated Gini and M_{20} Parameters

We also analyze our samples in the G'/M'_{20} parameter spaces, which are plane rotated versions of G/M_{20}. These versions are created by rotating G/M_{20} such that the locus of galaxies, spanning from late to early types, now lie along the M'_{20} axis. The locus is roughly parallel

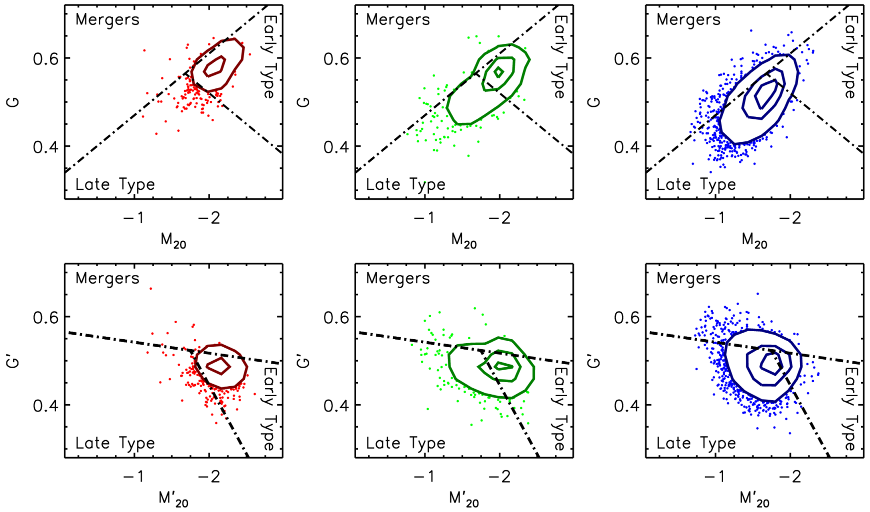

Figure 2.11: **Gini and M_{20} diagram of galaxy samples** — Using the cuts defined in Lotz, Primack, & Madau (2004), we divide the G/M_{20} space (top row) into areas with galaxies that are early-type (E/S0/Sa), late-type (Sb/Sc/Ir), or mergers and plot the locations of red, green, and blue galaxies. Contours and error bars are similar to Figure 2.8. The bottom row shows the same galaxy samples in a rotation version of this space in which the locus of galaxies lies along the G' axis (see text in Section 2.6.4 for details). Using this rotated definition, the M'_{20} axis relates more directly to the negative of the Sérsic index and G' correlates with merger identification. Due to the tight grouping of the red galaxy population in these spaces, the innermost 30% contour is not shown.

to the merger definition line and is perpendicular to the late and early type definition line. In Figure 2.11, we plot red, green, and blue galaxies in G/M_{20} bivariate space in the top row, along with the corresponding rotated G'/M'_{20} space in the bottom row. 30%, 50% and 80% contours are plotted, along with the morphological classification lines, for both the standard and rotated spaces. This rotation will not effect the rough morphological types found in Table 2.2, but it breaks the degeneracy between the G and M_{20} parameters, such that the G' parameter reflects merger activity, while M'_{20} correlates with Sérsic index. The rotated variables are defined as

$$\begin{bmatrix} M'_{20} \\ G' \end{bmatrix} = \begin{bmatrix} \cos(\theta) & -\sin(\theta) \\ \sin(\theta) & \cos(\theta) \end{bmatrix} \times \begin{bmatrix} M_{20} \\ G \end{bmatrix}$$

with $\theta = 0.164$ radians fit from the locus of galaxies in the G/M_{20} plane.

Similar to Figure 2.8, in Figure 2.12 we consider the rotated G'/M'_{20} space and joint distributions with both stellar mass and (U-B) color. Contours, histograms, and error bars are similar to Figure 2.8.

In the one-dimensional G' space (upper right panel of Figure 2.12), the blue population contains a wider distribution that extends to both larger and smaller values of G' compared to the red galaxy population. As higher G' values correlate with merger activity (reflecting both

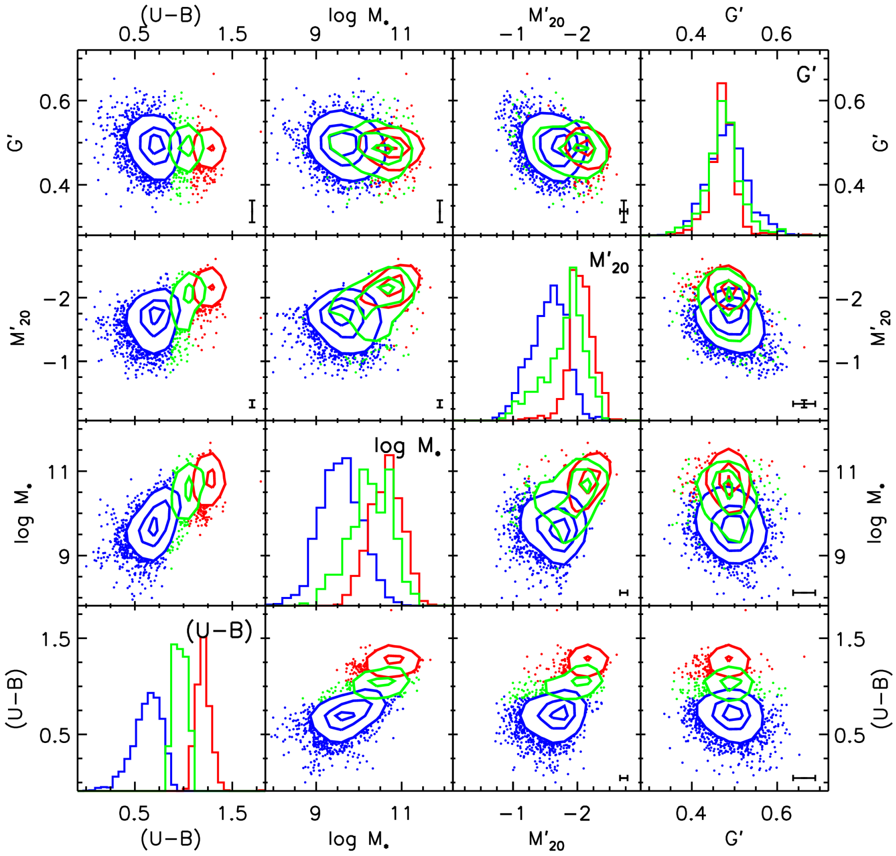

Figure 2.12: **Rotated Gini/M_{20} diagram for galaxy samples** — Measured G'/M'_{20}, stellar mass, and (U-B) color joint parameter spaces. Contours, histograms, and error bars are similar to Figure 2.8.

major and minor mergers), this implies a larger merger fraction for blue galaxies compared to red galaxies. Small values of G' can result from very dusty galaxies. The green galaxy population has an intermediate distribution in G' between the blue and red galaxy distributions. In particular, the green galaxy population has a lower fraction of objects with high G' values compared to blue galaxies and a higher fraction than red galaxies. This implies a merger fraction that is lower than what is found for the blue galaxy population but higher than the red galaxy population.

Similar to the concentration parameter distribution, the green galaxy population is intermediate between the red and blue galaxies in the M'_{20} parameter space, where red galaxies have a higher mean value of M'_{20} than blue galaxies. There is a sharp distinction between the red and blue galaxy populations in M'_{20} which is more pronounced in M'_{20} compared to G'. While the green galaxy distribution spans the majority of both the red and blue populations, it does not include the highest values of M'_{20} seen in the red galaxy distribution or the lowest values seen in the blue galaxy distribution.

In the joint M'_{20}-G' space, differences between the red, green, and blue populations are more distinct in M'_{20} than G'. While there is very little correlation seen between stellar mass and G', there is a strong correlation between stellar mass and M'_{20}. As with stellar mass and concentration, here again the red and blue galaxy populations lie in distinct areas of M_*-M'_{20} space. The green galaxy population appears to be intermediate, although their distribution is more similar to red galaxies than blue galaxies. For a given stellar mass, green galaxies have lower M'_{20} values than red galaxies, and the green galaxy population on the whole has many fewer galaxies with low M'_{20}, as seen for the blue galaxy population.

2.6.5 Environmental Dependence of the Color-Morphology Relation

We further investigate the joint environment-stellar mass-morphology distribution of red, green, and blue galaxies by comparing the morphological distributions as a function of stellar mass of each galaxy color sample in different environments. Using the projected third-nearest-neighbor density catalogs of Cooper et al. (2006), we estimate the local environment or over density of each red, green, and blue galaxy in our sample. We find no significant difference in the morphology-stellar mass distribution of galaxies of a given color when split into roughly equal-sized populations in over- or under-dense regions. To compare the morphology-stellar mass distributions of galaxies in the most extreme environments within our sample, we select galaxies such that they have $|\log_{10}(1+\delta_3)| > 0.25$, and do not find any significant differences in the C, A or B/T parameters. We additionally use the DEEP2 group catalogs of Gerke et al. (2007) to identify galaxies likely to be in groups, with velocity dispersions $\sigma_v \geq 150$ km s^{-1} or in the field. We compare the morphology-stellar mass distributions of red, green, and blue galaxies in groups versus the field and find no significant differences, though we note that the errors are somewhat large due to small numbers of galaxies in each color-stellar mass-morphology-environment bin.

2.7 Green versus Purple Galaxy Comparison

The second goal of this paper, beyond measuring the morphological distributions of green valley galaxies, is to quantitatively determine whether the green galaxy population can be explained from a morphological point of view as a simple mix of blue and red galaxies, or whether green galaxies have a distinct morphological make-up that defines them as a separate, distinct population. To undertake this second goal, we wish to compare the morphological distribution of green galaxies with the distribution of red and blue galaxies taken as a whole. However, we can not simply take the union of the red and blue galaxy samples used here to compare with the green galaxy sample, as the morphologies of the red and blue galaxy populations differ significantly. As a result, the morphological distribution of their union will depend on the ratio of red to blue galaxies in the combined sample. We therefore create "purple" galaxy comparison samples that have the same ratio of red to blue galaxies as within the green population itself. We also create comparison samples that have had dusty galaxies removed and have matched stellar mass distributions, to limit possible biases in our statistical tests.

We found in Section 2.6.1, when comparing red, green, and blue galaxies in various morphological parameter spaces that the green galaxy population appears to be intermediate between the red and blue galaxy populations. Using the purple comparison samples, we can test statistically if green galaxies are in a transition phase, moving from the blue cloud to the red sequence; however, these results could also potentially be consistent with green galaxies being a simple mix of the red and blue galaxy populations.

2.7.1 *Full* "Purple" Galaxy Comparison Sample

We first define a "purple" galaxy sample, which combines the red and blue galaxy populations to compare against the green galaxy population. Starting with the red and blue galaxy samples defined above, we weight the galaxies such that the combined sample has the same ratio of red to blue galaxies as galaxies in the green sample above and below the minimum in the color bimodality (the dashed line in Figure 2.2 defining the center of the green valley). In this way, the ratio of galaxies above and below the minimum in the color bimodality is the same for the green galaxy sample and the comparison "purple" galaxy sample. We refer to this sample as the 'full purple galaxy sample' (labeled Fullin the figures below). The Fullpurple galaxy sample contains a total of 2,037 galaxies, weighted to an effective sample size of 487 galaxies, with a ratio of red to blue galaxies of 0.82.

2.7.2 Removing Dust Obscured Galaxies

While the optical color of galaxies reflects their star formation history and the age of their stellar populations, it can be influenced by the presence of dust. In particular, galaxies in the green and red populations may have older stellar populations than blue galaxies, or they may appear to be redder due to dust obscuration. As the goal of this paper is to study the morphologies of green galaxies as a potential transition population of galaxies that are moving from the blue cloud to the red sequence, we would like to identify and remove interlopers from the green and red populations that are dusty star forming galaxies.

Salim et al. (2009) show that a comparison between the SSFR versus rest-frame (NUV-R) color of $z \sim 1$ galaxies (their Fig. 6) indicates that while the bulk of green galaxies (defined in Salim et al. (2009) using (NUV-R) color) are transition objects with SSFRs intermediate between blue and red galaxies, a fraction of green galaxies are likely green due to dust in the host galaxy. These dusty green galaxies may therefore not be transition objects moving from the blue cloud to the red sequence. Following (Salim et al. 2009), we identify and remove these dusty 'interlopers' in our green and red galaxy samples. We use SSFR as derived in (Salim et al. 2009), who use stellar population synthesis models to fit nine bands of photometry for AEGIS galaxies (FUV, NUV, $ugriz$, K_s). Figure 2.13 shows SSFR versus (NUV-R) color for our optical color-selected galaxy samples. There is a relatively tight, well-defined locus in this space, as indicated by the dot-dashed line. Galaxies that lie $\geq 3\sigma$ higher than this locus (in the upper right corner of Figure 2.13, above the dashed line) are likely to have optical colors affected by dust obscuration. We remove these galaxies from the green and red samples used here to create a "$Full_{\,\mathrm{NUV}}$ green sample" and a corresponding "$Full_{\,\mathrm{NUV}}$ purple sample" that has the same ratio of red to blue galaxies (0.83) as the "$Full_{\,\mathrm{NUV}}$ green galaxy" sample. All sample definitions denoted with subscript "NUV" have dusty obscured galaxies removed from the green and red populations. This procedure removes a total of 123(36%) green galaxies and 92(16%) red galaxies. The $Full_{\,\mathrm{NUV}}$ purple sample contains a total of 2003 galaxies, weighted to an effective sample size of 438 galaxies. The $Full_{\,\mathrm{NUV}}$ green sample contains 219 galaxies.

2.7.3 Matched Stellar Mass Galaxy Samples

Figure 2.14 shows the stellar mass distributions of the red, green, and blue galaxy samples (first panel), the *Full* green and purple samples (second panel), and the $Full_{\,\mathrm{NUV}}$ green and purple samples (third panel). As noted in Section 2.6.1, optical color and stellar mass are highly correlated. As a result, the green galaxy samples have higher stellar mass, on average, than the corresponding purple comparison samples. To remove any dependence of morphology on stellar mass when comparing the green and purple samples, we create a purple comparison sample that has the same stellar mass distribution as the green $Full_{\,\mathrm{NUV}}$ sample (shown in the right panel of Figure 2.14). To create this sample we assign weights to red and blue galaxies in the $Full_{\,\mathrm{NUV}}$ purple sample in bins of $\log(M_*/M_\odot) = 0.1$ such that the stellar mass in each bin matches that of the stellar mass distribution of green galaxies either above (for red galaxies) or below (for blue galaxies) the minimum of the green valley. By weighting the red and blue galaxies to the

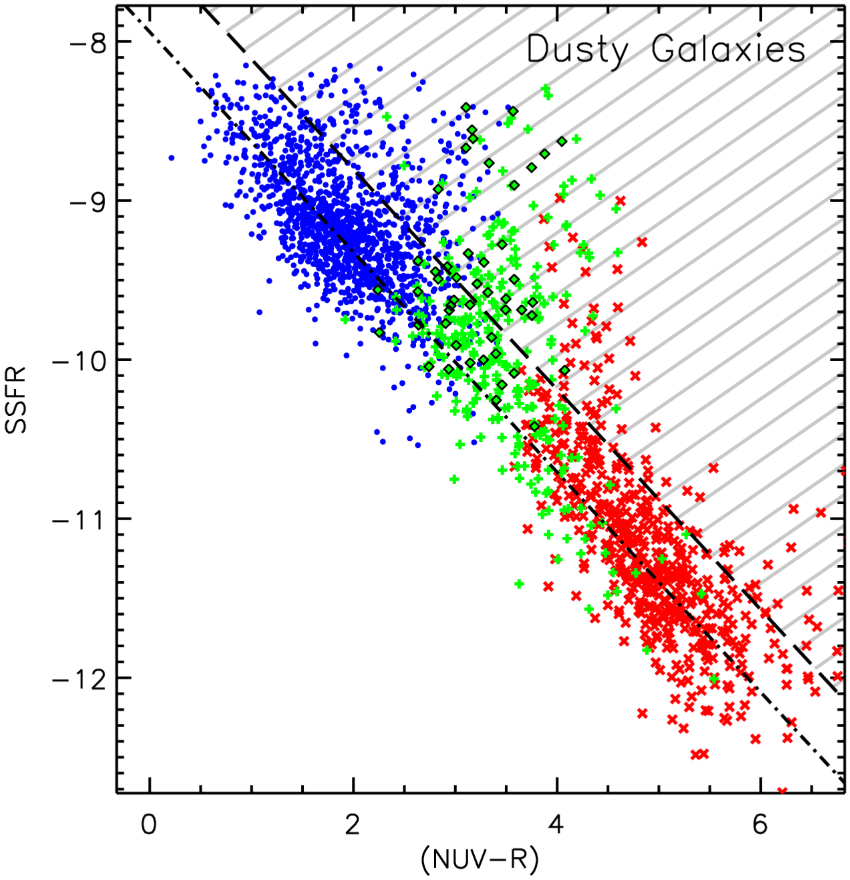

Figure 2.13: **(NUV-R) color to SSFR diagram** — (NUV-R) color plotted versus specific star formation rate (SSFR) for the red, green, and blue galaxy samples used here. Galaxies with optical colors affected by dust will be scattered into the upper right corner of this plot, away from the main locus of galaxies (dot-dashed line). We identify and remove green and red dusty galaxies that lie more than 3σ (the dashed line) above this locus in our "NUV" samples. Green galaxies with $B/T = 0$ are shown outlined by black diamonds.

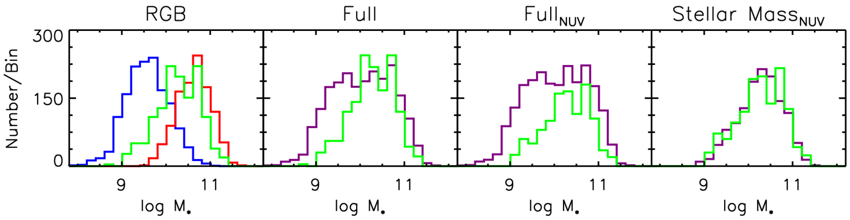

Figure 2.14: **Stellar mass distribution** — Stellar mass distributions for each galaxy sample. The left panel shows the red, green, and blue galaxy samples, while the other panels show various green and purple galaxy samples. For clarity we have weighted the histograms for red and blue galaxies by a factor of half and quarter, respectively.

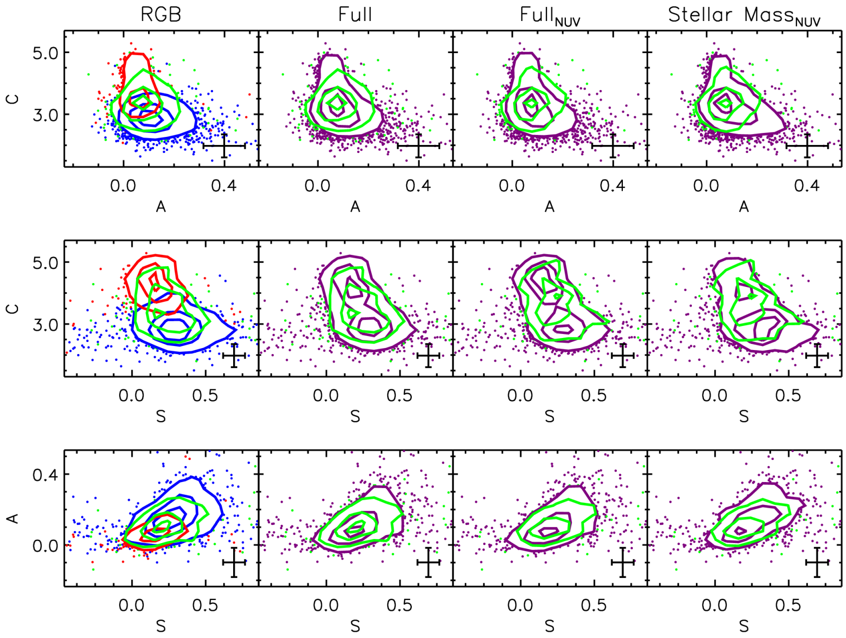

Figure 2.15: ***CAS* bivariate distribution diagrams** — *CAS* bivariate distributions shown for *RGB*, *Full*, *Full* $_{\mathrm{NUV}}$, and *Stellar Mass* $_{\mathrm{NUV}}$ samples. Contours are plotted to contain 30%, 50% and 80% of the galaxies within each sample, with outliers shown as dots outside the 80% contour. Estimates of 1 σ error bars are shown in lower right corner for the median S/N pixel^{-1} of the sample.

green galaxies above and below the color minimum, we also constrain the ratio of red to blue galaxies to be the same as that within the green population (defined as above and below the minimum color that defines the center of the green valley) to within a few precent. The resulting *Stellar Mass* $_{\mathrm{NUV}}$ sample contains a total of 1970 purple galaxies weighted to an effective sample size of 217 galaxies, with a red to blue ratio of 0.82.

2.7.4 "Purple" vs Green Galaxy Comparison

In Figures 2.15-2.17 we plot distributions in *CAS*, B/T, and G'/M'_{20} for the red, green and blue (*RGB*) samples, alongside each of the green and purple comparison samples, *Full*, *Full* $_{\mathrm{NUV}}$, and *Stellar Mass* $_{\mathrm{NUV}}$, to examine differences in the bivariate distributions of the green and purple galaxy samples. Contour levels and error bars are similar to Figure 2.8.

In Figure 2.15 we compare the joint *CAS* distributions of green and purple galaxies and find that the same trends that exist for the Fullsamples persist after we both remove dusty interlopers and match the samples in Stellar Mass distribution. In concentration and asymmetry,

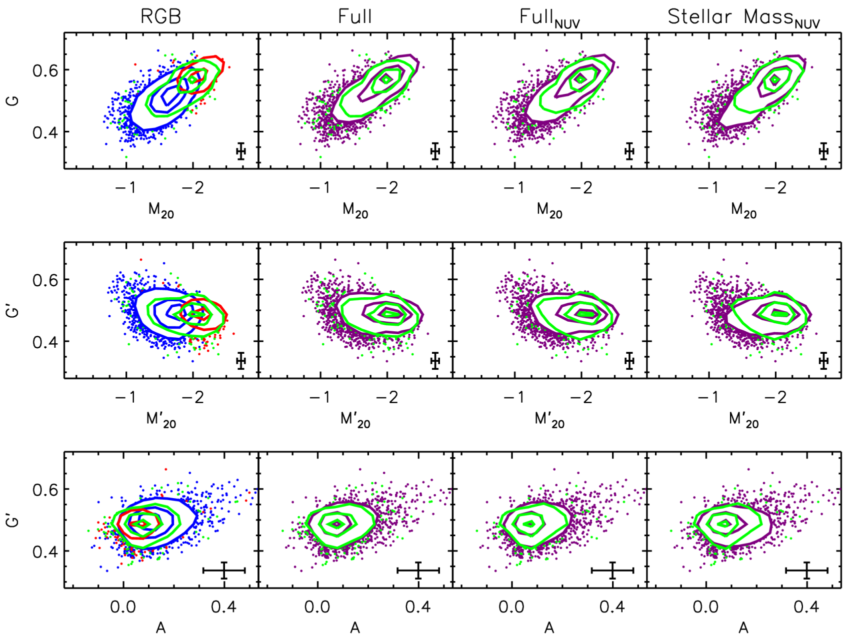

Figure 2.16: **G-M_{20}, $G' - M'_{20}$, and G'-A bivariate distribution diagrams** — G-M_{20}, $G' - M'_{20}$, and G'-A bivariate distributions shown for *RGB*, *Full*, *Full* $_{\mathrm{NUV}}$, and *Stellar Mass* $_{\mathrm{NUV}}$ samples. Contours and error bars are similar to Figure 2.15

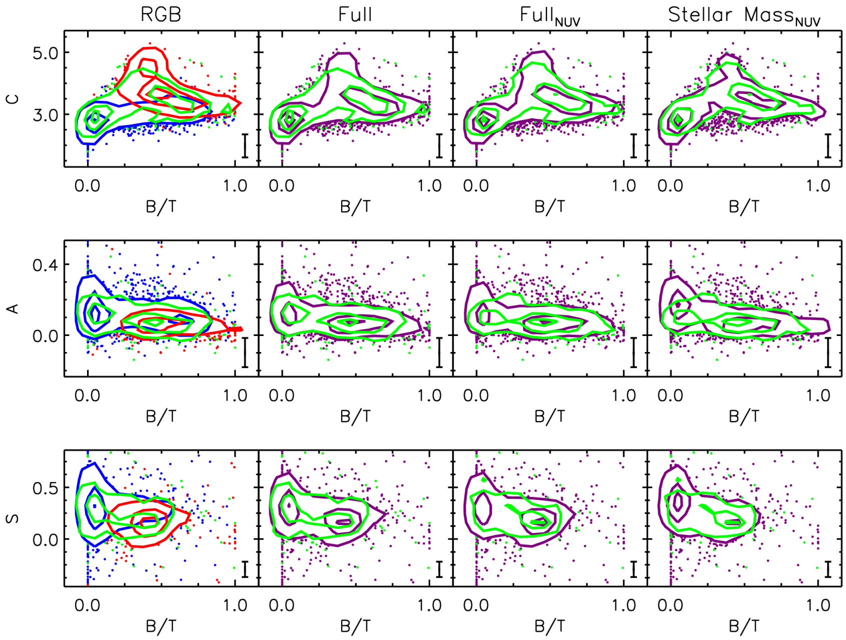

Figure 2.17: *B/T-CAS* **bivariate distribution digrams** — *B/T-CAS* bivariate distributions shown for *RGB*, *Full*, *Full* $_{\rm NUV}$, and *Stellar Mass* $_{\rm NUV}$ samples. Contours and error bars are similar to Figure 2.15

we find a missing tail of high asymmetry ($A > 0.2$) and low concentration ($C < 3.0$) galaxies in the green samples, when compared to the purple samples. Additionally, the green galaxy population is also missing a tail of higher concentration galaxies ($C > 4.5$) seen in the purple samples. These trends are reflected in the distributions of $C - S$ and $A - S$, where the green population is found to lack galaxies at the highest and lowest concentrations, as well as high asymmetry.

In Figure 2.16 we show bivariate distributions of the green and purple comparison samples in the standard G/M_{20} space as well as in the rotated $G' - M'_{20}$ space. We find that the green galaxy samples do not span the entire locus seen for the purple samples. In particular, the green galaxy samples do not contain objects with the lowest G or M_{20} values seen in the purple sample. This difference is particular clear in the $Stellar\ Mass_{\,\mathrm{NUV}}$ sample comparison. These differences are also seen in the rotated G'/M'_{20} plane. We also compare the G' and asymmetry distributions, as both parameters are sensitive to mergers. Asymmetry is a tracer of major mergers, while G' tracers both major and minor mergers (Lotz et al. 2010). We find that the green and purple samples have similar distributions in $G' - A$. The $Stellar\ Mass_{\,\mathrm{NUV}}$ samples show a tail of galaxies to high A values that is not seen in the green sample (as seen in Figure 2.15 above).

We note that in Figures 2.15-2.17 there are only minor differences between the $Full$, $Full_{\,\mathrm{NUV}}$, and $Stellar\ Mass_{\,\mathrm{NUV}}$ samples, indicating that our results are not dominated by effects due to dust obscuration or the stellar mass-dependence of the green and purple galaxy samples.

In Figure 2.17 we compare the distribution of B/T with C, A, and S for the green and purple samples. Here we find that the green galaxy population does not contain as many galaxies at high B/T as the purple population, in addition to lacking galaxies at the highest asymmetry and smoothness values.

2.7.5 Morphological Parameter Distribution Tests

For each of the measured morphological parameters, we apply the two-sided Kolmogorov-Smirnov (KS) statistic as a nonparametric null hypothesis test of the difference between the green and purple comparison samples. The null hypothesis is that both populations are drawn from the same parent sample. The KS statistic measures the maximal difference between the two normalized cumulative distribution functions and measures an associated significance level of rejecting the null hypothesis. In Figure 2.18, we plot the individual differential and cumulative distribution functions for each morphological parameter for the $Full_{\,\mathrm{NUV}}$ and $Stellar\ Mass_{\,\mathrm{NUV}}$ green and purple samples. For the KS Statistic, if the probability is below either a 1% or 5% significance level, we can reject the null-hypothesis that the two samples are drawn from a parent distribution at the 2 or 3 sigma levels, respectively.

For the KS tests, we limit the effect of noisy measurements by applying the test on galaxies

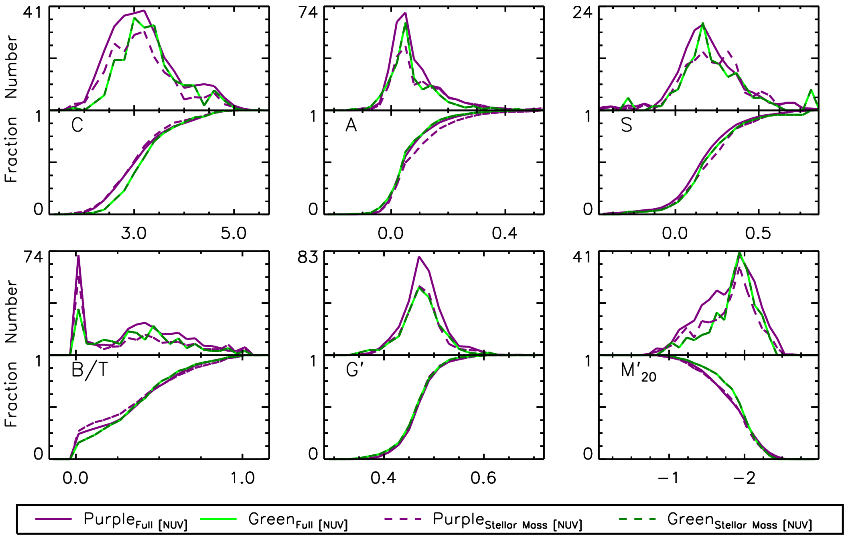

Figure 2.18: **One-dimensional morphological distribution function plot** — One-dimensional differential and cumulative distribution functions for the Full $_{\mathrm{NUV}}$ and Stellar Mass $_{\mathrm{NUV}}$ green and purple galaxy samples in C, A, S, B/T, G', and M'_{20} space. KS tests are performed for each of these comparison samples; the results are given in Table 2.3.

only within the parameter ranges shown in Figures 2.8 and 2.12 and listed in Table 2.3. We report the measured significance levels of the KS test results in Table 2.3. For each morphological parameter (as well as stellar mass and size), we compare the respective green and purple samples and highlight in Table 2.3 the parameters that we can reject at the 5% significance level in light grey and at the 1% significance level in dark grey. Thus parameters highlighted in dark gray have therefore been rejected at the 3σ level as being drawn from the same parent distribution. These include concentration for all of the *Full*, *Full* $_{\mathrm{NUV}}$, and *Stellar Mass* $_{\mathrm{NUV}}$ comparison samples, as well as size (r_p) for the *Full* sample and M_{20} and M'_{20} for the *Full* $_{\mathrm{NUV}}$ sample. At the 2σ level we can reject B/T for the Full sample and A, B/T, M_{20} and M'_{20} for the *Stellar Mass* $_{\mathrm{NUV}}$ sample.

We additionally performed KS tests to compare the morphological distributions of red and green, blue and green, and the union of red and blue to green samples, but we do not include them here as they are all rejected at the 1% level. Smoothness, asymmetry, and the Gini coefficient in the union of red and blue compared with green sample tests were not rejected by the KS test.

2.7.6 Morphological Type Comparison using Gini/M_{20}

We repeat the classification of galaxies into rough morphological types (early-type, late-type, or merger) using their location in G/M_{20} space. Table 2.4 contains the fraction of green and purple galaxies in each sample associated with each morphological type. As before, error bars include both Poisson errors as well as Monte Carlo simulations of the scatter due to measurements errors of G/M_{20}. We do not find that the morphological type fractions are statistically different (at the 2σ level) between any of the green and purple comparison samples.

2.8 Summary and Discussion

In this study we find that galaxies in the green valley at $0.4 < z < 1.2$ are an intermediate population between galaxies in the blue cloud and red sequence in terms of morphological type, concentration, asymmetry, smoothness, and merger fraction. Our results do not change if we select green valley galaxies using (NUV-R) color instead of (U-B) color. Using morphological types defined by G/M_{20}, we find that the merger fraction (14%), fraction of late-type galaxies (51%), and early-type galaxies (35%) in the green valley to be intermediate between the red and blue galaxy populations. We show that at a given stellar mass, green galaxies have higher concentration values and lower asymmetry and smoothness values than blue galaxies. They also have lower concentration values and higher asymmetry and smoothness values than red galaxies, at a given stellar mass. Additionally, 12% of our green galaxy sample is bulge-less, with $B/T = 0$. Our results show that green galaxies are generally massive ($M_* \sim 10^{10.5}\ M_\odot$) disk galaxies with high concentrations. Below we discuss the implications of these results.

2.8.1 Do green valley galaxies constitute a distinct population?

The idea that the bulk of the green valley galaxies are a transition population is clearly substantiated by our study of their morphological distribution compared to red sequence and blue cloud galaxies. While our optical color distribution is similarly fit by the two Gaussian distribution of Baldry et al. (2004), we find that galaxies in the green valley have significant morphological differences when compared to red and blue galaxies. This remains true if a UV-optical color selection is used instead.

An important issue when interpreting the observed color bimodality of the CMD is that optical colors reflect not only the star formation history of a galaxy but also its dust content. The degeneracy between star formation history and dust can be partially corrected using the SED modeling (particularly the UV color, e.g. Salim et al. 2007), the Balmer decrement (e.g. Hopkins et al. 2001; Brinchmann et al. 2004), or the IR to UV ratio (e.g. Buat et al. 2005). In contrast to claims that at higher redshifts there may not be a population of transition galaxies in the green valley (e.g. Brammer et al. 2009), we find that at $0.4 < z < 1.2$ in optically-selected samples there is a distinct population of galaxies that are green not due to dust obscuration but because they have an intermediate age stellar population (see also Salim et al. 2009). As we discuss in Section 2.7.2, while some galaxies in our green valley sample are green from large SFRs and dust obscuration, our results do not change if they are removed from the sample.

In addition to showing that green galaxies have different morphological distributions than either the red or blue galaxy populations alone, we further compare with control samples of joint red and blue galaxies with the same stellar mass. Our goal is to test whether the green galaxy population has a distinct distribution in any of our quantitative morphological measures than this joint set. This is difficult to test with the green galaxy sample being transition objects by nature and therefore having intermediate properties between the red and blue galaxy samples and is therefore a more stringent test. It is of course subject to errors and noise in the measured morphological parameters, and therefore a null result does not necessarily imply that there is not a difference; rather it may be hard to discern with these kinds of measurements. Additionally, the existence of other non-transition populations within the green galaxy population would only lessen the statistical differences detected between the green galaxy and comparison samples. However, we do find a 3σ difference in terms of the distributions of concentration values and weaker 2σ difference in the B/T, asymmetry, M_{20}, and G' distributions. Therefore it does appear that green galaxies must be a distinct population.

2.8.2 What mechanisms are quenching star formation in green valley galaxies?

Given that the green galaxy population is a transition population between the blue cloud and red sequence in which star formation was recently (within the last $\sim$ Gyr) quenched, it is the ideal population with which to study the quenching mechanism(s) at work. Merger-induced starbursts, which may quickly quench star formation, imprint high asymmetry and G' values on the galaxies. Importantly, we do *not* find that most galaxies in the green valley are experiencing on-going mergers. In fact, the fraction of green galaxies identified as mergers using G/M_{20} (and the fraction with high asymmetry, which is also often used to identify mergers) is *lower* than the fraction within the blue galaxy population. If many of the green valley galaxies have recently undergone merger events, they must be at least ∼0.4 Gyr past the merger stage to not be identified using either G/M_{20} or asymmetry (Lotz et al. 2010). Furthermore, 51% of the green galaxies in our sample are identified as late-type and either have not experienced a major merger recently or, if they did, it must have been gas rich (Cox et al. 2008). However, using both quantitative measures to identify mergers, we find that the merger fraction is lower than that of blue galaxies and higher than that of red galaxies. While Kartaltepe et al. (2010) find that most luminous infrared galaxies at $z \sim 1$ are mergers, we do not find that most optically-selected galaxies at these redshifts, even those in the green valley, are identified as mergers.

Additionally, we find that 12% of green galaxies are bulge-less, with $B/T = 0$. As a comparison, 30% of blue galaxies and no red galaxies in our sample have $B/T = 0$. The fact that 12% of the green galaxies are bulge-less raises the question of how these green galaxies were created. Most(64%) of these galaxies are not green due to dust obscuration, as they have low

SSFR indicative of intermediate age stellar populations. It is very unlikely that these galaxies have had major mergers in their recent past (which presumably would have built up a bulge component), and we have visually verified that they do not have central point sources indicative of an AGN, which could have biased the measured B/T values. Somehow star formation must have been quenched in these objects without mechanisms that would also lead to the creation of a bulge.

Higher concentration values seen in green galaxies could point to the presence of bars or other internal secular processes that slowly build a central bulge while allowing the disk structure to remain intact. In this scenario a gas-rich galaxy forms a stellar bar that funnels gas to the center of the galaxy, causing enhanced star formation and leading to the development of a bulge. This would increase the concentration measurement of these galaxies, though it does not explain the fraction of bulge-less green valley galaxies discussed above. Sheth et al. (2005) find that there is clear evidence of more centrally-concentrated molecular gas distributions in barred spirals, supporting bar-driven transport of molecular gas to the central kiloparsec of galaxies. Barred spirals of late Hubble-types are less centrally concentrated than early Hubble-types, and there is enhanced star formation activity observed in early Hubble-type bars, indicating higher mass accretion rates (Jogee, Scoville, & Kenney 2005; Kormendy & Kennicutt 2004). Secular processes may also lead to some of the clumpiness that is seen in the profiles of green galaxies.

The stellar disks of green galaxies do not appear to be truncated as they have similar, if not larger, sizes than blue galaxies, as indicated by their large Petrosian radii, which could be due to differences in their stellar mass distribution and the mass-size relationship (e.g. Shen et al. 2003) The tail of green galaxies with particularly large radii could reflect triggered star formation in the outer disks of these galaxies, possibly resulting from galaxy-galaxy interactions for a fraction of the sample. Green valley galaxies do not appear to be fading disks; the higher concentration values point to a different process. Fading disks would also produce higher B/T values, which are not clearly seen here at a given stellar mass (though can not be ruled out by our data). This likely means that simple gas exhaustion is not the dominant mechanism.

There may be a variety of quenching mechanisms responsible for the migration of galaxies from the blue cloud to the red sequence. While major mergers may play a role for some galaxies, we conclude that either a mild external process, such as galaxy harassment or tidal forces, or quite likely an internal process such as the creation of bars, is responsible for the quenching of star formation in many of green valley galaxies at $z \sim 1$.

2.9 Acknowledgments

We thank our anonymous referee for useful comments that have greatly improved this paper. We thank James Aird, TJ Cox, Aleks Diamond-Stanic, Jacqueline van Gorkom, and Jim Gunn for helpful suggestions and discussions. We use data from the DEEP2 survey, which

Table 2.1: Summary of Data Sets

Survey	Wavelengths/Bands	Sample Size [a]	Survey Limit
HST/ACS Imaging	V	2437	28.75(V_{AB})
”	I	2437	28.10(I_{AB})
DEEP2 Spectroscopic Redshifts	6400-9100Å	1220	24.1 (R_{AB})
CFHTLS Photometric Redshifts	*ugriz*	2324	25.(i_{AB})
GALEX Deep Imaging Survey	NUV	1021	26.5(AB)
”	FUV	345	25(AB)
CFHT Legacy Survey Photometry	*ugriz*	2437	~27(AB)

[a] Number of galaxies with redshift with $0.4 < z < 1.2$, average signal-to-noise per pixel greater than 4, Petrosian radius $r_p > 0.3''$, and $M_B > -18$.

was supported by NSF AST grants AST00-71048, AST00-71198, AST05-07428, AST05-07483, AST08-07630, AST08-08133. This study makes use of data from AEGIS Sruvey and in particular uses data from *GALEX*, *HST*, Keck, and CFHT. The AEGIS Survey was supported in part by the NSF, NASA, and the STFC. Based on observations obtained with MegaPrime/MegaCam, a joint project of CFHT and CEA/DAPNIA, at the Canada-France-Hawaii Telescope (CFHT) which is operated by the National Research Council (NRC) of Canada, the Institut National des Science de lUniversof the Centre National de la Recherche Scientifique (CNRS) of France, and the University of Hawaii. This work is based in part on data products produced at TERAPIX and the Canadian Astronomy Data Centre as part of the Canada-France-Hawaii Telescope Legacy Survey, a collaborative project of NRC and CNRS

This chapter, in full (with minor exceptions to conform to this thesis), is a reprint of material previously published as “AEGIS: The Morphologies of Green Galaxies at $0.4 < z < 1.2$”, by Alexander J. Mendez, Alison L. Coil, Jennifer Lotz, Samir Salim, John Moustakas, & Luc Simard, published in the The Astrophysical Journal, 2011, Vol. 736, p. 736. I was the primary investigator and author of this paper.

Table 2.2: RGB G/M_{20} Morphological Types[a]

	Red	Green	Blue
Mergers	12 ± 2 %	14 ± 2 %	19 ± 1 %
Early Type	66 ± 5 %	35 ± 4 %	8 ± 1 %
Late Type	22 ± 2 %	51 ± 5 %	73 ± 3 %

[a] Percentage of each galaxy sample with $0.4 < z < 1.2$ classified into morphological types using G/M_{20}. Uncertainties include both Poisson error and uncertainties in the measured values of G/M_{20}. These fractions are measured over a wide redshift range in samples that are not volume-limited and thus should not be taken as the global fractions for red, green and blue galaxies. Please see Table 3 in Lotz et al. (2008b) for a the redshift-evolving fraction. These results here are shown to emphasize the relative fractions in our red, green, and blue galaxy samples.

Table 2.3: Kolmogorov-Smirnov significance-levels[a]

	Range	Full	Full $_{\rm NUV}$	*Stellar Mass* $_{\rm NUV}$
log M_*	[7.8, 12.2]	< 0.01%	< 0.01%	72%
C	[1.3, 5.7]	0.32%	0.16%	0.73%
A	[-0.2, 0.5]	80%	52%	3.5%
S	[-0.5, 0.9]	55%	66%	77%
B/T	[-0.2, 1.2]	2.6%	12%	4.3%
M_{20}	[-0.1, -3.0]	7.5%	0.39%	2.0%
G	[0.3, 0.7]	43%	72%	25%
M'_{20}	[-0.1, -3.0]	7.3%	0.41%	1.9%
G'	[0.3, 0.7]	70%	69%	99%
$r_p\,[k{\rm pc}]$	[-0.8, 15.8]	0.34%	55%	32%

[a] KS test significance levels for each green and purple comparison sample.

Table 2.4: Purple G/M_{20} Morphological Types[a]

	Full		Full $_{\rm NUV}$		*Stellar Mass* $_{\rm NUV}$	
	Green	Purple	Green	Purple	Green	Purple
Mergers	14 ± 2 %	16 ± 2 %	15 ± 3 %	16 ± 2 %	15 ± 3 %	15 ± 3 %
Early Type	35 ± 4 %	34 ± 3 %	39 ± 5 %	36 ± 3 %	39 ± 5 %	34 ± 5 %
Late Type	51 ± 5 %	50 ± 4 %	46 ± 6 %	48 ± 4 %	46 ± 6 %	51 ± 6 %

[a] Percents of each morphological type for each galaxy comparison sample, from G/M_{20} classification for $0.4 < z \leq 1.2$. Uncertainties in each value are from Poisson errors and Monte Carlo Simulated Signal to Noise scatter using Median G/M_{20} errors from Lotz et al. (2006).

2.10 References

Abadi, M. G., Moore, B., & Bower, R. G. 1999, MNRAS, 308, 947

Abraham, R. G., Valdes, F., Yee, H. K. C., & van den Bergh, S. 1994, ApJ, 432, 75

Abraham, R. G., van den Bergh, S., & Nair, P. 2003, ApJ, 588, 218

Baldry, I. K., Glazebrook, K., Brinkmann, J., Ivezić, Ž., Lupton, R. H., Nichol, R. C., & Szalay, A. S. 2004, ApJ, 600, 681

Ball, N. M., Loveday, J., Brunner, R. J., Baldry, I. K., & Brinkmann, J. 2006, MNRAS, 373, 845

Balogh, M. L., Navarro, J. F., & Morris, S. L. 2000, ApJ, 540, 113

Barnes, J. E., & Hernquist, L. 1992, ARA&A, 30, 705

Barnes, J. E., & Hernquist, L. 1996, ApJ, 471, 115

Bell, E. F., & de Jong, R. S. 2001, ApJ, 550, 212

Bell, E. F., McIntosh, D. H., Katz, N., & Weinberg, M. D. 2003, ApJS, 149, 289

Bell, E. F., Wolf, C., Meisenheimer, K., Rix, H.-W., Borch, A., Dye, S., Kleinheinrich, M., Wisotzki, L., & McIntosh, D. H. 2004, ApJ, 608, 752–767

Bell, E. F., Phleps, S., Somerville, R. S., Wolf, C., Borch, A., & Meisenheimer, K. 2006, ApJ, 652, 270

Bershady, M. A., Jangren, A., & Conselice, C. J. 2000, AJ, 119, 2645

Bertin, E., & Arnouts, S. 1996, A&AS, 117, 393–404

Birnboim, Y., & Dekel, A. 2003, MNRAS, 345, 349

Birnboim, Y., Dekel, A., & Neistein, E. 2007, MNRAS, 380, 339

Blanton, M. R. 2006, ApJ, 648, 268

Blanton, M. R., & Moustakas, J. 2009, ARA&A, 47, 159

Blanton, M. R., & Roweis, S. 2007, AJ, 133, 734

Blanton, M. R., Hogg, D. W., Bahcall, N. A., Baldry, I. K., Brinkmann, J., Csabai, I., Eisenstein, D., Fukugita, M., Gunn, J. E., Ivezić, Ž., Lamb, D. Q., Lupton, R. H., Loveday, J., Munn, J. A., Nichol, R. C., Okamura, S., Schlegel, D. J., Shimasaku, K., Strauss, M. A., Vogeley, M. S., & Weinberg, D. H. 2003, ApJ, 594, 186–207

Bower, R. G., Benson, A. J., Malbon, R., Helly, J. C., Frenk, C. S., Baugh, C. M., Cole, S., & Lacey, C. G. 2006, MNRAS, 370, 645

Brammer, G. B., Whitaker, K. E., van Dokkum, P. G., Marchesini, D., Labbé, I., Franx, M., Kriek, M., Quadri, R. F., Illingworth, G., Lee, K.-S., Muzzin, A., & Rudnick, G. 2009, ApJL, 706, L173–L177

Brinchmann, J., Charlot, S., White, S. D. M., Tremonti, C., Kauffmann, G., Heckman, T., & Brinkmann, J. 2004, MNRAS, 351, 1151

Brooks, A. M., Governato, F., Quinn, T., Brook, C. B., & Wadsley, J. 2009, ApJ, 694, 396

Brown, M. J. I., Dey, A., Jannuzi, B. T., Brand, K., Benson, A. J., Brodwin, M., Croton, D. J., & Eisenhardt, P. R. 2007, ApJ, 654, 858

Bruzual, G., & Charlot, S. 2003, MNRAS, 344, 1000–1028

Buat, V., Iglesias-Páramo, J., Seibert, M., Burgarella, D., Charlot, S., Martin, D. C., Xu, C. K., Heckman, T. M., Boissier, S., Boselli, A., Barlow, T., Bianchi, L., Byun, Y.-I., Donas, J., Forster, K., Friedman, P. G., Jelinski, P., Lee, Y.-W., Madore, B. F., Malina, R., Milliard, B., Morissey, P., Neff, S., Rich, M., Schiminovitch, D., Siegmund, O., Small, T., Szalay, A. S., Welsh, B., & Wyder, T. K. 2005, ApJL, 619, L51–L54

Bundy, K., Georgakakis, A., Nandra, K., Ellis, R. S., Conselice, C. J., Laird, E., Coil, A., Cooper, M. C., Faber, S. M., Newman, J. A., Pierce, C. M., Primack, J. R., & Yan, R. 2008, ApJ, 681, 931–943

Bundy, K., Scarlata, C., Carollo, C. M., Ellis, R. S., Drory, N., Hopkins, P., Salvato, M., Leauthaud, A., Koekemoer, A. M., Murray, N., Ilbert, O., Oesch, P., Ma, C.-P., Capak, P., Pozzetti, L., & Scoville, N. 2010, ApJ, 719, 1969–1983

Cameron, E., Carollo, C. M., Oesch, P., Aller, M. C., Bschorr, T., Cerulo, P., Aussel, H., Capak, P., Le Floc'h, E., Ilbert, O., Kneib, J.-P., Koekemoer, A., Leauthaud, A., Lilly, S. J., Massey, R., McCracken, H. J., Rhodes, J., Salvato, M., Sanders, D. B., Scoville, N., Sheth, K., Taniguchi, Y., & Thompson, D. 2010, MNRAS, 409, 346–354

Cardamone, C. N., Urry, C. M., Schawinski, K., Treister, E., Brammer, G., & Gawiser, E. 2010, ApJL, 721, L38

Coil, A. L., Newman, J. A., Croton, D., Cooper, M. C., Davis, M., Faber, S. M., Gerke, B. F., Koo, D. C., Padmanabhan, N., Wechsler, R. H., & Weiner, B. J. 2008, ApJ, 672, 153–176

Coil, A. L., Georgakakis, A., Newman, J. A., Cooper, M. C., Croton, D., Davis, M., Koo, D. C., Laird, E. S., Nandra, K., Weiner, B. J., Willmer, C. N. A., & Yan, R. 2009, ApJ, 701, 1484–1499

Colless, M., Dalton, G., Maddox, S., Sutherland, W., Norberg, P., Cole, S., Bland-Hawthorn, J., Bridges, T., Cannon, R., Collins, C., Couch, W., Cross, N., Deeley, K., De Propris, R., Driver, S. P., Efstathiou, G., Ellis, R. S., Frenk, C. S., Glazebrook, K., Jackson, C., Lahav, O., Lewis, I., Lumsden, S., Madgwick, D., Peacock, J. A., Peterson, B. A., Price, I., Seaborne, M., & Taylor, K. 2001, MNRAS, 328, 1039–1063

Conselice, C. J. 2003, ApJS, 147, 1

Conselice, C. J., Bershady, M. A., & Jangren, A. 2000, ApJ, 529, 886

Cooper, M. C., Newman, J. A., Croton, D. J., Weiner, B. J., Willmer, C. N. A., Gerke, B. F., Madgwick, D. S., Faber, S. M., Davis, M., Coil, A. L., Finkbeiner, D. P., Guhathakurta, P., & Koo, D. C. 2006, MNRAS, 370, 198–212

Cox, T. J., Jonsson, P., Primack, J. R., & Somerville, R. S. 2006a, MNRAS, 373, 1013

Cox, T. J., Dutta, S. N., Di Matteo, T., Hernquist, L., Hopkins, P. F., Robertson, B., & Springel, V. 2006b, ApJ, 650, 791

Cox, T. J., Jonsson, P., Somerville, R. S., Primack, J. R., & Dekel, A. 2008, MNRAS, 384, 386

Croton, D. J., Springel, V., White, S. D. M., De Lucia, G., Frenk, C. S., Gao, L., Jenkins, A., Kauffmann, G., Navarro, J. F., & Yoshida, N. 2006, MNRAS, 365, 11–28

Davé, R., Cen, R., Ostriker, J. P., Bryan, G. L., Hernquist, L., Katz, N., Weinberg, D. H., Norman, M. L., & O'Shea, B. 2001, ApJ, 552, 473–483

Davis, M., Guhathakurta, P., Konidaris, N. P., Newman, J. A., Ashby, M. L. N., Biggs, A. D., Barmby, P., Bundy, K., Chapman, S. C., Coil, A. L., Conselice, C. J., Cooper, M. C., Croton, D. J., Eisenhardt, P. R. M., Ellis, R. S., Faber, S. M., Fang, T., Fazio, G. G., Georgakakis, A., Gerke, B. F., Goss, W. M., Gwyn, S., Harker, J., Hopkins, A. M., Huang, J.-S., Ivison, R. J., Kassin, S. A., Kirby, E. N., Koekemoer, A. M., Koo, D. C., Laird, E. S., Le Floc'h, E., Lin, L., Lotz, J. M., Marshall, P. J., Martin, D. C., Metevier, A. J., Moustakas, L. A., Nandra, K., Noeske, K. G., Papovich, C., Phillips, A. C., Rich, R. M., Rieke, G. H., Rigopoulou, D., Salim, S., Schiminovich, D., Simard, L., Smail, I., Small, T. A., Weiner, B. J., Willmer, C. N. A., Willner, S. P., Wilson, G., Wright, E. L., & Yan, R. 2007, ApJL, 660, L1–L6

Dekel, A., & Birnboim, Y. 2006, MNRAS, 368, 2

Downes, D., Reynaud, D., Solomon, P. M., & Radford, S. J. E. 1996, ApJ, 461, 186

Driver, S. P., Allen, P. D., Graham, A. W., Cameron, E., Liske, J., Ellis, S. C., Cross, N. J. G., De Propris, R., Phillipps, S., & Couch, W. J. 2006, MNRAS, 368, 414–434

Elmegreen, B. G., Elmegreen, D. M., & Hirst, A. C. 2004, ApJ, 612, 191

Eskridge, P. B., Frogel, J. A., Pogge, R. W., Quillen, A. C., Davies, R. L., DePoy, D. L., Houdashelt, M. L., Kuchinski, L. E., Ramírez, S. V., Sellgren, K., Terndrup, D. M., & Tiede, G. P. 2000, AJ, 119, 536–544

Faber, S. M., Willmer, C. N. A., Wolf, C., Koo, D. C., Weiner, B. J., Newman, J. A., Im, M., Coil, A. L., Conroy, C., Cooper, M. C., Davis, M., Finkbeiner, D. P., Gerke, B. F., Gebhardt, K., Groth, E. J., Guhathakurta, P., Harker, J., Kaiser, N., Kassin, S., Kleinheinrich, M., Konidaris, N. P., Kron, R. G., Lin, L., Luppino, G., Madgwick, D. S., Meisenheimer, K., Noeske, K. G., Phillips, A. C., Sarajedini, V. L., Schiavon, R. P., Simard, L., Szalay, A. S., Vogt, N. P., & Yan, R. 2007, ApJ, 665, 265–294

Farouki, R., & Shapiro, S. L. 1980, ApJ, 241, 928

Farouki, R., & Shapiro, S. L. 1981, ApJ, 243, 32

Gerke, B. F., Newman, J. A., Faber, S. M., Cooper, M. C., Croton, D. J., Davis, M., Willmer, C. N. A., Yan, R., Coil, A. L., Guhathakurta, P., Koo, D. C., & Weiner, B. J. 2007, MNRAS, 376, 1425–1444

Guillaume, M., Llebaria, A., Aymeric, D., Arnouts, S., & Milliard, B. 2006, Proc. SPIE, 6064, 332

Gunn, J. E., & Gott, III, J. R. 1972, ApJ, 176, 1

Hernquist, L. 1992, ApJ, 400, 460

Hernquist, L. 1993, ApJ, 409, 548

Hester, J. A. 2006, ApJ, 647, 910–921

Hickox, R. C., Jones, C., Forman, W. R., Murray, S. S., Kochanek, C. S., Eisenstein, D., Jannuzi, B. T., Dey, A., Brown, M. J. I., Stern, D., Eisenhardt, P. R., Gorjian, V., Brodwin, M., Narayan, R., Cool, R. J., Kenter, A., Caldwell, N., & Anderson, M. E. 2009, ApJ, 696, 891–919

Hopkins, A. M., Connolly, A. J., Haarsma, D. B., & Cram, L. E. 2001, AJ, 122, 288–296

Hopkins, P. F., Hernquist, L., Cox, T. J., Di Matteo, T., Robertson, B., & Springel, V. 2006, ApJS, 163, 1

Ilbert, O., Arnouts, S., McCracken, H. J., Bolzonella, M., Bertin, E., Le Fèvre, O., Mellier, Y., Zamorani, G., Pellò, R., Iovino, A., Tresse, L., Le Brun, V., Bottini, D., Garilli, B., Maccagni, D., Picat, J. P., Scaramella, R., Scodeggio, M., Vettolani, G., Zanichelli, A., Adami, C., Bardelli, S., Cappi, A., Charlot, S., Ciliegi, P., Contini, T., Cucciati, O., Foucaud, S., Franzetti, P., Gavignaud, I., Guzzo, L., Marano, B., Marinoni, C., Mazure, A., Meneux, B., Merighi, R., Paltani, S., Pollo, A., Pozzetti, L., Radovich, M., Zucca, E., Bondi, M., Bongiorno, A., Busarello, G., de La Torre, S., Gregorini, L., Lamareille, F., Mathez, G., Merluzzi, P., Ripepi, V., Rizzo, D., & Vergani, D. 2006, A&A, 457, 841–856

Jogee, S., Barazza, F. D., Rix, H.-W., Shlosman, I., Barden, M., Wolf, C., Davies, J., Heyer, I., Beckwith, S. V. W., Bell, E. F., Borch, A., Caldwell, J. A. R., Conselice, C. J., Dahlen, T., Häussler, B., Heymans, C., Jahnke, K., Knapen, J. H., Laine, S., Lubell, G. M., Mobasher, B., McIntosh, D. H., Meisenheimer, K., Peng, C. Y., Ravindranath, S., Sanchez, S. F., Somerville, R. S., & Wisotzki, L. 2004, ApJL, 615, L105–L108

Jogee, S., Scoville, N., & Kenney, J. D. P. 2005, ApJ, 630, 837

Johansson, P. H., Naab, T., & Ostriker, J. P. 2009, ApJL, 697, L38

Kang, X., Jing, Y. P., & Silk, J. 2006, ApJ, 648, 820

Kartaltepe, J. S., Sanders, D. B., Le Floc'h, E., Frayer, D. T., Aussel, H., Arnouts, S., Ilbert, O., Salvato, M., Scoville, N. Z., Surace, J., Yan, L., Capak, P., Caputi, K., Carollo, C. M., Cassata, P., Civano, F., Hasinger, G., Koekemoer, A. M., Le Fèvre, O., Lilly, S., Liu, C. T., McCracken, H. J., Schinnerer, E., Smolčić, V., Taniguchi, Y., Thompson, D. J., Trump, J., Baldassare, V. F., & Fiorenza, S. L. 2010, ApJ, 721, 98–123

Kauffmann, G., Heckman, T. M., White, S. D. M., Charlot, S., Tremonti, C., Brinchmann, J., Bruzual, G., Peng, E. W., Seibert, M., Bernardi, M., Blanton, M., Brinkmann, J., Castander, F., Csábai, I., Fukugita, M., Ivezic, Z., Munn, J. A., Nichol, R. C., Padmanabhan, N., Thakar, A. R., Weinberg, D. H., & York, D. 2003, MNRAS, 341, 33–53

Kereš, D., Katz, N., Weinberg, D. H., & Davé, R. 2005, MNRAS, 363, 2

Kereš, D., Katz, N., Davé, R., Fardal, M., & Weinberg, D. H. 2009, MNRAS, 396, 2332

Kimm, T., Somerville, R. S., Yi, S. K., van den Bosch, F. C., Salim, S., Fontanot, F., Monaco, P., Mo, H., Pasquali, A., Rich, R. M., & Yang, X. 2009, MNRAS, 394, 1131–1147

Kormendy, J., & Kennicutt, Jr., R. C. 2004, ARA&A, 42, 603

Kriek, M., van der Wel, A., van Dokkum, P. G., Franx, M., & Illingworth, G. D. 2008, ApJ, 682, 896

Larson, R. B., Tinsley, B. M., & Caldwell, C. N. 1980, ApJ, 237, 692

López-Sanjuan, C., Balcells, M., Pérez-González, P. G., Barro, G., García-Dabó, C. E., Gallego, J., & Zamorano, J. 2010, ApJ, 710, 1170

López-Sanjuan, C., Le Fèvre, O., de Ravel, L., Cucciati, O., Ilbert, O., Tresse, L., Bardelli, S., Bolzonella, M., Contini, T., Garilli, B., Guzzo, L., Maccagni, D., McCracken, H. J., Mellier, Y., Pollo, A., Vergani, D., & Zucca, E. 2011, A&A, 530, A20

Lotz, J. M., Primack, J., & Madau, P. 2004, AJ, 128, 163

Lotz, J. M., Madau, P., Giavalisco, M., Primack, J., & Ferguson, H. C. 2006, ApJ, 636, 592

Lotz, J. M., Jonsson, P., Cox, T. J., & Primack, J. R. 2008a, MNRAS, 391, 1137

Lotz, J. M., Davis, M., Faber, S. M., Guhathakurta, P., Gwyn, S., Huang, J., Koo, D. C., Le Floc'h, E., Lin, L., Newman, J., Noeske, K., Papovich, C., Willmer, C. N. A., Coil, A., Conselice, C. J., Cooper, M., Hopkins, A. M., Metevier, A., Primack, J., Rieke, G., & Weiner, B. J. 2008b, ApJ, 672, 177–197

Lotz, J. M., Jonsson, P., Cox, T. J., & Primack, J. R. 2010, MNRAS, 404, 575

Madgwick, D. S., Lahav, O., Baldry, I. K., Baugh, C. M., Bland-Hawthorn, J., Bridges, T., Cannon, R., Cole, S., Colless, M., Collins, C., Couch, W., Dalton, G., De Propris, R., Driver, S. P., Efstathiou, G., Ellis, R. S., Frenk, C. S., Glazebrook, K., Jackson, C., Lewis, I., Lumsden, S., Maddox, S., Norberg, P., Peacock, J. A., Peterson, B. A., Sutherland, W., & Taylor, K. 2002, MNRAS, 333, 133–144

Martin, D. C., Fanson, J., Schiminovich, D., Morrissey, P., Friedman, P. G., Barlow, T. A., Conrow, T., Grange, R., Jelinsky, P. N., Milliard, B., Siegmund, O. H. W., Bianchi, L., Byun, Y.-I., Donas, J., Forster, K., Heckman, T. M., Lee, Y.-W., Madore, B. F., Malina, R. F., Neff, S. G., Rich, R. M., Small, T., Surber, F., Szalay, A. S., Welsh, B., & Wyder, T. K. 2005, ApJL, 619, L1–L6

Martin, D. C., Wyder, T. K., Schiminovich, D., Barlow, T. A., Forster, K., Friedman, P. G., Morrissey, P., Neff, S. G., Seibert, M., Small, T., Welsh, B. Y., Bianchi, L., Donas, J., Heckman, T. M., Lee, Y.-W., Madore, B. F., Milliard, B., Rich, R. M., Szalay, A. S., & Yi, S. K. 2007, ApJS, 173, 342–356

Masters, K. L., Mosleh, M., Romer, A. K., Nichol, R. C., Bamford, S. P., Schawinski, K., Lintott, C. J., Andreescu, D., Campbell, H. C., Crowcroft, B., Doyle, I., Edmondson, E. M., Murray, P., Raddick, M. J., Slosar, A., Szalay, A. S., & Vandenberg, J. 2010, MNRAS, 405, 783–799

McNamara, B. R., & Nulsen, P. E. J. 2007, ARA&A, 45, 117

McNamara, B. R., Wise, M., Nulsen, P. E. J., David, L. P., Sarazin, C. L., Bautz, M., Markevitch, M., Vikhlinin, A., Forman, W. R., Jones, C., & Harris, D. E. 2000, ApJL, 534, L135–L138

McNamara, B. R., Wise, M. W., Nulsen, P. E. J., David, L. P., Carilli, C. L., Sarazin, C. L., O'Dea, C. P., Houck, J., Donahue, M., Baum, S., Voit, M., O'Connell, R. W., & Koekemoer, A. 2001, ApJL, 562, L149–L152

Menéndez-Delmestre, K., Sheth, K., Schinnerer, E., Jarrett, T. H., & Scoville, N. Z. 2007, ApJ, 657, 790

Mihos, J. C., & Hernquist, L. 1994, ApJL, 425, L13

Moore, B., Katz, N., Lake, G., Dressler, A., & Oemler, A. 1996, Nature, 379, 613

Moore, B., Lake, G., & Katz, N. 1998, ApJ, 495, 139

Morrissey, P., Conrow, T., Barlow, T. A., Small, T., Seibert, M., Wyder, T. K., Budavári, T., Arnouts, S., Friedman, P. G., Forster, K., Martin, D. C., Neff, S. G., Schiminovich, D., Bianchi, L., Donas, J., Heckman, T. M., Lee, Y.-W., Madore, B. F., Milliard, B., Rich, R. M., Szalay, A. S., Welsh, B. Y., & Yi, S. K. 2007, ApJS, 173, 682–697

Naab, T., & Burkert, A. 2003, ApJ, 597, 893

Nandra, K., Georgakakis, A., Willmer, C. N. A., Cooper, M. C., Croton, D. J., Davis, M., Faber, S. M., Koo, D. C., Laird, E. S., & Newman, J. A. 2007, ApJL, 660, L11–L14

Oesch, P. A., Carollo, C. M., Feldmann, R., Hahn, O., Lilly, S. J., Sargent, M. T., Scarlata, C., Aller, M. C., Aussel, H., Bolzonella, M., Bschorr, T., Bundy, K., Capak, P., Ilbert, O., Kneib, J.-P., Koekemoer, A. M., Kovač, K., Leauthaud, A., Le Floc'h, E., Massey, R., McCracken, H. J., Pozzetti, L., Renzini, A., Rhodes, J., Salvato, M., Sanders, D. B., Scoville, N., Sheth, K., Taniguchi, Y., & Thompson, D. 2010, ApJL, 714, L47–L51

Pannella, M., Gabasch, A., Goranova, Y., Drory, N., Hopp, U., Noll, S., Saglia, R. P., Strazzullo, V., & Bender, R. 2009, ApJ, 701, 787–803

Pierce, C. M., Lotz, J. M., Salim, S., Laird, E. S., Coil, A. L., Bundy, K., Willmer, C. N. A., Rosario, D. J. V., Primack, J. R., & Faber, S. M. 2010, MNRAS, 408, 139–156

Quilis, V., Moore, B., & Bower, R. 2000, Science, 288, 1617

Regan, M. W., Sheth, K., & Vogel, S. N. 1999, ApJ, 526, 97

Robertson, B., Bullock, J. S., Cox, T. J., Di Matteo, T., Hernquist, L., Springel, V., & Yoshida, N. 2006, ApJ, 645, 986

Salim, S., & Rich, R. M. 2010, ApJL, 714, L290

Salim, S., Rich, R. M., Charlot, S., Brinchmann, J., Johnson, B. D., Schiminovich, D., Seibert, M., Mallery, R., Heckman, T. M., Forster, K., Friedman, P. G., Martin, D. C., Morrissey, P., Neff, S. G., Small, T., Wyder, T. K., Bianchi, L., Donas, J., Lee, Y.-W., Madore, B. F., Milliard, B., Szalay, A. S., Welsh, B. Y., & Yi, S. K. 2007, ApJS, 173, 267–292

Salim, S., Dickinson, M., Michael Rich, R., Charlot, S., Lee, J. C., Schiminovich, D., Pérez-González, P. G., Ashby, M. L. N., Papovich, C., Faber, S. M., Ivison, R. J., Frayer, D. T., Walton, J. M., Weiner, B. J., Chary, R.-R., Bundy, K., Noeske, K., & Koekemoer, A. M. 2009, ApJ, 700, 161–182

Scarlata, C., Carollo, C. M., Lilly, S., Sargent, M. T., Feldmann, R., Kampczyk, P., Porciani, C., Koekemoer, A., Scoville, N., Kneib, J.-P., Leauthaud, A., Massey, R., Rhodes, J., Tasca, L., Capak, P., Maier, C., McCracken, H. J., Mobasher, B., Renzini, A., Taniguchi, Y., Thompson, D., Sheth, K., Ajiki, M., Aussel, H., Murayama, T., Sanders, D. B., Sasaki, S., Shioya, Y., & Takahashi, M. 2007, ApJS, 172, 406–433

Schawinski, K., Lintott, C. J., Thomas, D., Kaviraj, S., Viti, S., Silk, J., Maraston, C., Sarzi, M., Yi, S. K., Joo, S.-J., Daddi, E., Bayet, E., Bell, T., & Zuntz, J. 2009, ApJ, 690, 1672–1680

Sellwood, J. A., & Wilkinson, A. 1993, Reports on Progress in Physics, 56, 173

Sersic, J. L. 1968. Atlas de galaxias australes

Shen, S., Mo, H. J., White, S. D. M., Blanton, M. R., Kauffmann, G., Voges, W., Brinkmann, J., & Csabai, I. 2003, MNRAS, 343, 978

Sheth, K., Regan, M. W., Vogel, S. N., & Teuben, P. J. 2000, ApJ, 532, 221

Sheth, K., Vogel, S. N., Regan, M. W., Thornley, M. D., & Teuben, P. J. 2005, ApJ, 632, 217

Sheth, R. K., & Tormen, G. 2002, MNRAS, 329, 61

Sheth, R. K., Bernardi, M., Schechter, P. L., Burles, S., Eisenstein, D. J., Finkbeiner, D. P., Frieman, J., Lupton, R. H., Schlegel, D. J., Subbarao, M., Shimasaku, K., Bahcall, N. A., Brinkmann, J., & Ivezić, Ž. 2003, ApJ, 594, 225–231

Simard, L., Willmer, C. N. A., Vogt, N. P., Sarajedini, V. L., Phillips, A. C., Weiner, B. J., Koo, D. C., Im, M., Illingworth, G. D., & Faber, S. M. 2002, ApJS, 142, 1–33

Springel, V., Di Matteo, T., & Hernquist, L. 2005a, ApJL, 620, L79

Springel, V., Di Matteo, T., & Hernquist, L. 2005b, MNRAS, 361, 776

Steinmetz, M., & Navarro, J. F. 2002, New Astronomy, 7, 155

Strateva, I., Ivezić, Ž., Knapp, G. R., Narayanan, V. K., Strauss, M. A., Gunn, J. E., Lupton, R. H., Schlegel, D., Bahcall, N. A., Brinkmann, J., Brunner, R. J., Budavári, T., Csabai, I., Castander, F. J., Doi, M., Fukugita, M., Győry, Z., Hamabe, M., Hennessy, G., Ichikawa, T., Kunszt, P. Z., Lamb, D. Q., McKay, T. A., Okamura, S., Racusin, J., Sekiguchi, M., Schneider, D. P., Shimasaku, K., & York, D. 2001, AJ, 122, 1861–1874

Takamiya, M. 1999, ApJS, 122, 109

Tinker, J. L., Wechsler, R. H., & Zheng, Z. 2010, ApJ, 709, 67

Toomre, A. 1977, ARA&A, 15, 437

Toomre, A., & Toomre, J. 1972, ApJ, 178, 623

van den Bosch, F. C., Aquino, D., Yang, X., Mo, H. J., Pasquali, A., McIntosh, D. H., Weinmann, S. M., & Kang, X. 2008, MNRAS, 387, 79

Weiner, B. J., Phillips, A. C., Faber, S. M., Willmer, C. N. A., Vogt, N. P., Simard, L., Gebhardt, K., Im, M., Koo, D. C., Sarajedini, V. L., Wu, K. L., Forbes, D. A., Gronwall, C., Groth, E. J., Illingworth, G. D., Kron, R. G., Rhodes, J., Szalay, A. S., & Takamiya, M. 2005, ApJ, 620, 595–617

Weiner, B. J., Coil, A. L., Prochaska, J. X., Newman, J. A., Cooper, M. C., Bundy, K., Conselice, C. J., Dutton, A. A., Faber, S. M., Koo, D. C., Lotz, J. M., Rieke, G. H., & Rubin, K. H. R. 2009, ApJ, 692, 187–211

Williams, R. J., Quadri, R. F., Franx, M., van Dokkum, P., & Labbé, I. 2009, ApJ, 691, 1879

Willmer, C. N. A., Faber, S. M., Koo, D. C., Weiner, B. J., Newman, J. A., Coil, A. L., Connolly, A. J., Conroy, C., Cooper, M. C., Davis, M., Finkbeiner, D. P., Gerke, B. F., Guhathakurta, P., Harker, J., Kaiser, N., Kassin, S., Konidaris, N. P., Lin, L., Luppino, G., Madgwick, D. S., Noeske, K. G., Phillips, A. C., & Yan, R. 2006, ApJ, 647, 853–873

Wyder, T. K., Martin, D. C., Schiminovich, D., Seibert, M., Budavári, T., Treyer, M. A., Barlow, T. A., Forster, K., Friedman, P. G., Morrissey, P., Neff, S. G., Small, T., Bianchi, L., Donas, J., Heckman, T. M., Lee, Y.-W., Madore, B. F., Milliard, B., Rich, R. M., Szalay, A. S., Welsh, B. Y., & Yi, S. K. 2007, ApJS, 173, 293–314

York, D. G., Adelman, J., Anderson, Jr., J. E., Anderson, S. F., Annis, J., Bahcall, N. A., Bakken, J. A., Barkhouser, R., Bastian, S., Berman, E., Boroski, W. N., Bracker, S., Briegel, C., Briggs, J. W., Brinkmann, J., Brunner, R., Burles, S., Carey, L., Carr, M. A., Castander, F. J., Chen, B., Colestock, P. L., Connolly, A. J., Crocker, J. H., Csabai, I., Czarapata, P. C., Davis, J. E., Doi, M., Dombeck, T., Eisenstein, D., Ellman, N., Elms, B. R., Evans, M. L., Fan, X., Federwitz, G. R., Fiscelli, L., Friedman, S., Frieman, J. A., Fukugita, M., Gillespie, B., Gunn, J. E., Gurbani, V. K., de Haas, E., Haldeman, M., Harris, F. H., Hayes, J., Heckman, T. M., Hennessy, G. S., Hindsley, R. B., Holm, S., Holmgren, D. J., Huang, C.-h., Hull, C., Husby, D., Ichikawa, S.-I., Ichikawa, T., Ivezić, Ž., Kent, S., Kim, R. S. J., Kinney, E., Klaene, M., Kleinman, A. N., Kleinman, S., Knapp, G. R., Korienek, J., Kron, R. G., Kunszt, P. Z., Lamb, D. Q., Lee, B., Leger, R. F., Limmongkol, S., Lindenmeyer, C., Long, D. C., Loomis, C., Loveday, J., Lucinio, R., Lupton, R. H., MacKinnon, B., Mannery, E. J., Mantsch, P. M., Margon, B., McGehee, P., McKay, T. A., Meiksin, A., Merelli, A., Monet, D. G., Munn, J. A., Narayanan, V. K., Nash, T., Neilsen, E., Neswold, R., Newberg, H. J., Nichol, R. C., Nicinski, T., Nonino, M., Okada, N., Okamura, S., Ostriker, J. P., Owen, R., Pauls, A. G., Peoples, J., Peterson, R. L., Petravick, D., Pier, J. R., Pope, A., Pordes, R., Prosapio, A., Rechenmacher, R., Quinn, T. R., Richards, G. T., Richmond, M. W., Rivetta, C. H., Rockosi, C. M., Ruthmansdorfer, K., Sandford, D., Schlegel, D. J., Schneider, D. P., Sekiguchi, M., Sergey, G., Shimasaku, K., Siegmund, W. A., Smee, S., Smith, J. A., Snedden, S., Stone, R., Stoughton, C., Strauss, M. A., Stubbs, C., SubbaRao, M., Szalay, A. S., Szapudi, I., Szokoly, G. P., Thakar, A. R., Tremonti, C., Tucker, D. L., Uomoto, A., Vanden Berk, D., Vogeley, M. S., Waddell, P., Wang, S.-i., Watanabe, M., Weinberg, D. H., Yanny, B., Yasuda, N., & SDSS Collaboration 2000, AJ, 120, 1579–1587

Zamojski, M. A., Schiminovich, D., Rich, R. M., Mobasher, B., Koekemoer, A. M., Capak, P., Taniguchi, Y., Sasaki, S. S., McCracken, H. J., Mellier, Y., Bertin, E., Aussel, H., Sanders, D. B., Le Fèvre, O., Ilbert, O., Salvato, M., Thompson, D. J., Kartaltepe, J. S., Scoville, N., Barlow, T. A., Forster, K., Friedman, P. G., Martin, D. C., Morrissey, P., Neff, S. G., Seibert, M., Small, T., Wyder, T. K., Bianchi, L., Donas, J., Heckman, T. M., Lee, Y.-W., Madore, B. F., Milliard, B., Szalay, A. S., Welsh, B. Y., & Yi, S. K. 2007, ApJS, 172, 468–493

Zhu, G., Blanton, M. R., & Moustakas, J. 2010, ApJ, 722, 491

Chapter 3

Infrared and X-ray AGN Selection Techniques

3.1 Abstract

We present a study of *Spitzer*/IRAC and X-ray active galactic nucleus (AGN) selection techniques in order to quantify the overlap, uniqueness, contamination, and completeness of each. We investigate how the overlap and possible contamination of the samples depends on the depth of both the IR and X-ray data. We use *Spitzer*/IRAC imaging, *Chandra* and *XMM-Newton* X-ray imaging, and spectroscopic redshifts from the PRism MUlti-object Survey (PRIMUS) to construct galaxy and AGN samples at $0.2 < z < 1.2$ over 8 deg^2. We construct samples over a wide range of IRAC flux limits (SWIRE to GOODS depth) and X-ray flux limits (10 ks to 2 Ms). We compare IR-AGN samples defined using both the IRAC color selection of Stern et al. and Donley et al. with X-ray detected AGN samples. For roughly similar depth IR and X-ray surveys, we find that ∼75% of IR-selected AGNs are also identified as X-ray AGNs. This fraction increases to ∼90% when comparing against the deepest X-ray data, indicating that at most ∼10% of IR-selected AGNs may be heavily obscured. The IR-AGN selection proposed by Stern et al. suffers from contamination by star-forming galaxies at various redshifts when using deeper IR data, though the selection technique works well for shallow IR data. While similar overall, the IR-AGN samples preferentially contain more luminous AGNs, while the X-ray AGN samples identify a wider range of AGN accretion rates including low specific accretion rate AGNs, where the host galaxy light dominates at IR wavelengths. The host galaxy populations of the IR and X-ray AGN samples have similar restframe colors and stellar masses; both selections identify AGNs in blue, star-forming and red, quiescent galaxies.

3.2 Introduction

Understanding the nature and role of active galactic nuclei (AGNs) is crucial for understanding both the accretion history of the universe as well as galaxy evolution. There is mounting observational evidence that there is a connection between black hole growth and galaxy growth. This is shown both by the tight correlation between black hole mass and galaxy bulge mass (e.g., Magorrian et al. 1998; Ferrarese & Merritt 2000; Gebhardt et al. 2000), as well as the similar evolutionary history of star formation and AGN activity through cosmic time (e.g., Boyle & Terlevich 1998; Silverman et al. 2008; Aird et al. 2010). In order to understand and characterize AGNs, one must be able to identify a complete AGN sample, with full knowledge of any underlying biases or contamination in the sample. One can then better determine which processes (e.g. secular evolution, mergers, and environment) are the dominate fueling mechanisms in the growth and evolution of AGNs.

Deep X-ray surveys provide a reliable means of selecting AGNs, in that they introduce few false positives, as the AGN light generally outshines light from even highly active star-forming galaxies at X-ray wavelengths. However, high-column density gas ($N_{\rm H} > 10^{23}$ cm^{-2}) absorbs X-rays, such that X-ray surveys may fail to identify the most heavily absorbed AGNs. While the exact fraction of obscured AGNs ($N_{\rm H} > 10^{22}$ cm^{-2}) is not yet fully known, obscured AGNs likely represent a large fraction of the total AGN population at all luminosities. For example, Treister et al. (2004) predict that between $\sim 25\%$ to $\sim 50\%$ of AGNs are obscured, even at high luminosities ($L_{\rm X} > 10^{44}$ erg s^{-1}); Treister et al. (see also 2009a,b); Ballantyne et al. (see also 2011), while Gilli et al. (2007) use the cosmic X-ray background to predict that Compton-thick AGNs are four times as numerous as unobscured AGNs at low luminosity ($L_{\rm X} < 10^{43.5}$ erg s^{-1}). More recently, Akylas et al. (2012) predict that the number of Compton-thick AGNs may be 10 times as numerous as unobscured AGNs. Only with extremely deep X-ray data ($\gtrsim$1 Ms) does it become possible to detect and characterize the heavily obscured, moderate luminosity AGNs (e.g. Georgantopoulos et al. 2009; Brightman & Ueda 2012) that would otherwise be missed in shallower X-ray surveys. However, even the deepest X-ray surveys may still fail to identify low luminosity AGNs with moderate to heavy obscuration. Additionally, current deep X-ray surveys cover at most $\sim$1 deg^2 of sky, which limits the size of the resulting AGN samples. Ideally, both wide and deep X-ray surveys are required to identify statistically large, relatively complete AGN samples.

The use of mid-infrared (MIR) emission to identify AGNs began in the 1970s with the advent of sensitive IR detectors (Low & Kleinmann 1968) and continued with the *Infrared Astronomical Satellite* and the Infrared Array Camera (IRAC; Fazio et al. 2004) on board *Spitzer*. High-energy radiation from the AGN is reprocessed by dust near the AGN and re-radiated at MIR wavelengths. Luminous AGNs display a red MIR power-law spectral energy distribution (SED), which is dominated by thermal emission from hot dust (Neugebauer et al. 1979; Elvis et al. 1994; Rieke & Lebofsky 1981). Emission at MIR wavelengths can also potentially be used to detect Compton-thick AGNs that may be missed by deep X-ray surveys (e.g. Ivison et al. 2004; Lacy et al. 2004; Stern et al. 2005; Alonso-Herrero et al. 2006; Polletta et al. 2006). It has also been found that objects with similar MIR luminosities can have vastly different radio, optical, UV and soft X-ray luminosities (Mushotzky 2004), such that heavily obscured AGNs can be identified in the MIR as it is relatively insensitive to obscuration. Therefore MIR AGN identification is a potentially powerful tool that is sensitive to both obscured and unobscured AGNs, without requiring time-consuming deep X-ray data. Building on the above findings, a variety of selection techniques have been developed to identify large samples of AGNs from MIR imaging data. Within the MIR waveband there are many techniques to select infrared-AGNs (IR-AGNs), each taking advantage of the unique colors of AGNs. Stern et al. (2005) and Lacy et al. (2004) propose IRAC color-color cuts that were designed using shallow IRAC surveys and which effectively select luminous AGNs at low redshift. These selections identify the AGN population and separate them from the much larger galaxy population based on their characteristic MIR properties. Recently, a number of new MIR selection techniques have been suggested that use data from the *Wide field Infrared Survey Explorer* (*WISE*; Wright et al. 2010) survey, including those of Messias et al. (2012), who use the 4.5 $\mu m$and 8.0 μm bands, and Mateos et al. (2012), who use the 2.4 μm, 4.6 μm, and 12 μm bands. The *WISE* bands used in these results are not very different from the *Spitzer* IRAC bands and add techniques to fully probe the AGN population space. Alternatively, the IR SED can be fit using multiple bands and the associated photometric errors to estimate the probability that the source has a featureless power-law continuum (e.g. Alonso-Herrero et al. 2006; Polletta et al. 2006; Donley et al. 2007). Such techniques identify AGNs within similar regions in color–color space but are generally more reliable and lead to smaller samples.

Recent work using deeper IRAC and X-ray surveys (e.g. Barmby et al. 2006; Donley et al. 2007; Cardamone et al. 2008; Park et al. 2010; Eckart et al. 2010) has begun to investigate these MIR AGN selections beyond the shallow surveys for which they were designed. Barmby et al. (2006) use deep IR and X-ray data in the Extended Groth Strip (EGS) to find that X-ray AGN have a wide range of MIR colors, suggesting that there is no single method that will be able to identify a complete AGN sample. Likewise, Park et al. (2010) find that a majority (78%) of the X-ray AGN sources are not detected by the power-law AGN selection method. Together these studies suggest that there is a population of AGNs missed by IR-AGN selection techniques even at shallow X-ray and IR survey depths. Recently, Donley et al. (2012) revisit the Stern et al. and Lacy IRAC color-color selections, which were defined with relatively shallow surveys, and the power-law selection, which depends on both the photometry and (generally underestimated) photometric errors, and define a *new* IRAC color-color selection criteria, which they claim is more reliable than the previous IR selection criteria. Additionally, using an X-ray stacking analysis Georgantopoulos et al. (2008) find a soft mean X-ray spectrum in the Chandra Deep Field North (CDFN) suggesting contamination of the Stern wedge by normal galaxies. While each of these IR

AGN criteria select some fraction of the total underlying AGN population, Barmby et al. (2006) suggest that no proposed IR AGN color selection will identify *all* AGNs, given the wide range of spectral shapes exhibited by X-ray sources in the EGS.

With some possible issues, using the MIR to select AGNs is still an effective way to identify heavily obscured/Compton-thick AGNs that are an important population missed by X-ray surveys. In order to build more complete AGN samples it has become common to use multiple waveband selection techniques in the IR through X-ray. For example, Hickox et al. (2007), and Assef et al. (2010) combine different waveband selection techniques to probe the properties of the underlying AGN population. Combining both X-ray AGN samples and IR-AGN samples should provide a better census of the underlying AGN population. However, there has been relatively little study of the overlap and uniqueness of each AGN selection technique.

Comparing samples selected using different techniques could provide insight into the AGNs that are missed using different selection techniques. Similarly, it is important to understand the properties of AGNs and their host galaxies selected in each way.

Here we aim to quantify the overlap and uniqueness of various IR-AGN selection techniques compared to X-ray AGN selection. We use X-ray and IR data of varying depths in the Chandra Deep Field South (CDFS), COSMOS, Elias-S1 (ES1) and XMM-LSS (XMM) fields covered by the PRism MUlti-object Survey (PRIMUS) redshift survey. We use these datasets to investigate how the selected AGN population depends on the selection technique and the depth of the data, and we investigate the completeness, contamination, and uniqueness of X-ray versus IR-AGN selection. The paper is organized as follows. In Section 3.3, we present the relevant multi-wavelength datasets. In Section 3.4, we detail the different AGN selection techniques. In Section 3.5, we compare the number densities and overlap between X-ray AGN and IR-AGN selection techniques, as a function of survey depth. In Section 3.6, we investigate contamination of IR-AGN samples. In Section 3.7, we compare the AGN and host galaxy rest-frame properties of X-ray and IR selection techniques. We discuss our results in §3.8 and conclude in §3.9. Throughout the paper we assume a standard flat ΛCDM model with $\Omega_m = 0.3$, $\Omega_\Lambda = 0.7$, and $H_0 = 72$ km s^{-1} Mpc^{-1}.

3.3 Data

For this study, we use multi-wavelength data from the CDFS, COSMOS, ES1, and XMM fields. All of these fields have optical photometry, *Spitzer* IR imaging, spectroscopic redshifts from PRIMUS, and X-ray data from *Chandra* and *XMM-Newton*. We describe these datasets in detail in Sections 3.3.1–3.3.3 below. Figure 3.1 shows the IRAC (orange boxes), PRIMUS (blue), and X-ray coverage (green) for each of the fields.

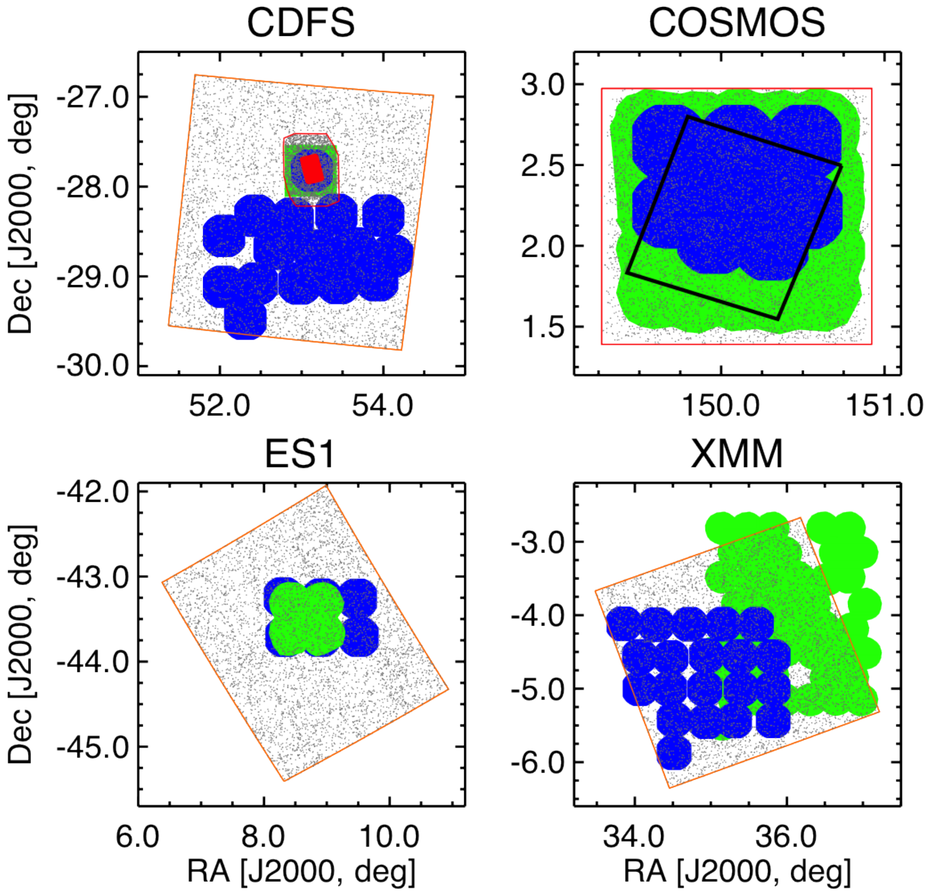

Figure 3.1: **Areal map of the multi-wavelength samples** — Map of the IR (orange box), PRIMUS (blue), and X-ray (green) coverage in the CDFS, COSMOS, ES1, and XMM fields. Ten thousand random objects detected in all four IRAC bands are shown with gray points. Within CDFS the red outline shows the SIMPLE region, which has deeper IR data, and the solid red polygon shows the GOODS region, which has the deepest IR and X-ray data. The SCOSMOS footprint is outlined in red in the COSMOS field, and the deeper X-ray footprint in the central 0.9 deg^2 of the COSMOS field is outlined in black.

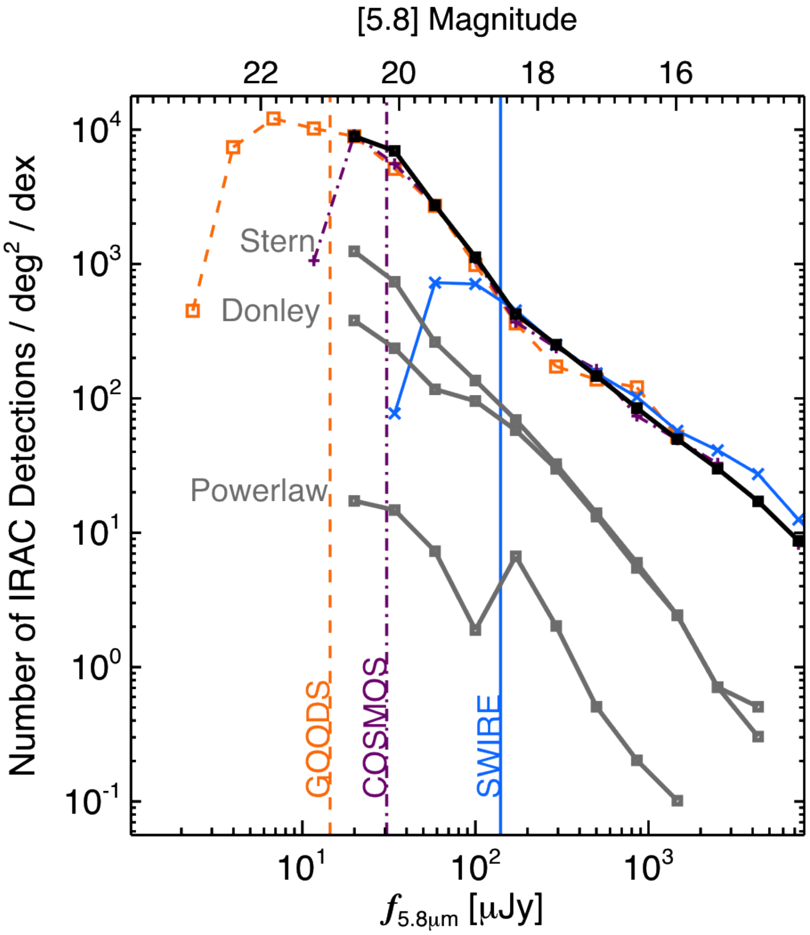

Figure 3.2: **Mid-IR flux distributions** — Number density (number of sources per logarithmic flux bin per square degree) detected in all four IRAC channels as a function of IRAC 5.8 μm flux. We show number densities for our three survey depths: `SWIRE` (orange squares), `COSMOS` (purple pluses), and `GOODS` (light blue crosses). The vertical colored lines indicate our chosen 5.8 μm flux limit for each survey depth, which is set at a flux brighter than the observed turn over in the number counts (see Table 3.1). The solid black line shows the combined number density of sources across all fields that reach our fixed 5.8 μm flux limits. We also show the Stern et al. , Donley et al. , and power-law IR-AGN total number densities from the combined sample (gray lines).

3.3.1 *Spitzer* IR Data

In the CDFS, ES1, and XMM fields, we use existing *Spitzer* IRAC imaging from Data Release 2 (DR2) of the *Spitzer* Wide-area Infrared Extragalactic Survey (Lonsdale et al. 2003, SWIRE;). Within the shallow CDFS-SWIRE (orange outline in Figure 3.1), we include deeper source catalogs within the CDFS-SIMPLE region (solid red outline) and even deeper data in CDFS-GOODS region (solid red polygon), both taken from version 3.0 of the *Spitzer* IRAC/MUSYC Public Legacy in E-CDFS (SIMPLE) survey data release (Damen et al. 2011). In the COSMOS field we use existing IRAC imaging from the S-COSMOS Survey (Sanders et al. 2007).

In fields with SWIRE coverage, we adopt source catalogs provided by the SWIRE team as part of their SWIRE DR2[1]. These catalogs were generated by performing source detection in each of the four IRAC channels and merging the source lists (see below for more details). For the CDFS-SIMPLE region with deeper IRAC data, we compared the measured fluxes for sources in both the SWIRE catalog and the SIMPLE catalog (Damen et al. 2011). Based on this comparison, we find that the SIMPLE fluxes need to be scaled by 2.02, 1.96, 1.69, and 1.56, in IRAC channels 1, 2, 3, and 4, respectively to match the measured fluxes from the CDFS-SWIRE catalog. This multiplication factor accounts for the total flux correction applied by the SWIRE team compared to the $4\farcs0$ aperture used by the SIMPLE team and a small zero point difference. The errors are also multiplied by the above factors, and agree with the SWIRE errors after accounting for the difference in exposure times. The SIMPLE catalog includes our deepest IRAC data in the CDFS-GOODS region.

For the S-COSMOS IRAC data, we reproduce the SWIRE source detection procedure (as outlined in the SWIRE DR2 documentation) to ensure we measure robust fluxes and errors using a consistent technique. We downloaded the mosaic images in each IRAC channel from the NASA/IPAC Infrared Science Archive[2] (May 2007 release). We use Astronomical Point source EXtractor pipeline in MOPEX to perform source detection in the mosaic for each channel on an individual basis. We combined the individual catalogs using the BANDMERGE procedure in MOPEX. The merged sources in the final catalog are required to be detected with signal-to-noise ratio (S/N) ≥ 10 in channel 1 and S/N ≥ 5 in channel 2. We follow the SWIRE handbook and apply a "coverage-S/N" flux limit, which is a factor proportional to the inverse of the square root of the coverage (C), the number of times that the object's location was scanned by IRAC in a given channel. This threshold limits flux measurements to where the flux of a detected object is large compared to the statistical fluctuations in the background sky in a given channel. Due to the deeper coverage of *Spitzer* IRAC scans in the COSMOS field, we require that the coverage threshold to be 3, 3, 16, and 50 $\mu Jy \times \sqrt{4/C}$ for channels 1, 2, 3, or 4, respectively, to match the SWIRE fields. For the majority of sources, our flux measurements are similar to those in the

---

[1] http://irsa.ipac.caltech.edu/data/SPITZER/SWIRE

[2] http://irsa.ipac.caltech.edu/data/COSMOS/images/spitzer/irac/

S-COSMOS public catalog, although the public catalog tends to have larger errors for all objects.

We combine our various fields and data sets into three "IR surveys depths" with data of comparable depth.

1. `GOODS`, the deepest area of IRAC imaging within the CDFS field.
2. `COSMOS`, including the S-COSMOS data *and* the SIMPLE coverage in the CDFS field that reaches comparable flux limits.
3. `SWIRE`, which includes the entire area of the XMM and ES1 fields as well as the large area in the CDFS field with SWIRE coverage.

In Figure 3.2, we show the number density of sources for each survey depth as a function of 5.8 μm flux. We require a source to be detected in all four IRAC bands, which is necessary for our analysis in this paper. We set a 5.8 μm flux limit for each IR survey depth that is just above the point where the number counts start to turn over (vertical colored lines), indicating incompleteness in the IRAC detected samples. Requiring a detection to the 5.8 μm flux limit guarantees an S/N above 2.4 and 2.1 in channels 3 and 4, respectively, with the median source having an S/N of approximately 10 in channels 3 and 4. These flux limits are given in Table 3.1. Our `SWIRE` IR survey depth includes the entire XMM, ES1 and CDFS fields (21.55 deg^2 in total); our `COSMOS` IR survey depth includes COSMOS and the SIMPLE region of the CDFS field (3.05 deg^2). Our deepest IR survey depth (`GOODS`) includes only the small GOODS region of the CDFS field (0.06 deg^2). In the rest of this paper we adopt these limits and the corresponding area coverages when analyzing data to a given IR survey depth. The solid black line in Figure 3.2 shows the overall number density combining all of our fields that probe above the flux limit for each IR survey depth.

3.3.2 PRIMUS Data

PRIMUS (Coil et al. 2011) is the largest intermediate-redshift, faint-galaxy spectroscopic survey performed to date and covers ~9 deg^2 in seven different fields with existing deep multi-wavelength imaging. We obtain low-resolution ($R \sim 40$) spectra for ~300,000 objects from the IMACS instrument on the Magellan I Baade 6.5m telescope, targeting 80% of galaxies with $i \lesssim 22$, with a statistically complete sample to a depth of $i \sim 23$. By fitting galaxy, broad-line AGNs, and stellar spectral templates to low-resolution spectra and optical ground-based photometry, we have measured ~120,000 robust redshifts with a precision of $\sigma_z/(1+z) < 0.5\%$ and a catastrophic outlier rate of $\lesssim 3\%$ ($\Delta z/(1+z) \geq 0.03$). We classify objects as galaxies, broad-line AGNs or stars based on the χ^2 of the best template fits. We derive K-corrections (Blanton & Roweis 2007) from the photometry. For further details of the survey design, targeting, and data see Coil et al. (2011); for details of the data reduction, redshift confidence and precision, and completeness, see Cool et al. (2013).

Here, we use PRIMUS redshifts between $0.2 < z < 1.2$ with high confidence quality flags ($Q \geq 3$; see Coil et al. (2011).) In the CDFS field, the PRIMUS science observations cover part of CDFS-SWIRE but are disjoint from the CDFS-SIMPLE and CDFS-GOODS area. We therefore also include the PRIMUS CDFS calibration field, which overlaps with the CDFS-GOODS and CDFS-SIMPLE areas, to increase the number of deep IRAC and X-ray detected objects with PRIMUS redshifts for Section 3.7. We thus have a total of 31,998 galaxies and broad-line AGNs with high-confidence PRIMUS redshifts in the COSMOS, CDFS, ES1, and XMM fields. Figure 3.1 shows the overlaps between the PRIMUS footprint and the IRAC and X-ray coverage. Table 3.2 gives the areas of the total and overlapping regions of each data set.

3.3.3 X-Ray Data

We have compiled published X-ray source catalogs based on existing *Chandra* and *XMM-Newton* X-ray data in the COSMOS, CDFS, ES1, and XMM fields (see Aird et al. (2012) for details). In all of the fields we use the likelihood ratio matching technique (e.g., Sutherland & Saunders 1992; Ciliegi et al. 2003; Brusa et al. 2007; Laird et al. 2009) to identify counterparts for each of the X-ray sources in the PRIMUS targeting optical photometry. We also apply the likelihood ratio technique to assign secure IRAC counterparts to the X-ray sources in the entire area with both X-ray and *Spitzer* IRAC coverage. Candidate counterparts are identified within $5''$, although over 80% of likelihood ratio matched IRAC counterparts are within $2''$ of their X-ray counterpart. The likelihood ratio matching technique accounts for optical, IR, and X-ray positional uncertainties, the probability of having a counterpart with a given magnitude, and the probability of a spurious match. Where multiple counterparts exist, we choose the match with the highest likelihood ratio and restrict to "secure" counterparts with likelihood ratios >0.5.

Within the CDFS field, we use the Luo et al. (2008) 2 Ms CDFS X-ray source catalog, one of the deepest *Chandra* survey to date, and the four overlapping 250 ks *Chandra* point source catalogs of Lehmer et al. (2005). The 2 Ms catalog covers all of the CDFS-GOODS IRAC coverage(0.058 deg^2), and part of CDFS-SIMPLE (0.25 deg^2) and CDFS-SWIRE (0.31 deg^2) coverage, to a depth of $f_{2-8\mathrm{keV}} \sim 5.5 \times 10^{-17}$ erg $\mathrm{s}^{-1}\mathrm{cm}^{-2}$. The 250 ks catalogs surrounds the CDFS-GOODS field, and covers more of the CDFS-SIMPLE(0.068 deg^2) and CDFS-SWIRE(0.12 deg^2) area to a depth of $f_{2-8\mathrm{keV}} \sim 6.7 \times 10^{-16}$ erg $\mathrm{s}^{-1}\mathrm{cm}^{-2}$.

The COSMOS field was observed with *XMM-Newton* (Hasinger et al. 2007) over the entire 2 deg^2 to a depth of $f_{2-10\mathrm{keV}} \sim 3 \times 10^{-15}$ erg $\mathrm{s}^{-1}\mathrm{cm}^{-2}$ and with much deeper *Chandra* data reaching $f_{2-10\mathrm{keV}} \sim 8 \times 10^{-16}$ erg $\mathrm{s}^{-1}\mathrm{cm}^{-2}$ for the central ~0.9 deg^2 (Elvis et al. 2009). There are a total of 2,769 X-ray sources in the area with both IR and X-ray coverage, and 2,075 X-ray sources with X-ray, PRIMUS, and IR coverage; 383 of these have robust PRIMUS redshifts and classifications.

We use the Puccetti et al. (2006) point source catalog in the ES1 field from a mosaic of four partially overlapping *XMM-Newton* pointings which reached a depth of $f_{2-10\mathrm{keV}} \sim 2 \times 10^{-15}$ erg s^{-1}cm^{-2} covering 0.52 deg^2 of the 0.9 deg^2 of PRIMUS and 2.16 deg^2 with IR coverage. Within the PRIMUS and IR areas (see Figure 3.1) there are 371 and 395 X-ray sources, respectively; there are 73 X-ray sources with secure PRIMUS redshifts.

The XMM X-ray data are from the Subaru/*XMM-Newton* Deep Survey (Ueda et al. 2008), which contains 7 deep *XMM-Newton* pointings, and the XMM-LSS X-ray survey (Pierre et al. 2007) which contains 45 pointings. The combined catalog contains X-ray sources to a depth of $f_{2-10\mathrm{keV}} \sim 2 \times 10^{-15}$ erg s^{-1}cm^{-2}, and covers 2.16 deg^2 of PRIMUS and 2.16 deg^2 of the IR area. There are 1840 and 4466 sources in the PRIMUS and IR overlap area, and 264 objects with secure redshifts.

3.4 AGN Sample Selection

In this section we define our samples of AGNs based on two IRAC color selection techniques and X-ray detections. No single selection technique can identify a complete parent sample of all AGNs; instead, we must study how the overlap between our different samples vary with the depths of the observations to determine selection biases and incompleteness effects. In Section 3.4.1, we define our Stern et al. IR-AGN sample using the MIR color selection criteria from Stern et al. (2005). We define our Donley et al. IR-AGN sample using the MIR color criteria from Donley et al. (2012) in Section 3.4.2. In Section 3.4.3, we discuss identification of IR-AGNs by fitting a power law to the MIR photometry (e.g., Alonso-Herrero et al. 2006; Polletta et al. 2006; Donley et al. 2007) and the reasons we choose not to use this technique in the remainder of this paper. We describe our X-ray-selected AGN sample in Section 3.4.4 and explain how we calculate completeness weights to account for the varying sensitivity of the X-ray observations.

3.4.1 Stern Color Selection

Objects that are detected in all four IRAC bands are defined to be Stern et al. selected IR-AGNs if they have IRAC colors such that they lie within the following region in color–color space:

$$([5.8] - [8.0]) > 0.6, \tag{3.1}$$

$$([3.6] - [4.5]) > 0.2 \cdot ([5.8] - [8.0]) + 0.18, \quad \text{and} \tag{3.2}$$

$$([3.6] - [4.5]) > 2.5 \cdot ([5.8] - [8.0]) - 3.5. \tag{3.3}$$

We apply this selection technique for samples reaching our three different "IR survey depths" defined in Section 3.3.1 above. We identify a total of 1137, 10,343, and 6687 Stern et al. IR-AGNs in our `GOODS`, `COSMOS`, and `SWIRE` depth surveys, respectively. We show the number density of Stern et al. selected objects with X-ray coverage in Figure 3.2.

3.4.2 Donley Color Selection

We also select IR-AGN samples using the IRAC color criteria presented by Donley et al. (2012). This color-selection technique was designed to limit contamination by star-forming galaxies, especially at high redshift, but still be both complete and reliable for the identification of luminous AGNs. We require that objects are detected in all four bands, and have IRAC colors such that they lie within the following region in IRAC color–color space:

$$x = \log_{10}\left(\frac{f_{5.8\mu\mathrm{m}}}{f_{3.6\mu\mathrm{m}}}\right), \quad y = \log_{10}\left(\frac{f_{8.0\mu\mathrm{m}}}{f_{4.5\mu\mathrm{m}}}\right) \tag{3.4}$$

$$x \geq 0.08 \quad \text{and} \quad y \geq 0.15 \tag{3.5}$$

$$y \geq (1.21 \times x) - 0.27 \tag{3.6}$$

$$y \leq (1.21 \times x) + 0.27 \tag{3.7}$$

$$f_{4.5\mu\mathrm{m}} > f_{3.6\mu\mathrm{m}} \quad \text{and} \quad f_{5.8\mu\mathrm{m}} > f_{4.5\mu\mathrm{m}}, \quad \text{and} \tag{3.8}$$

$$f_{8.0\mu\mathrm{m}} > f_{5.8\mu\mathrm{m}}. \tag{3.9}$$

Like in Section 3.4.1, we apply this selection method to our three different IR survey depth samples. We identify a total of 212, 2657, and 4151 Donley et al. IR-AGNs in our `GOODS`, `COSMOS`, and `SWIRE` depth surveys, respectively. The number density of Donley et al. selected objects with X-ray coverage is shown in Figure 3.2.

3.4.3 Power-law Selection

We also investigated the identification of IR-AGN samples using a power-law selection technique Alonso-Herrero et al. (2006); Polletta et al. (2006); Donley et al. (2007). This technique identifies IR-AGNs by fitting a power-law function to the IRAC fluxes, in contrast to the color selection techniques such as the Stern et al. and Donley et al. methods described above. Sources dominated by a power-law IR-AGN have a negative slope $\alpha < -0.5$ such that their νF_ν flux increases with wavelength (Alonso-Herrero et al. 2006). Following Donley et al. (2007), we identify sources with four detected IRAC flux measurements as power-law AGNs when they are well fit by a power law of slope $\alpha \leq -0.5$, where $f_\nu \propto \nu^\alpha$. We deem the power-law fit as good if $P_\chi > 0.1$ (probability that the fit would have a χ^2 greater than the found χ^2). We calculate the P_χ and fit parameters using the `linfit` procedure in IDL.

As in Sections 3.4.1 and 3.4.2, we apply the power-law selection technique to our `SWIRE`, `COSMOS`, and `GOODS` IR survey depths. To properly simulate a shallow `SWIRE`-like survey in our `COSMOS` depth fields (COSMOS and CDFS-SIMPLE), we apply not only the 5.8 μm flux limits but also scale up the errors in the flux measurements to accurately represent the characteristics of the shallower data. Specifically, we scale the errors in the fluxes by the square root of the differences in the exposure times for the `COSMOS` and `SWIRE` depth data. We verify that the median of our scaled errors matches the median error in the `SWIRE` depth fields.

In Figure 3.2, we show the number density of IR-AGNs identified using the power-law selection technique as a function of 5.8 μm flux. Unlike the Stern et al. and Donley et al. samples, the number density of the power-law sample is not a smooth function of IR flux. Donley et al. (2012) show that this is mainly due to the flux errors associated with each survey. While we have ensured similar data reduction and consistent error estimates for the different fields and samples, the uncertainty in a flux measurement will depend on the depth of the data. At a given flux, deeper IR surveys find fewer power-law AGNs as the smaller flux errors can result in larger χ^2 values for the power-law fit. Thus, a source identified as a power-law AGN in a shallow survey may not be identified in a deeper survey as the more precise photometry are found to deviate from a power-law. Additionally the power-law sample is a very small subsample of the total X-ray population, a major problem in selecting a large statistical population of AGNs.

Donley et al. (2012) suggest adopting a 10% uncertainty floor on all flux measurements. While this increases the number density of power-law-selected AGNs in our samples to that of Donley et al. (2012), the number density of these sources does not monotonically increase with increasing survey depth, due to the strong dependence of the power-law technique on the estimated flux uncertainty. The power-law technique appears to be a reliable method of selecting AGNs (in that a very high fraction have X-ray counterparts), however it selects a very small subsample of the full AGN population identified either with X-ray emission or with the Stern et al. or Donley et al. AGN selection techniques using SExtractor errors. Given the small sample size and the complex dependence on the depth of the IR data, we choose not to consider the power-law IR-AGN selection technique any further in the analysis of this paper.

3.4.4 X-Ray Selection

We define samples of X-ray-selected AGNs based on detection in the hard (2–10 keV) energy band in our compiled catalogs (see Section 3.3.3). A hard-band-selected sample includes both X-ray unabsorbed and moderately absorbed AGNs, but misses Compton-thick sources. We do not include a soft-band-selected sample even though it probes to fainter X-ray fluxes (providing a larger sample) because it is more biased toward the detection of unabsorbed sources (with equivalent hydrogen column densities $N_{\mathrm{H}} < 10^{22}$ cm^{-2}).

Selecting in a single band also ensures we can accurately track (and correct for) the effects of variation in the X-ray sensitivity in our observations. Within an individual *Chandra* or *XMM-Newton* pointing, variations due to the vignetting and point-spread function of the telescope lead to variations in the X-ray flux limit that is reached across the field of view. Furthermore, the exposure times between different pointings can vary within an X-ray survey, leading to substantial variations in sensitivity. The minor differences in the X-ray spectral shapes at $2-10$ keV have

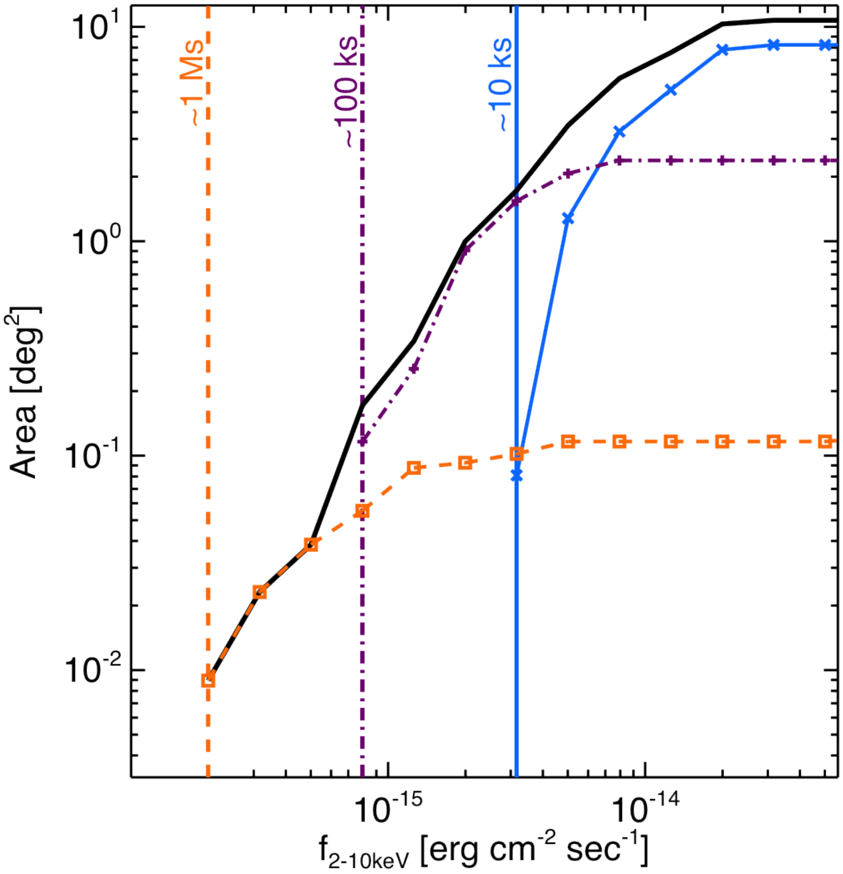

Figure 3.3: **X-ray area sensitivity curves** — X-ray area sensitivity curves that track the area which is sensitive for a given X-ray flux. We show the individual X-ray area sensitivity curves for the ∼1 Ms (orange squares), ∼100 ks (purple pluses), and ∼10 ks (light blue crosses) samples. The vertical colored lines indicate our chosen X-ray flux limit for each survey depth, which is set at the flux which we recover 10% or more of the expected sources (see Table 3.1). The solid black line shows the `All` sample, which combines all of our X-ray fields that probe above the flux limit for each field.

a minimal effect on the sensitivity and the differences are mainly due to the X-ray telescope. Furthermore, at the X-ray fluxes we are probing ($f_{2-10\mathrm{keV}} \sim \gtrsim \times 10^{-16}$ erg s^{-1}cm^{-2}), the X-ray point source number counts are dominated by AGNs (Georgakakis et al. 2008; Lehmer et al. 2012). Thus, by comparing observed point source counts as a function of flux to the expected number based on the intrinsic $\log N - \log S$ relation, we can estimate the fraction of our survey area that is sensitive to X-ray AGNs of a given X-ray flux.

In Figure 3.3, we show X-ray area curves (the area of a survey that is sensitive to sources above a given X-ray flux) for our various fields. We calculate these area curves using the ratio of the number of hard X-ray-detected sources in the parent X-ray source catalog and the predicted number of sources based on the X-ray $\log N - \log S$ relation of Georgakakis et al. (2008), using bins of 0.2 dex width. We fix the area curve at the total area coverage above the lowest flux where $\geq$90% of the predicted sources are detected to remove the effects of low source numbers at bright fluxes. To reduce the noise due to small numbers of sources at the faintest X-ray fluxes, we set a minimum flux threshold in each X-ray survey at the point where at least 10% of the expected number of sources are detected. These flux limits are shown in Figure 3.3 and given in Table 3.1.

Similar to our IR observations, we group our X-ray fields into three different "X-ray survey depths."

1. ~1 Ms, which includes our deepest, 2 Ms X-ray data in the CDFS field.
2. ~100 ks, including the E-CDFS, COSMOS, the deeper regions of the XMM field.
3. ~10 ks, including ES1 field and the remainders of the COSMOS and XMM fields.

We give nominal hard-band flux limits for each field and survey depth in Table 3.1. While there are slight differences in the exact X-ray flux limit for each individual survey we show the surveys at one of the three "X-ray survey depths" for simplicity. However, we note that this flux limit is only reached over a small fraction ($> 10\%$) of the total area covered by our fields with a given "X-ray survey depth".

Finally, we calculate an "X-ray weight" for each hard band X-ray detected source based on the ratio of the total area coverage to the value of the area curve at the flux of the source. We use these X-ray weights to correct observed number densities of X-ray sources to the intrinsic number density. A faint X-ray source will be given a large weight to account for the small area that is sensitive to faint fluxes. For the total X-ray sample, the X-ray weights ensure we recover the intrinsic X-ray $\log N - \log S$ as measured by Georgakakis et al. (2008) that was originally used to determine the area curves. However, the X-ray weights are also crucial when comparing between X-ray and IR-AGN samples (see Section 3.5).

In Section 3.7, we further limit our X-ray-detected sample to objects with an observed $L_{\mathrm{X}} > 10^{42}$ erg s^{-1}, calculated from the hard-band flux assuming a photon index of $\Gamma = 1.9$. This conservative limit ensures our sample contains objects where the X-ray flux is dominated by emission due to an AGN, rather than star formation processes in the galaxy.

When comparing the X-ray AGN sample with the IRAC AGN samples we require that both samples lie within the overlapping window functions. Likewise for Section 3.7 we require that the objects fall within the region with IRAC, X-ray, and PRIMUS coverage. For these studies, we recompute our X-ray weights using the overlapping areas only.

3.5 Sample Comparisons

In this section, we examine how the total numbers of sources and the overlap between our IR-AGN and X-ray AGN samples depend on the depths of the X-ray and IRAC data. In Section 3.5.1, we compare the IR-AGN and X-ray AGN selection techniques with respect to the bivariate IRAC and X-ray flux space. In Section 3.5.2, we determine the surface number densities of sources selected by the different techniques as a function of both IRAC and X-ray flux. In Section 3.5.3, we investigate how the overlap between the samples depends on the IR and X-ray survey depths.

3.5.1 X-Ray and IR Flux Comparison

Our first step is to examine the distribution of sources in the bivariate space of observed IRAC 5.8 μmflux and hard-band X-ray flux. In the center panel of Figure 3.4 we show contours (black) that trace the distribution of all sources (across our differing survey depths) with both X-ray and IRAC detections. The contours contain 30%, 50%, and 80% of these sources; the remaining 20% of sources outside these contours are shown by black squares. We also show the distribution of sources that are also identified as IR-AGNs using the Stern et al. (red) and Donley et al. (blue) selection techniques. Approximate IRAC and X-ray flux limits for the different survey depths are shown by the orange vertical and horizontal lines. We find that the majority of objects tend to be infrared bright when they are likewise X-ray bright. However, there is a population of objects that are infrared bright, but are X-ray faint, but very few that are X-ray bright but infrared faint. This is expected as it suggests that it is easier to have a Compton-thick source that obscures the X-rays, but much harder to obscure the infrared photons. Many of these infrared-bright, X-ray faint sources are not selected by either the Stern et al. or Donley et al. IR-AGN selection techniques and thus may not be AGNs or have dominate AGN components.

The right panel of Figure 3.4 shows the number density of all IRAC- and X-ray-detected objects (black), Stern et al. IR-AGNs (red), and Donley et al. IR-AGNs (blue) as a function of their observed hard-band X-ray flux. Likewise the bottom panel shows the number density of the same samples as a function of their IRAC 5.8 μmflux. The number density plots in each of the subpanels are limited to include selected sources above the flux limit in each field and normalized

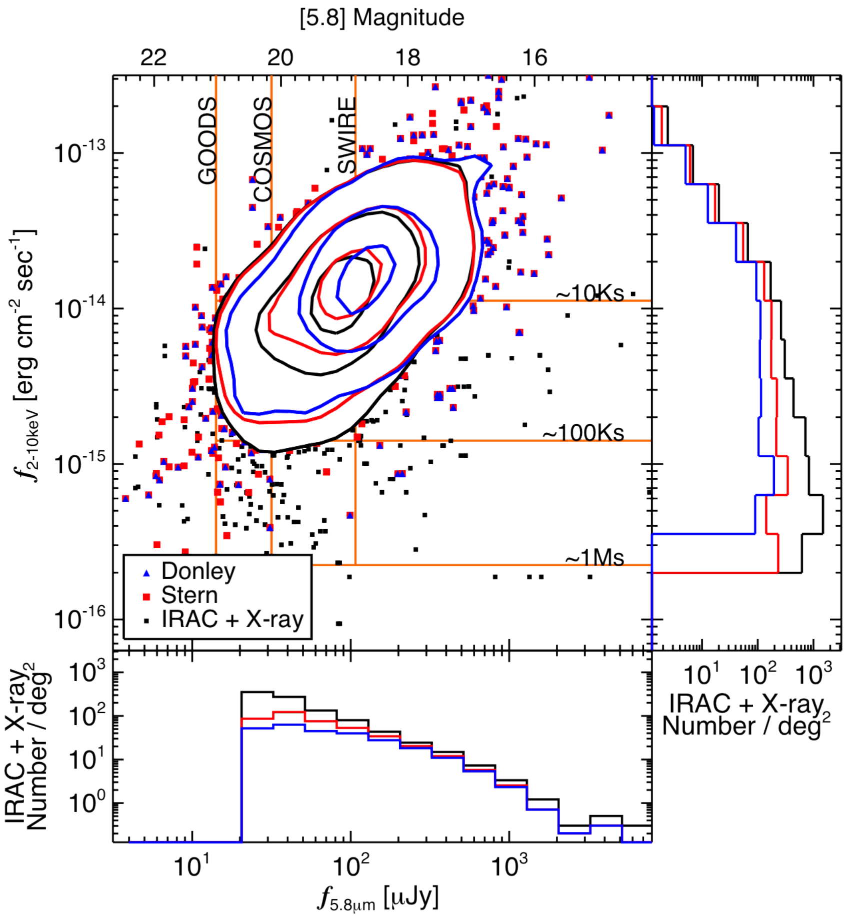

Figure 3.4: **Detected mid-IR flux versus X-ray flux diagram** — Observed IRAC 5.8 μm and hard-band X-ray flux number-density distributions. In the center panel, we show the sample of objects detected with four bands of IRAC and a hard-band X-ray detection. The Stern et al. IR-AGN-selected sample is shown with red squares, and the Donley et al. IR-AGN-selected sample is shown with blue triangles. The approximate `SWIRE`, `COSMOS`, and `GOODS` depth IR surveys limits are shown with vertical orange lines, and approximate X-ray survey depths are shown with horizontal orange lines. The right-side panel shows the total number of IRAC and X-ray detected of objects per logarithmic X-ray flux bin per area sensitive to that flux for the total (black), Stern et al. IR-AGN selected, (red) and Donley et al. IR-AGN selected (blue). The lower panel shows the total number of X-ray- and IR-AGN-detected objects per logarithmic IRAC flux bin per area sensitive to that flux for the respective samples. We include the X-ray completeness correction weights which corrects for the variation in X-ray flux limit in both side panels.

by the area that is sensitive to that flux. The number densities of either Stern et al. or Donley et al. IR-AGN sample do not increase toward fainter fluxes as steeply as the total number density of objects detected.

3.5.2 X-Ray and IR-AGN Surface Densities

Our next goal is to determine how the number of sources identified as AGNs using a given selection technique varies as a function of IR flux. In the top panels of Figure 3.5, the solid black line shows the surface number density (number per square degree per logarithmic flux interval) of sources as a function of IRAC 5.8 μmflux for the Stern et al. (left) and Donley et al. (right) IR-AGN samples. At the brightest fluxes ($f_{5.8\mu m} > 100\ \mu Jy$), we combine all of the different fields to estimate the surface number density. At fainter fluxes we only use the fields with sufficient IR depth (see Table 3.1 for flux limits). For both the Stern et al. and Donley et al. IR-AGN samples the number densities increase rapidly with decreasing flux with an approximately power-law form, although the slope of the power-law may flatten below $f_{5.8\mu m} \sim 100\ \mu Jy$ for the Donley et al. sample. The dashed lines show the surface number densities of the Stern et al. or Donley et al. IR-AGN sample that is also detected in our X-ray data for our three different X-ray survey depths: ∼10 ks (red), ∼100 ks (green), and ∼1 Ms (blue). These surface number densities are corrected for the variation in X-ray flux limit over the field (the X-ray incompleteness) by applying the weights described in Section 3.4.4.

The bottom panels show the fraction of the IRAC samples that are X-ray detected for each of the X-ray survey depths. These fractions vary significantly as a function of both IRAC flux and the depth of the X-ray data. At bright IR fluxes ($f_{5.8\mu m} > 100\ \mu Jy$) we find $\gtrsim$70% of the IR-AGN samples are detected in X-ray data of ∼100 ks–1000 ks depth, whereas with the shallow X-ray data (∼10 ks) this fraction is closer to 50%. At fainter IR fluxes the X-ray fraction decreases, although the fall off is highly dependent on the depth of the X-ray data. Figure 3.7 (left) directly compares the X-ray fractions of the Stern et al. and Donley et al. IR-AGN samples as a function of IR flux combining the different X-ray survey depths. At bright IR fluxes ∼60% of both IR-AGN samples are X-ray detected; at fainter IR fluxes a slightly higher fraction of the Donley et al. sources are identified in the X-ray data, although we note that the Donley et al. selection identifies a smaller sample of AGNs.

Our next step is to determine how the number of identified IR-AGN and X-ray AGN sources depends on the X-ray flux. In the top panels of Figure 3.6, we show the surface number density of X-ray-selected sources as a function of the X-ray flux. We only include fields that probe to sufficient X-ray depth (see Table 3.1 and Figure 3.2) in our estimates of the surface number density at any given X-ray flux. We apply our X-ray weights to account for the variation in X-ray depth within a field (see Section 3.4.4); only a limited fraction of the combined X-ray and IRAC area may be sensitive to a given X-ray flux, even above our nominal X-ray flux limits. The X-ray

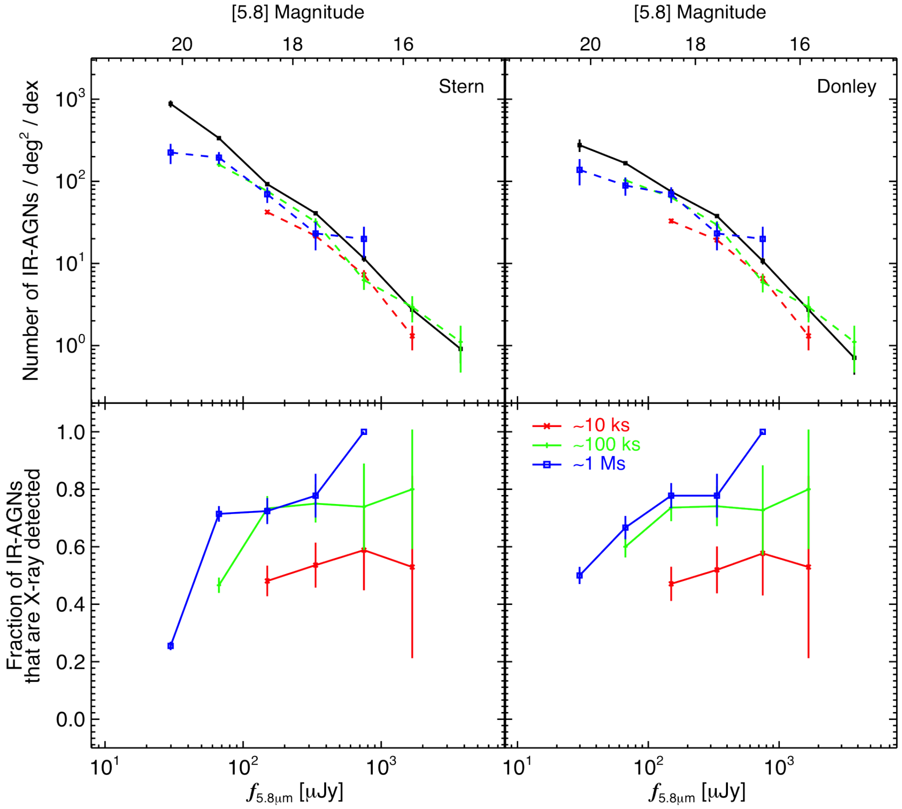

Figure 3.5: **IR-AGN selection X-ray depth detection fraction** — IR-AGN-selected number density and fractions of combined IR-AGN samples as a function of IRAC $f_{5.8\ \mu m}$ flux for the Stern et al. (left column) and Donley et al. (right column) IR-AGN selection techniques. The top panels show the number density (black solid line) of the Stern et al. (left) and Donley et al. (right) IR-AGN selection method for the entire sample. The dashed lines show the number density for individual X-ray comparison depth samples: shallow ∼10 ks (red), medium ∼100 ks (green), and deep ∼1Ms (blue) samples are shown with Poisson error bars. For objects with measured X-ray fluxes we use the X-ray sensitive area derived from the X-ray completeness weights rather than the intersected IR and X-ray area. The total sample (solid black line) may dip below an individual X-ray survey depth sample due to the X-ray completeness corrections and small number statistics, but the black line is consistent with the individual X-ray survey depth lines. The bottom panels show the X-ray-detected fraction of IR color-selected AGNs for each of the different X-ray survey depth bins.

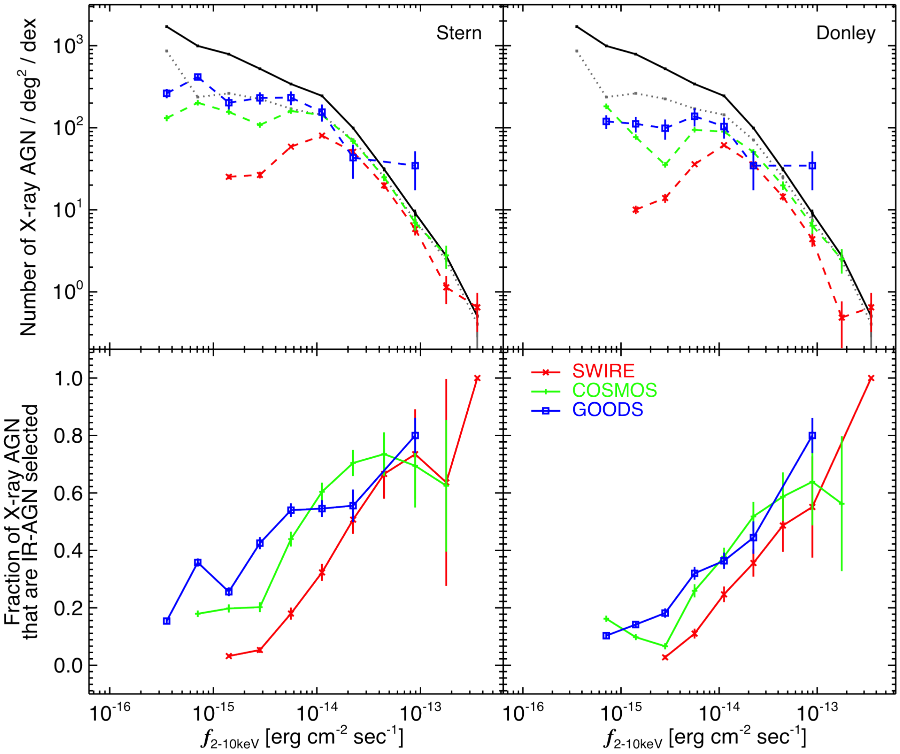

Figure 3.6: **X-ray AGN IRAC depth detection fraction** — Number density and fraction of the X-ray-detected sample that is selected using an IR-AGN selection technique. The top panels show the number density of all X-ray-detected objects (black solid line) and X-ray with IRAC detected objects(gray dotted lines) as a function of hard-band X-ray. The dashed lines show the number density of the Stern et al. (left) and Donley et al. (right) IR-AGN samples for the shallow (`SWIRE`), medium (`COSMOS`), and deep (`GOODS`) depth IR surveys. Each of these dashed lines can be above the total number density of IR-AGNs and X-ray AGNs due to individual sample areas and small numbers at the lowest bins. We remove bins with objects less than four objects, which happen at the largest X-ray fluxes. The bottom panels show the IR-AGN fraction of X-ray AGN sample of the total number density for each individual IRAC depth survey. Objects with measured X-ray fluxes have been normalized by the sensitive area for that flux measurement rather than the intersected IR and X-ray area.

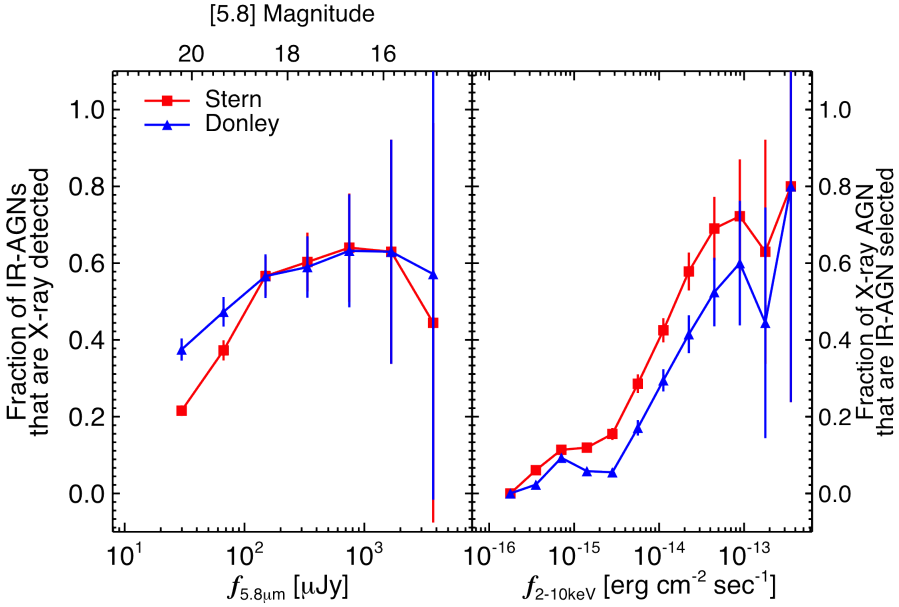

Figure 3.7: **Stern et al. and Donley et al. IR-AGN comparison** — X-ray-detected fraction of IR-AGNs (left panel) and the IR-AGN-selected fraction of the X-ray AGN sample (right panel) for all field depths. The Stern et al. (solid red squares) and Donley et al. (solid blue triangles) IR-AGN-selected fraction are for all samples which contains objects above the limits for that sample. Objects with measured X-ray fluxes have been normalized by the sensitive area for that flux measurement rather than the intersected IR and X-ray area.

surface number densities follow the double power-law distributions presented by Georgakakis et al. (2008). The dashed lines show the surface number densities of X-ray sources that also satisfy the Stern et al. (left column) and Donley et al. (right column) IR-AGN selection criteria in fields reaching three different IR survey depths: `SWIRE` (red), `COSMOS` (green), and `GOODS` (blue). These number densities are also corrected for variation in X-ray sensitivity within a field. The bottom panels show the fraction of the X-ray sample that satisfy the IR selection criteria for the three IR survey depths for each of the IR-AGN samples. At bright X-ray fluxes ($f_{\rm X}$~10^{-14} erg $\rm s^{-1} cm^{-2}$), a fairly high fraction of the X-ray sources (~60%) are identified as AGNs using either the Stern et al. or Donley et al. selection criteria, although substantially increasing the depth of the IR data does not appear to increase this fraction. At fainter X-ray fluxes the fraction of X-ray sources identified with the IR criteria reduces. Increasing the depth of the IR data from `SWIRE` to `COSMOS` recovers a higher fraction, but further increasing from `COSMOS` to `GOODS` depths does not appear to significantly increase the IR fraction at a given X-ray flux, especially for the Donley et al. selection criteria. The more restrictive Donley et al. selection criteria generally identifies a lower fraction of the X-ray sources as AGNs at any given X-ray flux compared to the Stern et al. selection (see Figure 3.7 (right panel) for a direct comparison of the fractions with `COSMOS` X-ray and IRAC depth data.

With either of the IR-AGN selection techniques, the total number densities and the overlap between the IR-AGN and X-ray AGN samples depends on the survey depth. In the left panel of Figure 3.7, we show the X-ray-detected fraction of the Stern et al. (red) and Donley et al. (blue) IR-AGN samples as a function of the IRAC flux. For sources fainter than $f_{5.8\mu m} \sim 100\ \mu Jy$ IRAC flux, the Stern et al. fraction is smaller than the Donley et al. fraction, and very similar for sources above $f_{5.8\mu m} \sim 100\ \mu Jy$. Below $f_{5.8\mu m} \sim 100\ \mu Jy$, the Stern et al. selection identifies a larger number of objects as AGNs than the Donley et al. selection (see Figure 3.8), which drives this fraction down. In the right panel of Figure 3.7, we show the Stern et al. (red) and Donley et al. (blue) IR-AGN fraction of the X-ray-detected sample. The Donley et al. IR-AGN selection identifies a lower fraction of X-ray-detected objects for most of X-ray fluxes compared to the Stern et al. IR-AGN selection.

3.5.3 Overlap of X-ray and IR-AGN samples

In this section, we examine in more detail the extent of the overlap between the IR-AGN and X-ray AGN samples and how this depends on both the IR and X-ray survey depth. In Figure 3.8 (left panels), we show the fraction of the IR-AGN samples that are X-ray detected as a function of both the X-ray and IRAC flux limits for the different survey depths. The top-left panel shows the fraction of Stern et al. IR-AGNs that are X-ray detected; the bottom-left panel shows the fraction of Donley et al. IR-AGNs that are X-ray detected. These fractions vary smoothly over the range of IR and X-ray flux limits between 47% and 90% for both Stern et al. and Donley

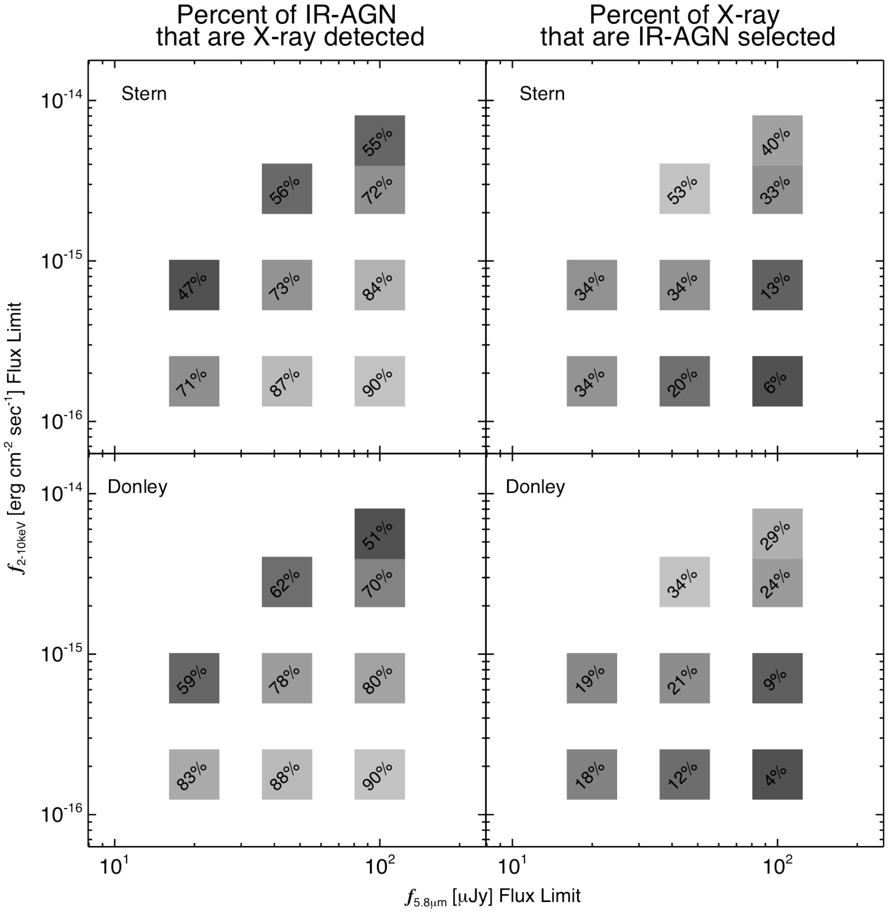

Figure 3.8: **Bivariate X-ray AGN and IR-AGN detection fraction diagram** — X-ray-detected fraction of IR-AGN selection techniques (left column) and the color-selected fraction of X-ray AGN detections (right column) for each IR-AGN sample. The fractions are shown at the IRAC 5.8 μm and X-ray flux limits with background points shown with darker gray background for lower fractions, and lighter squares for higher fractions. The upper panels show the Stern et al. IR-AGN selected fractions, whereas the lower panels show the Donley et al. IR-AGN selected fractions. We include in Tables 3.4 and 3.5 the fractions for samples with X-ray weights applied, while Tables 3.6 and 3.7 list the raw fractions, where X-ray weights have not been applied.

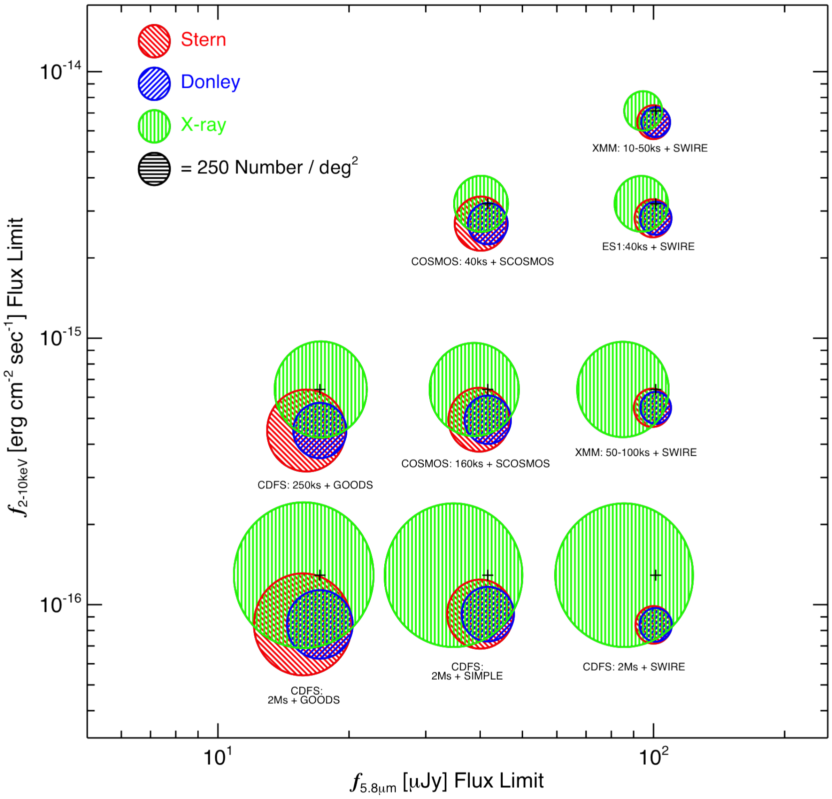

Figure 3.9: **X-ray AGN, and IR-AGN Venn diagrams** — Venn diagrams of the number density and overlap between the Stern et al. (red), Donley et al. (blue), and hard-band X-ray (green) selected AGN samples. The area and overlap of each circle is proportional to the surface number density of the sample and respective sample overlap. The different samples are located at the X-ray and IRAC flux limits shown as a black cross. Objects with X-ray detections have been normalized by the sensitive area for that flux, and included if they fall within the X-ray and IRAC limits for that sample. The X-ray and IRAC limit locations are plotted as a black plus at the center of the X-ray circle and Donley et al. selection circles, respectively. See Table 3.3 for individual fraction values.

et al. IR-AGN samples. For comparable depth surveys in IR and X-ray (roughly the diagonal through these panels) ∼70%– 80% of the IR-AGNs are detected at X-ray wavelengths. Increasing the depth of the IR data (moving to the left) reduces the fraction with X-ray detections; increasing the depth of the X-ray data (moving down) increases the fraction with X-ray detections. For our shallowest IR data, we find a very high fraction (90%) of the IR-AGNs are detected using our deepest X-ray data. Generally, the X-ray-detected fraction of the Donley et al. IR-AGN samples is higher than for the Stern et al. IR-AGN samples, particularly for deeper surveys.

In the two right-hand panels of Figure 3.8, we show the fraction of the X-ray AGN samples that are also identified as Stern et al. IR-AGNs (top-right panel) or Donley et al. IR-AGNs (bottom-right panel). For both selection techniques, the fraction varies smoothly between ∼4% - 53%, being smallest for shallow IR and deep X-ray samples (bottom right) and largest for deep IR and shallow X-ray samples (top left). The Donley et al. IR-AGN selection technique identifies a lower fraction of the X-ray sample than the Stern et al. IR-AGN selection technique. Comparing with Figure 3.6, we find that these low fractions are due to the large numbers of faint X-ray AGNs that are not selected by either IR-AGN technique, even with very deep IR data.

In Figure 3.9, we use Venn diagrams to examine the surface densities and overlap of the samples selected using our three AGN selection techniques as a function of both X-ray and IR survey depth. The number density of the different subsamples are represented by circles located at the IR and X-ray flux limits for the different surveys. The size of the circles are proportional to the surface number densities; the overlap between the samples are shown in Venn diagram form. The black cross indicates the X-ray and IR flux limits corresponding to the surveys used for each individual Venn diagram. The number density of X-ray AGNs (green circles) increases rapidly as the X-ray depth increases (moving down in Figure 3.9). Likewise, for deeper IRAC surveys we find a larger number density of both Stern et al. and Donley et al. IR-AGN samples. The overlap between the AGN samples varies substantially depending on the IR and X-ray survey depth. X-ray selection identifies a large population of sources at all survey depths that are not identified with the IR-AGN selection techniques, even with extremely deep IR data. The Donley et al. IR-AGN selection technique generally identifies a subset of the Stern et al. IR-AGN sample for all depths. At our shallowest IR survey depth (`SWIRE`: right-hand side of Figure 3.9), the IR-AGN samples overlap almost completely, while in deeper IR surveys an additional population is identified using the Stern et al. selection criteria. At the shallowest IR survey depth, a high fraction of the IR-AGNs are X-ray detected: up to 90% with our deepest X-ray data. Deeper IR data identifies additional IR-AGNs, including populations that are not identified at X-ray wavelengths.

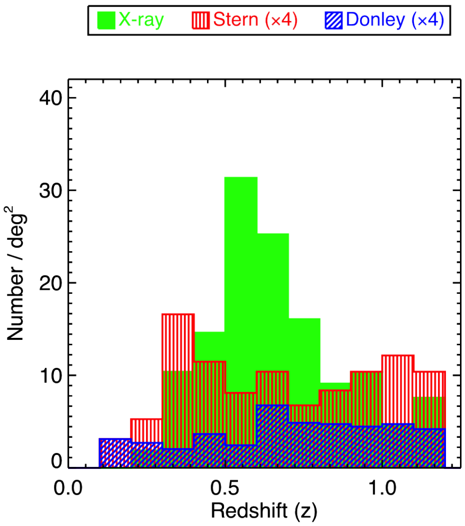

Figure 3.10: **Redshift number-density distribution** — Redshift number-density distributions for the X-ray (green solid), Stern et al. (red hatched) and Donley et al. (blue hatched) selected samples for all objects with secure PRIMUS redshifts in all fields. The Stern et al. and Donley et al. IR-AGN distributions have been scaled up by a factor of four to easily compare their distributions to the X-ray sample.

3.6 Contamination of IR-AGN selection

In this section, we investigate whether either of the IR-AGN samples are subject to contamination from non-AGN galaxies. In Section 3.6.1, we examine the redshift distributions of the IR-AGN and X-ray AGN samples (using spectroscopic redshifts from PRIMUS at $z < 1.2$) and find clear evidence for contamination of the Stern et al. IR-AGN sample at specific redshifts. In Section 3.6.2, we use MIR templates to characterize the contamination from non-AGN host galaxies that fall into the Stern et al. IR-AGN selection criteria compared to the Donley et al. IR-AGN selection criteria and X-ray detected AGNs at $z < 1.2$. Finally in Section 3.6.3 we extend our template-based analysis to higher redshifts (z $\sim$ 2–3), outside the range covered by the PRIMUS data, to investigate the contamination of the IR-AGN samples by star-forming galaxies at these redshifts. In this section, we focus on the templates and possible galaxy contamination in the Stern et al. and Donley et al. IR-AGN samples and leave discussion of contamination as a function of survey depth to Section 3.8.

3.6.1 Investigating Contamination with Redshift

In this section we compare the redshift distributions of our three AGN samples to investigate whether the selection techniques identifying the same underlying AGN population. In Figure 3.10, we show the number per square degree of Stern et al. IR-AGN (red hatched),

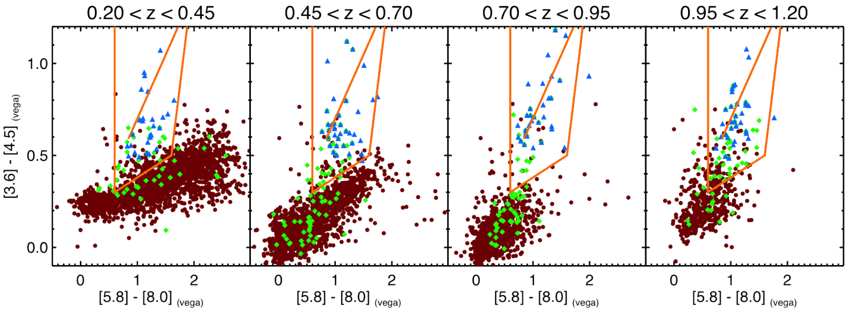

Figure 3.11: **IRAC color-color space diagram** — IRAC color-color space for sources with PRIMUS redshifts in four redshift bins between $0.2 < z < 1.2$. In each panel, the Stern et al. wedge is outlined in orange with the power-law $-0.5 < \alpha < -3$ line also shown in orange within the wedge. The Donley et al. IR-AGN sample (blue triangles) and X-ray AGN sample (green diamonds) are shown above all other objects (dark red circles) in each redshift bin. We find that the bimodal redshift peaks of the Stern et al. IR-AGN sample are due to a large number of objects entering the bottom of the wedge at both $z \sim 0.3$ and $z \sim 1.1$.

Donley et al. IR-AGN (blue hatched) and X-ray AGN (green solid) selected objects with PRIMUS redshifts. We restrict our samples to objects with secure PRIMUS redshifts between $0.2 < z < 1.2$, where PRIMUS provides reliable redshifts for sources where the optical light is dominated by either the AGN or galaxy light and there is enough volume to construct a statistical sample. For the X-ray detected sample we ensure that the sample is not contaminated by X-ray detected star-forming galaxies by restricting to sources with $L_{\mathrm{X}} > 10^{42}$ erg s^{-1}. We apply the weights calculated in Section 3.4.4 to correct for the varying depth of the X-ray data but we do not correct for the fraction without PRIMUS redshifts. Requiring a redshift reduces our AGN sample sizes and imposes an apparent limiting optical magnitude brighter than $i \sim 23$. The fraction of sources in our AGN samples that are brighter than this optical limit varies from ∼30% to ∼70%, depending on the depth of the corresponding IR or X-ray data. Of the sources targeted by PRIMUS, the fraction that have a high-quality redshift varies from ∼75% to ∼95%, depending on the depth of the IR or X-ray data, where the fraction is higher for shallower fields. This is comparable to the overall PRIMUS redshift success rate. We find comparably low catastrophic redshift outlier rates for the AGN samples compared to the full PRIMUS galaxy sample. The Stern et al. and Donley et al. distributions have been scaled up by a factor of four to show their relative redshift distributions compared to the completeness-corrected X-ray sample.

The Donley et al. IR-AGN sample and X-ray AGN sample number-density distributions peak around $z \sim 0.6$, which matches the peak of the entire PRIMUS galaxy sample, although the Donley et al. distribution does not falloff as quickly for higher redshifts compared to the X-ray AGN sample. We find that the redshift distribution of the Stern et al. IR-AGN sample has an unexpected shape with two peaks, at $z \sim 0.3$ and $z \sim 1.1$, which differs significantly from that of the Donley et al. IR-AGN and X-ray AGN samples or the overall PRIMUS galaxy sample. To

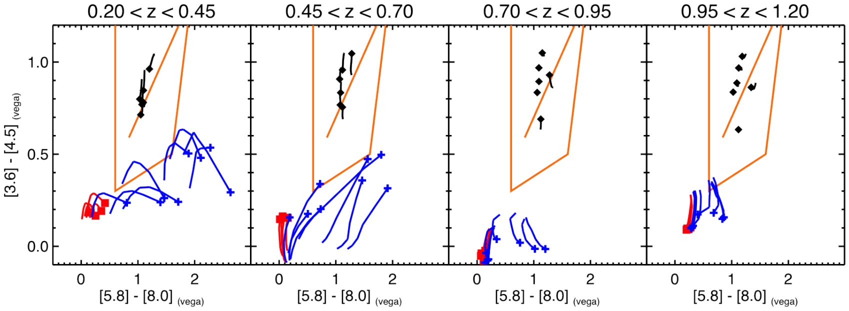

Figure 3.12: **IRAC color-color template diagram** — IRAC color–color spaces for galaxies and AGN templates in four redshift bins between $0.2 < z < 1.20$ to match the PRIMUS redshift sample. In each panel we show the redshifted colors of templates in that redshift bin (lines). The Stern et al. wedge is outlined in orange with the power-law $-0.5 < \alpha < -3.0$ line also shown in orange within the wedge. Quiescent galaxies (red square), star-forming galaxies (blue cross) and QSO/AGN (black diamond) redshift template tracks begin in each redshift bin at the filled symbol, and continue for the extent of that redshift bin. Generally, we find the Donley et al. and Stern et al. IR-AGN techniques select QSO/AGN templates. The Stern et al. IR-AGN technique additionally selects star-forming templates at both $z \sim 0.3$ and $z \sim 1.1$. Quiescent galaxy templates are not selected by either at these redshifts.

investigate this unusual distribution, in Figure 3.11 we present IRAC color–color plots for the entire sample with IRAC detections in all four bands separated into four distinct redshift ranges. We overplot the Donley et al. IR-AGN (blue triangle) and X-ray AGN (green diamond) selected samples. Generally, the Donley et al. IR-AGN sample is a subset of the Stern et al. IR-AGN sample, whereas the X-ray AGN sample includes objects both inside and outside of the Stern et al. color wedge. The Stern et al. IR-AGN sample includes many other objects that are neither X-ray detected nor Donley et al. selected. We see that the majority of these objects enter in at low redshifts ($z \sim 0.3$, left-most panel) and high redshifts ($z \sim 1.0$, right-most panel). These objects mostly enter into the wedge at low ([3.6]–[4.5]) color and appear to be consistent with scatter from the larger galaxy population (the dark red points in Figure 3.11). We thus conclude that the Stern et al. IR-AGN sample suffers from significant contamination by normal, non-AGN galaxies at redshifts $z \sim 0.3$ and $z \sim 1.1$, resulting in the bimodal peaks in the redshift distribution seen in Figure 3.10.

3.6.2 Comparison with IR SED Templates

In this section, we investigate the trends in the previous section using empirical galaxy and AGN SED templates. Following Donley et al. (2008, 2012), we redshift the Polletta et al. (2008) IR templates and examine the changes to the observed IRAC colors. The Polletta et al. (2008) IR template set consists of four quiescent galaxy templates, eight star-forming galaxy templates, and six AGN templates, based on the observed SED of a representative sample of local galaxies and AGNs. We convolve the redshifted SED with each IRAC filter to predict the observed IRAC colors. In Figure 3.12, we show the predicted colors in four redshift bins for all the star-forming galaxy (blue dots), quiescent galaxy (red squares) and AGN (black crosses) templates. The lines track the change in color within the redshift bin for a given template.

Generally, star-forming templates change the most in this color–color space, due to the polycyclic aromatic hydrocarbon (PAH) features in the SED. They start off with a very red ([5.8]–[8.0]) color that moves blue-ward due to the 8.0 μm PAH feature redshifting out of the 8.0 μm IRAC filter. The vertical ([3.6]–[4.5]) motion of star-forming templates is dominated by the 3.3 μm PAH feature moving from the 3.6 μm to the 4.5 μm IRAC filter[3]. Together, both of these features can move the star-forming templates into the Stern et al. wedge at both low redshift ($z \sim 0.3$) and high redshift ($z \sim 1.1$). The star-forming templates that come into the Stern et al. wedge are not selected by the Donley et al. IR-AGN criteria.

For quiescent templates (red squares), we find a much simpler motion through the IRAC color–color space. Comprised of older stars, these templates are generally dominated by the Rayleigh–Jeans tail with an IRAC power-law slope of $\alpha \sim 2$ located close to the origin. The SEDs are generally featureless, and the motion is dominated by the 1.6 μm stellar bump which redshifts into the 3.6 μm IRAC filter. These templates are generally excluded from either the Donley et al. or Stern et al. IR-AGN samples at these redshifts.

The predicted AGN template colors also show very little motion in this space. Their featureless, red power-law ($\alpha \sim -0.5 - -3$) SEDs tend to lie close to the power-law line. Both Donley et al. and Stern et al. IR-AGN selection techniques pick up these AGN/quasar (QSO) templates easily at $z < 1.2$.

The behaviors of the star-forming, quiescent, and AGN templates are consistent with the trends seen in the data in the previous section and explains the peaks in the Stern et al. IR-AGN redshift distribution. The Stern et al. IR-AGN sample is contaminated by star-forming galaxies at both low ($z \sim 0.3$) and high ($z \sim 1.1$) redshifts. The Donley et al. IR-AGN selection technique identifies AGN dominated templates at $z < 1.2$.

The addition of a small AGN contribution(5%–10%) may move star-forming and quiescent SEDs into the Stern et al. wedge, but such sources are not selected by the Donley et al. criteria (e.g., Donley et al. 2012). Thus the Stern et al. selection may identify a more complete sample of AGNs but it is hampered by a larger contamination by star-forming galaxies at particular redshifts.

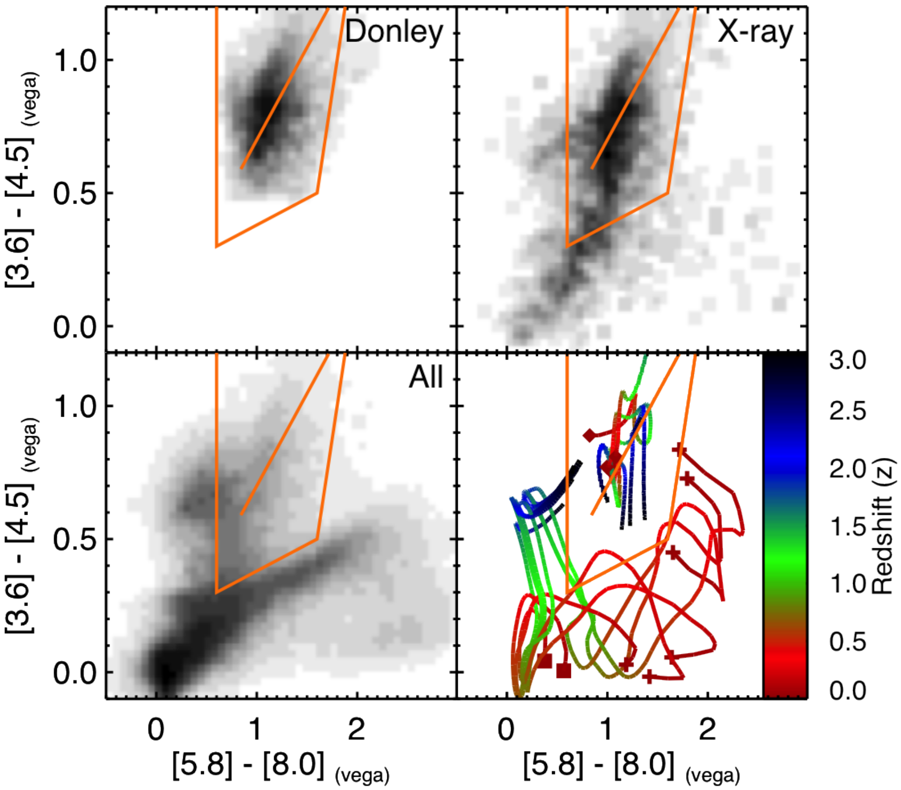

Figure 3.13: **Donley et al. and Stern et al. selected IRAC color-color comparison** — Comparison of the Donley et al. IR-AGN and X-ray AGN samples to the entire IR-AGN sample and the IR SED templates in IRAC color–color space. In the Donley et al. (top left), X-ray (top right), and `All` (bottom left) panels, we indicate the density of IRAC-detected objects by the grayscale color. We use a linear grayscale where black corresponds to the maximum density of objects in a given panel. The Stern et al. wedge is outlined in orange with the power-law $-0.5 < \alpha < -3.0$ line also shown in orange within the wedge. In the bottom-right panel, we show the IRAC colors of the templates from $z = 0$ to $z = 3$ (indicated by the color coding) for star-forming galaxies(cross at $z = 0$), quiescent galaxies (square at $z = 0$), and AGN (diamond at $z = 0$). The templates indicate that the Stern et al. IR-AGN sample is contaminated by galaxies at high redshifts($z \gtrsim 2$), which is confirmed by our observational dataset (the over-density in the `All` panel to the left of the Stern et al. wedge).

3.6.3 Extending Templates to Higher Redshifts

In this section, we extend the galaxy and AGN templates to higher redshifts ($z \geq 1.2$) beyond the range of PRIMUS to investigate the contamination of the IR-AGN samples. We track the templates out to $z = 3$ and compare to the full sample with IRAC detections thus including objects without spectroscopic redshifts. In Figure 3.13, we show the density of objects in IRAC color–color space for the Donley et al. IR-AGN (top-left panel), and X-ray AGN (top-right panel) samples, and for the entire sample (`All`) with IRAC detections (bottom-left panel). In the bottom-right panel we show the behavior of the templates from $z = 0$ to $z = 3$.

The Donley et al. IR-AGN sample (top-left panel) is centered around the power-law locus with the vast majority of the sample lying within the Stern et al. wedge. It spans the range of AGN/QSO templates (seen in the lower-right panel) over the entire redshift range ($z = 0 - 3$).

In comparison the X-ray AGN sample (top-right panel) not only spans the range of the Donley et al. sample, but also extends beyond the Donley et al. IR-AGN sample and the Stern et al. wedge. At ([3.5]–[4.5]) ~ 0.75 and ([5.8]–[8.0]) > 0.5 (left of the Stern et al. wedge) there is a spur of X-ray sources that do not have a secure PRIMUS redshift and are not selected with the Donley et al. IR-AGN method. Comparing this spur with the template track panel, this region of objects appears to match both high-redshift ($z \gtrsim 2.5$) quiescent galaxy (square) and star-forming galaxies (cross). It is unclear whether these objects contain an X-ray bright AGN and are missed by the Donley et al. and Stern et al. methods, or are merely X-ray-detected high-redshift star-forming galaxy contaminants. If we assume that these objects have a $z = 3$ redshift, the hard band X-ray luminosity would be distributed around $L_{\rm X} > 10^{44.6}$ erg s^{-1}, which is suggestive that they are highly luminous AGN and not high-redshift star-forming galaxy contaminants. The objects below the Stern et al. wedge generally match quiescent galaxy templates with $z < 1.5$ and star-forming templates with $0.7 < z < 1.5$. This population has been shown in Section 3.6.1 to be low redshift galaxies with PRIMUS redshifts ($z \sim 0.7$) containing genuine AGN ($L_{\rm X} > 10^{42}$ erg s^{-1}) that are not identified by either IR-AGN selection technique.

The small population of X-ray-detected sources with very red colors (([5.8]–[8.0]) > 2) to the bottom right of the Stern et al. wedge are generally identified as low-redshift ($z \lesssim 0.4$) star forming galaxies with low X-ray luminosities ($L_{\rm X} < 10^{42}$ erg s^{-1}) and thus the X-ray emission may be attributed to star formation rather than AGN activity. This population is easily identified and not selected by either the Stern et al. or Donley et al. IR-AGN selection techniques.

For the entire sample of IRAC-detected objects (`All`, bottom left panel), the bulk of the objects lie below the Stern et al. wedge, concentrating at colors of ([3.6]–[4.5]) < 0.0 and ([5.8]–[8.0]) > 0.1. The `All` sample contains four-bands IRAC detected objects from all of our

---

[3] The normalization of the 3.3 μm feature in the templates may be too high relative to the continuum, which results in redder colors than are seen in the PRIMUS sample. However, analyzing the detailed correspondence between star-forming galaxy templates and the IRAC colors of real galaxies is beyond the scope of this paper.

fields. The colors of these objects correlate with predicted star-forming and quiescent galaxy templates colors at $0.7 < z < 1.5$ There is also a large density of sources to the left side of the Stern et al. wedge, like the $z > 2.5$ spur of X-ray detected objects discussed earlier. The colors of these objects match both quiescent and star-forming galaxies SED templates at high redshift ($z \sim 2.5$). A low fraction (∼5%) of these objects are high-redshift high-luminosity X-ray-detected AGNs, but the majority of these objects are not X-ray detected. These objects are not identified by the Donley et al. selection technique, but extend into the Stern et al. wedge contaminating it with high-redshift galaxies.

Some of these sources in the Stern et al. wedge could have a low-luminosity AGN, but the AGN signature is being masked in the MIR by the dominant galaxy light. Such AGNs could be identified using other techniques (e.g., X-ray, or via their optical spectra), but the true AGNs are probably a minority of the contaminating population. The dominant galaxy light suggest that they are not generally broad-line QSOs, but could host narrow-line AGNs.

In summary, the Stern et al. IR-AGN technique selects a large population of AGNs but is contaminated by low-, intermediate-, and high-redshift galaxies ($z \sim 0.3$, $z \sim 1.1$, and $z \gtrsim 2.5$). The Donley et al. IR-AGN selection technique generally is free of these galaxy contaminants, selecting just the AGN population. The X-ray detected sample has colors that extend beyond the Stern et al. and Donley et al. selected samples, identifying a population of AGNs that are not detected by either IR selection technique and are not star-forming galaxy contaminants.

3.7 AGNs and Host Galaxy Rest-frame Properties

In this section, we investigate the AGN and host galaxy rest-frame properties of our IR-AGN and X-ray AGN samples. In Section 3.7.1, we create subsamples with PRIMUS spectroscopic redshifts in order to study restframe properties. In Section 3.7.2, we measure the AGN luminosity and hardness ratio (HR) distributions for the IR and X-ray AGN samples. We then investigate how the X-ray luminosities vary across the IRAC color–color space. In Section 3.7.3, we compare the host galaxy colors and stellar masses for the IR and X-ray AGN samples to investigate differences in the host galaxy properties.

3.7.1 The PRIMUS Redshift Sample

To investigate AGN and host galaxy rest-frame properties, we require a PRIMUS spectroscopic redshift. This reduces our AGN sample sizes and imposes an optical apparent magnitude limit. To be targeted by PRIMUS an object must have an optical magnitude brighter than $i \sim 23$. The fraction of sources in our AGN samples that are brighter than this optical limit varies from ∼30%–∼70% depending on the depth of the corresponding IR or X-ray data. Of these sources that are brighter than the PRIMUS targeting limit, ∼20% to ∼60% were targeted in PRIMUS (not all objects to the apparent magnitude limit can be targeted due to slit collisions). The fraction of targeted AGNs that have a high-quality redshift varies from ∼75% to ∼95% depending on the depth of the IR or X-ray data, where the fraction is higher for shallower fields. This is comparable to the overall PRIMUS redshift success rate. Some targeted sources for which we fail to measure a redshift lie at z > 1.2 where the Balmer break falls beyond the wavelength coverage of PRIMUS. Our redshift success range in the $0.2 < z < 1.0$ range is likely to be higher. The fraction of our IR- and X-ray-selected AGN with PRIMUS redshifts is ∼20%–∼70% depending on depth of the data. We find that the subsample with PRIMUS redshifts spans the full range of IR and X-ray fluxes in our IR and X-ray AGN samples. In the rest of this section, we use these subsamples to compare the rest-frame properties of the IR- and X-ray-selected AGNs to an optical limit of $i \sim 23$.

3.7.2 Rest-frame AGN Properties

In this section, we investigate rest-frame properties related to the AGN themselves. In Figure 3.14, we compare the IR and X-ray luminosities for the AGN samples. IR luminosities are calculated at a rest-frame wavelength of 3.6 μm by interpolating the log of the fluxes between the two nearest IRAC channels. IR luminosities are calculated at a rest-frame wavelength of 3.6 μm in two manners: (1) interpolating the log of the fluxes using the two nearest IRAC channels, and (2) using template fit synthesizes luminosities from K-correct (Blanton & Roweis 2007). We find no significant differences in the luminosity distributions between these two methods and use the former for the remainder of the paper. The solid green circles indicate PRIMUS AGNs that have IR and X-ray detections and are above $L_{\rm X} > 10^{42}$ erg s^{-1}. X-ray luminosities are calculated from the 2–10 keV fluxes, using an unobscured power-law with a photon index of $\Gamma = 1.9$. The light green arrows indicate upper limits on the 3.6 μm IR luminosity for X-ray-detected AGNs that lack IR detections. The IR luminosity upper limits are derived from the IR depth of the survey and the redshift of the object. The X-ray luminosity upper limits for the Stern et al. or Donley et al. IR-AGNs that are not X-ray detected are estimated from the X-ray depth of each field. We conservatively use the X-ray flux limit corresponding to the flux at which 50% of expected X-ray sources are detected in that field. For a more conservative 90% detection limit, the upper limits increase by roughly a factor of $2-4$. Objects that are selected by either Stern et al. or Donley et al. IR-AGN techniques are indicated by red squares or blue triangles, respectively. Generally, sources that are detected in both IR and X-ray have correlated luminosities which roughly follows the Richards et al. (2006) mean QSO SED shown as a solid orange line. The correlation does contain significant scatter with more sources scattering to much lower X-ray luminosities. The sources that scatter to lower X-ray luminosities are found two orders of magnitude below the mean QSO SED

We find that both IR-AGN color selection techniques tend to select sources with higher IR

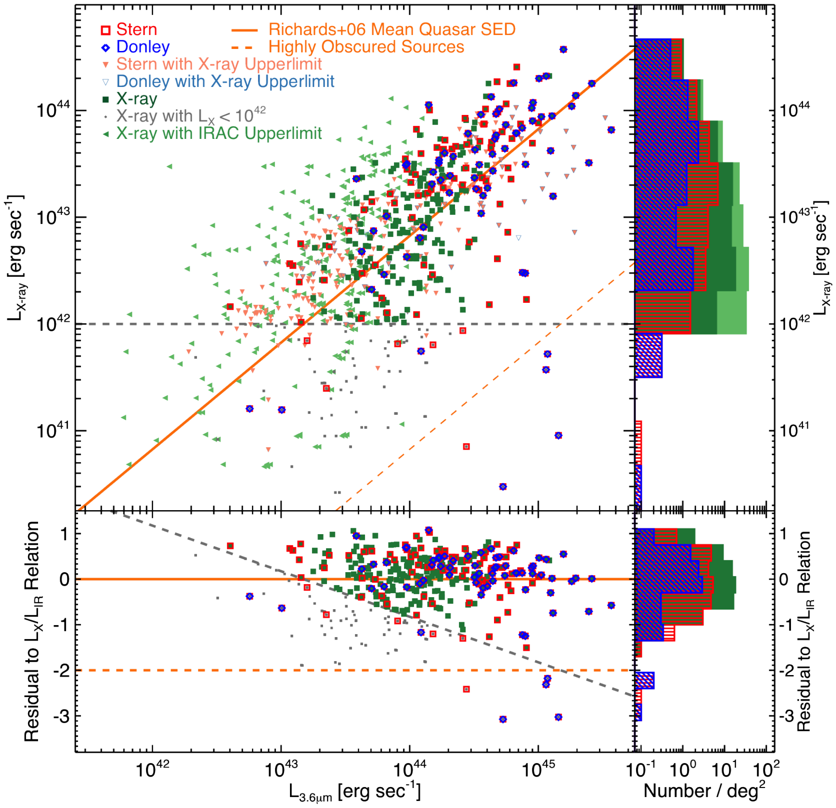

Figure 3.14: **X-ray versus mid-IR luminosity comparison diagram** — X-ray vs. IR luminosity comparison plot (top left) for the objects that are X-ray or IRAC detected. The Stern et al. selected objects are shown with a red square, the Donley et al. selected objects are shown with smaller blue square, and the X-ray-detected objects with $L_X > 10^{42}$ erg s^{-1} shown in green filled squares. We show the X-ray-detected objects with redshifts but not detected in the IRAC with light-green upper limits at the depth of the IR survey. We show the Stern et al. or Donley et al. IR-AGNs with redshifts but not X-ray detections with light red or blue upper limits at the X-ray flux corresponding to 50% of the expected number of X-ray sources are detected for each field. The IR and X-ray sample luminosities are correlated; the more luminous IR sources are also the more luminous X-ray sources. This correlation matches the Richards et al. (2006) mean quasar SED, which we show as an orange solid line. In the top-right panel, we show the X-ray luminosity number-density distribution for the sources in the previous panel. We show the Stern et al. distribution with a red hatched histogram, the Donley et al. distribution with a blue diagonal hatched histogram, and the X-ray and (not) IR-detected sample distribution in (light) green filled (arrows) circles. We do not show Stern et al. or Donley et al. IR-AGNs that are not X-ray detected in this histogram. In the bottom-left panel, we show the residuals between the source luminosity and the Richards et al. (2006) mean quasar SED line for the X-ray and IR detected objects. For the distribution panels, objects with X-ray detections have been normalized by the sensitive area for that flux. The points are shown with the same colors and styles as the top-left panel. We find that the residuals generally scatter below the mean SED line with more sources having a higher IR luminosity than X-ray luminosity.

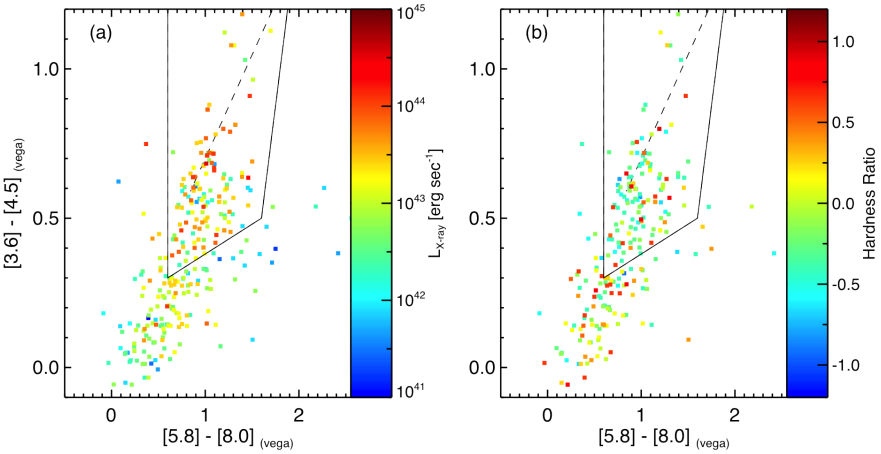

Figure 3.15: **IRAC color-color comparison of X-ray luminosity and hardness-ratio** — (a) IRAC color–color plot of the X-ray-detected population where we scale the color of each object to the X-ray luminosity. We show the border of the Stern et al. wedge as a solid black line, and the power-law locus as a dashed black line. We find a greater than average number of high X-ray luminosity sources to be within the Stern et al. wedge, and more than average numbers of sources with low X-ray luminosity to be outside of the wedge. There is a population of medium X-ray luminosity($L_X \sim 10^{43.5}$ erg s^{-1}) sources that are not selected by the Stern et al. or Donley et al. techniques. (b) IRAC color–color plot of the X-ray detected population with object color scaled to the X-ray flux hardness ratio. Generally, we find that hard sources (HR $\sim$ 1) are not preferentially found within the Stern et al. wedge compared to the full sample.

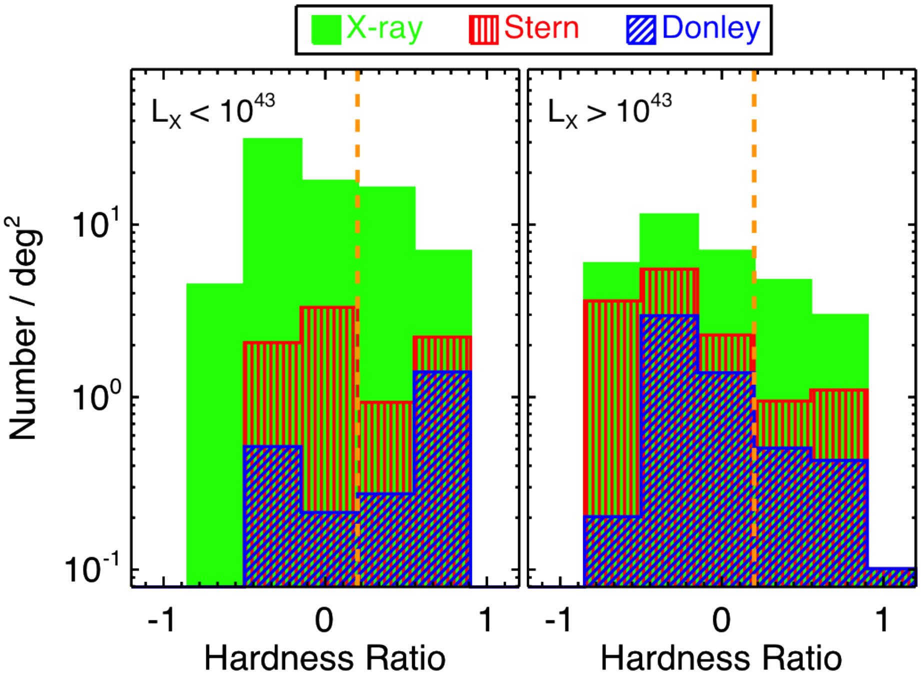

Figure 3.16: **X-ray hardness-ratio comparison of IR-AGN** — Hardness ratio comparison for the Stern et al. (horizontal hatched red shading), Donley et al. (diagonal hatched blue shading), and X-ray (green filled shading) identified samples. The two panels show the X-ray hardness ratio split up into X-ray faint sources ($L_X < 10^{43}$ erg s^{-1}, left) and X-ray luminous sources ($L_X > 10^{43}$ erg s^{-1}, right). For the low X-ray luminosities ($L_X < 10^{43}$ erg s^{-1}), there is a hint that the IR-AGN samples identify a *more* obscured population with a larger fraction of hard sources (HR > 0.2); however, this is not statistically significant.

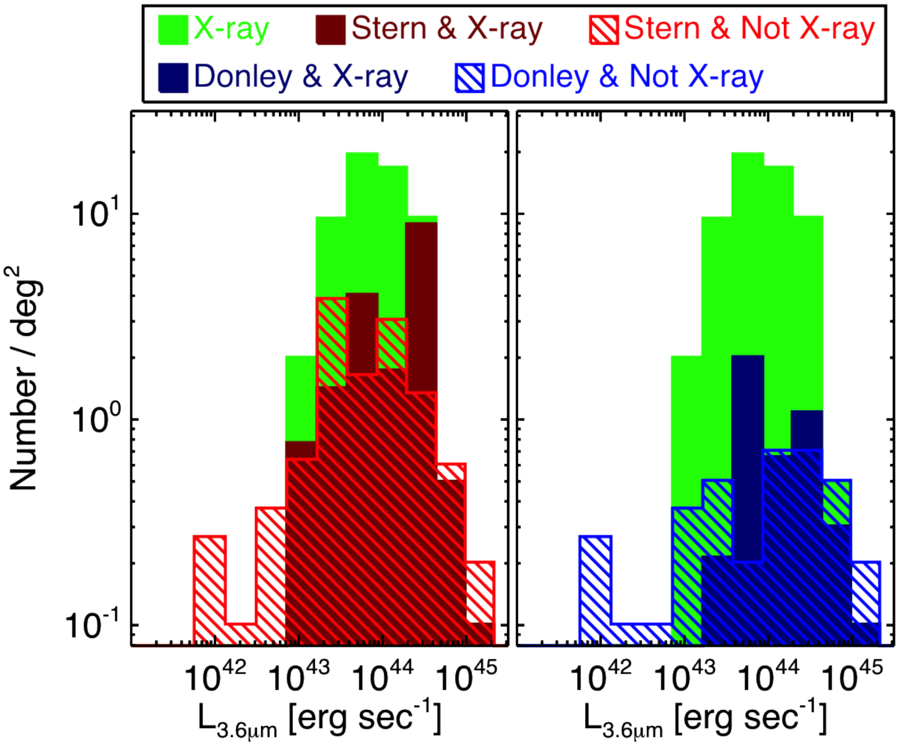

Figure 3.17: **Mid-IR luminosity comparison of number-density distribution** — $3.6\mu m$ IR luminosity number-density distributions for sample intersections. In both panels, we show the X-ray distribution in green. In the left panel, we show the number density of Stern et al. sources that are X-ray detected (red solid) and the number density of Stern et al. sources that are not X-ray detected (red hatched). In the right panel we show the number density of Donley et al. sources that are X-ray detected (blue solid) and the number density of Donley et al. sources that are not X-ray detected (blue hatched). We do not include the X-ray completeness correction weights for either IR selection. We find that the IR-AGN samples that are not X-ray detected have similar median luminosities compared to the X-ray detected sample.

and X-ray luminosities compared to the entire X-ray-selected AGN sample. A weighted K-S test of the distributions of the X-ray luminosities, as shown in the top-right subpanel of Figure 3.14, rejects the null hypothesis that either the Stern et al. or Donley et al. IR-AGNs are drawn from the same distribution as the X-ray selected AGN at the $> 99.9\%$ confidence level. X-ray selection identifies a large population of AGNs with low luminosities (below $L_{\rm X} < 10^{43.5}$ erg s^{-1}) that are not identified as either Stern et al. or Donley et al. IR-AGNs.

These trends are also shown in Figure 3.15(a), which plots the subset of X-ray AGNs detected in all four IRAC bands in IRAC color–color space, where the color of the points scale with X-ray luminosity. In this figure we do not limit sources to be above $L_{\rm X} > 10^{42}$ erg s^{-1}. Sources below this limit reside in the region below the Stern et al. or Donley et al. IR-AGN selection regions and are easily distinguished from IR-selected AGNs. Low X-ray luminosity ($L_{\rm X} < 10^{43.5}$ erg s^{-1}) AGNs are scattered throughout the IRAC color–color space, whereas high X-ray luminosity ($L_{\rm X} > 10^{43.5}$ erg s^{-1}) AGNs cluster near the power-law line within the Stern et al. wedge. For high X-ray luminosity ($L_{\rm X} > 10^{43.5}$ erg s^{-1}) AGNs with IRAC detections, $\sim$46%±6% to $\sim$79%±4% lie within the spaces defined by the Donley et al. and Stern et al. IR-AGN selections, respectively.

In the bottom panel of Figure 3.14, we plot the residuals X-ray to IR luminosity ratio from the Richards et al. (2006) mean quasar SED shown in the upper panel (solid orange line). In this panel, we have removed the AGN not detected in the IR. We find that there is a tail of sources with negative residuals such that their X-ray to IR luminosity ratio is below the Richards et al. (2006) mean quasar SED (solid orange) line. There are between 3%±1% and 6%±3% of Stern et al. and Donley et al. sources with residuals less than -2.0; these sources are particularly X-ray underluminous. These sources are likely obscured AGNs where the observed X-ray luminosity is suppressed due to absorption in the 2-10 keV X-ray band. We note that the IR luminosity $L_{3.6\mu m}$ may be systematically inflated by galaxy light for lower luminosity AGNs. In the IR, the galaxy light dominates over the AGN light above an accretion rate of 1% Eddington (see Section 3.7.3). However, the sources that are underluminous in X-rays are very luminous in the IR ($L_{3.6\mu m} > 10^{44}$ erg s^{-1}) such that the galaxy contribution is small relative to the AGN.

We also examine the obscuration of the X-ray AGN using HRs. We convert the hard- and soft-band fluxes to equivalent on-axis *Chandra* count rates and calculate the HRs as $(H-S)/(H+S)$ where H and S are the 2-10 keV and 0.5-2 keV count rates, respectively. Large HRs values (HR$\geq$ 0.2) indicate significant absorption in the hard X-ray band ($N_{\rm H} \gtrsim 3\times$ 10^{21} cm^{-2}) at $z \sim 0.6$ (Hasinger 2008). In Figure 3.15(b), we show the HRs for the subset of X-ray AGNs detected in all four IRAC bands in IRAC color–color space and find that lower HR (unobscured) AGNs tend to fall within the Stern et al. wedge. This is consistent with IR-AGN samples identifying primarily more luminous AGN, which tend to be unobscured. Obscured AGN lie throughout the IRAC color–color space, with 48%±3% in the Stern et al. wedge and the remainder in the region where the galaxy light dominates the IR colors.

We compare the HRs of the IR-AGN and X-ray AGN samples in a two X-ray luminosity bins to limit the large number of luminous IR-AGN sources from dominating the comparison. In the right panel of Figure 3.16, we show the distributions of HRs for X-ray luminous sources ($L_{\mathrm{X}} > 10^{43}$ erg s^{-1}). The Stern et al. IR-AGN, Donley et al. IR-AGN, and X-ray detected AGN samples all span a wide range of HRs. The fraction of obscured sources ($HR > 0.2$) is comparable for all three samples. The fraction in the X-ray AGN sample (28%±7%) is slightly larger than the fraction in the Stern et al. (18%±10%) or Donley et al. (20%±17%), although the differences are not statistically significant.

In the left panel of Figure 3.16, we show the distributions of HRs for lower luminosity X-ray sources ($L_{\mathrm{X}} < 10^{43}$ erg s^{-1}). The fraction of obscured sources (HR > 0.2) for the X-ray AGN sample (28%±5%) is slightly smaller than the fraction in the Stern et al. (36%±15%) or Donley et al. (67%±27%) AGN samples. Unlike at high X-ray ($L_{\mathrm{X}} > 10^{43}$ erg s^{-1}) luminosities, there is a hint at low X-ray luminosities that the IR-AGN samples identify a *more* obscured population for lower luminosity AGNs; however, there are not statistically significant differences between the HR distributions in either luminosity range. Larger deep-IR samples are needed to confirm if this small population of obscured sources statistically differs from the X-ray sample.

Finally, in Figure 3.17 we show the 3.6 μm IR luminosity number-density distribution for the IR-AGN samples that are divided into X-ray detected (solid histograms) and not X-ray detected (hatched histograms). We also show a subset in green of the X-ray AGN sample that is detected in all IRAC four bands. For both the Stern et al. and Donley et al. AGN samples, we do not find any significant differences in the $L_{3.6\mu m}$ distributions for the sources with X-ray detections to those without X-ray detections. These latter sources could be missed in X-ray due to heavy obscuration, but nevertheless they have a similar distribution of IR luminosities and do not outnumber the subsample of the X-ray AGN sample detected in IRAC. The low number density of IR-AGN sources without X-ray detections may partially be due to having relatively deeper X-ray survey data compared to the IRAC survey data. Using the 3.6 μm and X-ray luminosity from the Richards et al. (2006) mean quasar SED, we find that the depth of the X-ray data in our fields is typically 2–3 times deeper than the IRAC depth, for light that is dominated by luminous AGNs. Thus, while IR-AGN samples are efficient at identifying luminous AGNs, it remains unclear if they identify a large population of obscured sources relative to X-ray AGN samples due to the differences in survey depths.

3.7.3 Host Galaxy Properties

In this section, we investigate the optical rest-frame colors and stellar masses of the host galaxies for our IR-AGN and X-ray AGN samples with PRIMUS redshifts. For broad-line AGNs, the optical light is dominated by the AGN rather than the host galaxy light; this prevents an accurate estimate of the host galaxy properties. Therefore, in this section we exclude sources

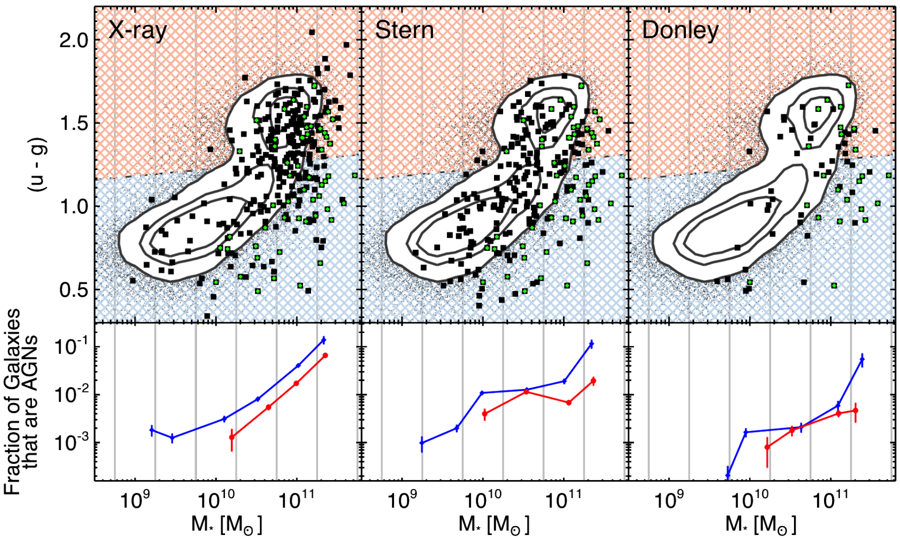

Figure 3.18: **Optical color versus stellar mass comparison for AGN samples** — Optical color vs. stellar mass diagram for the X-ray AGN (left column), Stern et al. IR-AGN (center column), and Donley et al. IR-AGN (right column) samples. In the top panel of each column we show the rest-frame $(u - g)$ optical colors on the vertical axis and the stellar mass estimates for PRIMUS galaxies (gray points and contours) and the AGN sample (black squares). In each panel we show the sources that are both X-ray detected and IR-AGNs selected with green diamonds. The background colored hatching shows the approximate red and blue galaxies definition at $z = 0$ and $m_g \sim 20$. In the bottom panel of each column, we show the fraction of detected AGNs compared to all PRIMUS galaxies at a given stellar mass for red and blue hosts. The fraction is calculated in six stellar mass bins and is shown at the median AGN mass in that bin.

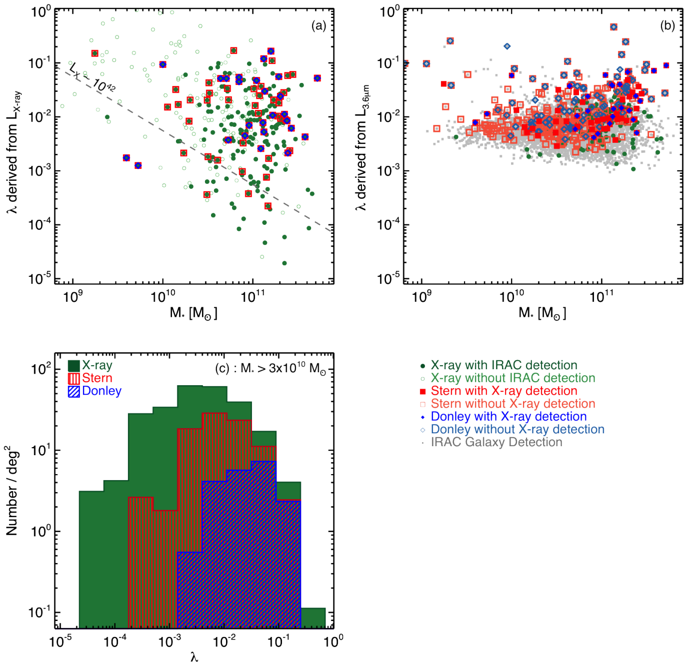

Figure 3.19: **Specific accretion rate comparison for AGN samples** — (a) Specific accretion rate (λ) derived from the X-ray luminosity vs. stellar mass. For sources that are detected in both IRAC and X-ray (filled dark green circles) we also show Stern et al. or Donley et al. IR-AGN sources as red squares or blue diamonds, respectively. The gray dashed line shows the approximate location of an $L_X \sim 10^{42}$ erg s^{-1} source. We find two populations of X-ray sources that are not identified as IR-AGNs: those that are not detected by IRAC and those that are detected by IRAC but do not meet either the Stern et al. or Donley et al. criteria. Many X-ray AGNs that are not IRAC detected have high specific accretion rates ($\lambda > 10^{-1}$) and have low stellar masses. The sources that are IRAC detected but not identified by either selection technique are low-luminosity sources that have low specific accretion rates and high stellar masses. (b) Specific accretion rate (λ) derived from the $L_{3.6\mu m}$ luminosity vs. stellar mass. X-ray detected sources are filled green circles, with filled red squares or blue diamonds for Stern et al. and Donley et al. IR-AGN, respectively. Stern et al. and Donley et al. sources that are not X-ray detected are shown with open light red squares and light blue diamonds, respectively. There is a floor near $10^{-2} < \lambda < 10^{-3}$ where galaxy light begins to dominate the MIR emission. (c) Specific accretion rate (λ) distribution for the X-ray, Stern et al. and Donley et al. AGN samples for $\mathcal{M}_* > 3\times 10^{10}\,\mathcal{M}_\odot$. The Stern et al. and Donley et al. IR-AGN techniques tend to identify higher specific accretion rate sources relative to the X-ray AGN sample. We include the X-ray completeness corrections for the X-ray detected sources.

classified as broad-line AGNs, where the PRIMUS spectrum is better fit with χ^2 of at least 50 by a broad-line AGN template compared to any galaxy template. These broad-line AGNs are a sizable fraction of the X-ray AGN (12%±1%), Stern et al. IR-AGN (16%±2%) and Donley et al. IR-AGN (32%±3%) samples.

In the top panels of Figure 3.18, we plot the rest-frame optical $(u - g)$ colors and stellar masses for the X-ray AGN (left), Stern et al. IR-AGN (center), and Donley et al. IR-AGN (right column) samples. We show the relevant AGN sample with black squares and PRIMUS galaxies with gray contours (30%, 50%, and 80% contours) and gray points for individual galaxies outside of the 80% contour. In the left panel, we show the X-ray AGN that are selected by either of the Stern et al. IR-AGN or Donley et al. IR-AGN selection techniques with green diamonds. In the center and right panels, we show IR-AGN that are also X-ray detected in green diamonds. The stellar masses are estimated using the SED fitting code iSEDfit (see Moustakas et al. 2013, for complete details). iSEDfit is a Bayesian fitting program that compares broadband photometry against large Monte Carlo grids of SED models that span a wide range of parameters (e.g. ages, metallicities, star formation histories, star bursts, and dust content). We construct our stellar mass models using the Bruzual & Charlot (2003) stellar population synthesis models assuming the (Chabrier 2003) initial mass function from 0.1 to $100\mathcal{M}_*$. We assume a uniform stellar metallicity prior in the range $0.004 < Z < 0.04$, and smooth, exponentially declining star formation histories, $\psi(t) \propto e^{-\gamma t}$, with γ drawn uniformly from the interval [0.01, 1] Gyr^{-1}, and we include bursts of star formation. In the bottom panels of Figure 3.18, we calculate the fraction of all PRIMUS galaxies that are detected in one of the AGN selection methods as a function of stellar mass for red and blue sources. We define each source as blue or red using the magnitude and redshift dependent cut from Aird et al. (2012)

$$C = (u - g) - (0.671 - 0.031 M_g - 0.065 z), \tag{3.10}$$

where M_g is the absolute g-band magnitude and z is the redshift. To calculate the number density and account for the variation in survey depth, we use the X-ray completeness corrections (X-ray sensitive area for a given X-ray flux) for the sources that are X-ray detected and the IR–optical overlap area for all other sources.

We find that the fraction of galaxies with detected X-ray AGNs increases with stellar mass. The fraction of blue galaxies with X-ray AGNs is a factor ∼2 higher than for red galaxies (across all stellar masses). These trends are in agreement with Aird et al. (2012), where the increase with stellar mass is attributed to a selection effect. AGNs in massive galaxies appear more luminous (for the same specific accretion rate scaled relative to the host stellar mass) and so are easier to detect. AGNs selected by either Stern et al. IR-AGN or Donley et al. IR-AGN techniques follow the same basic trend, although both techniques generally identify a lower fraction of AGNs in both red and blue galaxies at all stellar masses. The rate that the fraction of red galaxies with Stern et al. or Donley et al. AGNs increases with stellar mass is much slower than for red galaxies with X-ray AGNs. This lower rate of change for the IR-AGN selections suggests that they are less efficient at identifying AGNs in red, massive galaxies ($\mathcal{M}_* \gtrsim 10^{10.5}\,\mathcal{M}_\odot$). The fraction of galaxies with Stern et al. IR-AGNs is *higher* than the X-ray fraction at low masses which may be due to contamination of Stern et al. IR-AGNs by star-forming galaxies.

In Figure 3.19(a), we estimate the specific accretion rate (λ) of the X-ray-detected sample as a function of the host stellar mass. Following Aird et al. (2012), we define the specific accretion rate from the bolometric luminosity derived from the X-ray luminosity using the Hopkins, Richards, & Hernquist (2007) quasar bolometric corrections[4]. For the hard X-ray-selected sample, this is dominated by the emission from the AGN with possibly only minor contribution from the host galaxy. From the bolometric luminosity, we calculate the specific accretion rate

$$\lambda = \frac{L_{\rm bol}}{L_{\rm Edd}} = \frac{L_{\rm bol}}{1.3 \times 10^{38}\ {\rm erg\ s^{-1}} \times 0.002 \dfrac{\mathcal{M}_*}{\mathcal{M}_\odot}}, \tag{3.11}$$

where $\mathcal{M}_*$ is the host galaxy stellar mass and $L_{\rm bol}$ is the bolometric luminosity. The X-ray sources with IRAC detections are solid green circles and the sources without IRAC detections are open green circles. Sources with IRAC detections that are selected by either Stern et al. or Donley et al. IR-AGN selection technique are outlined with red squares or blue diamonds. The vast majority of Donley et al. IR-AGNs also satisfy the Stern et al. IR-AGN selection criteria. This figure shows two populations of X-ray sources that are not identified as IR-AGNs: those that are not detected by IRAC (see Section 3.5.3) and those that are detected by IRAC but do not meet either the Stern et al. or Donley et al. criteria. The former populations consists primarily of sources at low stellar masses and high specific accretion rates. These sources are primarily found in the fields that have shallower IRAC data compared to their X-ray data (`ES1`, *XMM*, and $\texttt{COSMOS}_{\texttt{Shallow}}$).

The majority of the X-ray AGNs that are not Stern et al. or Donley et al. selected (but do have IRAC detections: green solid symbols in Figure 3.19(a)) have large stellar masses ($\mathcal{M}_* > 3\times 10^{10}\,\mathcal{M}_\odot$), low-to-moderate X-ray luminosities ($L_{\rm X} < 10^{43}$ erg s^{-1}), and low specific accretion rates ($\lambda < 1\%$). Additionally, many of these sources have a moderate-to-large MIR to X-ray luminosity ratios ($L_{3.6\mu m}/L_{\rm X} > 1$). In fact, their $L_{3.6\mu m}/L_{\rm X}$ ratios are larger than typically found for the IR-AGN population and for optically selected quasars (e.g. Richards et al. 2006). This suggests that stellar light from their massive host galaxies is dominating the emission in the IRAC bands. Indeed, for a stellar mass-to-light ratio of order unity (e.g. Bell & de Jong 2001) and $L_{3.6\mu m}/L_{\rm X}$ for a pure AGN SED (Richards et al. 2006), a galaxy with a specific accretion rate of $\lambda = 1\%$ would have comparable emission at 3.6 μm from stellar light and from the central AGN. At lower specific accretion rates, the host galaxy would then dominate the emission in the IRAC bands. This provides a natural explanation for why many X-ray AGNs at lower specific accretion rates are not selected as IR-AGNs. These findings are in good agreement with Donley

---

[4] http://www.tapir.caltech.edu/~phopkins/Site/qlf

et al. (2012), who show that the average SED of luminous AGNs is missed due to a noticeable 1.6 μm stellar bump that prevalent in older, massive galaxies.

In Figure 3.19(b), we estimate the specific accretion rate based on MIR luminosity. The specific accretion rates for these sources are less well constrained due to the possible addition of galaxy light to the observed MIR flux. To ensure that the bolometric luminosity distribution are similar for the X-ray and IRAC overlapping sample, we first use the Richards et al. (2006) mean quasar SED to estimate the $L_{\rm X}$ luminosity from the $L_{3.6\mu m}$ luminosity (see the orange line in Figure 3.14). We apply the Hopkins, Richards, & Hernquist (2007) hard X-ray bolometric correction to the equivalent X-ray luminosity to calculate the specific accretion rate for these sources. We do not use the Hopkins, Richards, & Hernquist (2007) bolometric corrections for the IR luminosity due to the overprediction of the bolometric luminosity for IR-AGN sources that are also X-ray detected. This method for estimating specific accretion rates illustrates the floor near $10^{-2} < \lambda < 10^{-3}$, where galaxy light dominates the MIR luminosity.

In Figure 3.19(c), we show the specific accretion rate distribution for Stern et al. IR-AGNs, and Donley et al. IR-AGNs and X-ray AGNs. We restrict this comparison to AGNs in host galaxies with stellar mass $\mathcal{M}_* > 3\times 10^{10}\,\mathcal{M}_\odot$, due to incompleteness at lower stellar masses. For all AGNs with an X-ray detection, we use the specific accretion rate derived from the X-ray luminosity. For the IR-AGNs that are not detected in the X-rays we use their estimated specific accretion rate from their MIR luminosity. Some of the IR-AGNs with X-ray detections have significant absorption in the X-rays (e.g., Figure 3.14). For IR-AGNs with $L_{3.6\mu m}/L_{\rm X} > 10$, we use the specific accretion rates derived from their MIR luminosities. We note that this does not have a significant effect on the lambda distributions in Figure 3.19(c). Both the Stern et al. and Donley et al. IR-AGN samples have specific accretion rate distributions that do not match the X-ray distribution at the $> 99.7\%$ confidence level from using a two-sided weighted KS test. In particular, the X-ray sample includes a significant number of sources at low to moderate specific accretion rates that are not identified as IR-AGNs. These low to moderate specific accretion rate sources are preferentially found in red, high-mass galaxies, which explains the larger fraction of red host galaxies identified with X-ray AGNs compared to IR-AGN selection techniques.

3.8 Discussion

In this paper we compare AGN samples selected in the MIR to those selected using hard-band X-rays, in order to quantify both the overlap and uniqueness of each selection method as well as understand the AGN populations identified. We use the Stern et al. and Donley et al. IR-AGN selection methods (described in Section 3.4) to identify IR-AGN samples using *Spitzer*/IRAC data in four fields that have X-ray coverage from *Chandra* or *XMM-Newton*: CDFS, COSMOS, ES1, and the XMM field. We create IR-AGN and X-ray AGN samples to various depths in both the IR and X-ray data and find that the number density of AGNs recovered with each selection method varies strongly as a function of depth, as does the overlap between the IR-AGN and X-ray AGN samples. We use PRIMUS spectroscopic redshifts in these fields to study the AGN luminosities, host galaxy colors, and host stellar masses of the IR-AGN and X-ray AGN samples and investigate potential contamination in IR-AGN selection.

There are several advantages to our approach, compared to previous studies. We use large AGN samples (a total of 9005 Stern et al. IR-AGNs, 3569 Donley et al. IR-AGNs and 4886 X-ray AGNs) spanning multiple fields, which allows us to perform statistical comparisons as a function of joint parameters, while minimizing the effects of cosmic variance. We take advantage of the large number of spectroscopic redshifts in these fields provided by PRIMUS (a total of 1,541 AGNs with PRIMUS redshifts between $0.2< z <1.2$), so that we do not have to rely on photometric redshifts which have larger errors. We further study the overlap and uniqueness of IR-selected versus X-ray-selected AGNs as a function of both the depth of the IR data and the depth of the X-ray data. With a large dynamic range in survey depth, we can test how the completeness, purity, and contamination of the AGN selection depends on depth. Such tests are required to reconcile the often vastly different and seemingly conflicting results in the literature regarding IR and X-ray AGN selection.

Another key difference in our methodology is that we use hard-band (2–10 keV) X-ray selection, as opposed to soft or full band, and we use weights for X-ray detections to account for incompleteness in the X-ray data. Hard-band X-ray selection is sensitive to both unabsorbed and moderately absorbed AGNs, though it will miss heavily absorbed, Compton-thick AGNs. Soft (0.5–2 keV) or full (0.5–10 keV) band selection, by comparison, is biased toward unabsorbed sources (with column densities of $N_{\rm H} < 10^{22}$ cm^{-2}). We account for the large positional uncertainties in the X-ray data by using the likelihood ratio matching technique to securely match the X-ray sample to both the IR and optical samples. Finally, we account for the varying sensitivity of the X-ray data across individual fields by applying statistical completeness corrections to all X-ray sources. This last correction is crucial to accurately quantify the number density of X-ray AGNs as a function of depth and robustly compare with IR-AGN samples. We emphasize that this correction is not generally applied in the literature, where studies simply compare the fraction of IR-AGNs that are observed in X-ray data, without taking into account incompleteness in the X-ray data.

3.8.1 How AGN Selection Varies with Depth

We first consider the fraction of IR-AGNs that are detected in X-rays, as a function of both the IR and X-ray data depth. Generally, a higher fraction of Donley et al. IR-AGNs are X-ray detected than in the Stern et al. IR-AGN sample, consistent with our findings above that the Stern et al. IR-AGN selection can suffer from contamination. At the relatively shallow IR depth of the `SWIRE` survey, 60% of IR-AGN are X-ray detected when the X-ray depth is comparable to the IR depth. Using the deepest IR and X-ray data, the fraction of IR-AGNs that are X-ray detected rises to ∼70% – ∼80%. However, this fraction rises to ∼90% when combining shallow IR and deep X-ray data, indicating that the vast majority of IR-AGNs are indeed X-ray emitting AGNs.

As discussed above, IR-AGN selection methods identify additional AGNs not detected in X-rays, when the IR and X-ray data are of comparable depth. At shallow IR depths the Stern et al. and Donley et al. techniques recover very similar number densities of AGNs with a large overlap between the populations. As IR depth increases, both the Stern et al. and Donley et al. selections identify a larger population of AGNs. However, the number density recovered by the Stern et al. selection increases at a greater rate — in our deepest IR data Stern et al. recovers approximately twice the number density of AGNs as the Donley et al. IR-AGN selection. As discussed in Section 3.6, much of the relative increase is likely due to contamination. For any depth IR and X-ray data, the addition of Stern et al. IR-AGN sample to X-ray AGN sample increases the total AGN sample by 7%−27%, depending on the depth of the IR and X-ray data. In comparison, addition of Donley et al. IR-AGN selection to X-ray AGN selection increases the total AGN sample by 4%−20%. Both IR-AGN selection methods increase the total AGN samples more at shallower IR and X-ray depths. At all IR and X-ray depths studied here, X-ray AGN selection identifies a higher number density of AGNs than either IR-AGN selection method.

It is also extremely important to account for the well known and easily characterized incompleteness of X-ray selection. The variation in X-ray sensitivity over a field can substantially reduce the number of IR-AGNs with observed X-ray detections. It is vital to account for this effect to understand any true, underlying differences between AGN populations.

At all IR and X-ray depths studied here we find a much higher fraction of IR-AGNs are detected in X-rays, compared to values in the literature. This is due to the X-ray completeness corrections that we make, to account for the varying X-ray sensitivity within a field. If we do not apply these completeness weights, we find similar fractions to those in the literature. For example, in the XBoötes survey with shallow IR ($f_{5.8\mu m} \sim 51\ \mu Jy$) and shallow X-ray ($f_{\rm X}{\sim}10^{-15}$ erg s^{-1}cm^{-2}) data, Hickox et al. (2009) find that 38% of their Stern et al. IR-AGNs are X-ray detected. Using similar depth data if we do not apply X-ray completeness corrections we find that 37% of Stern et al. IR-AGNs are X-ray detected; however this fraction rises to 63% after applying the completeness corrections. Donley et al. (2007) use deep IR ($f_{5.8\mu m} \sim 14.5\ \mu Jy$) and medium-depth X-ray ($f_{\rm X}{\sim}10^{-15}$ erg s^{-1}cm^{-2}) data in the CDF-North field to find that 33% of the Stern et al. IR-AGN are X-ray detected. Using similar depth data if we do not apply X-ray completeness corrections we find a similar fraction of 35% of Stern et al. IR-AGNs are X-ray detected; however this fraction rises to 57% after applying the completeness corrections. Park et al. (2010) use very deep IR data ($f_{5.8\mu m} \sim 6.3\ \mu Jy$) and medium-depth X-ray ($f_{\rm X}{\sim}10^{-16}$ erg s^{-1}cm^{-2}) data in the EGS field and find that a comparatively low fraction of Stern et al. IR-AGNs are X-ray detected. As their X-ray data are not as deep as their IR data, it is not surprising that they find a low fraction. We do not have comparably deep IR data, however at a similar X-ray depth using the deepest IR data we have, we find that at most 35% of IR-AGNs should be X-ray detected, if X-ray completeness is not accounted for. This upper limit is consistent with their value.

Thus, we find that the wide range of X-ray detected IR-AGN fractions reported in the literature can be accounted for by the varying depths of both the IR and X-ray data used in these studies. We also find that accounting for X-ray incompleteness, which is generally not done in the literature, increases this fraction by a factor ∼2 which results in 25% more of the IR-AGNs being counted (statistically) as X-ray detected. This illustrates how differing depths of data can lead to very different conclusions in prior studies of IR and X-ray AGNs.

3.8.2 Contamination and Bias of IR-AGN Selection

Much, if not most, of the difference between the Stern et al. IR-AGN sample and Donley et al. IR-AGN sample is due to contamination by galaxies that do not host an AGN (or at least, are not dominated by a luminous AGN in the MIR). Using PRIMUS redshifts, we study the evolution of the distribution of Stern et al. and Donley et al. IR-AGNs and X-ray-detected AGNs in IRAC color–color space from $z \sim 0.2$ to $z \sim 1.2$ and compare our results to the predicted evolution of star-forming and quiescent galaxy and AGN SED templates in this space. We find that the Stern et al. IR-AGNs sample is contaminated at $z \sim 0.3$ by star-forming galaxies and at $z \sim 1.1$ by quiescent galaxies. This is reflected in the fraction of Stern et al. IR-AGN that are not detected in X-rays; for the full Stern et al. IR-AGN sample with PRIMUS redshifts, spanning $0.2 < z < 1.2$, this fraction is 27%±4%, while at $0.2 < z < 0.45$ it is 76%±10% and at $1.0 < z < 1.2$ it is 86%±13% when using the X-ray completeness weights.

Extending our analysis of the galaxy and AGN templates to higher redshift, beyond the reach of PRIMUS, we find that the Stern et al. IR-AGN samples will be contaminated by high-redshift star-forming galaxies. We do not find any galaxy contamination in the Donley et al. IR-AGN sample; this is reflected by the lack of evolution in the fraction of Donley et al. IR-AGNs that are not X-ray detected. Using the Donley et al. IR-AGN sample as a baseline, we find that galaxy contamination in the Stern et al. IR-AGN selection is significant only for IR surveys deeper than the SWIRE limit of $f_{5.8\mu m} \sim 100\ \mu Jy$.

Overall, we find that the Donley et al. IR-AGN selection is less complete than the Stern et al. IR-AGN selection. This is demonstrated by the fact that a smaller fraction of X-ray AGNs are also Donley et al. IR-AGNs. Additionally there are correctly identified AGNs within the Stern et al. IR-AGN sample that are not found by the Donley et al. IR-AGN selection. However, the Donley et al. IR-AGN selection is more reliable than the Stern et al. IR-AGN selection, in that a higher fraction of Donley et al. IR-AGNs are also X-ray detected, and the Donley et al. IR-AGN selection does not suffer from galaxy contamination. The Stern et al. and Donley et al. IR-AGN samples demonstrates the importance of finding a balance between minimizing both contamination and incompleteness.

Both the Donley et al. and Stern et al. IR-AGN selections appear to be biased, however, in that they select high luminosity AGN. This is seen in the X-ray luminosity distributions of the IR-AGN samples compared to the X-ray AGN sample, where the IR-AGN selection techniques preferentially sample the population of $L_{\rm X} \gtrsim 10^{43.5}$ erg s^{-1} AGN. These high luminosity sources have IRAC colors similar to power-law AGNs and are easily detected with shallow IR surveys.

3.8.3 Uniqueness of IR-AGN Selection

Even with a relatively deep X-ray survey and shallow IR data, we find that there is at least ~10% of the IR-AGN population which is not detected in X-rays even after correcting for the variable X-ray sensitivity. For samples of comparable X-ray and IR depth, this fraction is typically ~20% – ~30%. This reflects the *uniqueness* of IR-AGN selection, in that these are sources that are only identified in the IR and would typically be missed in X-ray surveys. What kind of AGNs does IR selection uniquely identify? These AGN could in theory be missed by X-ray selection either because they are intrinsically less X-ray luminous, due to a lower accretion rate onto the supermassive black hole, or they could be obscured by a high-column density of gas and dust, limiting the ability of even deep X-ray surveys to detect them. For the population of IR-AGNs that are X-ray detected, as discussed above we find that IR-AGN selection techniques preferentially select a population of luminous AGNs with $L_{\rm X} \gtrsim 10^{43.5}$ erg s^{-1}. However, there is a small fraction (~8%) of IR-AGN with very high IR to X-ray luminosity ratios, implying heavy obscuration. Therefore, up to ~20% of IR-AGNs could be sources with moderate to heavy obscuration.

In comparing the HR distributions of IR- and X-ray-selected AGNs, we find no statistically significantly difference in the distributions for X-ray AGNs with higher or lower X-ray luminosity. This comparison does not account for the ~10% of IR-AGN sources that are not X-ray detected. Thus, while the majority of IR-AGNs are also X-ray AGNs, the IR selection techniques adds a small but important population of obscured sources that are missed even with the deepest X-ray surveys. Additionally, the 10% of IR-AGN sources that are not X-ray detected may be Compton-thick and thus consistent with X-ray background synthesis models (e.g., Gilli et al. 2007).

3.8.4 Host Galaxies

With the exception of broad-line sources, the optical SEDs of the IR-AGN and X-ray AGN samples are dominated by light from the host galaxy, which allows us to determine galaxy properties for these sources. Generally, the Stern et al. and Donley et al. IR-AGN samples follow the same trends as the X-ray population, showing that IR-AGNs and X-ray AGNs do *not* populate vastly different host galaxy populations. The galaxy hosts span a similar range of stellar masses ($10^{10} < \mathcal{M}_*/\ \mathcal{M}_\odot < 10^{11.5}$) and optical colors compared to the PRIMUS parent galaxy sample. The Donley et al. IR-AGN and X-ray AGN samples identify similar fractions of AGNs in blue, star-forming hosts and red, quiescent hosts. These fractions of red and blue AGN hosts are similar to the red and blue fractions for all PRIMUS galaxies.

Hickox et al. (2009) find that X-ray AGNs are preferentially found in galaxy hosts in the green valley, the minimum of the optical color bimodality between the red sequence and the blue cloud (Martin et al. 2007), whereas Stern et al. IR-AGNs are typically in blue host galaxies. We do not agree with these results, which did not correct for X-ray incompleteness and contamination in the Stern et al. sample. Most recent papers (e.g., Silverman et al. 2009; Xue et al. 2010; Aird et al. 2012) find that the X-ray AGN fraction is highly stellar mass dependent. Similar to Nandra et al. (2007), Silverman et al. (2009) and Aird et al. (2012) we find that at a given stellar mass the fraction of galaxies with X-ray AGN is higher in the blue cloud. In particular for the green valley Nandra et al. (2007) using the ∼200 ks X-ray data in the Extended Groth Strip to find that 13% of X-ray-detected AGNs have green host galaxies, which is consistent with our X-ray AGN sample (9%) using a similar green valley definition. If X-ray completeness correction weights are not applied, the fraction of green host galaxies with X-ray AGNs rises only slightly, from 9% to 11%.

For the Stern et al. IR-AGNs, we generally find equal fractions of sources with blue or red host galaxies. There is a slightly larger fraction with blue hosts when compared using stellar-mass matched samples, but this is mainly due to blue star-forming host galaxies contaminating the sample rather than differences in the underlying population. The Donley et al. IR-AGN sample is more evenly distributed between red and blue host galaxies at fixed stellar mass.

We do find that the fraction of galaxies hosting an AGN increases with galaxy stellar mass. The fraction of massive ($\mathcal{M}_* > 10^{11}\,\mathcal{M}_\odot$) galaxy hosts is larger for the X-ray AGN sample (78%±2%) compared to the Stern et al. IR-AGN (52%±2%) or Donley et al. IR-AGN sample (69%±4%). Conversely, the fraction of less massive ($10^9 < \mathcal{M}_*/\ \mathcal{M}_\odot < 10^{10}$) galaxy hosts for the X-ray AGN sample (7%±1%) is smaller than either the Stern et al. IR-AGN sample (21%±2%) or the Donley et al. IR-AGN sample (11%±3%). However, these differences are minor compared to the similarity of the host galaxy stellar mass distribution between any of the AGN selection techniques.

From the host galaxy stellar masses and the estimated AGN bolometric luminosities we infer the specific accretion rates, which provide a valuable measure of the intrinsic differences of the selected AGN populations. While IR-AGN samples are generally found in similar host galaxies as X-ray AGNs, we find that IR-AGNs have relatively high specific accretion rates. X-ray AGNs that are not identified using IR-AGN techniques include both sources that are not detected by IRAC and have high accretion rates and low stellar masses and sources that are detected by IRAC that have low to moderate specific accretion rates and high stellar masses. Some of the sources that are not IRAC detected are from fields (`ES1`, *XMM*, and $\texttt{COSMOS}_{\texttt{Shallow}}$) with shallow IRAC data. For these luminous sources, we do not find any significant difference in the HRs of the X-ray AGN and IR-AGN samples, suggesting similar numbers of obscured sources. The X-ray sources with IRAC detections that are not IR-AGN selected have lower specific accretion rates and reside in red, massive galaxies and have large IR to X-ray luminosities. This suggests that they are not being identified by the IR-AGN techniques due to a bright galaxy component in the MIR due to the 1.6 μm stellar bump which is dominating the AGN light. They contribute to the large rise in the fraction of red massive galaxies that have a X-ray AGN. This accounts in part for the significant population of X-ray AGNs that is not identified by either IR-AGN technique.

3.9 Conclusions

In this paper, we compare the completeness, contamination, overlap and uniqueness of *Spitzer*/IRAC and X-ray-identified AGNs. We quantify the differences in X-ray AGNs and IR-AGN selection techniques due to IR and X-ray survey depths, X-ray obscuration, and survey completeness to assess the usefulness of these techniques to identify obscured AGNs. We use *Spitzer*/IRAC data, *XMM-Newton*, and *Chandra* X-ray data at multiple depths to construct the largest sample of IR and X-ray-selected AGNs to date. We focus on the Stern et al. (2005) and Donley et al. (2012) selection techniques which select AGNs that dominate the MIR with a red power-law SED. We statistically compare the IR-AGN populations against X-ray-selected AGN samples. The combination of multiple X-ray and IRAC depth surveys in four fields (CDFS, ES1, COSMOS, and XMM) allows us to study the overlap and uniqueness of the AGN selections as a function of both IR and X-ray depth; having multiple fields also reduces cosmic variance. This gives us a large sample with 9005 Stern et al. IR-AGNs, 3569 Donley et al. IR-AGNs and 4886 X-ray AGNs. Characterizing the variation of the samples as a function of survey depth also allows us to probe the bias and contamination of individual identification techniques.

We take advantage of the ∼1,500 secure PRIMUS redshifts in these fields to probe the intrinsic properties of the AGNs, including luminosity, specific accretion rate, and HR, as well as properties of the host galaxies, including color and stellar mass. We compare the AGN properties of the IR-AGN versus X-ray AGN samples and compare their host galaxies to the full PRIMUS galaxy population. The main results from our work are as follows:

1. IR-AGN selection identifies predominantly luminous AGNs, with $L_{3.6\mu m} \sim 10^{44.5}$ erg s^{-1} and $L_{\rm X} \sim 10^{43.5}$ erg s^{-1}. X-ray AGN selection identifies a larger population of AGNs, including those with lower luminosities and/or lower accretion rates, where the host galaxy light dominates the MIR emission. These AGNs are found throughout IRAC color–color space, with the bulk not easily identified using IR-AGN selection. These results indicate that IR-AGN selection techniques are not as efficient as X-ray selection in

identifying complete AGN samples.

2. IR-AGN selection does not identify a substantial population of obscured AGNs relative to X-ray samples. However, ∼10% of IR-AGNs are not detected in extremely deep X-ray data, setting an upper limit on the fraction that could be very heavily obscured, Compton-thick sources.
3. Stern et al. IR-AGN selection is contaminated by non-AGNs at specific redshifts ($z \sim 0.3$, $z \sim 1.1$, and $z \gtrsim 2.5$). The level of contamination depends on depth and is not significant at shallow (e.g., `SWIRE`) IR depths. Donley et al. IR-AGN selection is not contaminated.
4. IR-AGN and X-ray AGN samples both preferentially identify AGNs in massive galaxies. They further both identify AGNs in red and blue host galaxies, with a similar ratio of red to blue galaxies. The host galaxy stellar masses and colors are therefore quite comparable between IR and X-ray AGN selection.
5. Both the Stern et al. and Donley et al. IR-AGN samples identify AGNs with high specific accretion rates relative to the X-ray-detected AGN sample. The low and moderate accretion rate AGNs identified only in X-rays have large stellar mass host galaxies, which dominate the MIR SED. There are also high accretion rate X-ray AGNs that are not identified by either IR-AGN technique, which lack IRAC detections.

We find that the majority of current X-ray and IR surveys in cosmological fields are often not well matched in depth, in that the X-ray data are generally significantly deeper than the IR data. For example, a pure AGN SED shows that `GOODS`-depth IRAC data and ∼20 ks X-ray data will probe roughly the same intrinsic AGN luminosity. Therefore, while existing deep X-ray surveys ensure that we have a fairly complete X-ray AGN sample, deeper IR surveys are needed to build a comparably complete IR AGN sample. Moreover, larger shallow and wide X-ray surveys can be used to accurately compare to the luminous IR-AGN samples from these shallower and wider IR surveys.

IR and X-ray AGN selections appear to identify fairly similar AGN populations in similar high stellar mass galaxies, with no strong preference for either red or blue host galaxies. There is a large overlap between these selections, though IR selection preferentially identifies brighter AGNs. However IR-AGN selection techniques do identify a small population (∼10%) that is not identified in extremely deep X-ray surveys and could be very heavily obscured. A combined IR and X-ray AGN selection will identify a more complete sample than either selection alone, including both heavily obscured AGNs and AGNs that are under-luminous relative to their host galaxies.

3.10 Acknowledgments

We thank our anonymous referee and Jennifer Donley for useful comments that have improved this paper. We gratefully acknowledge helpful discussions and feedback from Ramin Skibba. Funding for PRIMUS has been provided by NSF Grants AST-0607701, 0908246, 0908442, 0908354, and NASA Grant 08-ADP08-0019. ALC acknowledges support from the Alfred P. Sloan Foundation and NSF CAREER Award AST-1055081. AJM and JA acknowledge support from NASA Grant NNX12AE23G through the Astrophysics Data Analysis Program.

We thank the CFHTLS, COSMOS, DLS, and SWIRE teams for their public data releases and/or access to early releases. This paper includes data gathered with the 6.5 m Magellan Telescopes located at Las Campanas Observatory, Chile. We thank the support staff at LCO for their help during our observations, and we acknowledge the use of community access through NOAO observing time. Some of the data used for this project are from the CFHTLS public data release, which includes observations obtained with MegaPrime/MegaCam, a joint project of CFHT and CEA/DAPNIA, at the Canada-France-Hawaii Telescope (CFHT) which is operated by the National Research Council (NRC) of Canada, the Institut National des Science de l'Univers of the Centre National de la Recherche Scientifique (CNRS) of France, and the University of Hawaii. This work is based in part on data products produced at TERAPIX and the Canadian Astronomy Data Centre as part of the Canada-France-Hawaii Telescope Legacy Survey, a collaborative project of NRC and CNRS. We also thank those who have built and operate the Chandra and XMM-Newton X-Ray Observatories. This research has made use of the NASA/IPAC Infrared Science Archive, which is operated by the Jet Propulsion Laboratory, California Institute of Technology, under contract with the National Aeronautics and Space Administration.

This chapter, in full (with minor exceptions to conform to this thesis), is a reprint of material previously published as "PRIMUS: Infrared and X-ray AGN Selection Techniques at $0.2 < z < 1.2$", by Alexander J. Mendez, Alison L. Coil, James Aird, Aleksandar M. Diamond-Stanic, John Moustakas, Michael R. Blanton, Richard J. Cool, Daniel J. Eisenstein, Kenneth C. Wong, & Guangtun Zhu, published in the The Astrophysical Journal, 2013, Vol. 770, p. 40. I was the primary investigator and author of this paper.

Table 3.1: IRAC and X-Ray Flux Limits

Field	X-Ray Depth	IR Depth	IRAC $f_{5.8\mu m}$ Limit [μJy]	X-ray $f_{\rm X}$ Limit [erg s^{-1}cm^{-2}]
CDFS	∼2Ms	`GOODS`	20.0	1.8×10^{-16}
		`COSMOS`	44.7	1.8×10^{-16}
		`SWIRE`	100.0	1.8×10^{-16}
	∼200ks	`GOODS`	20.0	7.1×10^{-16}
		`COSMOS`	44.7	7.1×10^{-16}
		`SWIRE`	100.0	7.1×10^{-16}
COSMOS	∼160ks	`COSMOS`	44.7	7.1×10^{-16}
	∼40ks		44.7	2.8×10^{-15}
ES1	∼40ks	`SWIRE`	100.0	2.8×10^{-15}
XMM	∼50-100ks	`SWIRE`	100.0	7.1×10^{-16}
	∼10-50ks		100.0	5.6×10^{-15}

Table 3.2: Field Areas and Overlap

			Area [deg^2]			Overlap Area [deg^2]			
Field	X-Ray Depth	IR Depth	X-ray	IRAC	PRIMUS	IRAC X-Ray	PRIMUS IRAC	PRIMUS X-Ray	PRIMUS IRAC X-Ray
CDFS	~2Ms	`GOODS`	0.12	0.06	2.90	0.06	0.06	0.12	0.06
		`COSMOS`	0.12	0.44	2.90	0.12	0.21	0.12	0.12
		`SWIRE`	0.12	7.24	2.90	0.12	2.57	0.12	0.12
	~200ks	`GOODS`	0.31	0.06	2.90	0.06	0.06	0.18	0.06
		`COSMOS`	0.31	0.44	2.90	0.30	0.21	0.18	0.18
		`SWIRE`	0.31	7.24	2.90	0.31	2.57	0.18	0.18
COSMOS	~160ks	`COSMOS`	1.00	2.61	1.18	1.00	1.18	0.81	0.81
	~40ks		2.16	2.61	1.18	2.16	1.18	1.18	1.18
ES1	~40ks	`SWIRE`	0.64	6.03	1.03	0.64	1.03	0.59	0.59
XMM	~50-100ks	`SWIRE`	1.07	8.28	3.41	1.03	3.37	0.91	0.88
	~10-50ks		5.43	8.28	3.41	4.07	3.37	1.30	1.30

Table 3.3: IR-AGN and X-ray AGN sample sizes

	Limits		Weighted Number/deg^2 (Raw Number)			Overlap Weighted Number/deg^2 (Raw Number)			
Field	X-Ray Depth	IR Depth	X-Ray[a]	Stern	Donley	Stern Donley	Stern X-Ray[a]	Donley X-Ray[a]	Stern Donley X-Ray[a]
CDFS	∼2Ms	`GOODS`	5055 (176)	2477 (115)	1118 (53)	1118 (53)	1769 (74)	928 (42)	928 (42)
		`COSMOS`	4912 (245)	1135 (91)	709 (59)	709 (59)	996 (74)	627 (49)	627 (49)
		`SWIRE`	4912 (245)	336 (33)	269 (26)	269 (26)	303 (29)	244 (23)	244 (23)
	∼200ks	`GOODS`	2204 (81)	1598 (84)	729 (38)	729 (38)	752 (35)	436 (21)	436 (21)
		`COSMOS`	2077 (418)	961 (240)	521 (139)	521 (139)	787 (187)	436 (113)	436 (113)
		`SWIRE`	2073 (421)	349 (96)	244 (69)	244 (69)	317 (86)	218 (61)	218 (61)
COSMOS	∼160ks	`COSMOS`	2067 (1176)	972 (766)	556 (443)	549 (436)	717 (510)	438 (324)	433 (320)
	∼40ks		750 (1104)	700 (1279)	408 (744)	403 (735)	399 (628)	256 (416)	253 (411)
ES1	∼40ks	`SWIRE`	740 (162)	345 (133)	259 (99)	257 (98)	250 (72)	182 (50)	180 (49)
XMM	∼50-100ks	`SWIRE`	2167 (1083)	348 (306)	244 (226)	242 (224)	295 (251)	198 (178)	198 (178)
	∼10-50ks		371 (892)	272 (902)	214 (717)	212 (709)	151 (409)	111 (296)	111 (296)

[a] For distributions where we require X-ray detections, we use the X-ray completeness weights.

Table 3.4: Stern et al. IR-AGN and X-ray AGN overlap fraction

Field	X-Ray Depth	IR Depth	Percent of IR-AGNs that are X-ray-Detected	Percent of X-Ray that are IR-AGN-Selected	Fraction of Total Sample detected by both	IR-AGNs Percent Increase to Total Sample Size	X-Ray AGNs Percent Increase to Total Sample Size
CDFS	$\sim$2Ms	GOODS	71.4%±0.9%	35.0%±0.7%	30.7%±0.6%	12.3%±0.4%	57.0%±0.7%
		COSMOS	87.7%±1.0%	20.3%±0.6%	19.7%±0.6%	2.8%±0.2%	77.5%±0.6%
		SWIRE	90%±2%	6.2%±0.3%	6.1%±0.3%	0.7%±0.1%	93.2%±0.4%
	$\sim$200ks	GOODS	47%±1%	34%±1%	24.7%±0.8%	27.7%±0.8%	47.6%±0.9%
		COSMOS	82%±1%	38%±1%	35%±1%	7.7%±0.6%	57%±1%
		SWIRE	91%±2%	15.3%±0.8%	15.0%±0.8%	1.5%±0.3%	83.4%±0.8%
COSMOS	$\sim$160ks	COSMOS	74%±1%	35%±1%	30.9%±1.0%	11.0%±0.6%	58%±1%
	$\sim$40ks		57%±2%	53%±2%	38%±1%	29%±1%	33%±1%
ES1	$\sim$40ks	SWIRE	72%±2%	34%±2%	30%±2%	11%±1%	59%±2%
XMM	$\sim$50-100ks	SWIRE	85%±2%	13.6%±0.7%	13.3%±0.7%	2.4%±0.3%	84.3%±0.8%
	$\sim$10-50ks		55%±3%	41%±3%	31%±2%	25%±2%	45%±2%

Table 3.5: Donley et al. IR-AGN and X-ray AGN overlap fraction

Field	X-Ray Depth	IR Depth	Percent of IR-AGNs that are X-ray-Detected	Percent of X-Ray that are IR-AGN-Selected	Fraction of Total Sample detected by both	IR-AGNs Percent Increase to Total Sample Size	X-Ray AGNs Percent Increase to Total Sample Size
CDFS	∼2Ms	`GOODS`	83%±1%	18.4%±0.5%	17.7%±0.5%	3.6%±0.3%	78.7%±0.6%
		`COSMOS`	88%±1%	12.8%±0.5%	12.6%±0.5%	1.6%±0.2%	85.8%±0.5%
		`SWIRE`	91%±2%	5.0%±0.3%	4.9%±0.3%	0.5%±0.1%	94.6%±0.3%
	∼200ks	`GOODS`	60%±2%	19.8%±0.8%	17.5%±0.8%	11.7%±0.6%	70.8%±0.9%
		`COSMOS`	84%±2%	21.0%±0.9%	20.2%±0.9%	3.9%±0.4%	75.9%±0.9%
		`SWIRE`	89%±2%	10.5%±0.7%	10.4%±0.7%	1.2%±0.2%	88.4%±0.7%
COSMOS	∼160ks	`COSMOS`	79%±2%	21.2%±0.9%	20.0%±0.9%	5.4%±0.5%	74.5%±0.9%
	∼40ks		63%±2%	34%±2%	28%±2%	17%±1%	55%±2%
ES1	∼40ks	`SWIRE`	70%±3%	25%±2%	22%±1%	9%±1%	68%±2%
XMM	∼50-100ks	`SWIRE`	81%±3%	9.1%±0.6%	8.9%±0.6%	2.1%±0.3%	89.0%±0.7%
	∼10-50ks		52%±3%	30%±2%	23%±2%	22%±2%	55%±2%

Table 3.6: Stern et al. IR-AGN and X-Ray AGN fractions without X-Ray Weights

Field	X-Ray Depth	IR Depth	Percent of IR-AGNs that are X-ray-Detected	Percent of X-Ray that are IR-AGN-Selected	Fraction of Total Sample detected by both	IR-AGNs Percent Increase to Total Sample Size	X-Ray AGNs Percent Increase to Total Sample Size
CDFS	$\sim$2Ms	GOODS	46%±1%	19.9%±0.7%	16.1%±0.6%	18.9%±0.6%	65.0%±0.8%
		COSMOS	67%±2%	14.3%±0.8%	13.4%±0.7%	6.5%±0.5%	80.2%±0.9%
		SWIRE	79%±3%	6.1%±0.5%	6.0%±0.5%	1.6%±0.3%	92.4%±0.6%
	$\sim$200ks	GOODS	36%±1%	33%±1%	20.8%±0.9%	38%±1%	42%±1%
		COSMOS	64%±2%	22%±1%	20%±1%	11.3%±0.8%	69%±1%
		SWIRE	81%±3%	10.0%±0.8%	9.7%±0.8%	2.3%±0.4%	87.9%±0.9%
COSMOS	$\sim$160ks	COSMOS	54%±2%	25%±1%	21%±1%	18%±1%	61%±1%
	$\sim$40ks		40%±2%	40%±2%	25%±2%	37%±2%	38%±2%
ES1	$\sim$40ks	SWIRE	40%±4%	25%±3%	18%±2%	27%±2%	54%±3%
XMM	$\sim$50-100ks	SWIRE	71%±3%	13%±1%	12.0%±1.0%	4.8%±0.6%	83%±1%
	$\sim$10-50ks		37%±3%	33%±3%	21%±2%	36%±3%	43%±3%

Table 3.7: Donley et al. IR-AGN and X-Ray AGN fractions without X-Ray Weights

Field	X-Ray Depth	IR Depth	Percent of IR-AGNs that are X-ray-Detected	Percent of X-Ray that are IR-AGN-Selected	Fraction of Total Sample detected by both	IR-AGNs Percent Increase to Total Sample Size	X-Ray AGNs Percent Increase to Total Sample Size
CDFS	∼2Ms	`GOODS`	68%±2%	13.1%±0.6%	12.3%±0.6%	5.9%±0.4%	81.8%±0.7%
		`COSMOS`	70%±3%	9.4%±0.7%	9.0%±0.6%	3.9%±0.4%	87.1%±0.7%
		`SWIRE`	82%±3%	5.7%±0.5%	5.6%±0.5%	1.2%±0.2%	93.1%±0.6%
	∼200ks	`GOODS`	50%±2%	21%±1%	17.3%±0.9%	17.3%±0.9%	65%±1%
		`COSMOS`	72%±3%	15.8%±1.0%	14.9%±0.9%	5.9%±0.6%	79%±1%
		`SWIRE`	83%±3%	9.0%±0.8%	8.9%±0.8%	1.9%±0.4%	89.3%±0.8%
COSMOS	∼160ks	`COSMOS`	66%±3%	19%±1%	17%±1%	9.2%±0.8%	73%±1%
	∼40ks		51%±3%	30%±2%	23%±2%	23%±2%	54%±2%
ES1	∼40ks	`SWIRE`	38%±4%	19%±2%	14%±2%	23%±2%	63%±3%
XMM	∼50-100ks	`SWIRE`	71%±4%	11.1%±1.0%	10.6%±0.9%	4.2%±0.6%	85%±1%
	∼10-50ks		35%±4%	26%±3%	17%±2%	32%±3%	50%±3%

3.11 References

Aird, J., Nandra, K., Laird, E. S., Georgakakis, A., Ashby, M. L. N., Barmby, P., Coil, A. L., Huang, J.-S., Koekemoer, A. M., Steidel, C. C., & Willmer, C. N. A. 2010, MNRAS, 401, 2531–2551

Aird, J., Coil, A. L., Moustakas, J., Blanton, M. R., Burles, S. M., Cool, R. J., Eisenstein, D. J., Smith, M. S. M., Wong, K. C., & Zhu, G. 2012, ApJ, 746, 90

Akylas, A., Georgakakis, A., Georgantopoulos, I., Brightman, M., & Nandra, K. 2012, A&A, 546, A98

Alonso-Herrero, A., Pérez-González, P. G., Alexander, D. M., Rieke, G. H., Rigopoulou, D., Le Floc'h, E., Barmby, P., Papovich, C., Rigby, J. R., Bauer, F. E., Brandt, W. N., Egami, E., Willner, S. P., Dole, H., & Huang, J.-S. 2006, ApJ, 640, 167–184

Assef, R. J., Kochanek, C. S., Brodwin, M., Cool, R., Forman, W., Gonzalez, A. H., Hickox, R. C., Jones, C., Le Floc'h, E., Moustakas, J., Murray, S. S., & Stern, D. 2010, ApJ, 713, 970–985

Ballantyne, D. R., Draper, A. R., Madsen, K. K., Rigby, J. R., & Treister, E. 2011, ApJ, 736, 56

Barmby, P., Alonso-Herrero, A., Donley, J. L., Egami, E., Fazio, G. G., Georgakakis, A., Huang, J.-S., Laird, E. S., Miyazaki, S., Nandra, K., Park, S. Q., Pérez-González, P. G., Rieke, G. H., Rigby, J. R., & Willner, S. P. 2006, ApJ, 642, 126–139

Bell, E. F., & de Jong, R. S. 2001, ApJ, 550, 212

Blanton, M. R., & Roweis, S. 2007, AJ, 133, 734

Boyle, B. J., & Terlevich, R. J. 1998, MNRAS, 293, L49–L51

Brightman, M., & Ueda, Y. 2012, MNRAS, 423, 702–717

Brusa, M., Zamorani, G., Comastri, A., Hasinger, G., Cappelluti, N., Civano, F., Finoguenov, A., Mainieri, V., Salvato, M., Vignali, C., Elvis, M., Fiore, F., Gilli, R., Impey, C. D., Lilly, S. J., Mignoli, M., Silverman, J., Trump, J., Urry, C. M., Bender, R., Capak, P., Huchra, J. P., Kneib, J. P., Koekemoer, A., Leauthaud, A., Lehmann, I., Massey, R., Matute, I., McCarthy, P. J., McCracken, H. J., Rhodes, J., Scoville, N. Z., Taniguchi, Y., & Thompson, D. 2007, ApJS, 172, 353–367

Bruzual, G., & Charlot, S. 2003, MNRAS, 344, 1000–1028

Cardamone, C. N., Urry, C. M., Damen, M., van Dokkum, P., Treister, E., Labbé, I., Virani, S. N., Lira, P., & Gawiser, E. 2008, ApJ, 680, 130–142

Chabrier, G. 2003, PASP, 115, 763–795

Ciliegi, P., Zamorani, G., Hasinger, G., Lehmann, I., Szokoly, G., & Wilson, G. 2003, A&A, 398, 901–918

Coil, A. L., Blanton, M. R., Burles, S. M., Cool, R. J., Eisenstein, D. J., Moustakas, J., Wong, K. C., Zhu, G., Aird, J., Bernstein, R. A., Bolton, A. S., & Hogg, D. W. 2011, ApJ, 741, 8

Cool, R. J., Moustakas, J., Blanton, M. R., Burles, S. M., Coil, A. L., Eisenstein, D. J., Wong, K. C., Zhu, G., Aird, J., Bernstein, R. A., Bolton, A. S., Hogg, D. W., & Mendez, A. J. 2013, ApJ, 767, 118

Damen, M., Labbé, I., van Dokkum, P. G., Franx, M., Taylor, E. N., Brandt, W. N., Dickinson, M., Gawiser, E., Illingworth, G. D., Kriek, M., Marchesini, D., Muzzin, A., Papovich, C., & Rix, H.-W. 2011, ApJ, 727, 1–+

Donley, J. L., Rieke, G. H., Pérez-González, P. G., Rigby, J. R., Alonso-Herrero, A., & Test, T. 2007, ApJ, 660, 167–190

Donley, J. L., Rieke, G. H., Pérez-González, P. G., & Barro, G. 2008, ApJ, 687, 111–132

Donley, J. L., Koekemoer, A. M., Brusa, M., Capak, P., Cardamone, C. N., Civano, F., Ilbert, O., Impey, C. D., Kartaltepe, J. S., Miyaji, T., Salvato, M., Sanders, D. B., Trump, J. R., & Zamorani, G. 2012, ApJ, 748, 142

Eckart, M. E., McGreer, I. D., Stern, D., Harrison, F. A., & Helfand, D. J. 2010, ApJ, 708, 584–597

Elvis, M., Wilkes, B. J., McDowell, J. C., Green, R. F., Bechtold, J., Willner, S. P., Oey, M. S., Polomski, E., & Cutri, R. 1994, ApJS, 95, 1–68

Elvis, M., Civano, F., Vignali, C., Puccetti, S., Fiore, F., Cappelluti, N., Aldcroft, T. L., Fruscione, A., Zamorani, G., Comastri, A., Brusa, M., Gilli, R., Miyaji, T., Damiani, F., Koekemoer, A. M., Finoguenov, A., Brunner, H., Urry, C. M., Silverman, J., Mainieri, V., Hasinger, G., Griffiths, R., Carollo, M., Hao, H., Guzzo, L., Blain, A., Calzetti, D., Carilli, C., Capak, P., Ettori, S., Fabbiano, G., Impey, C., Lilly, S., Mobasher, B., Rich, M., Salvato, M., Sanders, D. B., Schinnerer, E., Scoville, N., Shopbell, P., Taylor, J. E., Taniguchi, Y., & Volonteri, M. 2009, ApJS, 184, 158–171

Fazio, G. G., Hora, J. L., Allen, L. E., Ashby, M. L. N., Barmby, P., Deutsch, L. K., Huang, J.-S., Kleiner, S., Marengo, M., Megeath, S. T., Melnick, G. J., Pahre, M. A., Patten, B. M., Polizotti, J., Smith, H. A., Taylor, R. S., Wang, Z., Willner, S. P., Hoffmann, W. F., Pipher, J. L., Forrest, W. J., McMurty, C. W., McCreight, C. R., McKelvey, M. E., McMurray, R. E., Koch, D. G., Moseley, S. H., Arendt, R. G., Mentzell, J. E., Marx, C. T., Losch, P., Mayman, P., Eichhorn, W., Krebs, D., Jhabvala, M., Gezari, D. Y., Fixsen, D. J., Flores, J., Shakoorzadeh, K., Jungo, R., Hakun, C., Workman, L., Karpati, G., Kichak, R., Whitley, R., Mann, S., Tollestrup, E. V., Eisenhardt, P., Stern, D., Gorjian, V., Bhattacharya, B., Carey, S., Nelson, B. O., Glaccum, W. J., Lacy, M., Lowrance, P. J., Laine, S., Reach, W. T., Stauffer, J. A., Surace, J. A., Wilson, G., Wright, E. L., Hoffman, A., Domingo, G., & Cohen, M. 2004, ApJS, 154, 10–17

Ferrarese, L., & Merritt, D. 2000, ApJL, 539, L9–L12

Gebhardt, K., Bender, R., Bower, G., Dressler, A., Faber, S. M., Filippenko, A. V., Green, R., Grillmair, C., Ho, L. C., Kormendy, J., Lauer, T. R., Magorrian, J., Pinkney, J., Richstone, D., & Tremaine, S. 2000, ApJL, 539, L13–L16

Georgakakis, A., Nandra, K., Laird, E. S., Aird, J., & Trichas, M. 2008, MNRAS, 388, 1205–1213

Georgantopoulos, I., Georgakakis, A., Rowan-Robinson, M., & Rovilos, E. 2008, A&A, 484, 671–678

Georgantopoulos, I., Akylas, A., Georgakakis, A., & Rowan-Robinson, M. 2009, A&A, 507, 747–756

Gilli, R., Daddi, E., Chary, R., Dickinson, M., Elbaz, D., Giavalisco, M., Kitzbichler, M., Stern, D., & Vanzella, E. 2007, A&A, 475, 83–99

Hasinger, G. 2008, A&A, 490, 905–922

Hasinger, G., Cappelluti, N., Brunner, H., Brusa, M., Comastri, A., Elvis, M., Finoguenov, A., Fiore, F., Franceschini, A., Gilli, R., Griffiths, R. E., Lehmann, I., Mainieri, V., Matt, G., Matute, I., Miyaji, T., Molendi, S., Paltani, S., Sanders, D. B., Scoville, N., Tresse, L., Urry, C. M., Vettolani, P., & Zamorani, G. 2007, ApJS, 172, 29–37

Hickox, R. C., Jones, C., Forman, W. R., Murray, S. S., Brodwin, M., Brown, M. J. I., Eisenhardt, P. R., Stern, D., Kochanek, C. S., Eisenstein, D., Cool, R. J., Jannuzi, B. T., Dey, A., Brand, K., Gorjian, V., & Caldwell, N. 2007, ApJ, 671, 1365–1387

Hickox, R. C., Jones, C., Forman, W. R., Murray, S. S., Kochanek, C. S., Eisenstein, D., Jannuzi, B. T., Dey, A., Brown, M. J. I., Stern, D., Eisenhardt, P. R., Gorjian, V., Brodwin, M., Narayan, R., Cool, R. J., Kenter, A., Caldwell, N., & Anderson, M. E. 2009, ApJ, 696, 891–919

Hopkins, P. F., Richards, G. T., & Hernquist, L. 2007, ApJ, 654, 731–753

Ivison, R. J., Greve, T. R., Serjeant, S., Bertoldi, F., Egami, E., Mortier, A. M. J., Alonso-Herrero, A., Barmby, P., Bei, L., Dole, H., Engelbracht, C. W., Fazio, G. G., Frayer, D. T., Gordon, K. D., Hines, D. C., Huang, J.-S., Le Floc'h, E., Misselt, K. A., Miyazaki, S., Morrison, J. E., Papovich, C., Pérez-González, P. G., Rieke, M. J., Rieke, G. H., Rigby, J., Rigopoulou, D., Smail, I., Wilson, G., & Willner, S. P. 2004, ApJS, 154, 124–129

Lacy, M., Storrie-Lombardi, L. J., Sajina, A., Appleton, P. N., Armus, L., Chapman, S. C., Choi, P. I., Fadda, D., Fang, F., Frayer, D. T., Heinrichsen, I., Helou, G., Im, M., Marleau, F. R., Masci, F., Shupe, D. L., Soifer, B. T., Surace, J., Teplitz, H. I., Wilson, G., & Yan, L. 2004, ApJS, 154, 166–169

Laird, E. S., Nandra, K., Georgakakis, A., Aird, J. A., Barmby, P., Conselice, C. J., Coil, A. L., Davis, M., Faber, S. M., Fazio, G. G., Guhathakurta, P., Koo, D. C., Sarajedini, V., & Willmer, C. N. A. 2009, ApJS, 180, 102–116

Lehmer, B. D., Brandt, W. N., Alexander, D. M., Bauer, F. E., Schneider, D. P., Tozzi, P., Bergeron, J., Garmire, G. P., Giacconi, R., Gilli, R., Hasinger, G., Hornschemeier, A. E., Koekemoer, A. M., Mainieri, V., Miyaji, T., Nonino, M., Rosati, P., Silverman, J. D., Szokoly, G., & Vignali, C. 2005, ApJS, 161, 21–40

Lehmer, B. D., Xue, Y. Q., Brandt, W. N., Alexander, D. M., Bauer, F. E., Brusa, M., Comastri, A., Gilli, R., Hornschemeier, A. E., Luo, B., Paolillo, M., Ptak, A., Shemmer, O., Schneider, D. P., Tozzi, P., & Vignali, C. 2012, ApJ, 752, 46

Lonsdale, C. J., Smith, H. E., Rowan-Robinson, M., Surace, J., Shupe, D., Xu, C., Oliver, S., Padgett, D., Fang, F., Conrow, T., Franceschini, A., Gautier, N., Griffin, M., Hacking, P., Masci, F., Morrison, G., O'Linger, J., Owen, F., Pérez-Fournon, I., Pierre, M., Puetter, R., Stacey, G., Castro, S., Polletta, M. d. C., Farrah, D., Jarrett, T., Frayer, D., Siana, B., Babbedge, T., Dye, S., Fox, M., Gonzalez-Solares, E., Salaman, M., Berta, S., Condon, J. J., Dole, H., & Serjeant, S. 2003, PASP, 115, 897–927

Low, J., & Kleinmann, D. E. 1968, AJ, 73, 868

Luo, B., Bauer, F. E., Brandt, W. N., Alexander, D. M., Lehmer, B. D., Schneider, D. P., Brusa, M., Comastri, A., Fabian, A. C., Finoguenov, A., Gilli, R., Hasinger, G., Hornschemeier, A. E., Koekemoer, A., Mainieri, V., Paolillo, M., Rosati, P., Shemmer, O., Silverman, J. D., Smail, I., Steffen, A. T., & Vignali, C. 2008, ApJS, 179, 19–36

Magorrian, J., Tremaine, S., Richstone, D., Bender, R., Bower, G., Dressler, A., Faber, S. M., Gebhardt, K., Green, R., Grillmair, C., Kormendy, J., & Lauer, T. 1998, AJ, 115, 2285–2305

Martin, D. C., Wyder, T. K., Schiminovich, D., Barlow, T. A., Forster, K., Friedman, P. G., Morrissey, P., Neff, S. G., Seibert, M., Small, T., Welsh, B. Y., Bianchi, L., Donas, J., Heckman, T. M., Lee, Y.-W., Madore, B. F., Milliard, B., Rich, R. M., Szalay, A. S., & Yi, S. K. 2007, ApJS, 173, 342–356

Mateos, S., Alonso-Herrero, A., Carrera, F. J., Blain, A., Watson, M. G., Barcons, X., Braito, V., Severgnini, P., Donley, J. L., & Stern, D. 2012, MNRAS, 426, 3271–3281

Messias, H., Afonso, J., Salvato, M., Mobasher, B., & Hopkins, A. M. 2012, ApJ, 754, 120

Moustakas, J., Coil, A. L., Aird, J., Blanton, M. R., Cool, R. J., Eisenstein, D. J., Mendez, A. J., Wong, K. C., Zhu, G., & Arnouts, S. 2013, ApJ, 767, 50

Mushotzky, R. 2004, In Supermassive Black Holes in the Distant Universe, A. J. Barger, ed., volume 308 of *Astrophysics and Space Science Library*, p. 53

Nandra, K., Georgakakis, A., Willmer, C. N. A., Cooper, M. C., Croton, D. J., Davis, M., Faber, S. M., Koo, D. C., Laird, E. S., & Newman, J. A. 2007, ApJL, 660, L11–L14

Neugebauer, G., Oke, J. B., Becklin, E. E., & Matthews, K. 1979, ApJ, 230, 79–94

Park, S. Q., Barmby, P., Willner, S. P., Ashby, M. L. N., Fazio, G. G., Georgakakis, A., Ivison, R. J., Konidaris, N. P., Miyazaki, S., Nandra, K., & Rosario, D. J. 2010, ApJ, 717, 1181–1201

Pierre, M., Chiappetti, L., Pacaud, F., Gueguen, A., Libbrecht, C., Altieri, B., Aussel, H., Gandhi, P., Garcet, O., Gosset, E., Paioro, L., Ponman, T. J., Read, A. M., Refregier, A., Starck, J.-L., Surdej, J., Valtchanov, I., Adami, C., Alloin, D., Alshino, A., Andreon, S., Birkinshaw, M., Bremer, M., Detal, A., Duc, P.-A., Galaz, G., Jones, L., Le Fèvre, J.-P., Le Fèvre, O., Maccagni, D., Mazure, A., Quintana, H., Röttgering, H. J. A., Sprimont, P.-G., Tasse, C., Trinchieri, G., & Willis, J. P. 2007, MNRAS, 382, 279–290

Polletta, M., Weedman, D., Hönig, S., Lonsdale, C. J., Smith, H. E., & Houck, J. 2008, ApJ, 675, 960–984

Polletta, M. d. C., Wilkes, B. J., Siana, B., Lonsdale, C. J., Kilgard, R., Smith, H. E., Kim, D.-W., Owen, F., Efstathiou, A., Jarrett, T., Stacey, G., Franceschini, A., Rowan-Robinson, M., Babbedge, T. S. R., Berta, S., Fang, F., Farrah, D., González-Solares, E., Morrison, G., Surace, J. A., & Shupe, D. L. 2006, ApJ, 642, 673–693

Puccetti, S., Fiore, F., D'Elia, V., Pillitteri, I., Feruglio, C., Grazian, A., Brusa, M., Ciliegi, P., Comastri, A., Gruppioni, C., Mignoli, M., Vignali, C., Zamorani, G., La Franca, F., Sacchi, N., Franceschini, A., Berta, S., Buttery, H., & Dias, J. E. 2006, A&A, 457, 501–515

Richards, G. T., Lacy, M., Storrie-Lombardi, L. J., Hall, P. B., Gallagher, S. C., Hines, D. C., Fan, X., Papovich, C., Vanden Berk, D. E., Trammell, G. B., Schneider, D. P., Vestergaard, M., York, D. G., Jester, S., Anderson, S. F., Budavári, T., & Szalay, A. S. 2006, ApJS, 166, 470–497

Rieke, G. H., & Lebofsky, M. J. 1981, ApJ, 250, 87–97

Sanders, D. B., Salvato, M., Aussel, H., Ilbert, O., Scoville, N., Surace, J. A., Frayer, D. T., Sheth, K., Helou, G., Brooke, T., Bhattacharya, B., Yan, L., Kartaltepe, J. S., Barnes, J. E., Blain, A. W., Calzetti, D., Capak, P., Carilli, C., Carollo, C. M., Comastri, A., Daddi, E., Ellis, R. S., Elvis, M., Fall, S. M., Franceschini, A., Giavalisco, M., Hasinger, G., Impey, C., Koekemoer, A., Le Fèvre, O., Lilly, S., Liu, M. C., McCracken, H. J., Mobasher, B., Renzini, A., Rich, M., Schinnerer, E., Shopbell, P. L., Taniguchi, Y., Thompson, D. J., Urry, C. M., & Williams, J. P. 2007, ApJS, 172, 86–98

Silverman, J. D., Green, P. J., Barkhouse, W. A., Kim, D.-W., Kim, M., Wilkes, B. J., Cameron, R. A., Hasinger, G., Jannuzi, B. T., Smith, M. G., Smith, P. S., & Tananbaum, H. 2008, ApJ, 679, 118–139

Silverman, J. D., Lamareille, F., Maier, C., Lilly, S. J., Mainieri, V., Brusa, M., Cappelluti, N., Hasinger, G., Zamorani, G., Scodeggio, M., Bolzonella, M., Contini, T., Carollo, C. M., Jahnke, K., Kneib, J.-P., Le Fèvre, O., Merloni, A., Bardelli, S., Bongiorno, A., Brunner, H., Caputi, K., Civano, F., Comastri, A., Coppa, G., Cucciati, O., de la Torre, S., de Ravel, L., Elvis, M., Finoguenov, A., Fiore, F., Franzetti, P., Garilli, B., Gilli, R., Iovino, A., Kampczyk, P., Knobel, C., Kovač, K., Le Borgne, J.-F., Le Brun, V., Mignoli, M., Pello, R., Peng, Y., Perez Montero, E., Ricciardelli, E., Tanaka, M., Tasca, L., Tresse, L., Vergani, D., Vignali, C., Zucca, E., Bottini, D., Cappi, A., Cassata, P., Fumana, M., Griffiths, R., Kartaltepe, J., Koekemoer, A., Marinoni, C., McCracken, H. J., Memeo, P., Meneux, B., Oesch, P., Porciani, C., & Salvato, M. 2009, ApJ, 696, 396–410

Stern, D., Eisenhardt, P., Gorjian, V., Kochanek, C. S., Caldwell, N., Eisenstein, D., Brodwin, M., Brown, M. J. I., Cool, R., Dey, A., Green, P., Jannuzi, B. T., Murray, S. S., Pahre, M. A., & Willner, S. P. 2005, ApJ, 631, 163–168

Sutherland, W., & Saunders, W. 1992, MNRAS, 259, 413–420

Treister, E., Urry, C. M., Chatzichristou, E., Bauer, F., Alexander, D. M., Koekemoer, A., Van Duyne, J., Brandt, W. N., Bergeron, J., Stern, D., Moustakas, L. A., Chary, R.-R., Conselice, C., Cristiani, S., & Grogin, N. 2004, ApJ, 616, 123–135

Treister, E., Virani, S., Gawiser, E., Urry, C. M., Lira, P., Francke, H., Blanc, G. A., Cardamone, C. N., Damen, M., Taylor, E. N., & Schawinski, K. 2009a, ApJ, 693, 1713–1727

Treister, E., Virani, S., Gawiser, E., Urry, C. M., Lira, P., Francke, H., Blanc, G. A., Cardamone, C. N., Damen, M., Taylor, E. N., & Schawinski, K. 2009b, ApJ, 693, 1713–1727

Ueda, Y., Watson, M. G., Stewart, I. M., Akiyama, M., Schwope, A. D., Lamer, G., Ebrero, J., Carrera, F. J., Sekiguchi, K., Yamada, T., Simpson, C., Hasinger, G., & Mateos, S. 2008, ApJS, 179, 124–141

Wright, E. L., Eisenhardt, P. R. M., Mainzer, A. K., Ressler, M. E., Cutri, R. M., Jarrett, T., Kirkpatrick, J. D., Padgett, D., McMillan, R. S., Skrutskie, M., Stanford, S. A., Cohen, M., Walker, R. G., Mather, J. C., Leisawitz, D., Gautier, III, T. N., McLean, I., Benford, D., Lonsdale, C. J., Blain, A., Mendez, B., Irace, W. R., Duval, V., Liu, F., Royer, D., Heinrichsen, I., Howard, J., Shannon, M., Kendall, M., Walsh, A. L., Larsen, M., Cardon, J. G., Schick, S., Schwalm, M., Abid, M., Fabinsky, B., Naes, L., & Tsai, C.-W. 2010, AJ, 140, 1868–1881

Xue, Y. Q., Brandt, W. N., Luo, B., Rafferty, D. A., Alexander, D. M., Bauer, F. E., Lehmer, B. D., Schneider, D. P., & Silverman, J. D. 2010, ApJ, 720, 368–391

Chapter 4

Clustering of X-ray-, Radio- and IR-AGN at $z \sim 0.7$

4.1 Abstract

We present a clustering study of X-ray, radio, and mid-IR-selected active galactic nuclei (AGN) at $0.2 < z < 1.2$ using multi-wavelength imaging and spectroscopic redshifts from the PRIMUS and DEEP2 redshift surveys, covering 7 separate fields spanning ∼10 square degrees. Using the cross-correlation of AGN with dense galaxy samples, we measure the clustering scale length and slope, as well as the bias, of AGN selected at different wavelengths. We compare the clustering of each AGN sample with galaxy samples with the same stellar mass, star formation rate, and redshift distributions as the AGN host galaxies and find no significant difference in the clustering of AGN with matched galaxy samples. The observed differences in the clustering of AGN selected at different wavelengths can therefore be explained by the clustering differences of their host populations. We further find no significant difference between the clustering of obscured and unobscured AGN, using IRAC or WISE colors or X-ray hardness ratio.

4.2 Introduction

It is now well established that most galaxies host a supermassive black hole (SMBH) in their nuclei (for a review see: Kormendy & Richstone 1995; Richstone et al. 1998; Ferrarese & Ford 2005; Kormendy & Ho 2013). However, it is not well understood what physical processes can trigger intense episodes of accretion onto the SMBH, creating an observed active galactic nucleus (AGN). The broad similarities between the cosmic star formation history and AGN mass accretion history, both peaking at $z \sim 2$ and declining sharply at lower redshift (e.g., Soltan 1982;

Madau et al. 1996; Ueda et al. 2003; Franceschini et al. 1999; Zheng et al. 2009; Serjeant et al. 2010), and the relatively tight observed correlation between SMBH mass and mass of the host galaxy bulge ($M-\sigma$ relationship; e.g., Magorrian et al. 1998; Gebhardt et al. 2000; Tremaine et al. 2002) hint at the possibility of a coeval evolution between SMBHs and their host galaxies.

The vast scale difference between galaxies and SMBHs, coupled with the relative rarity of the active accretion phase, have made it difficult to determine the physical mechanism connecting galaxies and AGN. In order to understand their co-evolution, we must determine the AGN fueling source and accretion mechanism. Constraining the AGN triggering and fueling mechanism is key to inferring AGN lifetimes and uncovering the relevant physics connecting SMBHs and their host galaxies.

On the theoretical side, many studies using N-body simulations and semi-analytics models (SAM) have attempted to probe the physics of the evolution and growth of SMBH. While simulations have often had to rely on ad-hoc prescriptions for the details of AGN accretion, many suggest that galaxy mergers are important in triggering AGN (e.g., Sanders & Mirabel 1996; Di Matteo, Springel, & Hernquist 2005; Springel, Di Matteo, & Hernquist 2005a,b; Hopkins et al. 2005, 2006). Simulations have shown that mergers trigger tidal disruptions to the galactic disk which cause strong gas inflows to the inner kiloparsec, which in turn triggers bursts of star formation and may fuel the SMBH. Hopkins, Richards, & Hernquist (2007) and Snyder et al. (2011) further suggest that these merger events deepen the central potential well, increasing the binding energy, bulge mass, and velocity dispersion while fueling an AGN. If indeed AGN are due primarily to merger events, this should be observed both in the host galaxy properties. Indeed, a significant population of high-luminosity ($L_{bol} \gtrsim 10^{44}\mathrm{erg\ s^{-1}}$) optically-identified quasars at $z > 2$ are found in merging systems, adding evidence for this triggering mechanism at least for the most luminous AGN (e.g., Sanders et al. 1988; Canalizo & Stockton 2001). However, recent observations of low- and intermediate-luminosity AGN find that major mergers are *not* the dominate triggering mechanism, as many AGN are found in “normal” non-merging disk galaxies (e.g., Gabor et al. 2009; Schawinski et al. 2010; Cisternas et al. 2011; Rosario et al. 2011; Civano et al. 2012; Mullaney et al. 2012; Kocevski et al. 2012; Hickox et al. 2014).

Using merger histories derived from simulations, SAMs can quickly probe a large parameter space to study the evolution of the statistical properties of AGN (see Baugh 2006, for a review). Adopting different analytical prescriptions which connect the evolution of collapsed dark matter (DM) halos to the baryonic physics within the halos, SAMs are able to constrain the relevant physics which governs the gas processes driving AGN (e.g., Kauffmann & Haehnelt 2000; Menci et al. 2003, 2006; Croton et al. 2006; Bower et al. 2006; Cattaneo et al. 2006; Hopkins et al. 2006; Monaco, Fontanot, & Taffoni 2007; Marulli et al. 2008).

Measuring the large-scale clustering properties of AGN across a range of redshifts and luminosities provides strong constraints to theoretical models that test both internal and external triggering mechanisms. For example, Fanidakis et al. (2013) show that the observed spatial clustering of $\langle L_X \rangle \sim 10^{42}$ erg s^{-1} X-ray AGN samples since $z \sim 1$ is suggestive of two modes of accretion: one where low luminosity sources are driven by slow accretion from hot halo gas, while higher luminosity sources undergo mergers or disk instabilities, which drive their high accretion rates.

These theoretical models show that clustering measurements provide powerful constraints on AGN triggering physics. Historically, many observational clustering results utilize bright optical quasar surveys. While these surveys probe large volumes over wide areas of sky ($\lesssim 10^5\,\mathrm{deg}^2$) and cover a wide redshift range, they miss the bulk of the AGN population, which is more obscured (e.g., Risaliti et al. 1999; Ueda et al. 2003; Treister et al. 2004; Hopkins et al. 2004). They therefore do not constrain the physical mechanisms triggering the vast majority of AGN. More recently, X-ray and mid-IR AGN samples have begun to provide a more complete sample of obscured AGN. Although existing deep X-ray and IR samples with spectroscopic redshifts tend to cover much smaller areas on the sky (few, deg^2), they probe the more typical AGN population with lower luminosity and/or higher obscuration. To fully understand AGN physics, one must compare samples identified across a range of wavebands, in order to probe a more complete picture of AGN accretion.

The first robust clustering measurements of optically-selected quasars were enabled by the large 2dF QSO Redshift Survey Croom et al. (2004). Croom et al. (2005) found that the characteristic halo mass of quasars at $0.3 < z < 2.2$ is $M_{\mathrm{halo}} \sim 10^{12.5}\,\mathrm{h}^{-1}\,\mathcal{M}_{\odot}$ and did not find any significant luminosity dependent clustering in their sample. Similar halo masses for quasar hosts were estimated by Myers et al. (2006) for quasars in the Sloan Digital Sky Survey (SDSS) at $z \sim 1-2$ and by Coil et al. (2007), using the cross-correlation of quasars with galaxies in the DEEP2 survey at $z \sim 1$.

The advent of the *XMM* and *Chandra* X-ray telescopes revolutionized X-ray AGN clustering studies by targeting small fields with deep X-ray imaging. Studies of the clustering of X-ray AGN at $z \sim 1-2$ generally find that they are also strongly clustered and reside in relatively dense environments (e.g. Gilli et al. 2005; Yang et al. 2006; Puccetti et al. 2006; Coil et al. 2009; Hickox et al. 2009). Early measurements of the clustering of $z \sim 0.5-2$ X-ray AGN in single small area fields such as the *Chandra* Deep Field North (CDFN), *Chandra* Deep Field South (CDFS), and the CLASXS field (Gilli et al. 2005; Yang et al. 2006) generally found that X-ray AGN are in massive halos ($M_{\mathrm{halo}} \sim 10^{12}\,\mathrm{h}^{-1}\,\mathcal{M}_{\odot}$). Discrepancies in the clustering properties found in these first surveys were later explained by the small areas that they covered.

Later, Coil et al. (2009) measured the clustering of X-ray AGN sources at $z \sim 1$ in the AEGIS field. They used the cross-correlation of X-ray AGN sources with DEEP2 galaxies and found that the X-ray AGN sources reside in overdense regions of space. They found that X-ray AGN are as strongly clustered as red galaxies, which are more clustered than star forming galaxies. They further find that at $z \sim 1$ X-ray AGN AGN are more clustered than optically selected quasars (though only with a $\sim 2\sigma$ significance) and therefore may reside in more massive halos.

Additionally Coil et al. (2009) did not find any correlation of the clustering strength on X-ray luminosity or hardness ratio, which is an estimate of the AGN obscuration.

Concurrently, Hickox et al. (2009) studied the connection between AGN selected using X-ray, radio, and mid-IR techniques by measuring the clustering, host properties, and AGN properties of AGN in the Boötes field. They found that X-ray AGN and Radio AGN sources are in the dense environments with dark matter halos of mass $M_{\rm halo} \sim 10^{13}\,{\rm h}^{-1}\,\mathcal{M}_{\odot}$ and $M_{\rm halo} \sim 10^{13.5}\,{\rm h}^{-1}\,\mathcal{M}_{\odot}$, while IR-AGN typically reside in lower mass halos with $M_{\rm halo} < 10^{12}\,{\rm h}^{-1}\,\mathcal{M}_{\odot}$. Hickox et al. (2009) propose an evolutionary picture where star forming galaxies undergo a bright quasar phase before settling on the red sequence with a lower luminosity X-ray AGN, assuming that these objects are the same objects but at different evolutionary stages.

The measurements of the clustering of radio-loud AGN from wide-area radio surveys (e.g., NRAO VLA Sky Survey (NVSS; Condon et al. 1998) or the Faint Images of the Radio Sky at Twenty-centimeters (FIRST; Becker, White, & Helfand 1994) survey suggest that they reside in dense environments in massive halos ($M_{\rm halo} > 10^{13}\,{\rm h}^{-1}\,\mathcal{M}_{\odot}$). Magliocchetti et al. (2004) measure the clustering of Radio AGN at $z < 0.3$ and estimated a median halo mass of $M_{\rm halo} \sim 10^{13.4}\,{\rm h}^{-1}\,\mathcal{M}_{\odot}$ from the 2dF galaxy redshift survey. They found no dependence of the clustering amplitude on radio luminosity. Best et al. (2005) found that a local sample ($z < 0.3$) of $\sim 2,000$ radio-loud sources in the SDSS resides in large dark matter halos in richer environments. Mandelbaum et al. (2009) estimates the halo masses for local Radio AGN in the SDSS at $z \sim 0.1$ using weak lensing measurements and find that the dark matter halos of radio-loud sources are twice as massive as a control sample of galaxies with the same stellar masses. At somewhat higher redshifts ($z \sim 0.5$), Wake et al. (2008) find that radio-loud sources are more clustered than radio-quiet sources with similar optical luminosities and colors.

A key constraint that AGN clustering measurements provide is whether there is any luminosity-dependence to AGN clustering, which has been predicted by theoretical models. The observed differences in the clustering of X-ray AGN, Radio AGN, and IR-AGN samples hint at the possibility of different triggering mechanisms for each AGN population. In particular, Allevato et al. (2012) show that the X-ray AGN in the COSMOS field at $z < 2.2$ is more clustered than the more luminous optical quasar sample, which deviates significantly from the predictions of models where AGN activity is driven through mergers (Hopkins et al. 2006; Bonoli et al. 2009). This indicates that other mechanisms like disk/bar instabilities or tidal distributions may be triggering the lower luminosity X-ray AGN samples. They also find that Type 1 AGN are more clustered than Type 2 AGN at $z \sim 1.5$. At lower redshift $z \sim 0.1$, Cappelluti et al. (2010) using the Swift-BAT all sky survey find that low luminosity X-ray AGN to be less clustered than their high X-ray luminosity sources. Thus, the lack of significance in the correlation between the clustering amplitude and X-ray luminosity of the early X-ray AGN studies may be due to their limited size. Additionally Krumpe, Miyaji, & Coil (2010) propose a sequence of X-ray AGN clustering measurements where the strength is dominated by the host galaxy color from the clustering of broad-line quasars and soft X-ray AGN at $z \sim 0.3$ and .

The observed clustering differences between AGN selected at different wavelengths could be due in part to differences in their host populations. At $z \lesssim 2$, quiescent galaxies are more strongly clustered than star forming, blue, late-type galaxies (e.g., Le Fèvre et al. 2005; Zehavi et al. 2005; Coil et al. 2008; Skibba et al. 2014). Additionally, clustering strength correlates with luminosity of the host galaxy. The biases of each AGN selection technique may also contribute to the observed clustering differences, in that Radio AGN are generally found in quiescent galaxies, X-ray AGN are found in a mixture of quiescent and star forming galaxies, and IR-AGN are found in star forming galaxies; [e.g.,][](Hickox et al. 2009; Goulding et al. 2014; Aird et al. 2012). In order to understand this contribution, one can compare the clustering of AGN selected at different wavelengths to matched samples of inactive galaxies (e.g., Wake et al. 2008; Mandelbaum et al. 2009; Coil et al. 2009; Hickox et al. 2009). Coil et al. (2009) finds that X-ray AGN are more clustered ($\sim 2.8\sigma$) than optical color and magnitude matched galaxy samples at $z \sim 1$. At $z \sim 0.4$, Hickox et al. (2009) finds that IR-AGN are less clustered than optical color and magnitude matched samples.

Furthermore, the unified AGN model (Antonucci & Ulvestad 1985; Urry & Padovani 1995, e.g.,) would suggest that type-1 (unobscured) AGN and type-2 (obscured) AGN should reside in the same distribution of environments, with the differences in the observed obscuration due only to the orientation of the AGN relative to the observer. Proposals suggest, however, that obscured and unobscured AGN are observed at different evolutionary stages of SMBH accretion (e.g., Hopkins et al. 2008; Hickox et al. 2009). While most optical and X-ray AGN clustering studies do not find significant differences in the clustering amplitude as a function of obscuration, Hickox et al. (2011) finds a marginal ($\sim 2\sigma$) increase in the clustering amplitude between obscured and unobscured IR-AGN selected AGN at $z \sim 1.25$ in the Boötes Survey, suggesting that obscured AGN may reside in more massive halos. More recently, Donoso et al. (2013) find a significantly larger angular clustering amplitude for obscured WISE IR-AGN as compared to unobscured WISE IR-AGN at $z \sim 0.9$, suggesting that obscured sources inhabit denser environments. This result, however, uses an angular correlation function which measures the two-dimensional projected clustering, due to the lack of spectroscopic redshifts for the bulk of their sample. While they partially account for this by comparing the redshift distributions of their sources in the Boötes and COSMOS fields, the extreme large scale structure found in the COSMOS fields may limit their results.

In this paper, we measure the clustering properties of X-ray AGN, Radio AGN, and IR-AGN samples at $0.2 < z < 1.2$ using the DEEP2 and PRIMUS redshift surveys. The wealth of deep multi-wavelength data, combined with precise spectroscopic redshifts in these fields makes this sample both larger and deeper than previous studies at comparable redshifts. We use data from multiple fields, limiting the affects of cosmic variance. We measure the cross-correlation function of AGN with dense galaxy samples, used to trace the large scale structure in our fields, in order to infer the clustering of the AGN. This leads to lower statistical errors than measuring the auto-correlation function of the AGN themselves. We investigate the dependence of clustering with AGN luminosity, specific accretion rate, hardness ratio, and obscuration. We create galaxy samples that are matched in stellar mass, star formation rate (SFR), and redshift to the AGN samples identified in each waveband, to compare the clustering of AGN with similarly selected galaxies. This limits potential selection biases in comparing AGN samples selected at different wavelengths.

The paper is organized as follows. In §4.3 we present the relevant spectroscopic redshift surveys and multi-wavelength datasets used here. In §4.4 we detail the different AGN selection techniques and the AGN and galaxy samples used. In §4.6 we present the clustering measurements of the various AGN and matched galaxy samples. We discuss our results in §4.7 and conclude in §4.8. Throughout the paper we assume a standard flat ΛCDM model with $\Omega_m = 0.3$, $\Omega_\Lambda = 0.7$, and $H_0 = 72$ km s^{-1} Mpc^{-1}.

4.3 Data

Our analysis combines multi-wavelength imaging with spectroscopic redshifts from the PRIMUS and DEEP2 galaxy redshift surveys, covering eight well-known extragalactic fields: the CDFS-SWIRE field (Lonsdale et al. 2003), the COSMOS field (Scoville et al. 2007), the DEEP2 (DEEP2; Davis et al. 2003) 02hr and 23hr fields, as well as the EGS, the ES1 field (Oliver et al. 2000), and the XMM-Large Scale Structure field (XMM-LSS; Pierre et al. 2004). We describe the X-ray catalogs that we use in Section 4.3.1, the radio catalogs in Section 4.3.2, and the mid-IR catalogs in Section 4.3.3. In Section 4.3.4 and Section 4.3.5 we briefly describe the PRIMUS and DEEP2 redshift surveys, respectively. In Section 4.3.6 we explain the methods used to estimate stellar mass for PRIMUS and DEEP2 sources. In Section 4.3.7 we provide information on the spatial selection function of the PRIMUS and DEEP2 surveys that we use for our clustering analysis.

4.3.1 X-ray Imaging Data

We use existing *Chandra* and *XMM* X-ray source catalogs of various depths in the COSMOS, DEEP2, ES1, EGS, and XMM-LSS fields (see Aird et al. (2012) and Mendez et al. (2013) for details). Due to the large positional uncertainty of the X-ray point sources, we use the likelihood ratio matching technique (e.g., Sutherland & Saunders 1992; Ciliegi et al. 2003; Brusa et al. 2007; Laird et al. 2009) to identify optical counterparts to each X-ray source in each field. The likelihood-ratio technique accounts for both the optical and X-ray positional uncertainties, by calculating the probability of having a counterpart with a given magnitude above the probability of a spurious match. We place a lower limit on the positional uncertainty for the X-ray source location of $0.5''$ and require an optical match within $5''$ in any field. We restrict our sample to robust optical counterparts with likelihood ratios above > 0.5 and choose the counterpart with the largest likelihood, when there are multiple counterparts. Table 4.1 lists the area of the X-ray coverage in each field, as well as the number of X-ray sources with PRIMUS redshifts (see Section 4.3.4 for details).

In the COSMOS field, we use the public *XMM-Newton* X-ray point source catalog (Hasinger et al. 2007; Civano et al. 2012) which covers the entire 2 deg^2 to a depth of $f_{2-10\mathrm{keV}} \sim 3 \times 10^{-15}$ erg s^{-1}cm^{-2}. We further use the deeper *Chandra* data that has a depth of $f_{2-10\mathrm{keV}} \sim 8 \times 10^{-16}$ erg s^{-1}cm^{-2} and covers the central ~0.9 deg^2 (Elvis et al. 2009).

In the ES1 field, we use the Puccetti et al. (2006) point source catalog from four partially overlapping *XMM-Newton* pointings which has a depth of $f_{2-10\mathrm{keV}} \sim 2 \times 10^{-15}$ erg s^{-1}cm^{-2} and covers 0.52 deg^2 of the PRIMUS area in this field.

We use the public X-ray point source catalog from the deep *Chandra* Advanced CCD Imagining Spectrometer (ACIS-I) XDEEP2 survey (Goulding et al. 2012) for the EGS and DEEP2-02hr, DEEP2-16hr, and DEEP2-23hr fields. In the EGS the XDEEP2 survey contains 96 *Chandra* pointings across the field, covering an area of 0.66 deg^2. The typical full band flux limit in the merged observations in this field is $f_X \sim 2.8 \times 10^{-16}$ erg s^{-1}cm^{-2}, though this varies across the field due to the number of overlapping pointings. The DEEP2-02hr, DEEP2-16hr, and DEEP2-23hr fields contain 12, 12 and 17 *Chandra* pointings respectively, with a full-band flux-limit of $f_X \sim 4.6 \times 10^{-15}$ erg s^{-1}cm^{-2} for all fields. In order to match the reported hard-band flux in the other fields, we convert the reported $2 - 7$ keV hard X-ray band flux into an equivalent $2 - 10$ keV hard X-ray band flux assuming a $\Gamma = 1.9$ power-law.

In the XMM-LSS field we use the final release of the public XMM X-ray catalog from Chiappetti et al. (2012) which consists of 124 pointings of the XMM-Newton X-ray telescope which includes the Subaru XMM-Newton Deep Survey (SXDS; Ueda et al. 2008). This catalog contains sources to a hard-band flux limit of $f_X \sim 1.3 \times 10^{-15}$ erg s^{-1}cm^{-2} and $f_X \sim 9.3 \times 10^{-17}$ erg s^{-1}cm^{-2} in the shallower XMM-LSS and deeper XMM-SXDS regions, respectively. We match the X-ray catalogs using the likelihood ratio matching technique described above.

Following Aird et al. (2012) and Mendez et al. (2013), we apply an “X-ray weight” for each X-ray detected source based on the ratio of the total number of X-ray detected sources to the predicted Log(N)-log(S) relation of Georgakakis et al. (2008) at a given flux. These X-ray weights correct observed number densities of X-ray sources to the intrinsic number density and account for variations in the flux limit across the fields due to vignetting and the change in sensitivity of the telescope as a function of axis angle.

4.3.2 Radio Data

To select radio sources we use existing deep Very Large Array (VLA) 1.4 GHz radio data in the COSMOS, EGS, and XMM-LSS fields. In the COSMOS field, we use the VLA-COSMOS Deep Project (Schinnerer et al. 2010) that combines the shallower data of the VLA-COSMOS Large Project (Schinnerer et al. 2007) with deeper coverage in the central degree of the field. The survey provides radio continuum coverage for ∼2,900 sources with $\sim 1.5''$ resolution and a mean 1σ sensitivity of 12 $\mu Jy\,\mathrm{beam}^{-1}$ in the central square degree and $\sim 2''$ resolution and sensitivity of 15 $\mu Jy\,\mathrm{beam}^{-1}$ in the outer region. In the EGS, we use the AEGIS20 (Ivison et al. (2007); Willner et al. (2012)) VLA radio catalog which identifies 1,122 sources from six overlapping pointings in the northern two-thirds of the field. The lower third of the EGS was not imaged due to the proximity to a bright radio source, 3C 295. The data were obtained from the VLA with a 5σ sensitivity limit of 50 $\mu Jy\,\mathrm{beam}^{-1}$ with $\sim 3.8''$ resolution. In the XMM-LSS field, we use the $100 - \mu Jy$ catalog (Simpson et al. 2006) which contains fourteen overlapping pointings. The radio imaging identifies 505 radio sources and reaches an sensitivity limit of 12 $\mu Jy\,\mathrm{beam}^{-1}$ over 0.8 $\mathrm{deg}^2$of the field. In the DEEP2-02hr, DEEP2-16hr, and DEEP2-23hr fields we additionally include relatively shallow VLA data from the Faint Images of the Radio Sky at Twenty-one centimeters survey (FIRST; Becker, White, & Helfand 1995). We use the 14Mar04 catalog which contains 946,432 radio sources above the sensitivity limit of ~ 200 $\mu Jy\,\mathrm{beam}^{-1}$ and above the the detection limit of 1 mJy.

We use the Australian Telescope Large Area Survey (ATLAS) in the CDFS-SWIRE field (Norris et al. 2006) and ES1 field (Middelberg et al. 2007). ATLAS used the Australian Telescope Compact Array (ACTA) at 1.4 GHz to survey both fields. The CDFS-SWIRE data contains 21 pointings with 784 radio galaxies reaching a 1σ sensitivity limit of ~ 40 $\mu Jy\,\mathrm{beam}^{-1}$, while the ES1 data contains 12 pointings with 1276 radio galaxies reaching a 1σ sensitivity limit of ~ 30 $\mu Jy\,\mathrm{beam}^{-1}$. We find no major astrometric offsets between these radio catalogs and the PRIMUS spectroscopic catalog (described below), such that we assign radio counterparts to the optical redshift catalog by using SPHEREMATCH in IDL to identify counterparts within $2''$, which is approximately the astrometric uncertainty in each catalog.

4.3.3 Mid-IR Data

To identify mid-IR AGN, we use existing public *Spitzer* IRAC photometry in the CDFS-SWIRE, COSMOS, EGS, ES1, and XMM-LSS fields. IRAC provides 3.6, 4.5, 5.8, and 8.0 μmdata which we will reference as [3.6], [4.5], [5.8] and [8.0]. In the CDFS-SWIRE, ES1, and XMM-LSS fields we use existing shallow IRAC imaging from Data Release 2 (DR2) from the *Spitzer* Wide-area Infrared Extragalactic Survey (SWIRE; Lonsdale et al. 2003) (see Mendez et al. (2013) for details). We find no major astrometric offsets between these catalogs and the PRIMUS optical redshift catalog, and we assign IRAC counterparts to the optical redshift sources in all of the fields by matching to the closest object within $1''$. The CDFS "proper" field is not included here; instead, we use the larger CDFS-SWIRE field at slightly lower declination, which was covered in the primary sample of the PRIMUS redshift survey. In the COSMOS field, we reproduce the SWIRE source detection procedure from the SWIRE DR2 documentation using the IRAC mosaic images (see Mendez et al. 2013, for details). This ensures that we measure robust fluxes and flux uncertainties using a consistent technique across all of our fields. For the majority of sources, our flux measurements are similar to those in the S-COSMOS public catalog, although the public catalog tends to have larger uncertainties for similar brightness objects from the SWIRE catalogs due to their aggressive deblending of sources.

In the DEEP2-02hr field, we use a four-band detected catalog[1]. The sample is drawn from *Spitzer* IRAC observations as part of the DEEP2_CY5A/50660 program (PI: C. Jones). The IRAC imaging contains 34 pointings in each band covering the majority of the DEEP-02hr field. In the EGS field, we use the Barro et al. (2011) publicly-available IRAC [3.6] and [4.5] selected catalog. The catalog contains $\sim 76,000$ sources with $[3.6] \leq 23.75$. The sample is drawn from *Spitzer* as part of the Guaranteed Time Observations (GTO; PI: G. Fazio) and presented in Barmby et al. (2008) with additional data from the GO program (ID 41023; PI: K. Nandra). The GTO IRAC imaging comprises 52 pointing of all four IRAC bands over the central region of the EGS. The additional GO data cover the upper and lower regions of the EGS, flanking the original strip.

Additionally we use the *Wide-field Infrared Survey Explorer* (WISE; Wright et al. 2010) mid-IR survey which provides 3.4, 4.5, 12, and 22 μm photometry (bands W1, W2, W3, and W4, respectively) in all of our fields. Here we use the public all-sky catalog from March 2012 which has a 5σ point source sensitivity better than 0.08, 0.11, 1, and 6 mJy in each of the bands, respectively. We remove sources with spurious photometric detections and require sources to have SNR > 3 in the W1 and W2 bands (See Cutri et al. 2011, for more details). WISE surveyed the sky in an ecliptic polar-orbit, which increased the number of observations with increasing ecliptic latitude, causing the median coverage to vary for different fields. See Table 4.1 for the IRAC and WISE area of each field (where at least W1 and W2 photometry was required for WISE).

4.3.4 PRIMUS Spectroscopic Redshifts

We use spectroscopic redshifts from the PRIMUS survey to define samples for our clustering analysis. PRIMUS (Coil et al. 2011; Cool et al. 2013) is the largest faint galaxy redshift survey completed to date, covering $\sim 9\,\mathrm{deg}^2$ in seven well-studied fields on the sky with multi-wavelength imaging from the X-ray to the far infrared (IR). The survey obtained low-resolution ($\lambda/\Delta\lambda \sim 40$) spectra for $\sim 300,000$ objects, targeting 80% of galaxies in these fields with $i < 22$. PRIMUS used the the IMACS instrument (Bigelow & Dressler 2003) on

---

[1] Catalog from A. Goulding 2013, private communication

the Magellan-I Baade 6.5 m telescope to observe $\sim 2,500$ objects at once using a slitmask that covered 0.18 deg^2. PRIMUS contains a statistically-complete sample of $\sim 120,000$ spectroscopic redshifts to $i_{\rm AB} \sim 23.5$. Redshifts are derived by fitting a large suite of galaxy, broad-line AGN, and stellar spectral templates to the low-resolution spectra and optical photometry (see Cool et al. 2013, for details). Objects are classified as galaxies, broad-line AGN or stars depending on the best χ^2 template fit. The PRIMUS redshifts are very precise ($\sigma_z/(1+z) \sim 0.5\%$) and have a low catastrophic outlier rate, less than 3% ($\Delta z/(1+z) \geq 0.03$). Here we use robust ($z_{\rm quality} \geq 3$, see Coil et al. (2011)) PRIMUS redshifts between $0.2 < z < 1.2$ for the fields listed in Table 4.1. We use deep optical photometry in each field to derive K-corrections (Blanton & Roweis 2007) and stellar mass estimates using iSEDfit (Moustakas et al. 2013) (see Section 4.3.6 below). For further details of the survey design, targeting, and data see Coil et al. (2011); for details of the data reduction, redshift confidence, and completeness see Cool et al. (2013).

The PRIMUS survey generally targeted all sources above $i < 22.5$ and sparse-sampled $22.5 < i < 23$ sources, so that faint galaxy sources at the flux limit would not dominate the target selection. The sampling rates are well defined a-priori such that building a statistically complete flux-limited sample requires the tracking of both the "sparse sampling" weight and the "density dependent" weight of each object. The magnitude-dependent sparse sampling weight accounts for the fraction of sources selected at random in the 0.5 mag interval above the targeting limit in each field. The density-dependent weight accounts for the sources in high density areas on the sky that are missed due to slit collisions and the finite number of masks observed. In these regions the observed spectra of adjacent galaxies would overlap on the the detector if all galaxies were targeted (see Coil et al. 2011; Moustakas et al. 2013, for more details.).

Additionally, we include a spatially-varying redshift success fraction weight to account for changes in the observed redshift success rate across a field (i.e., due to differences in observing conditions for different slitmasks). In PRIMUS, we use the pixelize function in Mangle[2]. We estimate the redshift success fraction by taking the ratio of highly confident sources with $z_{\rm quality} \geq 3$ to all targeted sources in the field in pixels of size ~ 36 arcsec^2. We use a larger pixel size in the PRIMUS fields than in the DEEP2 fields (see Section 4.3.5) to limit Poisson noise in the shallower PRIMUS data as compared to the DEEP2 data.

4.3.5 DEEP2 Spectroscopic Redshifts

We also use spectroscopic redshifts from the Deep Extragalactic Evolutionary Probe (DEEP2; Davis et al. 2003; Newman et al. 2012) redshift survey. In the DEEP2-02hr and DEEP2-23hr fields, PRIMUS did not target the $0.7 < z < 1.4$ redshift range already covered by DEEP2. The combination of PRIMUS redshifts and DEEP2 redshifts in these fields selects galaxies uniformly from $z = 0.2$ to $z = 1.4$. The DEEP2 survey provides spectroscopic redshifts

---

[2] http://space.mit.edu/~molly/mangle/

in the Extended Groth Strip (EGS), the DEEP2-02hr field, the DEEP2-16hr field, and the DEEP2-23hr field. The DEEP2 survey was conducted with the DEIMOS spectrograph (Faber et al. 2003) on the 10m Keck-II telescope. In the EGS, the DEEP2 survey has measured $\sim 17,000$ high-confidence redshifts ($Q \geq 3$, See Newman et al. (2012)) to $R_{AB} < 24.1$. In the DEEP2-02hr, DEEP2-16hr and DEEP2-23hr fields, the survey used a photometric color selection to target galaxies in $0.7 < z < 1.4$ to $R_{AB} < 24.1$. We use the Data Release 4 (DR4) catalog[3] and associated window function from (Newman et al. 2012). Here we use redshifts between $0.2 < z < 1.2$ in the EGS and redshifts between $0.7 < z < 1.2$ in the other DEEP2 fields (in the non-EGS fields DEEP2 targeted above $z = 0.7$). For all of the DEEP2 fields we require a redshift with a confidence greater than 95% ($Q \geq 3$). We use the extended optical photometry from Matthews et al. (2013) which contains additional Canada-France-Hawaii Telescope Legacy Survey (CFHTLS) *ugriz* and the Sloan Digital Sky Survey (SDSS) *ugriz* photometry matched to the redshift catalog. K-corrections, absolute M_B magnitudes, and rest-frame colors are derived from K-correct (Blanton & Roweis 2007) from the optical photometry in the field. The numbers of sources with the above redshift quality cuts and with estimated stellar masses are given in Table 4.1.

We use those sources that fall within the recoverable spatial selection function of the DEEP2 survey. For the EGS, this precludes the use of the data from the northern 25% of the field, which had shallower BRI photometry and non-uniform targeting. For the other DEEP2 fields we include all of the pointings presented in Newman et al. (2012). The spatial redshift success fraction reflects the probability that a targeted source has a secure $z_{\text{quality}} \geq 3$ redshift. For the DEEP2 fields it is calculated in ~ 6 arcsec^2 pixels. Using the average of six adjacent pixels to match the ~ 36 arcsec^2 pixels used in PRIMUS does not change the clustering measurements in these fields.

4.3.6 iSEDfit Stellar Masses and Star Formation Rates

We estimate stellar masses and star formation rates (SFR) by fitting the spectral energy distributions (SEDs) of our sources with population synthesis models using iSEDfit (Moustakas et al. 2013). iSEDfit is a Bayesian fitting code that compares the observed photometry for each source to a large Monte Carlo grid of SED models which span a wide range of stellar population parameters (e.g. age, metallicity, and star formation history) to estimate the stellar mass and SFR of a galaxy. We assume a Chabrier (2003) initial mass function from 0.1 to 100 $\mathcal{M}_*$ and use Bruzual & Charlot (2003) stellar population synthesis models. We assume the following priors to construct the Monte Carlo grids: uniform stellar metallicity in the range of $0.004 < Z < 0.04$; Charlot & Fall (2000) dust attenuation law, with an exponential distribution of dust, ($0.25 < \gamma < 2.0$); an exponentially declining-τ ($\phi_s(t) = (\mathcal{M}/\tau)e^{-t/\tau}$) star-formation

---

[3] http://deep.ps.uci.edu/dr4/home.html

history (SFH) with $0.01 < \tau < 5.0$. Stochastic bursts of star formation of varying amplitude, duration, and onset time are superimposed, allowing for a wide range of possible star formation histories (Kauffmann et al. 2003; Salim et al. 2007). While a delayed-τ model encompasses both a linearly rising ($t/\tau \ll 1$) and an exponentially declining ($t/\tau \gg 1$) SFH history, we find no significant SFR or stellar mass offsets or trends using different SFH models for our sources at $z < 1.2$, and we therefore choose to use the simpler model of an exponentially declining SFH. iSEDfit marginalizes the full posterior probability distribution of stellar masses and SFRs over all other parameters and thus encapsulates both the uncertainties in the observations and the model parameter degeneracies. For each source we take the median stellar mass and SFR from the full probability distribution functions as the best estimate of the stellar mass and SFR. In our analysis below we use only the relative stellar mass and SFR between sources, such that any overall offsets do not matter here.

We use iSEDfit stellar masses derived from photometry spanning the UV to the optical bands. Including the first two IRAC bands ([3.6] and [4.5]) systematically increases the median galaxy sample stellar mass by 0.1 dex. This is the case for the X-ray detected sample; however, for the IRAC Donley et al. selected sample (details are given below in Section 4.4.3) the median mass offset is much larger (0.5 dex). As shown in Mendez et al. (2013), this is due to AGN light contributing to these channels causing the IR-AGN to have overestimated masses. We therefore do not include the IRAC bands in any of our stellar mass estimates, such that all stellar masses are derived using the same photometric bands, minimizing systematic offsets between our samples. While not all of the fields have full GALEX UV coverage ($\sim 82\%$), we include the observed the FUV and NUV photometry where available to improve the SFR measurements. Including GALEX UV bands (compared to just using optical bands alone) slightly decreases the estimated stellar mass (~ 0.02 dex) for the galaxy and AGN samples. There is an increase in the estimated SFR for the highest SFR galaxies; including GALEX leads to better estimates of the SFR for galaxies where we have GALEX data. We do not estimate stellar masses or SFRs for sources that are deemed to be broad-line AGN (BLAGN), where their spectra are better matched by BLAGN templates than by galaxy templates, as their optical photometry will be dominated by light from the AGN. Table 4.1 lists the total number of sources with spectroscopic redshifts in each field (N_{galaxy}) and the number of sources which we estimate a stellar mass (N_{mass}).

4.3.7 Spatial Selection Function

In order to perform accurate clustering measurements, we require that all of the PRIMUS and DEEP2 sources used here are located within the area of each survey that has a well-understood spatial selection function. This ensures that any spatial densities in the survey that are due to target selection or missing data, such as in CCD chip gaps or around bright stars, as well accounted for. Coil et al. (2011) provides details on the spatial selection function of PRIMUS, and Coil et al. (2004) and Newman et al. (2012) provide details for the DEEP2 survey.

In PRIMUS we require that sources fall within the observed window function area targeted with at least two slitmasks. For the DEEP2 fields, we require that sources fall within the window function discussed above. The X-ray AGN, Radio AGN, and IR-AGN samples are identified within the areas with observed X-ray, radio, or mid-IR coverage. While there is generally overlap between the multi-wavelength imaging coverage, there are some areas that lack full multi-wavelength coverage.

4.4 AGN and Galaxy Samples

The goal of this paper is to quantify and compare the clustering properties of X-ray-, radio-, and mid-IR-selected AGN at $z \sim 0.7$ with each other, as well as with similarly-selected non-AGN galaxies with matched stellar mass, SFR and redshift distributions. To do this we select AGN and galaxy samples using the PRIMUS and DEEP2 surveys in regions with either X-ray, radio or mid-IR imaging coverage. Below we present our selection criteria for our X-ray, radio, and mid-IR AGN samples, as well as the matched galaxy samples.

4.4.1 X-ray AGN Samples

For our full X-ray AGN sample we require that the detected X-ray sources have a hard-band X-ray luminosity $L_{\mathrm{X}} > 10^{41}$ erg s^{-1} and a redshift in the range $0.2 < x < 1.2$. We have applied X-ray K-corrections ($(1+z)^{(\Gamma-2)}$; $\Gamma \sim 1.7$) to estimate the hard-band X-ray luminosity. We create a 'no broadline' subsample where we remove the BLAGN identified by their PRIMUS or DEEP2 spectra. Additionally, the full X-ray AGN sample is also divided into six different samples defined either by an AGN property (luminosity, specific accretion rate, or hardness ratio) or a host galaxy property (redshift, stellar mass, and specific star-formation rate (sSFR)), in order to investigate clustering trends with AGN or host galaxy properties. We use the specific accretion rate, proportional to the bolometric luminosity per unit stellar mass, as an estimate of the Eddington ratio. This assumes a constant scaling relationship between the black hole mass and the host stellar mass (e.g., $\mathcal{M}_{\mathrm{BH}} \sim 0.002\,\mathcal{M}_{*}$; Marconi & Hunt 2003). While the scatter in the $M - \sigma$ relationship and the scatter in the mass of the stellar bulge to the stellar mass of the galaxy, is expected to be significant, the specific accretion rate is a robust tracer of the rate at which the SMBH is growing relative to the stellar mass despite this scatter (Aird et al. 2012). Using this relation we estimate the Eddington ratio as,

$$\begin{aligned} \lambda_{\mathrm{Edd}} &= \frac{L_{\mathrm{Bol}}}{L_{\mathrm{Edd}}} && (4.1) \\ &= \frac{L_{\mathrm{Bol}}}{1.3\,\times\,10^{38}\,\times\,0.002\,\frac{\mathcal{M}_{*}}{\mathcal{M}_{\odot}}} && (4.2) \end{aligned}$$

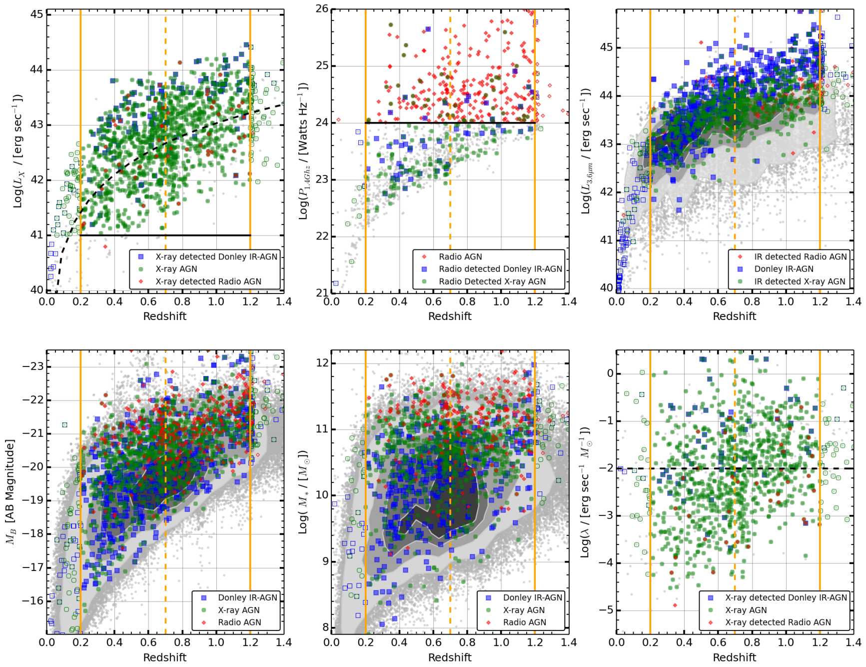

Figure 4.1: **Redshift dependence of the AGN samples** — The distributions of X-ray AGN, Radio AGN, and Donley et al. samples in X-ray AGN luminosity (upper left), radio power (upper center), and $3.6\mu m$ IR luminosity (upper right), as well as host galaxy absolute optical magnitude (M_B) (lower left), stellar mass (lower center), and X-ray specific accretion rate (lower right), all as a function of redshift for $0 < z < 1.4$. The X-ray AGN sample shown with green circles, the Radio AGN sample shown with red diamonds, and the Donley et al. sample shown with blue squares are displayed above the PRIMUS and DEEP2 galaxy tracer sample shown as grey dots with greyscale contours containing 30%, 50% and 80% of the sample. Sources are included on this plot if they have a robust spectroscopic redshift and are not classified as broad-line AGN. Solid vertical orange lines show the full redshift range used here ($0.2 < z < 1.2$), while the dashed vertical orange line shows the redshift used ($z = 0.7$) to split the full samples into higher and lower redshift samples. In the X-ray luminosity panel (upper left) we show as a dashed black line the redshift-dependent cut used to create high and low X-ray luminosity samples, while the solid black line shows the lower $L_{\rm X} = 10^{41}$ erg s^{-1} luminosity cut used for all of the X-ray AGN samples.

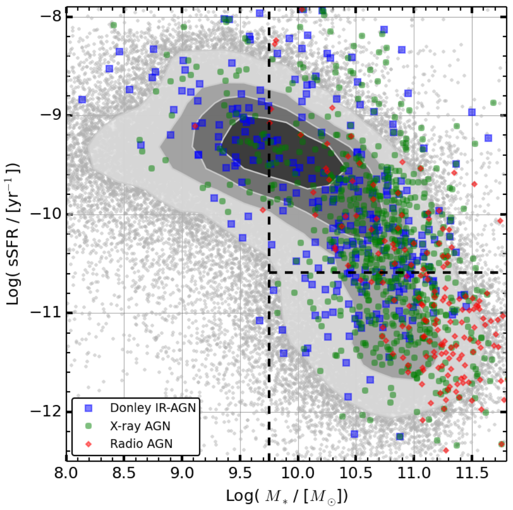

Figure 4.2: **SSFR/mass diagram** — Specific star-formation rate (sSFR) versus stellar mass (bottom) for the X-ray AGN, Radio AGN, and Donley et al. sources. Colors and contours are similar to Figure 4.1. We show in dashed black lines the stellar mass and sSFR cuts used to define the sSFR selected samples. All AGN samples are seen to be biased to more massive host galaxies. Additionally there is a large difference in the sSFR for the host galaxies of the different AGN samples.

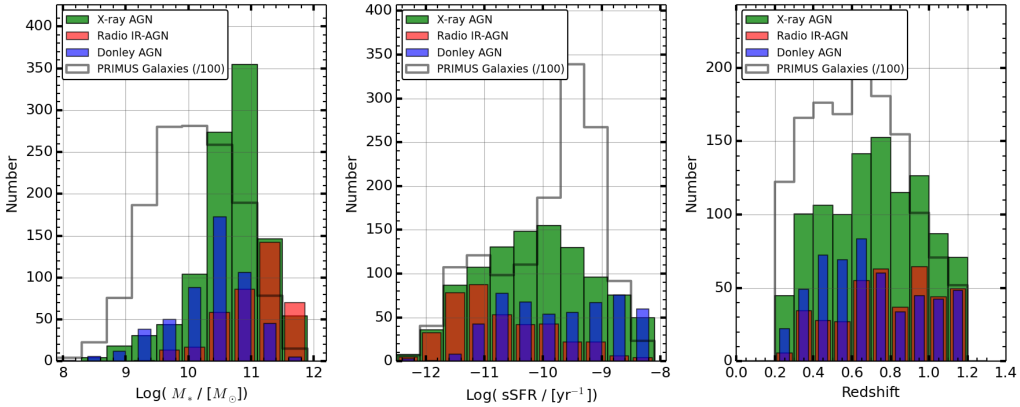

Figure 4.3: **Stellar Mass, SSFR, and redshift distributions for the AGN samples** — Stellar mass, specific star formation rate (sSFR), and redshift distributions for the X-ray AGN sample, Radio AGN sample, Donley et al. sample, and galaxy tracer samples. The green, blue, and red filled histograms show the distributions of the X-ray AGN, Donley et al. , and Radio AGN samples, respectively. The grey outline of the distributions for the galaxy tracer sample is scaled down by a factor of 100 for ease of comparison.

where $L_{\rm Edd}$ is the Eddington limit, and $L_{\rm Bol}$ is the bolometric luminosity derived from the X-ray luminosity using the X-ray luminosity to bolometric luminosity relationship of Hopkins et al. (2008) in units of erg s^{-1}. Details of each sample are given in Table 4.1.

For the X-ray AGN samples split by AGN luminosity, we divide the full X-ray AGN sample into low luminosity ($\langle L_X \rangle \sim 10^{42.4}$ erg s^{-1}) and high luminosity ($\langle L_X \rangle \sim 10^{43.2}$ erg s^{-1}) samples using a redshift dependent luminosity cut (shown in the upper left panel of Figure 4.1). This cut mimics the relatively high X-ray luminosity above which the Donley et al. population (described below) is X-ray detected, as seen in the figure.

The high and low specific accretion rate (λ) samples are defined for AGN with a host galaxy stellar mass above $\mathcal{M}_* > 10^{9.75}\,\mathcal{M}_\odot$ which limits low-mass sources below the X-ray luminosity limit from biasing the results. To match the specific accretion rates for X-ray detected Radio AGN and Donley et al. samples, we divide the full X-ray sample at a specific accretion rate of $\lambda = 10^{-2}\,$erg s$^{-1}\,\mathcal{M}_\odot^{-1}$ (see the lower right panel of Figure 4.1).

We define samples based on the hardness ratio of the X-ray AGN, creating hard and soft samples by dividing the sample at $HR = 0$. This cut requires that the AGN included are identified in both the soft and hard X-ray bands.

We also divide the full X-ray AGN sample by various host galaxy properties, to quantify how the clustering of X-ray AGN depends on the host galaxy. First, we create a high and low redshift sample by dividing the full X-ray AGN sample at $z \sim 0.7$. For both the stellar mass samples and sSFR samples, we create a roughly volume limited sample by requiring that the samples have a stellar mass above $\mathcal{M}_* > 10^{9.75}\,\mathcal{M}_\odot$ (see Figure 4.2). Including the large number of low-redshift galaxies below this limit would bias the results for the galaxy samples which vastly outnumber the AGN samples. We define the high and low stellar mass samples using the median stellar mass of the full X-ray AGN sample ($\mathcal{M}_* \sim 10^{10.65}\,\mathcal{M}_\odot$). This cut gives roughly comparable numbers of high- and low-stellar mass X-ray AGN samples.

We define high and low sSFR samples by dividing the sSFR at sSFR $= 10.65\,{\rm yr}^{-1}$ (bottom panel of Figure 4.2). This cut roughly matches the evolving SFR-mass cut of Moustakas et al. (2013) at $z \sim 0.7$ that divides the galaxy sample into quiescent and star-forming galaxies.

4.4.2 Radio AGN Samples

We define four Radio AGN samples based on the observed optical broad lines and measured radio luminosity of each source. For our full Radio AGN sample we require a redshift in the range $0.2 < x < 1.2$. We create a 'no broadline' subsample where we remove the BLAGN identified by their PRIMUS or DEEP2 optical spectra. Radio continuum emission may contain contributions from thermal bremsstrahlung (free-free) emission in star forming galaxies as well as from non-thermal synchrotron emission associated with radio jets emanating from an AGN. To separate these two population, we follow Condon (1992) and Murphy et al. (2011), and define a high luminosity radio sample with $P_{1.4\mathrm{Ghz}}{>}10^{24}$ Watts Hz^{-1} to remove any potential contamination from luminous starburst galaxies. We have applied a radio K-correction ($(1+z)^{(\alpha-1)}$; $\alpha \sim 0.5$) when estimating the radio luminosity. Above this luminosity the radio emission cannot be explained by even extreme star formation (SFR $> 10^3 \mathcal{M}_\odot\,\mathrm{yr}^{-1}$) (Goulding et al. 2012; Hickox et al. 2009). This Radio AGN sample reliably contains radio-loud (Class FR-II; Fanaroff & Riley 1974) sources. The small sample size in the high luminosity sample limits our analysis of the Radio AGN sample to the full redshift range ($0.2 < z < 1.2$), as we do not have enough sources to create subsamples at different redshifts.

This sample of radio-loud sources necessarily does not contain radio-quiet AGN (Mullaney et al. 2013). Optical, mid-IR, or far-IR to radio flux ratio excess techniques have been suggested identify more complete samples of radio-quiet AGN while limiting contamination from star forming galaxies (e.g. Smolčić et al. 2008; Park et al. 2008; Donley et al. 2005; Appleton et al. 2004). To investigate the dependence of clustering of these samples, we define a low luminosity radio sample ($P_{1.4\mathrm{Ghz}}{<}10^{24}$ Watts Hz^{-1}). This sample includes all radio-detected sources below the luminosity limit identifying all possible optical- or IR-excess selected samples. While this low luminosity sample may suffer from contamination by star forming galaxies, we do not find a significant difference in the fraction of X-ray or mid-IR AGN identified at these lower radio luminosities, compared to the high luminosity radio sample. In fact, the X-ray and mid-IR AGN samples that are also radio-detected have radio flux distributions that peak below $P_{1.4\mathrm{Ghz}}{<}10^{24}$ Watts Hz^{-1}, such that the bulk of the X-ray and mid-IR AGN are in the low radio luminosity sample.

4.4.3 IR-AGN Samples

We use the Donley et al. (2012) IRAC color-color selection to identify mid-IR red power-law AGN. As shown in Mendez et al. (2013) this provides reliable identification of luminous mid-IR AGNs with limited contamination by star forming galaxies in the deep IR data contained in the PRIMUS survey. We require that objects are detected in all four IRAC bands, and have colors such that they lie within the following region in IRAC color-color space:

$$x = \log_{10}\left(\frac{f_{5.8\mu\mathrm{m}}}{f_{3.6\mu\mathrm{m}}}\right), \quad y = \log_{10}\left(\frac{f_{8.0\mu\mathrm{m}}}{f_{4.5\mu\mathrm{m}}}\right) \tag{4.3}$$

$$x \geq 0.08 \;\text{ and }\; y \geq 0.15 \;\text{ and} \tag{4.4}$$

$$y \geq (1.21 \times x) - 0.27 \;\text{ and} \tag{4.5}$$

$$y \leq (1.21 \times x) + 0.27 \;\text{ and} \tag{4.6}$$

$$f_{4.5\mu\mathrm{m}} > f_{3.6\mu\mathrm{m}} \;\text{ and }\; f_{5.8\mu\mathrm{m}} > f_{4.5\mu\mathrm{m}} \;\text{ and} \tag{4.7}$$

$$f_{8.0\mu\mathrm{m}} > f_{5.8\mu\mathrm{m}}. \tag{4.8}$$

The small sample size of the Donley et al. sample limits our analysis to the full redshift range ($0.2 < z < 1.2$).

Additionally, we identify WISE-selected IR-AGN using Assef et al. (2013) magnitude dependent selection. We require sources to have measured W1 and W2 fluxes such that,

$$W1 - W2 > 0.662 \exp\left[0.232\ (W2 - 13.97)^2\right] \tag{4.9}$$

$$W2 < 17.11 \tag{4.10}$$

where W1 and W2 are in Vega magnitudes. Assef et al. (2013) show that it is 90% reliable in its identification of IRAC selected AGN. This selection extends the Stern et al. (2012) WISE IR-AGN color selection to fainter limiting magnitudes, while controlling for contamination (see Assef et al. (2013) for more detail).

We divide the WISE IR-AGN sample into obscured and unobscured sub-samples. Yan et al. (2013) identified a color difference in obscured and unobscured templates at $z < 1.5$, and define an IR-to-optical $(r - W2) \sim 6$ color cut to separate these sources. We follow this color cut, and identify obscured sources as having a red IR-to-optical color ($(r_{vega} - W2_{vega}) > 6$), while unobscured sources have a blue color ($((r_{vega} - W2_{vega}) < 6)$). Due to differences in the photometric filters in our measured r-band magnitudes, we use a synthesized SDSS r-band magnitude from K-Correct to ensure a uniform selection in each field.

We additionally test the Mateos et al. (2012) WISE IR selection technique. Similar to the Donley et al. selection technique, it identifies sources with mid-IR fluxes indicative of a red power-law. This technique is more robust than that of Assef et al. (2013) as it uses a longer wavelength (W3: $12\mu m$) to ensure a monotonic mid-IR SED, but is less complete due to the relatively shallow W3 coverage in the WISE survey. As we find no significant differences in the clustering properties of either the Mateos et al. (2012) or Assef et al. (2013) defined AGN samples, we use the slightly larger Assef et al. IR-AGN sample throughout this paper.

4.4.4 Galaxy Tracer Samples

We use the dense galaxy sample provided by the PRIMUS and DEEP2 redshift surveys to measure the clustering of AGN using a cross-correlation measurement with galaxies. To do this we define galaxy "tracer" samples that are used to trace the cosmic web in the fields and at the redshifts of interest. For the full galaxy tracer sample, we use all galaxies with robust redshifts within the full redshift range used here, $0.2 < z < 1.2$. We do not require that the galaxy tracer sample be volume limited, as we are using it only to trace the large-scale structure in these fields; it therefore needs to span the same volume as our AGN samples, but it does not need to have the same median luminosity at all redshifts. We additionally split the full galaxy tracer sample into low and high redshift samples for the X-ray AGN sample, split at the redshift of $z = 0.7$ (Figure 4.1, dashed orange line in each panel). This redshift cut divides the number of X-ray

AGN into approximately equal sized samples and results in 30% more tracer galaxies at lower redshifts than at higher redshifts.

4.4.5 Galaxy Matched Control Samples

We construct galaxy samples for each of the X-ray AGN, Radio AGN, and Donley et al. samples with matched stellar mass, star formation rate, and redshift distributions. We use these as control samples to compare of the clustering of galaxies that host AGN and galaxies without AGN limiting selection biases (For a discussion see: Aird et al. 2012). Additionally these large control samples constrain the maximal relative clustering amplitude for the X-ray AGN, Radio AGN, and Donley et al. samples, assuming fixed depth. This any differences between the clustering amplitudes of the control samples represents the clustering differences for much larger AGN surveys with the assumption that the selected AGN population mimics the underlying population. Coil et al. (2009) and Hickox et al. (2009) created similar matched samples, however they match the optical magnitude and color. These samples match the observed properties of the host galaxies, however, they may miss the intrinsic host population properties. While we find no significant differences in using the stellar mass, star formation rates, and redshift joint-distribution rather than the color-magnitude and redshift joint-distribution, we choose these parameters as they represent the intrinsic host galaxy distribution.

We measure the joint stellar mass, star formation rate, and redshift distribution of the galaxy sample and each of the X-ray AGN, Radio AGN, and Donley et al. samples in stellar mass bins of $\Delta\mathcal{M}_* \;\, 10^{=}\mathcal{M}_{\odot}\, 0.2$ dex, star formation rate bins of $\Delta SFR = 0.2$ dex, and redshift bins $\Delta z = 0.1$. The projected distributions for the X-ray AGN, Radio AGN, and Donley et al. are shown in Figure 4.3. Normalizing this by the number of galaxies in each bin, gives the expected fraction of observed AGN in each bin, effectively estimating the probability density in this three-dimensional parameter space. We use this probability density to weight each of the galaxies so that the joint distributions match each of the AGN samples. Using this weighting method more precisely estimates the clustering of each AGN population using the power of the entire galaxy population. We use individual matched galaxy control samples for each of the X-ray AGN, Radio AGN, and Donley et al. samples to control for differences in the joint distribution of host galaxies that each selection identifies.

4.5 Clustering Analysis

We measure the spatial distribution of AGN using the two-point correlation function, which quantifies the excess probability above Poisson of finding two sources with a given physical separation. While most studies measure the auto-correlation function (ACF) of the AGN sample of interest, here we measure the cross-correlation function (CCF) of AGNs with galaxies as a tracer sample. From this we can then infer the ACF of the AGN alone. As discussed in Coil et al. (2009), there are two main advantages to this method. First, the CCF of AGN and galaxies has a much greater statistical power due to the larger number density of galaxies, which better probe the underlying mass distribution where AGN are located. Second, it does not require a complete understanding of the AGN selection function, which may not be well understood due to the limits of multi-wavelength observations. Instead, all that is required is an understanding of the selection function of the galaxy tracer sample.

4.5.1 Measuring the Cross-Correlation Function

The two-point correlation function $\xi(r)$ is defined as the excess probability density, dP/dV, above that of a Poisson random field, of a second source being physically separated by a distance r from a given source,

$$\frac{dP}{dV} = n[1 + \xi(r)] \tag{4.11}$$

where n is the mean number density of the sample of interest (Peebles 1980). The ACF measures the clustering of a single sample, where the two sources are from the same sample, while the CCF measures the clustering of one type of source, taken from one sample, around that of another type of source, taken from a second sample. Here we measure the CCF of AGN (A) around galaxies (G), which are used as a tracer sample, and find the excess probability above random (R) of finding AGN and galaxies with a given separation (r) using the Davis & Peebles (1983) estimator:

$$\xi(r) = \frac{AG(r)}{AR(r)} - 1 \tag{4.12}$$

where $AG(r)$ is the sum of the weighted AGN-galaxy pairs and $AR(r)$ is the sum of the weighted AGN-random pairs, both as a function of separation. Weights are used to account for target selection in the PRIMUS sample (see Section 4.3.4); by applying these weights we are able to create a statistically-complete sample that is not subject to spatial biases. In the DEEP2 fields the weights are included in the spatial selection function which we use to generate the random catalogs, so we give each source unity weight.We calculate the pair counts in twelve $\Delta\mathrm{Log}(\mathrm{r_p}\,/\,[\mathrm{h^{-1}\,Mpc}]) = 0.2$ dex logarithmic bins and sixteen $\Delta(\pi) = 5\ h^{-1}\,\mathrm{Mpc}$ bins. When calculating the number of pairs in each bin, we calculate the weighted number of pairs:

$$AG = \sum_{\substack{i \in A,\\ j \in G}} \frac{w_{\mathrm{AGN};i} \times w_{\mathrm{galaxy};j}}{W_{\mathrm{AGN}} \times W_{\mathrm{galaxy}}} \tag{4.13}$$

$$AR = \sum_{i \in A} \frac{w_{\mathrm{AGN};i}}{W_{\mathrm{AGN}} \times N_{\mathrm{random}}} \tag{4.14}$$

$$\tag{4.15}$$

where w_{AGN} is the AGN weight, w_{galaxy} is the PRIMUS targeting weights for the tracer galaxy sample, W_{AGN} is the total AGN completeness and targeting weight, W_{galaxy} is the total PRIMUS targeting weight, and $N_{\rm random}$ is the number of random objects. The AGN weight is the multiplicative combination of the PRIMUS targeting weight for the source and any additional completeness weight for the AGN sample. In particular for the X-ray AGN sample this includes the X-ray AGN weight (see Section 4.3.1 for details). For the DEEP2 fields the targeting weight is unity for each source.

Peculiar velocities distort $\xi(r)$ measurements in the redshift direction, along the line of sight. We therefore measure $\xi(r)$ in two dimensions, $\xi(r_p, \pi)$, where r_p is the separation perpendicular to the line of sight, which is unaffected by peculiar velocities, and π is the separation along the line of sight. Integrating $\xi(r_p, \pi)$along the π dimension leads to a statistic that is independent of redshift space distortions, the projected correlation function:

$$w_p(r_p) = 2\int_0^\infty d\pi\, \xi(r_p, \pi) \tag{4.16}$$

$$\approx 2\int_0^{\pi_{\rm max}} d\pi\, \xi(r_p, \pi) \tag{4.17}$$

where $\pi_{\rm max}$ is the maximum π separation to which we integrate. As the signal to noise of $\xi(r_p, \pi)$declines quickly for large π separations, we measure the projected correlation function by integrating to a given $\pi_{\rm max}$to limit shot noise. We use a larger $\pi_{\rm max}$value in the PRIMUS fields than the DEEP2 fields to account for the larger redshift uncertainty in the PRIMUS fields. This uncertainty tends to "smear" out the large scale structure and distributing the signal from correlated pairs to larger π separations. Integrating to larger $\pi_{\rm max}$captures the full clustering signal. In the PRIMUS fields, we use a $\pi_{\rm max} = 80\,h^{-1}$ Mpc limit, whereas we use a smaller $\pi_{\rm max} = 20\,h^{-1}$ Mpc limit.

4.5.2 Jackknife Uncertainty Estimation

We estimate the uncertainty in our measurements using jackknife resampling of the data (e.g., Lupton 1993; Scranton et al. 2002). Generally, jackknife resampling approximates the variance in w_p derived from simulated mock catalogs (e.g., Zehavi et al. 2005; Coil et al. 2008; Skibba et al. 2014), and accounts for the significant correlation between adjacent scale bins. For each of our samples, we use between 10 and 12 jackknife subsamples across our 8 fields where we have spatially subdivided the larger fields into two or more subfields. The different number of subsamples is due to the multi-wavelength coverage in each field (i.e. CDFS does not contain X-ray data; See Table 4.1 for field details.) We subdivide the large fields (CDFS and XMM) along lines of constant RA and declination such that the resulting sub-samples probe the roughly same volume. We use samples of area approximately equal to $\sim$1deg^{2}which are sufficiently large enough to measure the projected correlation function to up to $\sim 10\,h^{-1}$ Mpc at $\langle z\rangle \sim 0.7$.

The uncertainty in w_p is estimated by calculating the projected correlation function using each jackknife resamples which removes one area at a time. From this collection of w_p estimates we calculate the variance in the projected correlation function,

$$\sigma^2_{w_p}(r_p) = \frac{N-1}{N} \sum_j^N (w_p(r_p) - \hat{w}_j(r_p))^2, \tag{4.18}$$

where the N is the number of jackknife samples, j indexes each jackknife resample, and $\hat{w}_j(r_p)$ is the projected correlation function computed with one area removed.

By measuring the projected correlation function using multiple fields across the sky, we are able to quantify the uncertainty on our measurements due to cosmic variance. While the large volume from the combination of the PRIMUS and DEEP2 fields include a wide range of cosmic densities, the COSMOS field in particular includes areas with extremely high densities (e.g., Lilly et al. 2007; McCracken et al. 2007; Meneux et al. 2009; Kovač et al. 2010; de la Torre et al. 2010; Skibba et al. 2014). Such that we show clustering results with and without the COSMOS fields. The overdensity of galaxies in the COSMOS field is similar to the Sloan Great Wall.

4.5.3 Inferring the AGN Auto-correlation Function

Following Coil et al. (2009), we infer the AGN ACF from measurements of the AGN-galaxy CCF and the galaxy ACF. We calculate the galaxy ACF using the Landy & Szalay (1993) estimator:

$$\xi(r_p, \pi) = \frac{GG(r_p, \pi) - 2\,GR(r_p, \pi) + RR(r_p, \pi)}{RR(r_p, \pi)} \tag{4.19}$$

where GG, GR, RR are the galaxy-galaxy, galaxy-random, and random-random weighted pair counts, respectively. For the pair counts we include the galaxy targeting weights similar to Section 4.5.2 The Davis & Peebles (1983) estimator gives similar results, since we are dominated by cosmic variance rather than small number statistics when determining the galaxy ACF. We calculate the AGN-galaxy CCF and galaxy ACF in the same volume. As with the AGN-galaxy CCF, we integrate the galaxy ACF projected correlation function to the same $\pi_{\rm max}$limits for the DEEP2 and PRIMUS fields.

We then infer the autocorrelation function of the AGN-AGN sample by dividing the AGN-galaxy CCF by the galaxy ACF,

$$w_{\rm AA}(r_p) = \frac{w^2_{\rm AG}(r_p)}{w_{\rm GG}(r_p)} \tag{4.20}$$

where $w_{\rm AA}$ is the projected AGN ACF, $w_{\rm AG}$ is the projected AGN CCF, and $w_{\rm GG}$ is the projected galaxy ACF. Inferring the AGN ACF assumes that the two estimated correlation functions are dominated by the correlations of sources linearly related to the underlying density distribution. This relation between the spatial distribution of galaxies and the underlying dark matter density field is called the bias and described in more detail in Section 4.5.5.

4.5.4 Power law fit

Following Davis & Peebles (1983), we assume a power law distribution for the excess probability density ($\xi(r) = (r/r_0)^\gamma$). The power law function is represented by two terms: a slope (γ) determining by the scale dependent growth in the linear regime, and scale factor (r_0) at which there is unity excess probability density. The analytic form of $w_p(r_p)$ is then:

$$w_p(r_p) = r_p \left(\frac{r_0}{r_p}\right)^\gamma \frac{\Gamma(\frac{1}{2})\Gamma(\frac{\gamma-1}{2})}{\Gamma(\frac{\gamma}{2})} \tag{4.21}$$

where Γ is the Gamma function. We fit this analytic function to our clustering measurements in the approximately linear regime of $r_p = 1 - 10\,h^{-1}$ Mpc. For scales below $r_p < 1\,h^{-1}$ Mpc, galaxy interactions within a single halo contribute and add additional clustering power. For scales above $r_p > 10\,h^{-1}$ Mpc, the size of our fields limits the number of pair counts, leading to large statistical fluctuations. Additionally, we do not probe larger scales above $\sim 10\,h^{-1}$ Mpc due to the "the Kaiser effect" which causes flattening of the $\xi(r_p,\, \pi)$from galaxies coherently falling into structures that are still undergoing gravitational collapse.

4.5.5 Bias estimation

To investigate any redshift evolution of the AGN clustering signal, we estimate the dark matter bias of the AGN ACF. The bias (b) measures the relative clustering strength of the AGN sample to that of dark matter particles. We estimate the bias at the median redshift of each AGN sample using the publicly available code of Smith et al. (2003). We integrate the dark matter correlation function to a $\pi_{\max} = 80\ h^{-1}$ Mpc and then calculate the bias as

$$b = \sqrt{\frac{w_{\mathrm{AGN}}}{w_{\mathrm{DM}}}} \tag{4.22}$$

where w_{AGN} is the AGN ACF, and w_{DM} is the dark matter ACF on scales of $r_p = 1 - 10\,h^{-1}$ Mpc. The comparison of different samples using the bias value accounts for differences in median sample redshift and alleviates the distribution is a power law assumption for the distribution.

Additionally, the relative bias between two AGN or galaxy samples is defined as the square root of the ratio of their respective projected correlation functions. This allows for a simple comparison of the clustering strength of two samples and is akin to comparing their bias (relative to dark matter) values. Below we present the mean and 1σ uncertainty of the relative bias across the jackknife samples when comparing two samples below. We estimate the relative bias on scales of $r_p = 1 - 10\,h^{-1}$ Mpc.

4.6 Results

In this section, we discuss the results of the cross-correlation analysis. We measure the cross-correlation of AGNs relative to the tracer-galaxy sample to estimate the bias relative to the

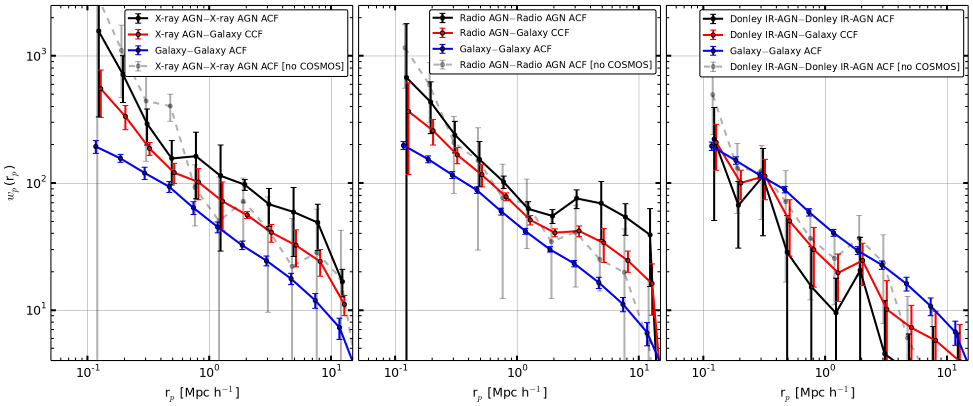

Figure 4.4: **Projected correlation functions for the AGN samples** — Projected AGN-AGN correlation function $w_p(r_p)$ (black) as a function of scale for the X-ray AGN sample (left), Radio AGN sample (center), and Donley et al. sample (right) for the entire redshift range ($0.2 < z < 1.2$). In each panel we show the AGN-AGN auto-correlation function (ACF; black), galaxy-AGN cross-correlation function (CCF; red) and galaxy-galaxy tracer ACF (blue) and estimated uncertainty from jackknife resampling of the fields. The jackknife estimated uncertainty accounts for both statistical and cosmic variance uncertainties. We show the projected correlation functions for the sample excluding COSMOS as a light grey dashed line to highlight the additional clustering signal due to the observed over-density in the COSMOS field.

galaxy samples and using the galaxy ACF, the absolute bias and dark-matter halo mass for each sample. We present these results for the X-ray AGN sample in Section 4.6.1, the Radio AGN sample in Section 4.6.2, and the Donley et al. sample in Section 4.6.3. We then compare the obscured and un-obscured WISE IR-AGN samples in Section 4.6.4, and the relative clustering of all of our samples in Section 4.6.5. Finally, we compare the clustering strength of each sample relative to matched-galaxy control samples in Section 4.6.6.

4.6.1 Clustering of X-ray AGN

The X-ray AGN sample (Figure 4.4, left-panel) is more clustered than the tracer-galaxy sample, and clusters similar to massive galaxies (Figure 4.5, left-panel). They are found in massive dark-matter halos ($M_{\rm halo} \sim 10^{13.3}\,{\rm h}^{-1}\,\mathcal{M}_\odot$) which is generally characterized by large galaxy groups. The clustering strength increases for smaller projected separations ($r_p < 0.7$) indicating that on small scales, there is a increase in the number of pairs of objects within the same dark matter halo. The clustering of the X-ray AGN sample is systematically (N% higher bias) larger when including the COSMOS field which over-dense relative to the other fields.

In Figure 4.6, we divide the full X-ray AGN sample into different sub-samples depending on both AGN properties and host galaxy properties. For each of the luminosity, specific-accretion rate and hardness-ratio divided sub-samples, we do not find any statistically significant difference in the clustering of any of the sub-samples. The statistical differences in the two-halo term

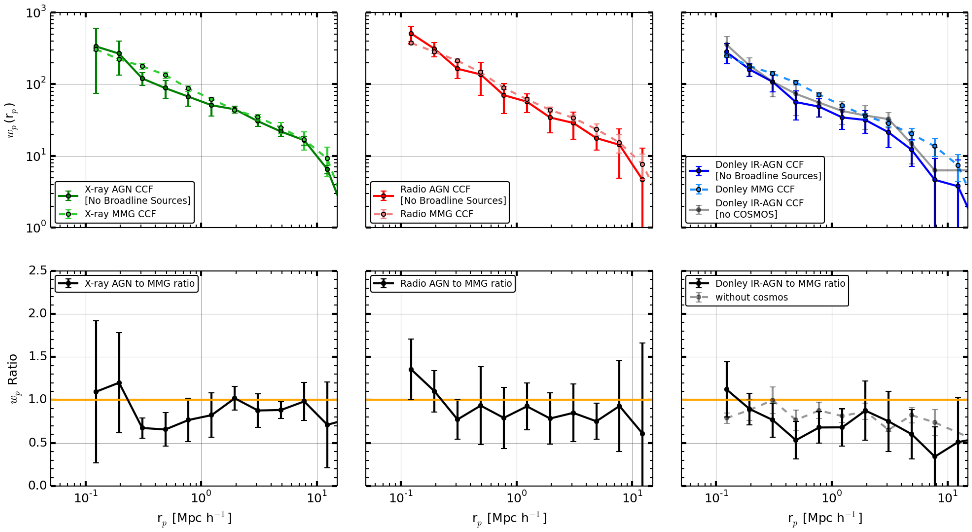

Figure 4.5: **Clustering comparison of the AGN samples and matched galaxy samples** — Clustering of X-ray AGN, Radio AGN, and Donley et al. samples relative to the matched galaxy samples. For each sample we show the AGN CCF as a solid dark line with jackknife error bars and the matched galaxy sample as a dashed light line. We do not include broad line sources in this comparison as that the stellar mass estimated for broad-line sources is over predicted due to the AGN contribution to the galaxy light. In the lower panels we show the ratio of each sample relative to the matched galaxy sample. The clustering strength of the X-ray AGN and Radio AGN samples can be reproduced by the clustering of the matched galaxy sample, but the Donley et al. sample is less clustered than similarly matched galaxies.

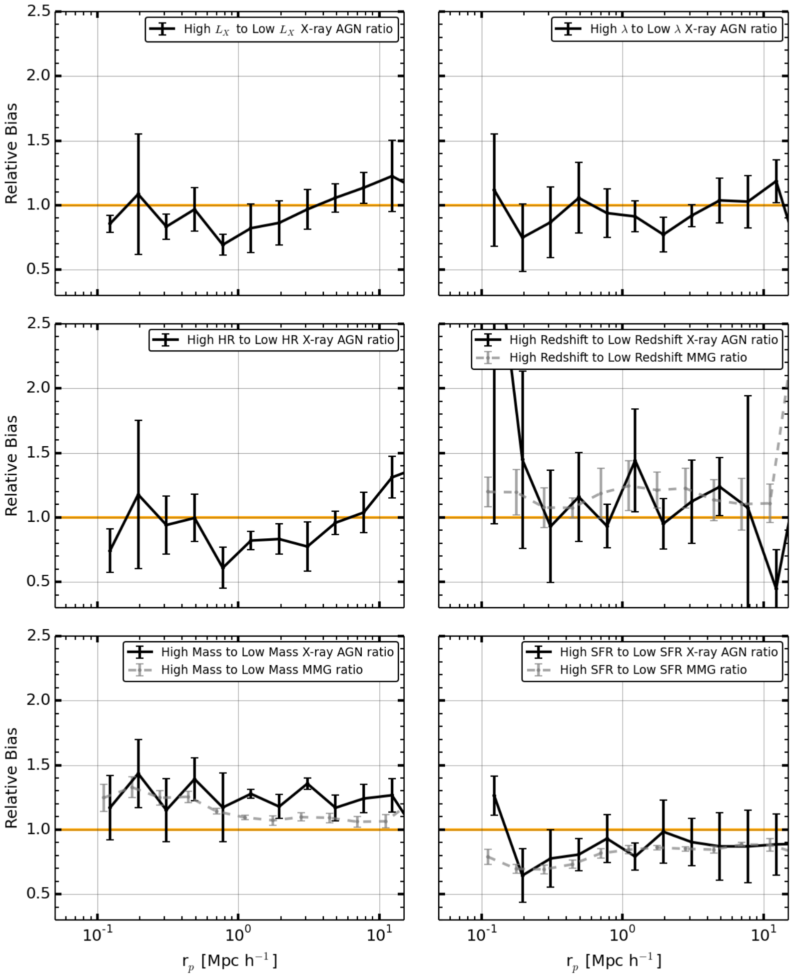

Figure 4.6: **Clustering of X-ray AGN sample properties and host galaxy properties** — Clustering as a function of X-ray AGN sample properties and host galaxy properties. In each panel we show the relative bias for each subsample with jackknife error bars. For host galaxy properties (stellar mass, star formation rate, and redshift) we also include relative bias estimate for the matched galaxy sample with similar cuts.

($1.0\,h^{-1}\,\mathrm{Mpc} < r_p < 10\,h^{-1}\,\mathrm{Mpc}$) are $< 1\sigma$, suggesting that the mass of dark matter halo does not correlate with any of the intrinsic properties of the X-ray AGN sample. Additionally, the similarity in the one-halo term ($0.1\,h^{-1}\,\mathrm{Mpc} < r_p < 1.0\,h^{-1}\,\mathrm{Mpc}$) suggests that the properties of the X-ray AGN sample are not affecting the number of galaxy pairs within a single dark matter halo.

We do not find any significant differences in the X-ray AGN samples relative to the host-galaxy properties (redshift, stellar mass, star-formation rate). All of the differences ($\sim 2\sigma$) can be explained by comparisons to matched-galaxy control samples (shown in light grey). In particular the differences in star-formation rate suggest that X-ray AGN sources are limited in the amount which they can quench star formation. Together these results show that there is no significant difference in the evolution of the galaxies that host an active X-ray AGN source and all galaxies. See Table 4.4 for the individual sample significances between the different samples.

For all of the samples we additionally test the significance of the clustering measurement for the upper and lower quartiles of both the AGN and host galaxy properties. This comparison examines the differences of the most extreme objects in each parameter. We find no significant differences in any of the parameters due to the significant increase in the uncertainty of each measurement.

4.6.2 Clustering of Radio AGN

We find that the Radio AGN sample is strongly clustered relative to the tracer-galaxy sample (Figure 4.4, center panel), but similarly clustered to the matched control galaxy sample (Figure 4.5, center panels). They reside in $M_{\mathrm{halo}} \sim 10^{13.6}\,\mathrm{h}^{-1}\,\mathcal{M}_{\odot}$ dark matter halos suggesting that they are generally found in massive galaxy groups or small galaxy clusters. The significant bump found at $r_p \sim 6$ in the projected correlation function is due to the highly clustered COSMOS sample; removing this field does not change the results that we find, but lowers the results by N%. This is not surprising as that the over-densities found in this field would drive up the relative mass of the dark matter halos found in these massive structures. For the one- or two-halo terms we do not find a significant difference in the clustering of luminous Radio AGN sources and matched galaxies.

Compared to the high-luminosity Radio AGN sources (Figure 4.7, top-left) we find that there is no significant difference ($\sim 2.8\sigma$) in the clustering of Radio AGN sources in the two-halo term. While there appears to be a large difference in the one-halo term, we do not find any significant difference in the clustering due mainly to the low number of high-luminosity radio sources and the associated large uncertainties due to the limited number of pairs counts.

The uncorrelated clustering with radio luminosity of the Radio AGN sample may be surprising as that the high-luminosity Radio AGN sample is more concentrated in high-mass quiescent galaxies than the low-luminosity radio sample (see Figure 4.7, top-left). The population of low-

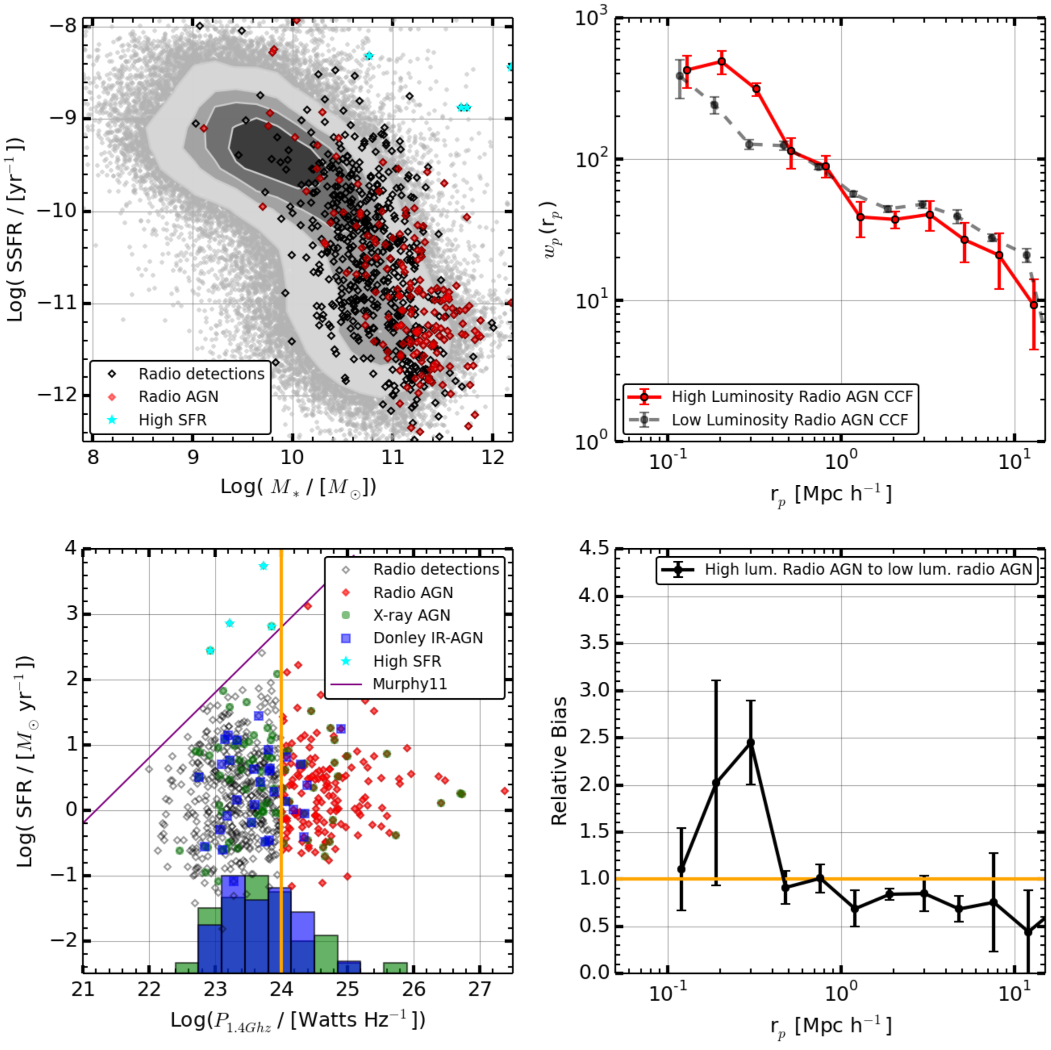

Figure 4.7: **Properties and projected correlation function of Radio AGN sources.** — Properties and clustering of Radio AGN sources. Top-left: Comparison of all radio detected sources and Radio AGN sources with $P_{1.4\mathrm{Ghz}}{>}10^{24}$ Watts Hz^{-1} in the specific star formation rate and mass plane. Sources with a star formation rate that can be explained by the Murphy+11 SFR-to-radio luminosity relationship are shown as cyan points. Bottom-left: Star formation rate compared to radio luminosity for the radio detected sources. X-ray AGN and Donley et al. sources are shown with green and blue points, respectively, with relative distributions shown at the bottom. The Murphy+11 SFR to Radio luminosity relationship is shown in purple. Top-right: Clustering of low-luminosity ($P_{1.4\mathrm{Ghz}}{<}10^{24}$ Watts Hz^{-1}) radio-detected sources (black dashed) and Radio AGN sources in red. Bottom-right: Jackknife ratio of the Radio sources. We do not find a significant difference in the clustering of either sample suggesting that there is not a dominate number of SF galaxies in the low-luminosity radio-sample.

luminosity likely Radio AGN sources found in quiescent galaxies with masses ($\mathcal{M}_* \gtrsim 10^{10.6}\,\mathcal{M}_\odot$) dominates the low-luminosity population which sustains the large clustering amplitude in these galaxies. We do not think that these sources have highly-obscured star-formation and a under-estimated extinction due to similarities in the estimated SFR from *Herschel-Spire* 250 μmfar-IR estimated SFRs. Likewise we do not find any trends in star-formation rate with respect to the radio luminosity suggesting a homogeneous population in the Radio AGN sample (Figure 4.7, bottom-left panel).

While there is not a significant difference in the clustering of these two Radio AGN samples, there is a significant difference in the median redshift of the two samples and thus a differences in the median dark-matter halo mass. The low-luminosity sample has a median redshift of $\langle z \rangle \sim 0.5$ whereas the high-luminosity sample has a median redshift of $\langle z \rangle \sim 0.8$. This difference in the median redshift suggests that the strong clustering of the lower luminosity sample resides in higher mass dark matter halos ($\langle M_{\rm halo} \rangle \sim 10^{13.6}\,{\rm h}^{-1}\,\mathcal{M}_\odot$ versus $\langle M_{\rm halo} \rangle \sim 10^{13.9}\,{\rm h}^{-1}\,\mathcal{M}_\odot$), but have smaller stellar masses ($\langle \mathcal{M}_* \rangle \sim 10^{11.2}\,\mathcal{M}_\odot$ versus $\langle \mathcal{M}_* \rangle \sim 10^{10.8}\,\mathcal{M}_\odot$).

4.6.3 Clustering of IR-AGN

We find that the Donley et al. sample is less clustered than the tracer-galaxy sample (Figure 4.4) and reside in $\langle M_{\rm halo} \rangle \sim 10^{11.6}\,{\rm h}^{-1}\,\mathcal{M}_\odot$ dark matter halos. The halo mass is not well estimated due low clustering strength of the sample, which may under estimate the mass of the dark-matter halo for these small halo masses. Additionally, we find that the Donley et al. sample is less clustered than the matched galaxy control sample (Figure 4.3). For both the one- and two-halo terms the Donley et al. sample is consistently less biased relative to the matched galaxy sample. While the significance of this is small ($\sim 2.6\sigma$), the difference in relative-bias between the two samples is high $\sim 33\%$. The projected correlation function is closer to the matched galaxy sample in the one halo term (25%, $\sim 2.2 sigma$) than in the two-halo term (33%, $\sim 2.5\sigma$). The relative bias between these two samples suggests that the physical triggering process for IR-AGN samples depends on a lower density of pairs and lower dark-matter halo mass. Unlike the Radio AGN and X-ray AGN samples, we note that the Donley et al. sample in the COSMOS field is less clustered than the other fields.

There is not a statistically significant difference when comparing the broad-line and non-broad-line Donley et al. samples. Removing the population of broad-line sources increases the relative bias by $\sim$15%. This does not significantly changes the bias measured of these sources due to the large uncertainty in these measurements, even though the broad-line population represents a relatively large fraction (31%) of the Donley et al. sample.

We find that the Assef et al. IR-AGN sample clusters similarly to the Donley et al. sample; the Assef et al. IR-AGN sample is both less clustered than the tracer sample, and less clustered than the matched galaxy control sample. The median dark-matter halo mass of the

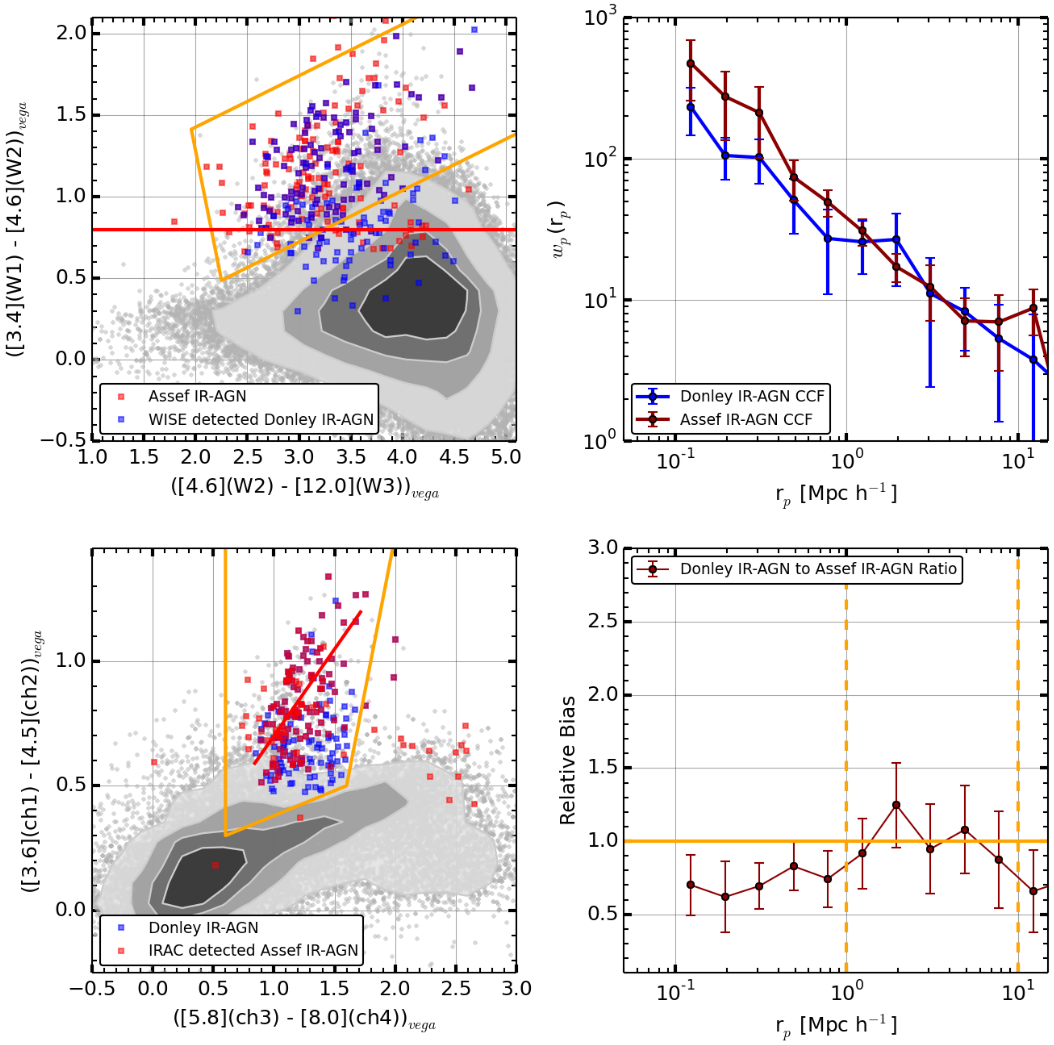

Figure 4.8: **Comparison of the IR-AGN samples** — Comparison of the Donley et al. selected sample (blue) and Assef et al. IR-AGN selected sample (red). In the top-left panel we show the WISE selection color-color diagram with the Mateos et al. (2013) selection wedge shown in orange, and Stern et al. (2012) color selection in red. In the background we show all WISE sources identified in the PRIMUS sample. In the bottom-left panel we show the IRAC selection color-color diagram with the Stern et al. (2005) selection wedge in orange, and the power-law locus in red. A small number of the Assef et al. IR-AGN sources that are IRAC detected fall outside of the locus of power-law like sources due to the selection not placing restraints on longer wavelengths. In the right panels we show the clustering of the Donley et al. and Assef et al. IR-AGN samples, and the relative bias for the two samples. We find no significant different in the clustering strength of either the Donley et al. or Assef et al. IR-AGN sources.

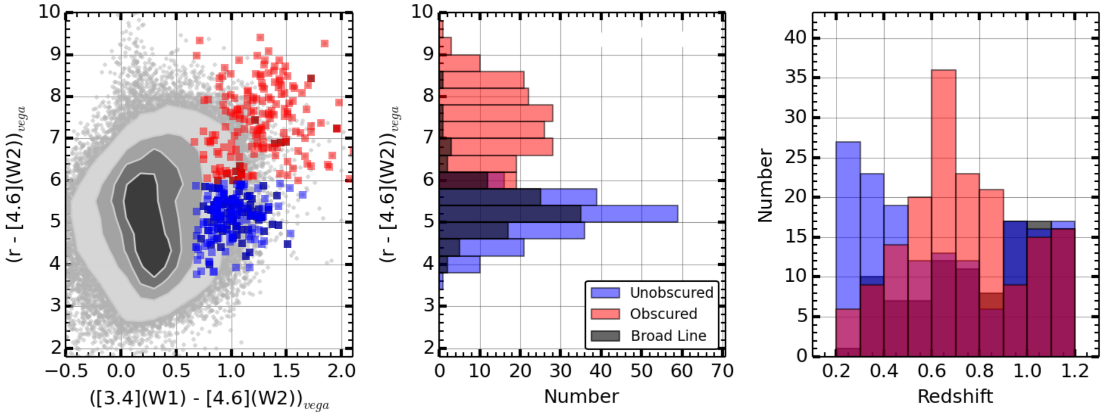

Figure 4.9: **Obscured and unobscured Assef et al. IR-AGN sample properties** — No significant differences in obscured vs unobscured samples. Showing the sample locations and properties of the un-obscured / obscured AGN samples. Obscured (red) sources are generally at higher redshift . Broadline sources which are generally blue are also at higher redshift. Differences in clustering are partially due to selecting different redshift samples. WISE IR-AGN samples miss a number of X-ray AGN and radio AGN.

Assef et al. IR-AGN sample is $\langle M_{\rm halo}\rangle = 10^{11.3}\,{\rm h}^{-1}\,\mathcal{M}_{\odot}$. While there is a population of Assef et al. IR-AGN sources that would not be identified by the Donley et al. sample (see Figure 4.8, bottom-left panel), this population is small enough to not change the results. These sources are not being excluded by the Assef et al. IR-AGN selected sample as it does not use the longer wavebands to ensure a red monotonically increasing flux in the mid-IR.

The Donley et al. sample has a shallower slope ($\gamma \sim 1.46$) as compared to the Assef et al. IR-AGN sample ($\gamma \sim 1.94$). This difference can be seen in the relative bias of the one- and two-halo terms with the Assef et al. IR-AGN sample being more clustered on smaller scales. The Donley et al. slope is comparable to the Stern IR-AGN sample of Hickox et al. ($\gamma = 1.5$ 2009). This difference goes away when removing the broad-line sources $\gamma \sim 1.65$, and indicates that the broad-line population identified in the Donley et al. sample is driving down the clustering in that sample.

Finally, we mention that we test the Assef et al. IR-AGN sample, and find no significant differences to either the Donley et al. sample or the Assef et al. IR-AGN samples.

4.6.4 Clustering of Obscured vs Unobscured WISE IR-AGN

Following Donoso et al. (2013) we compare the clustering of obscured and unobscured WISE IR-AGN. In Figure 4.10, we show the CCF for the two samples and the full Assef et al. IR-AGN sample. We do not find any significant differences in the clustering of obscured and unobscured sources in the Assef et al. IR-AGN sample.

We note that while this is a null result, inferring conclusions from this sample is difficult.

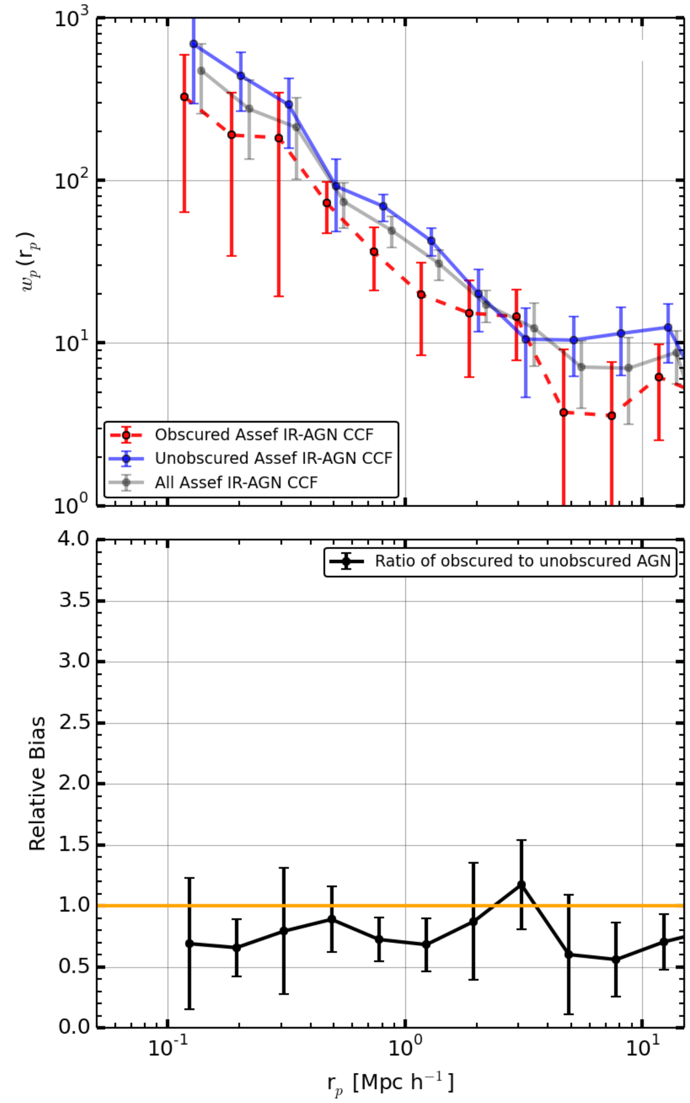

Figure 4.10: **Clustering measurement of obscured and unobscured samples** — Clustering measurement of obscured and unobscured Assef et al. IR-AGN samples. We find that there is not a significant difference in the clustering of the two samples.

For the obscured sources, we predominately identify broad-line sources with these colors at high redshift ($z \sim 1.0$; Figure 4.9 dark histogram in center and right panels). In addition to this population we find a second population of low redshift ($z \sim 0.3$) sources that also have similar colors but no detectable broad-lines suggesting a possible contaminate in the sample. Compared to the obscured sample we find a significantly different redshift distribution which peaks at $z \sim 0.7$, suggesting that the interpretation of the angular clustering of these populations is difficult at best.

The lack of correlation in the clustering strength in these samples matches the quasar clustering comparison of Hickox et al. (2011). This comparison may be somewhat of a stretch as they are both looking at higher redshift ($\langle z \rangle \sim 1.2$) and higher luminosities $\langle L_X \rangle \sim 10^{44}\,\mathrm{erg\ s^{-1}}$. However both suggest that there is not a significant difference in the clustering of obscured and unobscured sources for a range of different dark matter halo masses.

Likewise we test both the Donley et al. sample and Assef et al. IR-AGN sample for correlations between the clustering strength and obscuration and find no significant differences for any of the samples. For the Donley et al. selected sample we test both the optical-to-WISE color cut, and optical-to-IRAC color cut ((R-[4.6])=6.1) and find no significant differences for either sample.

4.6.5 Comparison of the Clustering of AGN Samples

Between the different selected AGN samples, we find that the Radio AGN sample is more strongly clustered than the X-ray AGN sample which is more clustered than the IR-AGN samples (Figure 4.11). In the two-halo term, the Radio AGN sample is only somewhat (13% higher bias, $\sim 1.1\sigma$) more clustered than the X-ray AGN sample. Likewise, the X-ray AGN sample is only somewhat (50% higher bias, $\sim 2.4\sigma$) more clustered than the Donley et al. sample. These differences account for the field-to-field variations since we resample each jackknife sample to estimate the relative bias which normalizes out the cosmic variance differences.

The X-ray AGN sample and Radio AGN sample both significantly increase in the one-halo term, whereas the Donley et al. sample increases less strongly. There is a $\sim 40\%$ relative bias in the one-halo term between the X-ray AGN and Donley et al. samples and the differences are significant at the $\sim 4\sigma$ level. These differences suggest a difference in the relative number of AGN identified within a single halo, implying more pairs of X-ray AGN and Radio AGN sources are identified in a single halo relative to Donley et al. sources. Some of this difference may be due to the strong anti-bias of Donley et al. selected sources to be identified in quiescent galaxies due to the $1.4\mu m$stellar bump entering into the mid-IR photometry Mendez et al. (2013) which would drive down the clustering in the one-halo term.

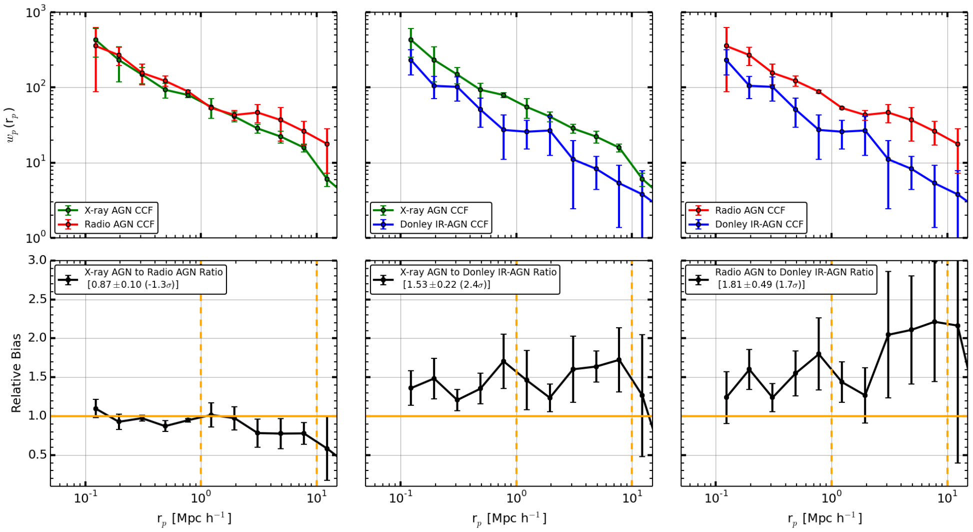

Figure 4.11: **Clustering comparison of the AGN samples** — Comparison of the projected cross-correlation function between the X-ray AGN, Radio AGN, and Donley et al. samples. In the top panel of each column we show the CCF for two samples and the ratio of the two samples in the bottom panel. We take the ratio of each jackknife sample for both samples to show the variation in the clustering signal between the two samples while limiting the dominate cosmic variance uncertainty. In the left most panels, we find that the X-ray AGN sample is somewhat less clustered than the Radio AGN sample. In the center panels we find that the X-ray AGN sample is significantly more clustered than the Donley et al. sample.

4.6.6 Comparison with Matched Galaxy Samples

AGN identification techniques are highly biased to selecting specific types of AGN, and more importantly AGN in specific types of galaxies. Generally AGN are more easily identifiable in more massive galaxies (Aird et al. 2012), with possible differences in both their star-formation rates, and redshift distributions (e.g., Goulding et al. 2014; Hickox et al. 2009; Coil et al. 2009). To normalize away these differences we compare our AGN samples to stellar mass, star-formation rate, and redshift matched-galaxy control samples for each sample to identify differences between the AGN and similarly selected galaxies.

In Figure 4.3, we find no significant differences in the clustering properties of the X-ray AGN sample and the Radio AGN sample at the $< 1\sigma$ level. This suggests that the physical effect of host environment on active galaxies and normal galaxies is a sub-dominate. The strong agreement in both the one- and two-halo terms indicates that the triggering mechanism is not strongly dependent on the number of galaxies within a single halo or mass of the halo. This is consistent with Ellison et al. (2011), who use pairs of optically selected AGN, to identify a sharp increase in the activity of AGN at close separations ($< 80\ h^{-1}$ Kpc), as that we are only sensitive to $> 100\ h^{-1}$ Kpc.

We find a departure for the IR-AGN selected samples and the host galaxies, with a high relative bias between the control and AGN samples. Both the Donley et al. sample and Assef et al. IR-AGN sample are less clustered than the matched-galaxy control samples with a relative bias between ∼20% to ∼40%. We currently cannot accurately determine the host galaxy properties as that the optical light is dominated by the AGN which leads to very high star-formation estimates and low stellar mass estimates. The large number of these broad-line sources in the Donley et al. sample limits the statistical significance of these results. Removing these sources increases the clustering measurement by $\sim 26\%$ in the two-halo term, but this significance of the differences is dominated by poisson statistics.

4.7 Discussion

We have used a large collection of multi-wavelength observations to probe the environmental dependance of different AGN samples. In the following sections, we discuss the implications of these findings in context of the current AGN literature and the AGN and galaxy connection. First, in Section 4.7.1, we discuss our findings relative to other multi-wavelength AGN studies. Following, in Section 4.7.2, we address the effects of the intrinsic differences in the samples Finally, in Section 4.7.3, we discuss the effects of AGN relative to inactive galaxies.

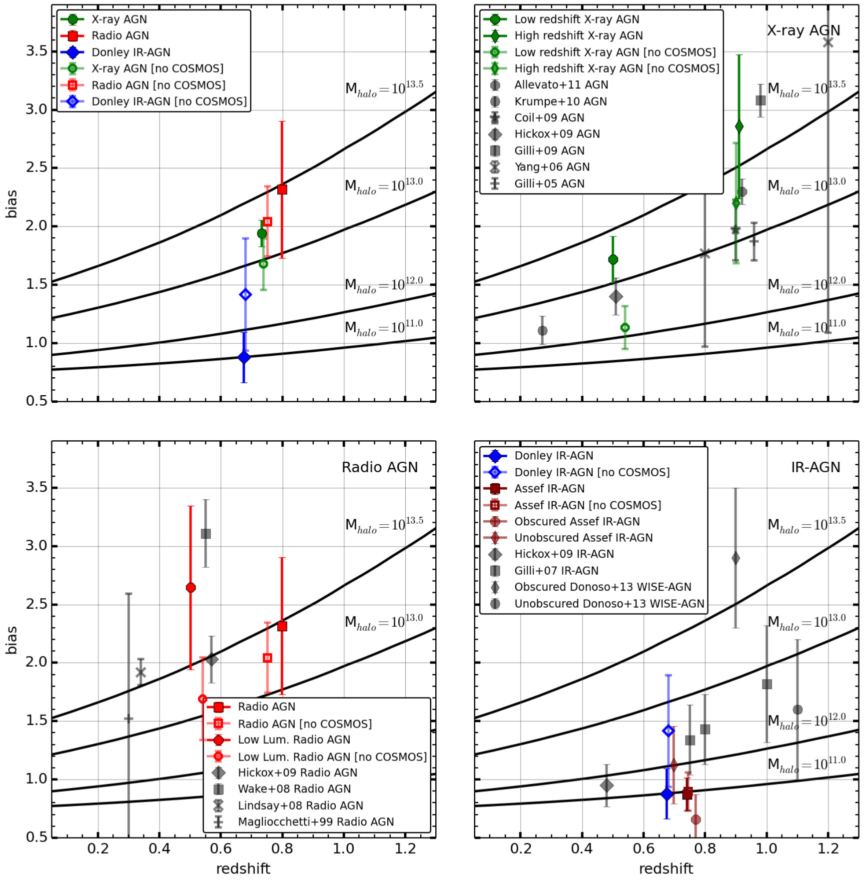

Figure 4.12: **Comparison of the redshift dependent absolute bias AGN samples** — Comparison of the absolute bias as a function of redshift for the different mutli-wavelength selected samples. (Top-left panel) bias estimate for the X-ray AGN sample (green square), Radio AGN sample (red square), and Donley et al. sample (blue square) presented in this work. For all panels, we show the samples without the COSMOS field with light open markers and color matching each sample. Additionally, we include lines of constant dark-matter halo mass ($M_{\rm halo} = 10^{11}\,{\rm h}^{-1}\,\mathcal{M}_{\odot}$ - $M_{\rm halo} = 10^{13.5}\,{\rm h}^{-1}\,\mathcal{M}_{\odot}$; black lines). (Top-right panel) literature comparison for for our redshift dependent X-ray AGN samples. We show the low-redshift X-ray AGN sample (green circle) and high-redshift X-ray AGN sample (green diamond). Additionally we show X-ray AGN samples from the literature which span a range of redshifts (left to right: Krumpe, Miyaji, & Coil (2010), Hickox et al. (2009), Yang et al. (2006), Gilli et al. (2005), Coil et al. (2009), Allevato et al. (2011), and Gilli et al. (2009)). (Bottom-left panel) bias estimate for the high-luminosity Radio AGN sample (square), and low-luminosity Radio AGN sample (circle). Additionally we show Radio AGN samples from the literature which span a range of redshifts (left to right: Magliocchetti et al. (1999), Lindsay et al. (2014), Wake et al. (2008), and Hickox et al. (2009)). (Bottom-right panel) bias estimates for the Donley et al. sample (blue square), and Assef et al. IR-AGN sample (red square). We show the Assef et al. IR-AGN WISE obscured sub-sample (cross), and unobscured sub-sample (circle). The Assef et al. IR-AGN sample is a superset of the obscured and un-obscured subsamples. We show angular clustering clustering estimates of Donoso et al. (2013) for obscured and unobscured sources as an open circle, and an open square. Additionally we show the Hickox et al. (2009) and Gilli et al. (2007) IR-AGN sample with a grey diamond.

4.7.1 How do these results compare to others?

We compare our results to others in the literature using the absolute bias parameter measured in the two-halo term, due to the degeneracy in the γ and r_0 fit parameters.

In the X-ray AGN sample (Figure 4.12 top-left) we find that our results are generally consistent with the bulk of other measurements from other fields. Including the COSMOS field systematically overestimate the absolute bias by n% at these redshifts due to the over-density found in the field at $z \sim 0.3$ and $z \sim 0.7$. This matches the published clustering value in this field. Without the COSMOS field, we find similar results to Coil et al. (2009) and Hickox et al. (2009). This is not surprising as we use a portion of the EGS similar to Coil et al. (2009). Together these results suggest that X-ray AGN sources consistently are found in $M_{\rm halo} \sim 10^{12.5}\,{\rm h}^{-1}\,\mathcal{M}_{\odot}$ to $M_{\rm halo} \sim 10^{13}\,{\rm h}^{-1}\,\mathcal{M}_{\odot}$ dark matter halos over a wide redshift range since $z \sim 1.2$.

The Radio AGN sample agrees with literature and generally shows a higher absolute-bias than the X-ray AGN sample indicating a higher dark-matter halo mass of $\langle M_{\rm halo} \rangle \sim 10^{13.5}\,{\rm h}^{-1}\,\mathcal{M}_{\odot}$. The low-luminosity Radio AGN sample is high in value, but does not constrain the halo mass with significance due to the uncertainty in the measurement. Like the X-ray AGN sample we find that the COSMOS field drives the clustering of the Radio AGN sample; the absolute bias is less when excluding the COSMOS field and follows a similar systematic offset of $\sim N\%$ that is seen in the X-ray AGN sample. The number of clustering estimates for Radio AGN is overall smaller, and our values match them well.

Finally, the IR-AGN samples match the literature values and suggest that the IR-AGN samples reside in low-mass dark-matter halos ($M_{\rm halo} \sim 10^{11.5}\,{\rm h}^{-1}\,\mathcal{M}_{\odot}$). While we present slightly different selection (e.g. Donley et al. , Stern et al. , $f_{24\mu m}$) the absolute bias are all consistent with these sources residing in low-mass dark-matter halos. Additionally, we do not agree with the angular clustering estimated values from Donoso et al. (2013) for the obscured and unobscured sources; we do not find a correlation between the clustering strength and obscuration of the source.

4.7.2 Does clustering depend on specific accretion rate?

In Mendez et al. (2013), we concluded that a significant difference in the IR-AGN and X-ray AGN samples was due to the large number of quiescent galaxies not identified by the IR-AGN sample due to the $1.6\mu m$stellar bump entering the mid-IR waveband. This difference limited the identified IR samples to be generally luminous AGN where the AGN light dominated the light from the galaxy. Combined with the high-mass AGN selection bias, this implies that the samples have different median accretion rate sources. Additionally we have now extended our sample to include Radio AGN sources, which probe lower specific-accretion rate sources (Hickox et al. 2009).

Using the Radio AGN sample, and the Donley et al. sample with two specific-accretion

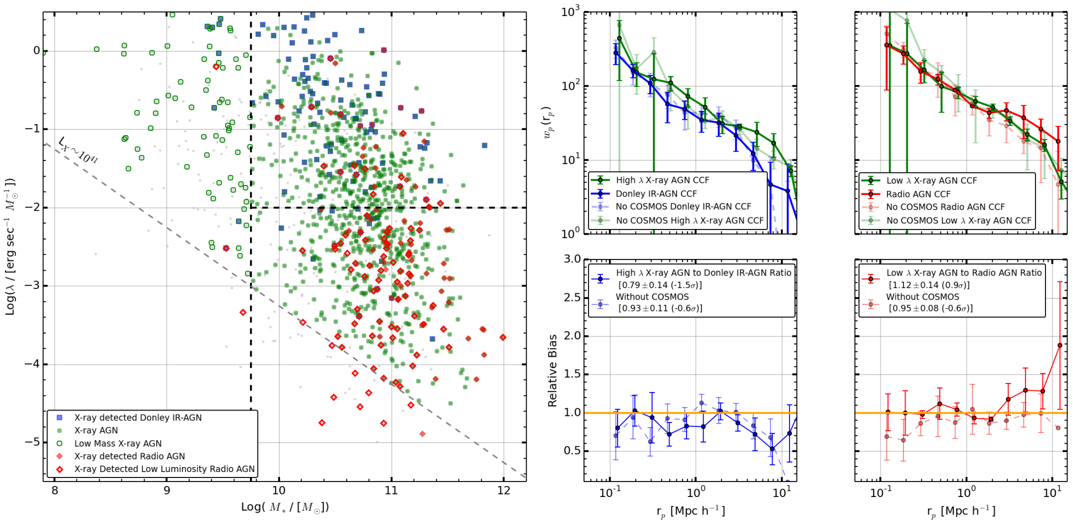

Figure 4.13: **Clustering comparison relative to the specific-accretion rate** — Comparison of the specific accretion rate samples. Large left panel: specific accretion rate and mass limits. Center panels: comparison of high λ X-ray AGN and Donley et al. samples. Right panels: comparison of low λ X-ray AGN and Radio AGN samples. We find that the Donley et al. sample is clustered like high specific accretion rate X-ray AGN sources and the Radio AGN sample is clustered like low specific accretion rate X-ray AGN sources.

rate sub-samples of the X-ray AGN population will allow us to determine the significance of the clustering differences between the multi-wavelength samples. We remove all broad-line sources from this comparison as we require a stellar mass estimate for the High-λX-ray AGN and Low-λX-ray AGN samples. This does not cause a significant difference ($\sim 1\sigma$) between the samples with or without the broad line sources. Of these sources we sub-divide the X-ray AGN sample with a specific-accretion rate of $\lambda = 10^{-2}$ erg s^{-1} $\mathcal{M}_\odot^{-1}$ and above a stellar-mass of $\mathcal{M}_* = 10^{9.75}\,\mathcal{M}_\odot$. This roughly separates the bulk of the X-ray detected Radio AGN sample and Donley et al. sample. We note that the left panel of Figure 4.13 only shows the subset of the Radio AGN sources and Donley et al. sources that are X-ray detected. Additionally both samples overlap in the specific-accretion rates, so this cut should be taken as a simple rough dividing-line comparison between the two specific-accretion rate extrema.

We find that the relative bias between the Radio AGN and Low-λX-ray AGN samples is less significant; The difference in the relative bias has gone down from 13% (1.1σ) to 12% (0.9σ). Additionally, we find that the relative bias between the Donley et al. and High-λX-ray AGN samples is less significant; the relative bias has gone down from 53% (2.4σ) to 21% (1.5σ). Some of the difference in the significance is due to the limits on the number of sources for each comparison. In the figure, we also show the [no COSMOS] samples for each of the comparisons to show the systematic bias that the COSMOS raises the relative bias for this comparison. Removing the COSMOS field from the comparison lowers the relative bias difference between the samples to

$\sim 0.6\sigma$ for both the High-λ and Low-λ samples.

4.7.3 Are there environmental differences for AGN samples?

Correlations between the AGN and host galaxy may prevent the actual estimate of the clustering strength of different samples relative to AGN properties. We find that the matched stellar mass, star-formation rate, and redshift control samples have similar clustering properties to each of the AGN samples at the $\sim 2\sigma$ level. This suggests that the physical mechanism that is fueling and triggering the AGN correlates with environmental scales much smaller than the length scales that we can probe here ($0.1\ h^{-1}$ Mpc), or are a sub-dominantly related to the mass of the dark matter halo.

Additionally we can use the matched-galaxy control sample as an estimator of the differences in the underlying AGNs identified in each technique. Assuming to our limiting depths, the underlying AGNs are distributed similarly to our measured samples, we would expect that the different waveband clustering measurements should converge upon the control galaxy sample with large enough samples. This gives us a more accurate estimate of the predicted differences in the host galaxies due to underlying selection effects imposed by each selection technique. While this does not rule out correlations between AGN properties and the host galaxy, it puts an upper limit on the significance of the differences. We find $\sim 2-3\sigma$ differences between the control samples suggesting even with larger surveys the intrinsic differences of the host galaxies will limit the accuracy in measuring correlations between the clustering strength and AGN properties only.

4.8 Conclusions

In this paper we measure the clustering amplitude of the X-ray AGN, Radio AGN, and IR-AGN populations in the DEEP2 and PRIMUS fields. We focus on these samples to identify a large range of specific accretion rate (Eddington ratio) sources to correlate environmental trends with respect to different accretion rates. We measure the clustering strength of the X-ray AGN sample relative to X-ray luminosity, specific accretion rate, hardness ratio subsamples. We estimate the clustering strength of the radio-loud and put an upper bound on the radio-quiet samples. We use WISE mid-IR to compare obscured and unobscured Assef et al. IR-AGN samples. We quantify the relative clustering strengths between each sample, and compared to stellar mass, star formation rate and redshift matched galaxy control samples. The main results from our work are as follows:

1. The inferred two-point auto-correlation function of X-ray AGN, Radio AGN and Donley et al. sources to reside in different mass dark matter halos. From the two-halo term ($1 < r_p\ /\ h^{-1}\,\mathrm{Mpc} < 10$) we estimate that the X-ray AGN, Radio AGN, and Donley et al. samples

have median dark matter halo masses of $M_{\rm halo} \sim 10^{13.3}\,{\rm h}^{-1}\,\mathcal{M}_{\odot}$, $M_{\rm halo} \sim 10^{13.6}\,{\rm h}^{-1}\,\mathcal{M}_{\odot}$, and $M_{\rm halo} \sim 10^{11.6}\,{\rm h}^{-1}\,\mathcal{M}_{\odot}$, respectively.

2. The X-ray AGN sample clusters similarly to the Radio AGN sample. Both are more ($\gtrsim$50%; $\sim$2σ) clustered than the Donley et al. sample. The X-ray AGN and Radio AGN samples are much more clustered in the one halo term as compared to the Donley et al. sample.

3. We find no significant correlations ($<$2σ) between the clustering amplitude and subsamples of the X-ray AGN population with X-ray luminosity, specific accretion rate, and hardness ratio. Trends with respect to stellar mass, star formation rate, and redshift are well within the expected trend for inactive matched galaxy control samples.

4. We find no significant difference in the clustering amplitude of Radio-loud and all radio detected galaxies. Since these samples probe different median redshifts ($z \sim 0.5$ vs. $z \sim 0.8$), we find that the radio-quiet sample to have a larger dark matter halo mass ($M_{\rm halo} \sim 10^{13.6}\,{\rm h}^{-1}\,\mathcal{M}_{\odot}$ vs. $M_{\rm halo} \sim 10^{13.9}\,{\rm h}^{-1}\,\mathcal{M}_{\odot}$).

5. The Donley et al. and Assef et al. IR-AGN samples have similar clustering amplitudes. For either we find no significant difference in the clustering amplitude of obscured and un-obscured Assef et al. IR-AGN sources. This suggests differences found in angular clustering results are dominated by the uncertainty of the redshift distribution.

6. From the large range of specific accretion rates that the X-ray AGN sample probes we can explain the bulk of the differences in clustering amplitudes found in the X-ray AGN, Radio AGN, and IR-AGN samples. The high specific-accretion rate X-ray AGN sources cluster more similar to the Donley et al. sample. The low specific-accretion rate X-ray AGN sources cluster similar to the Radio AGN sample. This suggests that the environmental dependance on the different multi-wavelength AGN samples is sub-dominate on the scales that we probe $\gtrsim 100\,h^{-1}\,$Kpc.

7. The stellar mass, star formation rate, and redshift matched galaxy control samples are clustered similarly for the X-ray AGN, Radio AGN samples. The Donley et al. sample is less clustered than the matched galaxy control sample. This may suggest contamination of the host galaxy light overpredicting the matched mass galaxy sample mass, and thus clustering amplitude.

4.9 Acknowledgments

We thank our anonymous referee for useful comments that have greatly improved this paper. We thank Andy Goulding for reducing and extracting the DEEP2 02hr IRAC data.

Funding for PRIMUS has been provided by NSF grants AST-0607701, 0908246, 0908442, 0908354, and NASA grant 08-ADP08-0019. ALC acknowledges support from the Alfred P. Sloan Foundation and NSF CAREER award AST-1055081. AJM and JA acknowledges support from NASA grant NNX12AE23G through the Astrophysics Data Analysis Program.

We thank the CFHTLS, COSMOS, DLS, and SWIRE teams for their public data releases and/or access to early releases. This paper includes data gathered with the 6.5 m Magellan Telescopes located at Las Campanas Observatory, Chile. We thank the support staff at LCO for their help during our observations, and we acknowledge the use of community access through NOAO observing time. We use data from the DEEP2 survey, which was supported by NSF AST grants AST00-71048, AST00-71198, AST05-07428, AST05-07483, AST08-07630, AST08-08133. This study makes use of data from AEGIS Survey and in particular uses data from *GALEX*, Keck, and CFHT. The AEGIS Survey was supported in part by the NSF, NASA, and the STFC. Some of the data used for this project are from the CFHTLS public data release, which includes observations obtained with MegaPrime/MegaCam, a joint project of CFHT and CEA/DAPNIA, at the Canada-France-Hawaii Telescope (CFHT) which is operated by the National Research Council (NRC) of Canada, the Institut National des Science de l'Univers of the Centre National de la Recherche Scientifique (CNRS) of France, and the University of Hawaii. This work is based in part on data products produced at TERAPIX and the Canadian Astronomy Data Centre as part of the Canada-France-Hawaii Telescope Legacy Survey, a collaborative project of NRC and CNRS. We also thank those who have built and operate the Chandra and XMM-Newton X-Ray Observatories. This research has made use of the NASA/IPAC Infrared Science Archive, which is operated by the Jet Propulsion Laboratory, California Institute of Technology, under contract with the National Aeronautics and Space Administration.

This chapter is a draft of material that will be submitted as "AEGIS + PRIMUS: Clustering of X-ray-, Radio- and IR-AGN at $z \sim 0.7$" by Alexander J. Mendez, Alison L. Coil, James Aird, Ramin A. Skibba, Aleksandar M. Diamond-Stanic, John Moustakas, Michael R. Blanton, Richard J. Cool, Daniel J. Eisenstein, Kenneth C. Wong, & Guangtun Zhu, to the The Astrophysical Journal. I am the primary investigator and author of this paper.

Table 4.1: Multi-wavelength coverage areas, and numbers.

	Area [deg^2]				Sample Size					
Field	X-ray	Radio	IRAC	WISE	N_{Galaxy}[a]	N_{Mass}[b]	$N_{\mathrm{X\text{-}ray}}$[c]	N_{Radio}[d]	N_{Donley}	N_{Assef}
Chandra Deep Field South	-	-	1.77	1.77	19,612	18,510	-	-	121	46
COSMOS	0.93	0.93	0.93	0.93	15,574	15,330	276	126 (276)	58	31
Elais - South 1	0.51	-	0.90	0.90	8,663	8,400	59	-	45	14
Extended Groth Strip	0.69	0.71	0.61	0.71	10,508	9,769	261	37 (278)	34	12
DEEP2 02hr PRIMUS[e]	0.48	0.58	0.47	0.58	6,338	6,325	41	9 (41)	21	20
DEEP2 02hr DEEP2	0.58	0.61	0.60	0.61	6,635	6,354	34	5 (34)	20	12
DEEP2 16hr DEEP2	0.73	0.73	-	0.73	5,645	5,408	31	6 (31)	-	9
DEEP2 23hr PRIMUS[e]	0.66	0.67	-	0.67	6,275	6,262	35	6 (35)	-	9
DEEP2 23hr DEEP2	0.89	0.92	-	0.92	6,720	6,428	56	6 (56)	-	14
XMM LSS/SXDS	2.88	2.88	2.84	2.88	37,849	37,764	160	61 (161)	143	70
Totals:	8.35	8.03	8.11	10.69	123,819	120,550	953	256 (971)	442	237

[a] Redshifts limited to $0.2 < z \leq 1.2$ and $z_{\mathrm{quality}} \geq 3$.

[b] The optical light for Broad-line AGN is contaminated and prevents an accurate estimate of the stellar mass.

[c] X-ray detected sources with $L_{\mathrm{X}} > 10^{41}$ erg s^{-1}.

[d] Radio AGN with $P_{1.4\mathrm{Ghz}} \geq 10^{24}$ Watts Hz^{-1}. In parenthesis shows all detected radio sources.

[e] The DEEP2 PRIMUS fields area are a partial subset of the DEEP2 fields and not added to the total.

Table 4.2: Numbers, densities, median redshift, median luminosity and median stellar mass for clustering samples.

AGN	Sample Name	Redshift Range	Number[a]	Density[b]	$\langle z \rangle$	$\langle L \rangle^{c}$	$\langle M_* \rangle^{d}$
X-ray AGN	Full Redshift	0.2 – 1.2	958	0.79	0.73	42.8	10.73
Radio AGN	Full Redshift	0.2 – 1.2	327	0.21	0.80	24.3	11.17
Donley IR-AGN	Full Redshift	0.2 – 1.2	583	0.44	0.68	44.2	10.45
X-ray AGN	No Broadline	0.2 – 1.2	633	0.53	0.72	42.7	10.76
Radio AGN	No Broadline	0.2 – 1.2	272	0.17	0.80	24.3	11.17
Donley IR-AGN	No Broadline	0.2 – 1.2	328	0.25	0.61	44.0	10.39
X-ray AGN	Low L_X	0.2 – 1.2	570	0.49	0.74	42.5	10.76
X-ray AGN	High L_X	0.2 – 1.2	388	0.30	0.67	43.4	10.71
X-ray AGN	Low λ	0.2 – 1.2	329	0.27	0.65	42.4	10.87
X-ray AGN	High λ	0.2 – 1.2	305	0.26	0.90	43.4	10.69
X-ray AGN	Low HR	0.2 – 1.2	671	0.54	0.73	42.9	10.70
X-ray AGN	High HR	0.2 – 1.2	287	0.25	0.73	42.7	10.78
X-ray AGN	Low Redshift	0.2 – 0.7	422	1.24	0.50	42.5	10.71
X-ray AGN	High Redshift	0.7 – 1.2	536	0.61	0.91	43.2	10.77
Radio AGN	All Radio Sources	0.2 – 1.2	894	0.55	0.62	23.5	10.91
Radio AGN	Low Luminosity Radio Sources	0.2 – 1.2	569	0.34	0.50	23.3	10.78
Assef IR-AGN	Full Redshift	0.2 – 1.2	234	0.14	0.74	44.5	10.59
Assef IR-AGN	Obscured WISE color	0.2 – 1.2	129	0.08	0.77	44.5	10.59
Assef IR-AGN	Unobscured WISE color	0.2 – 1.2	106	0.06	0.70	44.5	10.57

[a] Number of sources in window function with applied selection cuts.

[b] Density is in units of $[10^{-4} * h^3\,\mathrm{Mpc}^{-3}]$.

[c] $\langle L \rangle$ is $\langle L_X \rangle$ $[\log(\mathrm{erg\,s^{-1}})]$ for X-ray AGN samples, $\langle L_{3.6\,\mu m} \rangle$ $[\log(\mathrm{erg\,s^{-1}})]$ for IR-AGN samples, and $\langle P_{1.4Ghz} \rangle$ $[\log(\mathrm{Watts\,Hz^{-1}})]$ for Radio AGN.

[d] Mass is in units of $[\log(h^{-1}\,\mathcal{M}_\odot)]$

Table 4.3: X-ray AGN, Radio AGN, and IR-AGN clustering results.

AGN	Sample Name	r_0[a]	γ	Bias[b]	$\langle M_{DM} \rangle$[c]
X-ray AGN	Full Redshift	5.81 ± 0.59	1.71 ± 0.13	1.91 ± 0.11	13.3
Radio AGN	Full Redshift	6.6 ± 2.5	1.5 ± 1.1	2.17 ± 0.56	13.6
Donley IR-AGN	Full Redshift	2.0 ± 1.3	1.46 ± 0.22	0.85 ± 0.21	11.6
X-ray AGN	No Broadline	5.4 ± 2.4	1.45 ± 0.29	1.95 ± 0.18	13.4
Radio AGN	No Broadline	4.3 ± 3.1	2.6 ± 1.3	1.91 ± 0.56	13.4
Donley IR-AGN	No Broadline	3.6 ± 1.1	1.64 ± 0.19	1.14 ± 0.29	12.5
X-ray AGN	Low L_X	6.1 ± 1.7	2.03 ± 0.55	1.95 ± 0.11	13.4
X-ray AGN	High L_X	2.0 ± 1.0	1.13 ± 0.13	1.84 ± 0.38	13.3
X-ray AGN	Low λ	6.65 ± 0.82	1.60 ± 0.19	2.11 ± 0.15	13.5
X-ray AGN	High λ	5.3 ± 1.5	1.62 ± 0.28	1.84 ± 0.29	13.3
X-ray AGN	Low HR	6.26 ± 0.52	1.96 ± 0.16	2.033 ± 0.037	13.4
X-ray AGN	High HR	2.00 ± 0.45	1.17 ± 0.10	1.61 ± 0.36	13.1
X-ray AGN	Low Redshift	5.64 ± 0.80	1.71 ± 0.15	1.69 ± 0.20	13.4
X-ray AGN	High Redshift	8.1 ± 4.3	1.46 ± 0.13	2.81 ± 0.60	13.7
Radio AGN	All Radio Sources	6.4 ± 1.8	1.22 ± 0.58	2.72 ± 0.69	13.8
Radio AGN	Low Luminosity Radio Sources	5.8 ± 1.8	1.17 ± 0.29	2.85 ± 0.74	13.9
Assef IR-AGN	Full Redshift	2.58 ± 0.31	1.94 ± 0.55	0.82 ± 0.15	11.3
Assef IR-AGN	Obscured WISE color	2.00 ± 0.21	2.03 ± 0.80	0.60 ± 0.16	11.1
Assef IR-AGN	Unobscured WISE color	3.51 ± 0.47	2.02 ± 0.35	1.09 ± 0.31	12.4

[a] Correlation scale length, r_0, is in units of $[h^{-1}\,\mathrm{Mpc}]$.

[b] Absolute Bias estimated on scales of $1.0 < r_p / [h^{-1}\,\mathrm{Mpc}] \leq 10.0$.

[c] Dark matter halo median mass, M_{DM}, is in units of $[\log(h^{-1}\,\mathcal{M}_{\odot})]$.

Table 4.4: Relative clustering strengths for the AGN samples.

Sample	AGN	Relative Bias $0.1 < r_p < 1$	N_σ	Relative Bias $1 < r_p < 10$	N_σ
Full Redshift Range	X-ray AGN to Radio AGN ratio	0.964 ± 0.036	-1.0	0.87 ± 0.10	-1.3
Full Redshift Range	X-ray AGN to Donley IR-AGN ratio	1.422 ± 0.097	4.4	1.53 ± 0.22	2.4
Full Redshift Range	Radio AGN to Donley IR-AGN ratio	1.49 ± 0.16	3.0	1.81 ± 0.49	1.7
X-ray AGN	No Broadline to Full Redshift ratio	0.950 ± 0.052	-0.97	1.010 ± 0.017	0.62
Radio AGN	No Broadline to Full Redshift ratio	1.029 ± 0.017	1.7	0.940 ± 0.067	-0.89
Donley et al.	No Broadline to Full Redshift ratio	1.150 ± 0.094	1.6	1.155 ± 0.071	2.2
X-ray AGN	High L_X to Low L_X ratio	0.887 ± 0.077	-1.5	0.97 ± 0.11	-0.29
X-ray AGN	High λ to Low λ ratio	0.95 ± 0.18	-0.31	0.933 ± 0.092	-0.73
X-ray AGN	High HR to Low HR ratio	0.89 ± 0.15	-0.71	0.885 ± 0.091	-1.3
X-ray AGN	High Redshift to Low Redshift ratio	1.54 ± 0.42	1.3	1.16 ± 0.30	0.56
X-ray AGN	High Mass to Low Mass ratio	1.264 ± 0.088	3.0	1.244 ± 0.035	7.1
X-ray AGN	High SFR to Low SFR ratio	0.884 ± 0.072	-1.6	0.88 ± 0.21	-0.55
Radio AGN	Radio AGN to All Radio Sources ratio	1.16 ± 0.11	1.5	0.893 ± 0.077	-1.4
Radio AGN	Radio AGN to Low Luminosity Radio Sources ratio	1.20 ± 0.15	1.4	0.87 ± 0.11	-1.2
Specific Accretion Rate	High-λ X-ray AGN to Radio AGN ratio	0.83 ± 0.26	-0.65	1.09 ± 0.12	0.74
Specific Accretion Rate	Low-λ X-ray AGN to Donley IR-AGN ratio	1.18 ± 0.13	1.4	1.33 ± 0.26	1.3
Assef et al. IR-AGN	Obscured WISE color to Unobscured WISE color ratio	0.72 ± 0.14	-2.0	0.76 ± 0.24	-1.0

Table 4.5: Relative clustering strengths compared to control galaxy sample.

Sample	AGN	Relative Bias $0.1 < r_p < 1$	N_σ	Relative Bias $1 < r_p < 10$	N_σ
Galaxy Control Sample	X-ray AGN to X-ray Matched ratio	0.93 ± 0.12	-0.59	0.957 ± 0.051	-0.84
Galaxy Control Sample	Radio AGN to Radio Matched ratio	1.118 ± 0.054	2.2	0.95 ± 0.13	-0.41
Galaxy Control Sample	Donley IR-AGN to Donley Matched ratio	0.887 ± 0.076	-1.5	0.80 ± 0.16	-1.3
Galaxy Control Sample	X-ray Matched to Radio Matched ratio	1.033 ± 0.019	1.8	1.180 ± 0.060	3.0
Galaxy Control Sample	X-ray Matched to Donley Matched ratio	1.104 ± 0.033	3.1	1.25 ± 0.13	1.9
Galaxy Control Sample	Radio Matched to Donley Matched ratio	1.070 ± 0.037	1.9	1.061 ± 0.080	0.76
Low L_X	X-ray AGN to X-ray Matched ratio	1.00 ± 0.13	0.012	0.950 ± 0.054	-0.93
High L_X	X-ray AGN to X-ray Matched ratio	0.69 ± 0.12	-2.6	0.771 ± 0.096	-2.4
Low λ	X-ray AGN to X-ray Matched ratio	1.05 ± 0.34	0.14	1.152 ± 0.057	2.6
High λ	X-ray AGN to X-ray Matched ratio	0.945 ± 0.097	-0.56	0.974 ± 0.052	-0.50
Low HR	X-ray AGN to X-ray Matched ratio	1.038 ± 0.079	0.48	0.986 ± 0.036	-0.38
High HR	X-ray AGN to X-ray Matched ratio	0.72 ± 0.10	-2.8	0.797 ± 0.046	-4.4
Low Redshift	X-ray AGN to X-ray Matched ratio	1.093 ± 0.081	1.1	1.10 ± 0.10	1.0
High Redshift	X-ray AGN to X-ray Matched ratio	1.52 ± 0.47	1.1	1.08 ± 0.27	0.29
Low Mass	X-ray AGN to X-ray Matched ratio	1.01 ± 0.11	0.064	0.902 ± 0.039	-2.5
High Mass	X-ray AGN to X-ray Matched ratio	1.02 ± 0.12	0.13	1.034 ± 0.051	0.68
Low SFR	X-ray AGN to X-ray Matched ratio	0.91 ± 0.20	-0.42	0.97 ± 0.17	-0.19
High SFR	X-ray AGN to X-ray Matched ratio	1.07 ± 0.16	0.43	1.00 ± 0.12	-0.030

Table 4.6: Relative clustering of sources with or without the COSMOS field.

Sample	AGN	Relative Bias $0.1 < r_p < 1$	N_σ	Relative Bias $1 < r_p < 10$	N_σ
Full Redshift	X-ray AGN	0.92 ± 0.19	-0.40	1.132 ± 0.081	1.6
Full Redshift	Radio AGN	1.03 ± 0.17	0.17	1.10 ± 0.17	0.59
Full Redshift	Donley IR-AGN	0.85 ± 0.18	-0.82	0.82 ± 0.20	-0.89
Low L_X	X-ray AGN	0.81 ± 0.22	-0.86	1.029 ± 0.070	0.41
High L_X	X-ray AGN	1.00 ± 0.32	0.011	1.40 ± 0.19	2.0
Low λ	X-ray AGN	0.72 ± 0.23	-1.2	1.046 ± 0.075	0.61
High λ	X-ray AGN	0.92 ± 0.29	-0.26	1.16 ± 0.13	1.2
Low HR	X-ray AGN	0.89 ± 0.30	-0.36	1.20 ± 0.10	2.0
High HR	X-ray AGN	0.83 ± 0.26	-0.66	1.00 ± 0.13	0.0031
Low Redshift	X-ray AGN	0.94 ± 0.21	-0.28	1.31 ± 0.13	2.3
High Redshift	X-ray AGN	1.20 ± 0.82	0.24	1.16 ± 0.18	0.85
Low Mass	X-ray AGN	0.96 ± 0.22	-0.19	1.17 ± 0.12	1.4
High Mass	X-ray AGN	0.83 ± 0.27	-0.61	1.121 ± 0.075	1.6
Low SFR	X-ray AGN	0.81 ± 0.21	-0.89	1.034 ± 0.090	0.38
High SFR	X-ray AGN	0.85 ± 0.31	-0.47	1.13 ± 0.12	1.1
All Radio Sources	Radio AGN	0.93 ± 0.13	-0.57	1.21 ± 0.17	1.2
Low Luminosity Radio Sources	Radio AGN	0.89 ± 0.30	-0.38	1.27 ± 0.21	1.3
Full Redshift	Assef IR-AGN	1.11 ± 0.29	0.39	1.01 ± 0.12	0.056
Obscured WISE color	Assef IR-AGN	0.99 ± 0.43	-0.031	0.93 ± 0.22	-0.30
Unobscured WISE color	Assef IR-AGN	1.18 ± 0.30	0.61	1.10 ± 0.21	0.47

4.10 References

Aird, J., Coil, A. L., Moustakas, J., Blanton, M. R., Burles, S. M., Cool, R. J., Eisenstein, D. J., Smith, M. S. M., Wong, K. C., & Zhu, G. 2012, ApJ, 746, 90

Allevato, V., Finoguenov, A., Cappelluti, N., Miyaji, T., Hasinger, G., Salvato, M., Brusa, M., Gilli, R., Zamorani, G., Shankar, F., James, J. B., McCracken, H. J., Bongiorno, A., Merloni, A., Peacock, J. A., Silverman, J., & Comastri, A. 2011, ApJ, 736, 99

Allevato, V., Finoguenov, A., Hasinger, G., Miyaji, T., Cappelluti, N., Salvato, M., Zamorani, G., Gilli, R., George, M. R., Tanaka, M., Brusa, M., Silverman, J., Civano, F., Elvis, M., & Shankar, F. 2012, ApJ, 758, 47

Antonucci, R. R. J., & Ulvestad, J. S. 1985, ApJ, 294, 158–182

Appleton, P. N., Fadda, D. T., Marleau, F. R., Frayer, D. T., Helou, G., Condon, J. J., Choi, P. I., Yan, L., Lacy, M., Wilson, G., Armus, L., Chapman, S. C., Fang, F., Heinrichson, I., Im, M., Jannuzi, B. T., Storrie-Lombardi, L. J., Shupe, D., Soifer, B. T., Squires, G., & Teplitz, H. I. 2004, ApJS, 154, 147–150

Assef, R. J., Stern, D., Kochanek, C. S., Blain, A. W., Brodwin, M., Brown, M. J. I., Donoso, E., Eisenhardt, P. R. M., Jannuzi, B. T., Jarrett, T. H., Stanford, S. A., Tsai, C.-W., Wu, J., & Yan, L. 2013, ApJ, 772, 26

Barmby, P., Huang, J.-S., Ashby, M. L. N., Eisenhardt, P. R. M., Fazio, G. G., Willner, S. P., & Wright, E. L. 2008, ApJS, 177, 431–445

Barro, G., Pérez-González, P. G., Gallego, J., Ashby, M. L. N., Kajisawa, M., Miyazaki, S., Villar, V., Yamada, T., & Zamorano, J. 2011, ApJS, 193, 13

Baugh, C. M. 2006, Reports on Progress in Physics, 69, 3101–3156

Becker, R. H., White, R. L., & Helfand, D. J. 1994, In Astronomical Data Analysis Software and Systems III, D. R. Crabtree, R. J. Hanisch, and J. Barnes, eds., volume 61 of *Astronomical Society of the Pacific Conference Series*, p. 165

Becker, R. H., White, R. L., & Helfand, D. J. 1995, ApJ, 450, 559

Best, P. N., Kauffmann, G., Heckman, T. M., Brinchmann, J., Charlot, S., Ivezić, Ž., & White, S. D. M. 2005, MNRAS, 362, 25–40

Bigelow, B. C., & Dressler, A. M. 2003, In Society of Photo-Optical Instrumentation Engineers (SPIE) Conference Series, M. Iye and A. F. M. Moorwood, eds., volume 4841 of *Society of Photo-Optical Instrumentation Engineers (SPIE) Conference Series*, pp. 1727–1738

Blanton, M. R., & Roweis, S. 2007, AJ, 133, 734

Bonoli, S., Marulli, F., Springel, V., White, S. D. M., Branchini, E., & Moscardini, L. 2009, MNRAS, 396, 423–438

Bower, R. G., Benson, A. J., Malbon, R., Helly, J. C., Frenk, C. S., Baugh, C. M., Cole, S., & Lacey, C. G. 2006, MNRAS, 370, 645

Brusa, M., Zamorani, G., Comastri, A., Hasinger, G., Cappelluti, N., Civano, F., Finoguenov, A., Mainieri, V., Salvato, M., Vignali, C., Elvis, M., Fiore, F., Gilli, R., Impey, C. D., Lilly, S. J., Mignoli, M., Silverman, J., Trump, J., Urry, C. M., Bender, R., Capak, P., Huchra, J. P., Kneib, J. P., Koekemoer, A., Leauthaud, A., Lehmann, I., Massey, R., Matute, I., McCarthy, P. J., McCracken, H. J., Rhodes, J., Scoville, N. Z., Taniguchi, Y., & Thompson, D. 2007, ApJS, 172, 353–367

Bruzual, G., & Charlot, S. 2003, MNRAS, 344, 1000–1028

Canalizo, G., & Stockton, A. 2001, ApJ, 555, 719–743

Cappelluti, N., Ajello, M., Burlon, D., Krumpe, M., Miyaji, T., Bonoli, S., & Greiner, J. 2010, ApJL, 716, L209–L213

Cattaneo, A., Dekel, A., Devriendt, J., Guiderdoni, B., & Blaizot, J. 2006, MNRAS, 370, 1651

Chabrier, G. 2003, PASP, 115, 763–795

Charlot, S., & Fall, S. M. 2000, ApJ, 539, 718–731

Chiappetti, L., Clerc, N., Pacaud, F., Pierre, M., Gueguen, A., Paioro, L., Polletta, M., Melnyk, O., Elyiv, A., Surdej, J., & Faccioli, L. 2012, ArXiv e-prints

Ciliegi, P., Zamorani, G., Hasinger, G., Lehmann, I., Szokoly, G., & Wilson, G. 2003, A&A, 398, 901–918

Cisternas, M., Jahnke, K., Inskip, K. J., Kartaltepe, J., Koekemoer, A. M., Lisker, T., Robaina, A. R., Scodeggio, M., Sheth, K., Trump, J. R., Andrae, R., Miyaji, T., Lusso, E., Brusa, M., Capak, P., Cappelluti, N., Civano, F., Ilbert, O., Impey, C. D., Leauthaud, A., Lilly, S. J., Salvato, M., Scoville, N. Z., & Taniguchi, Y. 2011, ApJ, 726, 57

Civano, F., Elvis, M., Brusa, M., Comastri, A., Salvato, M., Zamorani, G., Aldcroft, T., Bongiorno, A., Capak, P., Cappelluti, N., Cisternas, M., Fiore, F., Fruscione, A., Hao, H., Kartaltepe, J., Koekemoer, A., Gilli, R., Impey, C. D., Lanzuisi, G., Lusso, E., Mainieri, V., Miyaji, T., Lilly, S., Masters, D., Puccetti, S., Schawinski, K., Scoville, N. Z., Silverman, J., Trump, J., Urry, M., Vignali, C., & Wright, N. J. 2012, VizieR Online Data Catalog, 220, 10030

Coil, A. L., Newman, J. A., Kaiser, N., Davis, M., Ma, C.-P., Kocevski, D. D., & Koo, D. C. 2004, ApJ, 617, 765–781

Coil, A. L., Hennawi, J. F., Newman, J. A., Cooper, M. C., & Davis, M. 2007, ApJ, 654, 115–124

Coil, A. L., Newman, J. A., Croton, D., Cooper, M. C., Davis, M., Faber, S. M., Gerke, B. F., Koo, D. C., Padmanabhan, N., Wechsler, R. H., & Weiner, B. J. 2008, ApJ, 672, 153–176

Coil, A. L., Georgakakis, A., Newman, J. A., Cooper, M. C., Croton, D., Davis, M., Koo, D. C., Laird, E. S., Nandra, K., Weiner, B. J., Willmer, C. N. A., & Yan, R. 2009, ApJ, 701, 1484–1499

Coil, A. L., Blanton, M. R., Burles, S. M., Cool, R. J., Eisenstein, D. J., Moustakas, J., Wong, K. C., Zhu, G., Aird, J., Bernstein, R. A., Bolton, A. S., & Hogg, D. W. 2011, ApJ, 741, 8

Condon, J. J. 1992, ARA&A, 30, 575–611

Condon, J. J., Cotton, W. D., Greisen, E. W., Yin, Q. F., Perley, R. A., Taylor, G. B., & Broderick, J. J. 1998, AJ, 115, 1693–1716

Cool, R. J., Moustakas, J., Blanton, M. R., Burles, S. M., Coil, A. L., Eisenstein, D. J., Wong, K. C., Zhu, G., Aird, J., Bernstein, R. A., Bolton, A. S., Hogg, D. W., & Mendez, A. J. 2013, ApJ, 767, 118

Croom, S. M., Smith, R. J., Boyle, B. J., Shanks, T., Miller, L., Outram, P. J., & Loaring, N. S. 2004, MNRAS, 349, 1397–1418

Croom, S. M., Boyle, B. J., Shanks, T., Smith, R. J., Miller, L., Outram, P. J., Loaring, N. S., Hoyle, F., & da Ângela, J. 2005, MNRAS, 356, 415–438

Croton, D. J., Springel, V., White, S. D. M., De Lucia, G., Frenk, C. S., Gao, L., Jenkins, A., Kauffmann, G., Navarro, J. F., & Yoshida, N. 2006, MNRAS, 365, 11–28

Cutri, R. M., Wright, E. L., Conrow, T., Bauer, J., Benford, D., Brandenburg, H., Dailey, J., Eisenhardt, P. R. M., Evans, T., Fajardo-Acosta, S., Fowler, J., Gelino, C., Grillmair, C., Harbut, M., Hoffman, D., Jarrett, T., Kirkpatrick, J. D., Liu, W., Mainzer, A., Marsh, K., Masci, F., McCallon, H., Padgett, D., Ressler, M. E., Royer, D., Skrutskie, M. F., Stanford, S. A., Wyatt, P. L., Tholen, D., Tsai, C. W., Wachter, S., Wheelock, S. L., Yan, L., Alles, R., Beck, R., Grav, T., Masiero, J., McCollum, B., McGehee, P., & Wittman, M. 2011. Explanatory Supplement to the WISE Preliminary Data Release Products. Technical report,

Davis, M., & Peebles, P. J. E. 1983, ApJ, 267, 465–482

Davis, M., Faber, S. M., Newman, J., Phillips, A. C., Ellis, R. S., Steidel, C. C., Conselice, C., Coil, A. L., Finkbeiner, D. P., Koo, D. C., Guhathakurta, P., Weiner, B., Schiavon, R., Willmer, C., Kaiser, N., Luppino, G. A., Wirth, G., Connolly, A., Eisenhardt, P., Cooper, M., & Gerke, B. 2003, In Society of Photo-Optical Instrumentation Engineers (SPIE) Conference Series, P. Guhathakurta, ed., volume 4834 of *Society of Photo-Optical Instrumentation Engineers (SPIE) Conference Series*, pp. 161–172

de la Torre, S., Guzzo, L., Kovač, K., Porciani, C., Abbas, U., Meneux, B., Carollo, C. M., Contini, T., Kneib, J. P., Le Fèvre, O., Lilly, S. J., Mainieri, V., Renzini, A., Sanders, D., Scodeggio, M., Scoville, N., Zamorani, G., Bardelli, S., Bolzonella, M., Bongiorno, A., Caputi, K., Coppa, G., Cucciati, O., de Ravel, L., Franzetti, P., Garilli, B., Iovino, A., Kampczyk, P., Knobel, C., Koekemoer, A. M., Lamareille, F., Le Borgne, J.-F., Le Brun, V., Maier, C., Mignoli, M., Pelló, R., Peng, Y., Perez-Montero, E., Ricciardelli, E., Silverman, J., Tanaka, M., Tasca, L., Tresse, L., Vergani, D., Welikala, N., Zucca, E., Bottini, D., Cappi, A., Cassata, P., Cimatti, A., Fumana, M., Ilbert, O., Leauthaud, A., Maccagni, D., Marinoni, C., McCracken, H. J., Memeo, P., Nair, P., Oesch, P., Pozzetti, L., Presotto, V., & Scaramella, R. 2010, MNRAS, 409, 867–872

Di Matteo, T., Springel, V., & Hernquist, L. 2005, Nature, 433, 604–607

Donley, J. L., Rieke, G. H., Rigby, J. R., & Pérez-González, P. G. 2005, ApJ, 634, 169–182

Donley, J. L., Koekemoer, A. M., Brusa, M., Capak, P., Cardamone, C. N., Civano, F., Ilbert, O., Impey, C. D., Kartaltepe, J. S., Miyaji, T., Salvato, M., Sanders, D. B., Trump, J. R., & Zamorani, G. 2012, ApJ, 748, 142

Donoso, E., Yan, L., Stern, D., & Assef, R. J. 2013, ArXiv e-prints

Ellison, S. L., Patton, D. R., Mendel, J. T., & Scudder, J. M. 2011, MNRAS, 418, 2043–2053

Elvis, M., Civano, F., Vignali, C., Puccetti, S., Fiore, F., Cappelluti, N., Aldcroft, T. L., Fruscione, A., Zamorani, G., Comastri, A., Brusa, M., Gilli, R., Miyaji, T., Damiani, F., Koekemoer, A. M., Finoguenov, A., Brunner, H., Urry, C. M., Silverman, J., Mainieri, V., Hasinger, G., Griffiths, R., Carollo, M., Hao, H., Guzzo, L., Blain, A., Calzetti, D., Carilli, C., Capak, P., Ettori, S., Fabbiano, G., Impey, C., Lilly, S., Mobasher, B., Rich, M., Salvato, M., Sanders, D. B., Schinnerer, E., Scoville, N., Shopbell, P., Taylor, J. E., Taniguchi, Y., & Volonteri, M. 2009, ApJS, 184, 158–171

Faber, S. M., Phillips, A. C., Kibrick, R. I., Alcott, B., Allen, S. L., Burrous, J., Cantrall, T., Clarke, D., Coil, A. L., Cowley, D. J., Davis, M., Deich, W. T. S., Dietsch, K., Gilmore, D. K., Harper, C. A., Hilyard, D. F., Lewis, J. P., McVeigh, M., Newman, J., Osborne, J., Schiavon, R., Stover, R. J., Tucker, D., Wallace, V., Wei, M., Wirth, G., & Wright, C. A. 2003, In Society of Photo-Optical Instrumentation Engineers (SPIE) Conference Series, M. Iye and A. F. M. Moorwood, eds., volume 4841 of *Society of Photo-Optical Instrumentation Engineers (SPIE) Conference Series*, pp. 1657–1669

Fanaroff, B. L., & Riley, J. M. 1974, MNRAS, 167, 31P–36P

Fanidakis, N., Georgakakis, A., Mountrichas, G., Krumpe, M., Baugh, C. M., Lacey, C. G., Frenk, C. S., Miyaji, T., & Benson, A. J. 2013, MNRAS, 435, 679–688

Ferrarese, L., & Ford, H. 2005, Space Sci. Rev., 116, 523–624

Franceschini, A., Hasinger, G., Miyaji, T., & Malquori, D. 1999, MNRAS, 310, L5–L9

Gabor, J. M., Impey, C. D., Jahnke, K., Simmons, B. D., Trump, J. R., Koekemoer, A. M., Brusa, M., Cappelluti, N., Schinnerer, E., Smolčić, V., Salvato, M., Rhodes, J. D., Mobasher, B., Capak, P., Massey, R., Leauthaud, A., & Scoville, N. 2009, ApJ, 691, 705–722

Gebhardt, K., Bender, R., Bower, G., Dressler, A., Faber, S. M., Filippenko, A. V., Green, R., Grillmair, C., Ho, L. C., Kormendy, J., Lauer, T. R., Magorrian, J., Pinkney, J., Richstone, D., & Tremaine, S. 2000, ApJL, 539, L13–L16

Georgakakis, A., Nandra, K., Laird, E. S., Aird, J., & Trichas, M. 2008, MNRAS, 388, 1205–1213

Gilli, R., Daddi, E., Zamorani, G., Tozzi, P., Borgani, S., Bergeron, J., Giacconi, R., Hasinger, G., Mainieri, V., Norman, C., Rosati, P., Szokoly, G., & Zheng, W. 2005, A&A, 430, 811–825

Gilli, R., Daddi, E., Chary, R., Dickinson, M., Elbaz, D., Giavalisco, M., Kitzbichler, M., Stern, D., & Vanzella, E. 2007, A&A, 475, 83–99

Gilli, R., Zamorani, G., Miyaji, T., Silverman, J., Brusa, M., Mainieri, V., Cappelluti, N., Daddi, E., Porciani, C., Pozzetti, L., Civano, F., Comastri, A., Finoguenov, A., Fiore, F., Salvato, M., Vignali, C., Hasinger, G., Lilly, S., Impey, C., Trump, J., Capak, P., McCracken, H., Scoville, N., Taniguchi, Y., Carollo, C. M., Contini, T., Kneib, J.-P., Le Fevre, O., Renzini, A., Scodeggio, M., Bardelli, S., Bolzonella, M., Bongiorno, A., Caputi, K., Cimatti, A., Coppa, G., Cucciati, O., de La Torre, S., de Ravel, L., Franzetti, P., Garilli, B., Iovino, A., Kampczyk, P., Knobel, C., Kovač, K., Lamareille, F., Le Borgne, J.-F., Le Brun, V., Maier, C., Mignoli, M., Pellò, R., Peng, Y., Perez Montero, E., Ricciardelli, E., Tanaka, M., Tasca, L., Tresse, L., Vergani, D., Zucca, E., Abbas, U., Bottini, D., Cappi, A., Cassata, P., Fumana, M., Guzzo, L., Leauthaud, A., Maccagni, D., Marinoni, C., Memeo, P., Meneux, B., Oesch, P., Scaramella, R., & Walcher, J. 2009, A&A, 494, 33–48

Goulding, A. D., Forman, W. R., Hickox, R. C., Jones, C., Kraft, R., Murray, S. S., Vikhlinin, A., Coil, A. L., Cooper, M. C., Davis, M., & Newman, J. A. 2012, ApJS, 202, 6

Goulding, A. D., Forman, W. R., Hickox, R. C., Jones, C., Murray, S. S., Paggi, A., Ashby, M. L. N., Coil, A. L., Cooper, M. C., Huang, J.-S., Kraft, R., Newman, J. A., Weiner, B. J., & Willner, S. P. 2014, ApJ, 783, 40

Hasinger, G., Cappelluti, N., Brunner, H., Brusa, M., Comastri, A., Elvis, M., Finoguenov, A., Fiore, F., Franceschini, A., Gilli, R., Griffiths, R. E., Lehmann, I., Mainieri, V., Matt, G., Matute, I., Miyaji, T., Molendi, S., Paltani, S., Sanders, D. B., Scoville, N., Tresse, L., Urry, C. M., Vettolani, P., & Zamorani, G. 2007, ApJS, 172, 29–37

Hickox, R. C., Jones, C., Forman, W. R., Murray, S. S., Kochanek, C. S., Eisenstein, D., Jannuzi, B. T., Dey, A., Brown, M. J. I., Stern, D., Eisenhardt, P. R., Gorjian, V., Brodwin, M., Narayan, R., Cool, R. J., Kenter, A., Caldwell, N., & Anderson, M. E. 2009, ApJ, 696, 891–919

Hickox, R. C., Myers, A. D., Brodwin, M., Alexander, D. M., Forman, W. R., Jones, C., Murray, S. S., Brown, M. J. I., Cool, R. J., Kochanek, C. S., Dey, A., Jannuzi, B. T., Eisenstein, D., Assef, R. J., Eisenhardt, P. R., Gorjian, V., Stern, D., Le Floc'h, E., Caldwell, N., Goulding, A. D., & Mullaney, J. R. 2011, ApJ, 731, 117

Hickox, R. C., Mullaney, J. R., Alexander, D. M., Chen, C.-T. J., Civano, F. M., Goulding, A. D., & Hainline, K. N. 2014, ApJ, 782, 9

Hopkins, P. F., Strauss, M. A., Hall, P. B., Richards, G. T., Cooper, A. S., Schneider, D. P., Vanden Berk, D. E., Jester, S., Brinkmann, J., & Szokoly, G. P. 2004, AJ, 128, 1112–1123

Hopkins, P. F., Hernquist, L., Cox, T. J., Di Matteo, T., Martini, P., Robertson, B., & Springel, V. 2005, ApJ, 630, 705–715

Hopkins, P. F., Hernquist, L., Cox, T. J., Di Matteo, T., Robertson, B., & Springel, V. 2006, ApJS, 163, 1

Hopkins, P. F., Richards, G. T., & Hernquist, L. 2007, ApJ, 654, 731–753

Hopkins, P. F., Hernquist, L., Cox, T. J., & Kereš, D. 2008, ApJS, 175, 356–389

Ivison, R. J., Chapman, S. C., Faber, S. M., Smail, I., Biggs, A. D., Conselice, C. J., Wilson, G., Salim, S., Huang, J.-S., & Willner, S. P. 2007, ApJL, 660, L77–L80

Kauffmann, G., & Haehnelt, M. 2000, MNRAS, 311, 576–588

Kauffmann, G., Heckman, T. M., White, S. D. M., Charlot, S., Tremonti, C., Brinchmann, J., Bruzual, G., Peng, E. W., Seibert, M., Bernardi, M., Blanton, M., Brinkmann, J., Castander, F., Csábai, I., Fukugita, M., Ivezic, Z., Munn, J. A., Nichol, R. C., Padmanabhan, N., Thakar, A. R., Weinberg, D. H., & York, D. 2003, MNRAS, 341, 33–53

Kocevski, D. D., Faber, S. M., Mozena, M., Koekemoer, A. M., Nandra, K., Rangel, C., Laird, E. S., Brusa, M., Wuyts, S., Trump, J. R., Koo, D. C., Somerville, R. S., Bell, E. F., Lotz, J. M., Alexander, D. M., Bournaud, F., Conselice, C. J., Dahlen, T., Dekel, A., Donley, J. L., Dunlop, J. S., Finoguenov, A., Georgakakis, A., Giavalisco, M., Guo, Y., Grogin, N. A., Hathi, N. P., Juneau, S., Kartaltepe, J. S., Lucas, R. A., McGrath, E. J., McIntosh, D. H., Mobasher, B., Robaina, A. R., Rosario, D., Straughn, A. N., van der Wel, A., & Villforth, C. 2012, ApJ, 744, 148

Kormendy, J., & Ho, L. C. 2013, ARA&A, 51, 511–653

Kormendy, J., & Richstone, D. 1995, ARA&A, 33, 581

Kovač, K., Lilly, S. J., Cucciati, O., Porciani, C., Iovino, A., Zamorani, G., Oesch, P., Bolzonella, M., Knobel, C., Finoguenov, A., Peng, Y., Carollo, C. M., Pozzetti, L., Caputi, K., Silverman, J. D., Tasca, L. A. M., Scodeggio, M., Vergani, D., Scoville, N. Z., Capak, P., Contini, T., Kneib, J.-P., Le Fèvre, O., Mainieri, V., Renzini, A., Bardelli, S., Bongiorno, A., Coppa, G., de la Torre, S., de Ravel, L., Franzetti, P., Garilli, B., Guzzo, L., Kampczyk, P., Lamareille, F., Le Borgne, J.-F., Le Brun, V., Maier, C., Mignoli, M., Pello, R., Perez Montero, E., Ricciardelli, E., Tanaka, M., Tresse, L., Zucca, E., Abbas, U., Bottini, D., Cappi, A., Cassata, P., Cimatti, A., Fumana, M., Koekemoer, A. M., Maccagni, D., Marinoni, C., McCracken, H. J., Memeo, P., Meneux, B., & Scaramella, R. 2010, ApJ, 708, 505–533

Krumpe, M., Miyaji, T., & Coil, A. L. 2010, ApJ, 713, 558–572

Laird, E. S., Nandra, K., Georgakakis, A., Aird, J. A., Barmby, P., Conselice, C. J., Coil, A. L., Davis, M., Faber, S. M., Fazio, G. G., Guhathakurta, P., Koo, D. C., Sarajedini, V., & Willmer, C. N. A. 2009, ApJS, 180, 102–116

Landy, S. D., & Szalay, A. S. 1993, ApJ, 412, 64–71

Le Fèvre, O., Vettolani, G., Garilli, B., Tresse, L., Bottini, D., Le Brun, V., Maccagni, D., Picat, J. P., Scaramella, R., Scodeggio, M., Zanichelli, A., Adami, C., Arnaboldi, M., Arnouts, S., Bardelli, S., Bolzonella, M., Cappi, A., Charlot, S., Ciliegi, P., Contini, T., Foucaud, S., Franzetti, P., Gavignaud, I., Guzzo, L., Ilbert, O., Iovino, A., McCracken, H. J., Marano, B., Marinoni, C., Mathez, G., Mazure, A., Meneux, B., Merighi, R., Paltani, S., Pellò, R., Pollo, A., Pozzetti, L., Radovich, M., Zamorani, G., Zucca, E., Bondi, M., Bongiorno, A., Busarello, G., Lamareille, F., Mellier, Y., Merluzzi, P., Ripepi, V., & Rizzo, D. 2005, A&A, 439, 845–862

Lilly, S. J., Le Fèvre, O., Renzini, A., Zamorani, G., Scodeggio, M., Contini, T., Carollo, C. M., Hasinger, G., Kneib, J.-P., Iovino, A., Le Brun, V., Maier, C., Mainieri, V., Mignoli, M., Silverman, J., Tasca, L. A. M., Bolzonella, M., Bongiorno, A., Bottini, D., Capak, P., Caputi, K., Cimatti, A., Cucciati, O., Daddi, E., Feldmann, R., Franzetti, P., Garilli, B., Guzzo, L., Ilbert, O., Kampczyk, P., Kovac, K., Lamareille, F., Leauthaud, A., Borgne, J.-F. L., McCracken, H. J., Marinoni, C., Pello, R., Ricciardelli, E., Scarlata, C., Vergani, D., Sanders, D. B., Schinnerer, E., Scoville, N., Taniguchi, Y., Arnouts, S., Aussel, H., Bardelli, S., Brusa, M., Cappi, A., Ciliegi, P., Finoguenov, A., Foucaud, S., Franceschini, R., Halliday, C., Impey, C., Knobel, C., Koekemoer, A., Kurk, J., Maccagni, D., Maddox, S., Marano, B., Marconi, G., Meneux, B., Mobasher, B., Moreau, C., Peacock, J. A., Porciani, C., Pozzetti, L., Scaramella, R., Schiminovich, D., Shopbell, P., Smail, I., Thompson, D., Tresse, L., Vettolani, G., Zanichelli, A., & Zucca, E. 2007, ApJS, 172, 70–85

Lindsay, S. N., Jarvis, M. J., Santos, M. G., Brown, M. J. I., Croom, S. M., Driver, S. P., Hopkins, A. M., Liske, J., Loveday, J., Norberg, P., & Robotham, A. S. G. 2014, MNRAS, 440, 1527–1541

Lonsdale, C. J., Smith, H. E., Rowan-Robinson, M., Surace, J., Shupe, D., Xu, C., Oliver, S., Padgett, D., Fang, F., Conrow, T., Franceschini, A., Gautier, N., Griffin, M., Hacking, P., Masci, F., Morrison, G., O'Linger, J., Owen, F., Pérez-Fournon, I., Pierre, M., Puetter, R., Stacey, G., Castro, S., Polletta, M. d. C., Farrah, D., Jarrett, T., Frayer, D., Siana, B., Babbedge, T., Dye, S., Fox, M., Gonzalez-Solares, E., Salaman, M., Berta, S., Condon, J. J., Dole, H., & Serjeant, S. 2003, PASP, 115, 897–927

Lupton, R. 1993. Statistics in theory and practice

Madau, P., Ferguson, H. C., Dickinson, M. E., Giavalisco, M., Steidel, C. C., & Fruchter, A. 1996, MNRAS, 283, 1388–1404

Magliocchetti, M., Maddox, S. J., Lahav, O., & Wall, J. V. 1999, MNRAS, 306, 943–953

Magliocchetti, M., Maddox, S. J., Hawkins, E., Peacock, J. A., Bland-Hawthorn, J., Bridges, T., Cannon, R., Cole, S., Colless, M., Collins, C., Couch, W., Dalton, G., de Propris, R., Driver, S. P., Efstathiou, G., Ellis, R. S., Frenk, C. S., Glazebrook, K., Jackson, C. A., Jones, B., Lahav, O., Lewis, I., Lumsden, S., Norberg, P., Peterson, B. A., Sutherland, W., Taylor, K., & 2dFGRS Team 2004, MNRAS, 350, 1485–1494

Magorrian, J., Tremaine, S., Richstone, D., Bender, R., Bower, G., Dressler, A., Faber, S. M., Gebhardt, K., Green, R., Grillmair, C., Kormendy, J., & Lauer, T. 1998, AJ, 115, 2285–2305

Mandelbaum, R., Li, C., Kauffmann, G., & White, S. D. M. 2009, MNRAS, 393, 377–392

Marconi, A., & Hunt, L. K. 2003, ApJL, 589, L21–L24

Marulli, F., Bonoli, S., Branchini, E., Moscardini, L., & Springel, V. 2008, MNRAS, 385, 1846–1858

Mateos, S., Alonso-Herrero, A., Carrera, F. J., Blain, A., Watson, M. G., Barcons, X., Braito, V., Severgnini, P., Donley, J. L., & Stern, D. 2012, MNRAS, 426, 3271–3281

Mateos, S., Alonso-Herrero, A., Carrera, F. J., Blain, A., Severgnini, P., Caccianiga, A., & Ruiz, A. 2013, MNRAS, 434, 941–955

Matthews, D. J., Newman, J. A., Coil, A. L., Cooper, M. C., & Gwyn, S. D. J. 2013, ApJS, 204, 21

McCracken, H. J., Peacock, J. A., Guzzo, L., Capak, P., Porciani, C., Scoville, N., Aussel, H., Finoguenov, A., James, J. B., Kitzbichler, M. G., Koekemoer, A., Leauthaud, A., Le Fèvre, O., Massey, R., Mellier, Y., Mobasher, B., Norberg, P., Rhodes, J., Sanders, D. B., Sasaki, S. S., Taniguchi, Y., Thompson, D. J., White, S. D. M., & El-Zant, A. 2007, ApJS, 172, 314–319

Menci, N., Cavaliere, A., Fontana, A., Giallongo, E., Poli, F., & Vittorini, V. 2003, ApJL, 587, L63–L66

Menci, N., Fontana, A., Giallongo, E., Grazian, A., & Salimbeni, S. 2006, ApJ, 647, 753–762

Mendez, A. J., Coil, A. L., Aird, J., Diamond-Stanic, A. M., Moustakas, J., Blanton, M. R., Cool, R. J., Eisenstein, D. J., Wong, K. C., & Zhu, G. 2013, ApJ, 770, 40

Meneux, B., Guzzo, L., de la Torre, S., Porciani, C., Zamorani, G., Abbas, U., Bolzonella, M., Garilli, B., Iovino, A., Pozzetti, L., Zucca, E., Lilly, S. J., Le Fèvre, O., Kneib, J.-P., Carollo, C. M., Contini, T., Mainieri, V., Renzini, A., Scodeggio, M., Bardelli, S., Bongiorno, A., Caputi, K., Coppa, G., Cucciati, O., de Ravel, L., Franzetti, P., Kampczyk, P., Knobel, C., Kovač, K., Lamareille, F., Le Borgne, J.-F., Le Brun, V., Maier, C., Pellò, R., Peng, Y., Perez Montero, E., Ricciardelli, E., Silverman, J. D., Tanaka, M., Tasca, L., Tresse, L., Vergani, D., Bottini, D., Cappi, A., Cimatti, A., Cassata, P., Fumana, M., Koekemoer, A. M., Leauthaud, A., Maccagni, D., Marinoni, C., McCracken, H. J., Memeo, P., Oesch, P., & Scaramella, R. 2009, A&A, 505, 463–482

Middelberg, E., Norris, R. P., Cornwell, T. J., Voronkov, M. A., Siana, B. D., Boyle, B. J., Ciliegi, P., Jackson, C. A., Huynh, M. T., Berta, S., Rubele, S., Lonsdale, C. J., Ivison, R. J., Smail, I., & Oliver, S. J. 2007, ArXiv e-prints

Monaco, P., Fontanot, F., & Taffoni, G. 2007, MNRAS, 375, 1189–1219

Moustakas, J., Coil, A. L., Aird, J., Blanton, M. R., Cool, R. J., Eisenstein, D. J., Mendez, A. J., Wong, K. C., Zhu, G., & Arnouts, S. 2013, ApJ, 767, 50

Mullaney, J. R., Daddi, E., Béthermin, M., Elbaz, D., Juneau, S., Pannella, M., Sargent, M. T., Alexander, D. M., & Hickox, R. C. 2012, ApJL, 753, L30

Mullaney, J. R., Alexander, D. M., Fine, S., Goulding, A. D., Harrison, C. M., & Hickox, R. C. 2013, MNRAS, 433, 622–638

Murphy, E. J., Condon, J. J., Schinnerer, E., Kennicutt, R. C., Calzetti, D., Armus, L., Helou, G., Turner, J. L., Aniano, G., Beirão, P., Bolatto, A. D., Brandl, B. R., Croxall, K. V., Dale, D. A., Donovan Meyer, J. L., Draine, B. T., Engelbracht, C., Hunt, L. K., Hao, C.-N., Koda, J., Roussel, H., Skibba, R., & Smith, J.-D. T. 2011, ApJ, 737, 67

Myers, A. D., Brunner, R. J., Richards, G. T., Nichol, R. C., Schneider, D. P., Vanden Berk, D. E., Scranton, R., Gray, A. G., & Brinkmann, J. 2006, ApJ, 638, 622–634

Newman, J. A., Cooper, M. C., Davis, M., Faber, S. M., Coil, A. L., Guhathakurta, P., Koo, D. C., Phillips, A. C., Conroy, C., Dutton, A. A., Finkbeiner, D. P., Gerke, B. F., Rosario, D. J., Weiner, B. J., Willmer, C. N. A., Yan, R., Harker, J. J., Kassin, S. A., Konidaris, N. P., Lai, K., Madgwick, D. S., Noeske, K. G., Wirth, G. D., Connolly, A. J., Kaiser, N., Kirby, E. N., Lemaux, B. C., Lin, L., Lotz, J. M., Luppino, G. A., Marinoni, C., Matthews, D. J., Metevier, A., & Schiavon, R. P. 2012, ArXiv e-prints

Norris, R. P., Afonso, J., Appleton, P. N., Boyle, B. J., Ciliegi, P., Croom, S. M., Huynh, M. T., Jackson, C. A., Koekemoer, A. M., Lonsdale, C. J., Middelberg, E., Mobasher, B., Oliver, S. J., Polletta, M., Siana, B. D., Smail, I., & Voronkov, M. A. 2006, AJ, 132, 2409–2423

Oliver, S., Rowan-Robinson, M., Alexander, D. M., Almaini, O., Balcells, M., Baker, A. C., Barcons, X., Barden, M., Bellas-Velidis, I., Cabrera-Guerra, F., Carballo, R., Cesarsky, C. J., Ciliegi, P., Clements, D. L., Crockett, H., Danese, L., Dapergolas, A., Drolias, B., Eaton, N., Efstathiou, A., Egami, E., Elbaz, D., Fadda, D., Fox, M., Franceschini, A., Genzel, R., Goldschmidt, P., Graham, M., Gonzalez-Serrano, J. I., Gonzalez-Solares, E. A., Granato, G. L., Gruppioni, C., Herbstmeier, U., Héraudeau, P., Joshi, M., Kontizas, E., Kontizas, M., Kotilainen, J. K., Kunze, D., La Franca, F., Lari, C., Lawrence, A., Lemke, D., Linden-Vørnle, M. J. D., Mann, R. G., Márquez, I., Masegosa, J., Mattila, K., McMahon, R. G., Miley, G., Missoulis, V., Mobasher, B., Morel, T., Nørgaard-Nielsen, H., Omont, A., Papadopoulos, P., Perez-Fournon, I., Puget, J.-L., Rigopoulou, D., Rocca-Volmerange, B., Serjeant, S., Silva, L., Sumner, T., Surace, C., Vaisanen, P., van der Werf, P. P., Verma, A., Vigroux, L., Villar-Martin, M., & Willott, C. J. 2000, MNRAS, 316, 749–767

Park, S. Q., Barmby, P., Fazio, G. G., Nandra, K., Laird, E. S., Georgakakis, A., Rosario, D., Willner, S. P., Rieke, G. H., Ashby, M. L. N., Ivison, R. J., Coil, A. L., & Miyazaki, S. 2008, ApJ, 678, 744–750

Peebles, P. J. E. 1980. The large-scale structure of the universe

Pierre, M., Valtchanov, I., Altieri, B., Andreon, S., Bolzonella, M., Bremer, M., Disseau, L., Dos Santos, S., Gandhi, P., Jean, C., Pacaud, F., Read, A., Refregier, A., Willis, J., Adami, C., Alloin, D., Birkinshaw, M., Chiappetti, L., Cohen, A., Detal, A., Duc, P.-A., Gosset, E., Hjorth, J., Jones, L., Le Fèvre, O., Lonsdale, C., Maccagni, D., Mazure, A., McBreen, B., McCracken, H., Mellier, Y., Ponman, T., Quintana, H., Rottgering, H., Smette, A., Surdej, J., Starck, J.-L., Vigroux, L., & White, S. 2004, , 9, 11

Puccetti, S., Fiore, F., D'Elia, V., Pillitteri, I., Feruglio, C., Grazian, A., Brusa, M., Ciliegi, P., Comastri, A., Gruppioni, C., Mignoli, M., Vignali, C., Zamorani, G., La Franca, F., Sacchi, N., Franceschini, A., Berta, S., Buttery, H., & Dias, J. E. 2006, A&A, 457, 501–515

Richstone, D., Ajhar, E. A., Bender, R., Bower, G., Dressler, A., Faber, S. M., Filippenko, A. V., Gebhardt, K., Green, R., Ho, L. C., Kormendy, J., Lauer, T. R., Magorrian, J., & Tremaine, S. 1998, Nature, 395, A14

Risaliti, G., Bassani, L., Comastri, A., Dadina, M., Della Ceca, R., Gilli, R., Maiolino, R., Matt, G., Salvati, M., & Zamorani, G. 1999, Mem. Soc. Astron. Italiana, 70, 73–76

Rosario, D. J., McGurk, R. C., Max, C. E., Shields, G. A., Smith, K. L., & Ammons, S. M. 2011, ApJ, 739, 44

Salim, S., Rich, R. M., Charlot, S., Brinchmann, J., Johnson, B. D., Schiminovich, D., Seibert, M., Mallery, R., Heckman, T. M., Forster, K., Friedman, P. G., Martin, D. C., Morrissey, P., Neff, S. G., Small, T., Wyder, T. K., Bianchi, L., Donas, J., Lee, Y.-W., Madore, B. F., Milliard, B., Szalay, A. S., Welsh, B. Y., & Yi, S. K. 2007, ApJS, 173, 267–292

Sanders, D. B., & Mirabel, I. F. 1996, ARA&A, 34, 749

Sanders, D. B., Soifer, B. T., Elias, J. H., Madore, B. F., Matthews, K., Neugebauer, G., & Scoville, N. Z. 1988, ApJ, 325, 74–91

Schawinski, K., Dowlin, N., Thomas, D., Urry, C. M., & Edmondson, E. 2010, ApJL, 714, L108–L112

Schinnerer, E., Smolčić, V., Carilli, C. L., Bondi, M., Ciliegi, P., Jahnke, K., Scoville, N. Z., Aussel, H., Bertoldi, F., Blain, A. W., Impey, C. D., Koekemoer, A. M., Le Fevre, O., & Urry, C. M. 2007, ApJS, 172, 46–69

Schinnerer, E., Sargent, M. T., Bondi, M., Smolčić, V., Datta, A., Carilli, C. L., Bertoldi, F., Blain, A., Ciliegi, P., Koekemoer, A., & Scoville, N. Z. 2010, ApJS, 188, 384–404

Scoville, N., Aussel, H., Brusa, M., Capak, P., Carollo, C. M., Elvis, M., Giavalisco, M., Guzzo, L., Hasinger, G., Impey, C., Kneib, J.-P., LeFevre, O., Lilly, S. J., Mobasher, B., Renzini, A., Rich, R. M., Sanders, D. B., Schinnerer, E., Schminovich, D., Shopbell, P., Taniguchi, Y., & Tyson, N. D. 2007, ApJS, 172, 1–8

Scranton, R., Johnston, D., Dodelson, S., Frieman, J. A., Connolly, A., Eisenstein, D. J., Gunn, J. E., Hui, L., Jain, B., Kent, S., Loveday, J., Narayanan, V., Nichol, R. C., O'Connell, L., Scoccimarro, R., Sheth, R. K., Stebbins, A., Strauss, M. A., Szalay, A. S., Szapudi, I., Tegmark, M., Vogeley, M., Zehavi, I., Annis, J., Bahcall, N. A., Brinkman, J., Csabai, I., Hindsley, R., Ivezic, Z., Kim, R. S. J., Knapp, G. R., Lamb, D. Q., Lee, B. C., Lupton, R. H., McKay, T., Munn, J., Peoples, J., Pier, J., Richards, G. T., Rockosi, C., Schlegel, D., Schneider, D. P., Stoughton, C., Tucker, D. L., Yanny, B., & York, D. G. 2002, ApJ, 579, 48–75

Serjeant, S., Negrello, M., Pearson, C., Mortier, A., Austermann, J., Aretxaga, I., Clements, D., Chapman, S., Dye, S., Dunlop, J., Dunne, L., Farrah, D., Hughes, D., Lee, H.-M., Matsuhara, H., Ibar, E., Im, M., Jeong, W.-S., Kim, S., Oyabu, S., Takagi, T., Wada, T., Wilson, G., Vaccari, M., & Yun, M. 2010, A&A, 514, A10

Simpson, C., Martínez-Sansigre, A., Rawlings, S., Ivison, R., Akiyama, M., Sekiguchi, K., Takata, T., Ueda, Y., & Watson, M. 2006, MNRAS, 372, 741–757

Skibba, R. A., Smith, M. S. M., Coil, A. L., Moustakas, J., Aird, J., Blanton, M. R., Bray, A. D., Cool, R. J., Eisenstein, D. J., Mendez, A. J., Wong, K. C., & Zhu, G. 2014, ApJ, 784, 128

Smith, R. E., Peacock, J. A., Jenkins, A., White, S. D. M., Frenk, C. S., Pearce, F. R., Thomas, P. A., Efstathiou, G., & Couchman, H. M. P. 2003, MNRAS, 341, 1311–1332

Smolčić, V., Schinnerer, E., Scodeggio, M., Franzetti, P., Aussel, H., Bondi, M., Brusa, M., Carilli, C. L., Capak, P., Charlot, S., Ciliegi, P., Ilbert, O., Ivezić, Ž., Jahnke, K., McCracken, H. J., Obrić, M., Salvato, M., Sanders, D. B., Scoville, N., Trump, J. R., Tremonti, C., Tasca, L., Walcher, C. J., & Zamorani, G. 2008, ApJS, 177, 14–38

Snyder, G. F., Cox, T. J., Hayward, C. C., Hernquist, L., & Jonsson, P. 2011, ApJ, 741, 77

Soltan, A. 1982, MNRAS, 200, 115–122

Springel, V., Di Matteo, T., & Hernquist, L. 2005a, ApJL, 620, L79

Springel, V., Di Matteo, T., & Hernquist, L. 2005b, MNRAS, 361, 776

Stern, D., Eisenhardt, P., Gorjian, V., Kochanek, C. S., Caldwell, N., Eisenstein, D., Brodwin, M., Brown, M. J. I., Cool, R., Dey, A., Green, P., Jannuzi, B. T., Murray, S. S., Pahre, M. A., & Willner, S. P. 2005, ApJ, 631, 163–168

Stern, D., Assef, R. J., Benford, D. J., Blain, A., Cutri, R., Dey, A., Eisenhardt, P., Griffith, R. L., Jarrett, T. H., Lake, S., Masci, F., Petty, S., Stanford, S. A., Tsai, C.-W., Wright, E. L., Yan, L., Harrison, F., & Madsen, K. 2012, ApJ, 753, 30

Sutherland, W., & Saunders, W. 1992, MNRAS, 259, 413–420

Treister, E., Urry, C. M., Chatzichristou, E., Bauer, F., Alexander, D. M., Koekemoer, A., Van Duyne, J., Brandt, W. N., Bergeron, J., Stern, D., Moustakas, L. A., Chary, R.-R., Conselice, C., Cristiani, S., & Grogin, N. 2004, ApJ, 616, 123–135

Tremaine, S., Gebhardt, K., Bender, R., Bower, G., Dressler, A., Faber, S. M., Filippenko, A. V., Green, R., Grillmair, C., Ho, L. C., Kormendy, J., Lauer, T. R., Magorrian, J., Pinkney, J., & Richstone, D. 2002, ApJ, 574, 740–753

Ueda, Y., Akiyama, M., Ohta, K., & Miyaji, T. 2003, ApJ, 598, 886–908

Ueda, Y., Watson, M. G., Stewart, I. M., Akiyama, M., Schwope, A. D., Lamer, G., Ebrero, J., Carrera, F. J., Sekiguchi, K., Yamada, T., Simpson, C., Hasinger, G., & Mateos, S. 2008, ApJS, 179, 124–141

Urry, C. M., & Padovani, P. 1995, PASP, 107, 803

Wake, D. A., Croom, S. M., Sadler, E. M., & Johnston, H. M. 2008, MNRAS, 391, 1674–1684

Willner, S. P., Ashby, M. L. N., Barmby, P., Chapman, S. C., Coil, A. L., Cooper, M. C., Huang, J.-S., Ivison, R., & Koo, D. C. 2012, ApJ, 756, 72

Wright, E. L., Eisenhardt, P. R. M., Mainzer, A. K., Ressler, M. E., Cutri, R. M., Jarrett, T., Kirkpatrick, J. D., Padgett, D., McMillan, R. S., Skrutskie, M., Stanford, S. A., Cohen, M., Walker, R. G., Mather, J. C., Leisawitz, D., Gautier, III, T. N., McLean, I., Benford, D., Lonsdale, C. J., Blain, A., Mendez, B., Irace, W. R., Duval, V., Liu, F., Royer, D., Heinrichsen, I., Howard, J., Shannon, M., Kendall, M., Walsh, A. L., Larsen, M., Cardon, J. G., Schick, S., Schwalm, M., Abid, M., Fabinsky, B., Naes, L., & Tsai, C.-W. 2010, AJ, 140, 1868–1881

Yan, L., Donoso, E., Tsai, C.-W., Stern, D., Assef, R. J., Eisenhardt, P., Blain, A. W., Cutri, R., Jarrett, T., Stanford, S. A., Wright, E., Bridge, C., & Riechers, D. A. 2013, AJ, 145, 55

Yang, Y., Mushotzky, R. F., Barger, A. J., & Cowie, L. L. 2006, ApJ, 645, 68–82

Zehavi, I., Zheng, Z., Weinberg, D. H., Frieman, J. A., Berlind, A. A., Blanton, M. R., Scoccimarro, R., Sheth, R. K., Strauss, M. A., Kayo, I., Suto, Y., Fukugita, M., Nakamura, O., Bahcall, N. A., Brinkmann, J., Gunn, J. E., Hennessy, G. S., Ivezić, Ž., Knapp, G. R., Loveday, J., Meiksin, A., Schlegel, D. J., Schneider, D. P., Szapudi, I., Tegmark, M., Vogeley, M. S., York, D. G., & SDSS Collaboration 2005, ApJ, 630, 1–27

Zheng, Z., Zehavi, I., Eisenstein, D. J., Weinberg, D. H., & Jing, Y. P. 2009, ApJ, 707, 554–572

Chapter 5

Conclusions and future work

The work contained in this dissertation constrains the evolution of galaxies and AGNs using morphological galaxy measurements, multi-wavelength AGN identification techniques, and three-dimensional clustering analyses.

The first chapter presents a study of transition galaxies in the green valley using HST data in the AEGIS survey and concludes that the physical process(es) quenching star-formation in galaxies since $z \sim 1$ are not dominated by major mergers but instead must build up the central mass concentration in these galaxies, while retaining a disk. We find 1) that the merger fraction is lower in the green valley compared to the blue cloud, both for major and minor mergers (from G/M_{20} and A measurements), 2) that at a given stellar mass the B/T ratio and median concentration (C) is higher in the green valley than in the blue cloud, reflecting the build up of the bulge component, and 3) that half (51%) of the green valley galaxies are disk-dominated, implying that they have not had a major merger in the recent past. These results show that the paradigm of major mergers dominating the quenching of galaxies at $z < 1$ is incorrect and that the quenching mechanism must be more mild and likely involve secular processes.

The second chapter presents a study of the demographics of the AGN populations identified through X-ray and mid-IR selection techniques using deep X-ray and IR data in the PRIMUS redshift survey. We characterize the overlap, completeness, reliability, and demographics of these identified AGN populations as a function of both X-ray and IR imaging depth. We determine the AGN and host galaxy properties of the AGN populations selected at each wavelength. We further resolve the disparate conclusions found in the previous literature and show that the discrepancies arose because of differences in the depths of the data considered, as well as selection effects that were not taken into account. We find that the vast majority (90%) of IR-AGN identified with shallow IR surveys are X-ray detected with deep X-ray surveys, which clarifies that IR-AGN samples add an important but minor (10%) population of possibly heavily-obscured AGN. We further find that IR-selected AGN are limited to the most luminous AGN with high specific accretion rates (and therefore Eddington ratios), while X-ray selection additionally probes lower luminosity and lower specific accretion rate AGN. Combining IR and X-ray AGN selection leads to a more complete census of accretion activity.

The third chapter presents measurements of the three-dimensional clustering properties of X-ray AGN, radio AGN, and IR-AGN in the DEEP2 and PRIMUS fields, which allows us to place AGNs selected at different wavelengths in a cosmological context and estimate dark matter halo masses for each population. The different clustering amplitudes of X-ray AGN, radio AGN, and IR-AGN are shown to correlate with the specific accretion rate differences of the different AGN populations, and we show that each AGN population has similar clustering as galaxy samples that have the same distributions in stellar mass, star formation rate and redshift. The differences observed in the AGN clustering are therefore due to differences in their host galaxy populations.

There are many key open questions in galaxy and AGN evolution which can be addressed using this wealth of in-hand observational data and future data from the next generation of telescopes. An immediate next step will be to extend the stellar mass, star formation rate, and specific star formation rate dependent AGN clustering measurements to a framework for all galaxies in the PRIMUS and DEEP2 fields. Most galaxy clustering studies have quantified the clustering of galaxies based on relatively simple observed properties such as magnitude and color. Using instead derived physical parameters such as stellar mass and star formation rate will greatly improve comparisons to simulations and theory, while accounting for dust reprocessing, and the star formation-dependance of the luminosity-to-mass relationship (Zhu et al. 2011). The few existing results that estimate the stellar mass dependent galaxy clustering at intermediate redshifts use smaller samples that probe smaller volume and have large SFR uncertainties due to a lack of multi-wavelength imaging (e.g., DEEP2, VVDS, VIPERS Mostek et al. 2013; Meneux et al. 2008; Marulli et al. 2013). Combining the PRIMUS and the DEEP2 surveys creates the largest intermediate redshift clustering sample to date. Measuring the galaxy clustering amplitude with larger samples will allow for robust comparison with low redshift results (Li et al. 2006), constraining systematics and intrinsic environmental differences in these samples. Additionally, we will use cross-correlation measurements, as we have done with the AGN samples, which will result in smaller error bars on estimates of the dark matter halo masses, compared to estimates from auto-correlation measurements, as are usually done. We will place tight constraints on the environmental dependence of stellar mass buildup and star formation, while controlling for cosmic variance uncertainties. The long cosmological time baseline of the combined SDSS, DEEP2, and PRIMUS samples will allow a determination of the role of halo mass in quenching star formation and its role in limiting the infall of cold gas into galaxies.

In addition, improved multi-wavelength AGN identification techniques are needed to build a complete census of AGNs in the universe. Most current AGN selection techniques are entropy maximization techniques, in that they identify AGN that are most different from galaxy templates or most like known AGN templates. Combined with the fact that many techniques only use a portion of the available measured photometry (e.g. selection using one waveband), the identification of AGN is biased to a subset of the entire AGN population. Instead the next generation of identification techniques will identify AGN through multi-wavelength observations. The combination of simple stellar population (SSP) models, to estimate the galaxy SED light, combined with empirical AGN templates can be used to measure the likelihood that a given observed multi-wavelength SED contains AGN light. This will allow us to estimate both the probability that a given galaxy hosts an AGN and improve the measurements of the galaxy host properties by removing AGN contamination. Using a combination of X-ray, UV, optical, IR, and radio detections, or inferred upper limits, maximizes the number of possible AGN that can be identified far better than would any single waveband selection technique.

Accurately detecting and characterizing AGN and their host galaxies in this way across a wide range of redshifts opens up a large number of possible studies. Using this approach, every galaxy in existing and future large surveys can enter, in a statistical sense, into an AGN sample, which will vastly improve our understanding of the AGN population. Measuring the dependence of AGN clustering on both AGN luminosity and host galaxy stellar mass across a wider redshift range will be possible as AGN clustering measurements are currently limited by the low relative numbers of AGN, identified at an individual waveband, as compared to galaxies. We will further be able to probe to lower AGN luminosities than before, leading to stronger constraints on the triggering and fueling mechanisms of low luminosity AGN.

The bolometric AGN luminosity function (e.g., Hopkins, Richards, & Hernquist 2007) traces the growth of SMBH. Currently, luminosity functions are generally measured for AGN identified with individual wavebands, each with their own selection biases. The uniform and complete AGN selection described above can then be used to determine the AGN luminosity function, both limiting potential biases and extending to lower luminosities. In particular, this method determines the probability distribution of possible AGN luminosities for every galaxy in a given sample and additionally sets upper-limits on the possible AGN contribution to the SED. Integrating over this probability distribution for each source will provide the best estimate of the bolometric AGN luminosity function.

Finally, combining these studies at intermediate redshifts with low-redshift ($z \lesssim 0.1$) all-sky multi-wavelength surveys will precisely constrain the demographics of the AGN population across cosmic time. WISE mid-IR photometry, ROSAT X-ray point source catalogs, SDSS optical photometry and SDSS spectroscopic redshifts provide a large sample to identify and characterize AGN at low-redshift ($z \sim 0.05$) using the above multi-wavelength AGN selection technique. Such studies will improve current predictions for the AGN populations identified by the future eROSITA X-ray survey and the next generation WFIRST IR survey. Extrapolating from Mendez et al. (2013), at the depth of WISE, one should detect ∼100 IR-AGN per square degree, which matches the predicted numbers in Eisenhardt et al. (2011). WISE therefore will allow the precise characterization of both AGN and host galaxy properties using millions of AGN. This low-redshift sample complements our previous work on the AEGIS and PRIMUS redshift surveys by increasing the volume probed, cosmic time baseline, and luminosity range.

Accounting for the depth-dependent variations due to the spatially variable WISE depth photometry, as well as ROSAT X-ray data systematics due both to the limitations of the X-ray telescope optics and the survey scanning strategy are critically important (Mendez et al. 2013). Not controlling for these systematics would lead to biased results. The median depths of WISE and ROSAT are comparable, which ensures a fair comparison and allows for a robust determination of the obscured AGN fraction at low redshift. Additionally, the large number of derived products in the SDSS enables comparisons of AGN and galaxy host properties (e.g., stellar mass distribution, host galaxy type, accretion rates). The combination of multi-wavelength AGN samples at low and intermediate redshift provide a long cosmological time baseline which will be useful to identify trends and improve our understanding of the accretion history of the Universe, the growth of SMBH, and the relationship between AGN and their host galaxies.

5.1 References

Eisenhardt, P. R., Benford, D., Blain, A., Bridge, C., Cutri, R., Donoso, E., Griffith, R., Jarrett, T., Lake, S., Lonsdale, C., Masci, F., Petty, S., Stanford, S. A., Tsai, C., Wright, E. L., Wu, J., & Yan, L. 2011, In AAS #217, volume 43 of *BAAS*, p. 301.06

Hopkins, P. F., Richards, G. T., & Hernquist, L. 2007, ApJ, 654, 731–753

Li, C., Kauffmann, G., Jing, Y. P., White, S. D. M., Börner, G., & Cheng, F. Z. 2006, MNRAS, 368, 21–36

Marulli, F., Bolzonella, M., Branchini, E., Davidzon, I., de la Torre, S., Granett, B. R., Guzzo, L., Iovino, A., Moscardini, L., Pollo, A., Abbas, U., Adami, C., Arnouts, S., Bel, J., Bottini, D., Cappi, A., Coupon, J., Cucciati, O., De Lucia, G., Fritz, A., Franzetti, P., Fumana, M., Garilli, B., Ilbert, O., Krywult, J., Le Brun, V., Le Fèvre, O., Maccagni, D., Małek, K., McCracken, H. J., Paioro, L., Polletta, M., Schlagenhaufer, H., Scodeggio, M., Tasca, L. A. M., Tojeiro, R., Vergani, D., Zanichelli, A., Burden, A., Di Porto, C., Marchetti, A., Marinoni, C., Mellier, Y., Nichol, R. C., Peacock, J. A., Percival, W. J., Phleps, S., Wolk, M., & Zamorani, G. 2013, A&A, 557, A17

Mendez, A. J., Coil, A. L., Aird, J., Diamond-Stanic, A. M., Moustakas, J., Blanton, M. R., Cool, R. J., Eisenstein, D. J., Wong, K. C., & Zhu, G. 2013, ApJ, 770, 40

Meneux, B., Guzzo, L., Garilli, B., Le Fèvre, O., Pollo, A., Blaizot, J., De Lucia, G., Bolzonella, M., Lamareille, F., Pozzetti, L., Cappi, A., Iovino, A., Marinoni, C., McCracken, H. J., de la Torre, S., Bottini, D., Le Brun, V., Maccagni, D., Picat, J. P., Scaramella, R., Scodeggio, M., Tresse, L., Vettolani, G., Zanichelli, A., Abbas, U., Adami, C., Arnouts, S., Bardelli, S., Bongiorno, A., Charlot, S., Ciliegi, P., Contini, T., Cucciati, O., Foucaud, S., Franzetti, P., Gavignaud, I., Ilbert, O., Marano, B., Mazure, A., Merighi, R., Paltani, S., Pellò, R., Radovich, M., Vergani, D., Zamorani, G., & Zucca, E. 2008, A&A, 478, 299–310

Mostek, N., Coil, A. L., Cooper, M., Davis, M., Newman, J. A., & Weiner, B. J. 2013, ApJ, 767, 89

Zhu, G., Zaw, I., Blanton, M. R., & Greenhill, L. J. 2011, ApJ, 742, 73